



UNIVERSITY OF
LIVERPOOL

Evaluation of novel combination drug protocols for neuroblastoma using advanced imaging in a chick embryo model

**The thesis was submitted in accordance with the requirements of the
University of Liverpool for the degree of**

Doctor in Philosophy by

Keerthika Sampat

Date 31.08.2022

Declaration

This thesis is entitled:

“Evaluation of novel combination drug protocols for neuroblastoma using advanced imaging in a chick embryo model”

is entirely my work, except where indicated in the text.

The material contained within this thesis has not been presented for any other degree qualification.

This research was undertaken at the Institute of Systems, Molecular and Integrative Biology at the University of Liverpool and under the supervision of Professor Violaine See and Professor Paul Losty.

Acknowledgements

I want to express my deepest gratitude to my supervisors, Professor Violaine See and Professor Paul Losty, for their guidance and support throughout this work. I am genuinely grateful for the opportunity to do this work and for all the lessons I have learned along the way. I want to also extend my sincere thanks to Professor Barry Pizer and Dr Diana Moss for all their assistance.

I want to acknowledge several people and facilities. I am incredibly grateful to Dr Anne Herrmann for guiding me with all the chick embryo work; Dr Sandra Perera Cachinho for assisting with the FACS experiments, and Dr Chris Clarke for brainstorming and troubleshooting the immunofluorescence experiments with me (and for his unrelenting optimism!) and the staff at the Centre for Cell Imaging who supported me with all the microscopy work.

A special thank you to Rebecca and Claire, whose daily counsel and encouragement over the past few years have helped me get this PhD over the line. I cherished our time in the lab together and I am grateful for the friendship we now have.

Finally, I would like to thank my family. To my parents, Sampath and Vimala, my husband Richard and my daughter Maya, this endeavour would not have been possible without your sacrifices and unwavering support. And for this, I dedicate this thesis to you.

Abstract

Neuroblastoma is a complex and devastating paediatric cancer. Despite advances in multimodal therapies, the outcomes remain poor in patients with high-grade disease. This thesis aims to systematically investigate neuroblastoma's heterogenous and unique biology, especially in the hypoxic tumour environment, and to screen potential novel therapeutic drug compounds in an ethically responsible, 3R-compliant *in vivo* chick embryo model. As a chemotherapy screening tool, the chick embryo model has been optimised to observe neuroblastoma growth and metastasis and yielded tumours to develop advanced 3D imaging protocols.

High-risk neuroblastoma has been shown to express abnormally high levels of genes promoting cell cycle progression. We hypothesised that cell cycle and signalling pathway-specific inhibitors might be an alternative strategy to treat neuroblastoma. In this work, we assessed the efficacy of cyclin-dependent kinase (CDK4/6 & CDK1) NF-KB and hypoxia-inducible factor (HIF) inhibitors against MYC-N amplified and non-amplified neuroblastoma cells, both *in vitro* and in the chick model. Both MYC-N amplified, and 11q deleted neuroblastoma cell lines have shown reduced proliferation when dosed with CDK inhibitors and NF-KB inhibitors *in vitro*. *In vivo*, there was a significant reduction in the overall number of tumours seen in chick embryos treated with CDK4/6 and CDK1 inhibitors but not with the NF-kB inhibitor. Histopathological analysis showed that CDK4/6 inhibitor Palbociclib reduced the overall percentage of proliferating cells in neuroblastoma tumours.

The role of hypoxia is well established as being crucial in the development, progression, and invasion of neuroblastoma. We further aimed to enhance the anti-tumour effects of Palbociclib on cell proliferation by combining it with a novel HIF-2 α inhibitor (PT2385). The HIF-2 α inhibitor alone did not inhibit the tumourigenic gene expression *in vitro* but reduced the number of primary and metastatic tumours *in vivo*. This highlights the importance of testing compounds in an *in vivo* model recapitulating the interactions with the tumour microenvironment. As Palbociclib inhibits cell cycle progression, combined inhibition of HIF-2 α and CDK4/6 is expected to inhibit tumour growth. The combination therapy in the chick embryo had more significant toxicity than either drug alone. However, there was a statistically significant reduction in metastasis formation in those chicks that did survive.

Preclinical models, such as genetically modified mice, are highly specialised and expensive and can take many weeks to yield results. We confirmed that the chick embryo model is a versatile experimental and conveniently very cost-effective model in cancer research.

To further exploit the chick embryo model's usefulness, fluorescently labelled neuroblastoma tumours grown within the chick embryo were imaged *in toto* using advanced microscopy techniques. To enable adequate light penetration through the thick sample, methods of clearing the tissue to transparency were evaluated. The outcome of this is a fully rendered three-dimensional image of neuroblastoma tumours within their tumour microenvironment. This alternative to traditional 2D tumour sectioning may now be deployed as a proxy for quantifying chemotherapy efficacy on cancer cell proliferation, differentiation and death.

Presentations and Publications:

Presentations

- **NWCR Research Day Liverpool** – April 2018, Liverpool. Poster Presentation
- **Faculty Poster Day** - June 2018, Liverpool. Poster Presentation
- **CPI Imaging Symposium** - June 2018, Liverpool. Attendance
- **IIB Away Day** - July 2018, Liverpool. Teaser Talk – 1st Prize
- **NC3Rs symposium** - July 2018, Liverpool. Poster Presentation
- **CCI Imaging Symposium** - September 2018. Liverpool. Oral Presentation – 1st Prize
- **International Society of Paediatric Surgical Research Conference** - October 2018, Taormina Sicily. Oral Presentation
- **International Society of Paediatric Oncology (SIOP)** - November 2018, Kyoto, Japan. Oral Poster Presentation – 1st Prize

Publications:

- **CDK inhibitors reduce cell proliferation and reverse hypoxia-induced metastasis of neuroblastoma tumours in a chick embryo model.** Swadi RR, Sampat K, Herrmann A, Losty PD, See V, Moss DJ. Sci Rep. 2019 Jun 24;9(1):9136. doi: 10.1038/s41598-019-45571-8. PMID: 31235824; PMCID: PMC6591221.

Acknowledgments	iii
Abstract	iv
Presentations and Publications	vi
Table of contents	vii
List of Abbreviations	xii
List of Figures	xvii
List of Tables	xxi

Table of Contents

Chapter 1 : Introduction	21
1.1 Cancer	22
1.2 Neuroblastoma	24
1.2.1 Epidemiology	24
1.2.2 Aetiology	25
1.2.3 The neural crest and the development of neuroblastoma	26
1.2.4 Genetic and Molecular biology of neuroblastoma	29
1.2.5 Spontaneous regression and Screening	36
1.2.6 Clinical Presentation	37
1.2.7 Diagnostic workup	38
1.2.8 Staging	39
1.2.9 Treatment by risk group	45
1.3 Development of new therapies	47
1.4 The Cell Cycle	49
1.5 Cell cycle inhibitors	51
1.5.1 CDK4/6 inhibition in cancer therapy	52
1.5.2 CDK1 inhibition in cancer therapy	53
1.6 NF-KB	54
1.7 Hypoxia	56
1.8 Models for neuroblastoma research	63
1.8.1 <i>In vitro</i> models	63
1.8.2 <i>In vivo</i> models	64
1.8.3 The chick embryo model	67
1.9 Three-dimensional imaging	72
1.9.1 Light scattering and a tissue sample	73
1.9.2 Tissue clearing	74

1.10 Project Aims & Objectives.....	83
Chapter 2 : Materials & Methods	84
2.1 Tissue culture	85
2.1.1 Cell lines	85
2.1.2 Cell culture	86
2.1.3 Long-term cryogenic cell storage	86
2.1.4 Thawing of stored cell lines	87
2.2 Therapeutic compounds	87
2.3 Functional Assays	88
2.3.1 MTT (3-(4,5-dimethylthiazol-2-yl)-2,5-diphenyltetrazolium bromide) assay.....	88
2.3.2 Trypan Blue Exclusion Assay.....	89
2.3.3 Cell Cycle Analysis	89
2.4 Chick embryo experiments	91
2.4.1 Egg preparation for <i>in-ovo</i> experiments	93
2.4.2 Cell Preparation and Implantation	93
2.4.3 Drug injection into the chick allantoic sac.....	94
2.4.4 Dissection of tumours.....	95
2.5 Fixing, Sectioning and staining tissue	97
2.5.1 Cryofixing tissue	97
2.5.2 Histopathology and Immunohistochemistry	99
2.6 Tumour Imaging	100
2.6.1 Advanced microscopy for 3D tumour imaging.....	100
2.6.2 Image acquisition	101
2.7 Clearing protocols	102
2.7.1 CUBIC Cancer Clearing	102
2.7.2 Ethyl cinnamate clearing.....	105
2.7.3 Cleared sample immunostaining	106
2.8 Western Blotting.....	107
2.8.1 Protein Extraction and quantification	107
2.8.2 Sample Preparation	107
2.8.3 Preparation and running of polyacrylamide gels.....	108
2.8.4 Protein Detection.....	109
2.9 Quantitative Polymerase Chain Reaction (qPCR)	110
2.9.1 RNA extraction in neuroblastoma cells.....	110
2.9.2 RNA extraction from tumour tissue	110

2.9.3 cDNA synthesis	111
2.9.4 Reference genes	111
2.9.5 Target gene selection	111
2.9.6 Primers.....	111
2.9.7 Controls	113
2.9.8 Plate design	113
2.9.9 Fold Gene Expression	114
Chapter 3 : Assessing the potential of cell cycle inhibition and NF-KB inhibition of primary neuroblastoma tumour growth <i>in vitro</i> and <i>in vivo</i>	115
3.1 Introduction.....	116
3.1.1 Targeting Cell cycle progression and pathways involved in drug resistance in neuroblastoma.	116
3.1.2 Utilising metastatic 'high risk' (as per INRG staging) neuroblastoma cell lines for <i>in vitro</i> and <i>in vivo</i> drug testing.....	117
3.1.3 Developing the use of the chick embryo model as a tool for drug screening in neuroblastoma.	118
3.2 Results	120
3.2.1 Investigation of drug treatment on survival of MYC-N amplified (SK-N-BE(2)C) and 11q deleted (SK-N-AS) cell lines <i>in vitro</i>	120
3.2.2 Assessing the efficiency of neuroblastoma tumour formation on the chorioallantoic membrane (CAM) in the chick embryo model.	134
3.3 Discussion	146
3.3.1 The potential of CDK4/6 inhibition in NB	146
3.3.2 CDK1 inhibition in NB	148
3.3.3 Tumour hypoxia and its role in NB development	149
3.3.4 Cross-talk between hypoxia and CDK and NF-KB signalling.....	150
Chapter 4 : Assessing the effect of HIF-2α inhibitor, PT2385, on neuroblastoma metastasis, alone and in combination with CDK4/6 inhibition	153
4.1 Introduction.....	154
4.1.1 The role of HIF-2 in neuroblastoma	154
4.1.2 Hypoxia, the neural crest and neuroblastoma	154
4.1.3 HIF-2 α inhibition.	155
4.2 RESULTS.....	157
4.2.1 Correlation of <i>HIF-1α</i> and <i>HIF-2α</i> expression with clinical outcomes of neuroblastoma patients.....	157
4.2.2 Evaluation of Hypoxia-Inducible Factors levels in SK-N-BE(2)C and SK-N-AS cell lines.	159

4.2.3 The effect of PT2385 on neuroblastoma cell survival	160
4.2.4 The effect of PT2385 and Palbociclib in combination	161
4.2.5 The effect of HIF-2 α inhibition on cell cycle	162
4.2.6 The effect of HIF-2 α inhibition on downstream target genes in cell culture.	165
4.2.7 The effect of HIF-2 α inhibition on chick survival and growth <i>in vivo</i>	178
4.2.8 The effect of HIF inhibition on tumour formation in the chick embryo.	181
4.2.9 Metastatic tumour formation in chick embryos after treatment with HIF-2 α inhibitor.	182
.....	190
4.3 Discussion	191
Chapter 5 : Utilising advanced microscopy techniques to monitor neuroblastoma growth and tumour response to therapy	196
5.1 Introduction.....	197
5.2 Chapter objectives	201
5.3 Results	202
5.3.1 Assessing the compatibility of clearing methods with neuroblastoma tumour samples grown in the chick embryo	202
5.3.2 Optimising the increase in light transmission and GFP intensity as a function of incubation times for the CUBIC clearing protocol.	205
<i>Acquisition settings were kept constant between measurements. Samples were imaged 3 times in different orientations, and the difference in mean intensity calculated. Intensity was calculated using Fiji software. The tumours within the images were marked as a region of interest and the average signal intensity within that area was calculated by the software. This was done using 3 different images for each sample at each time point and the average value taken. Images taken using Zeiss Axiovert S100 TV Inverted Microscope with the: 5x, 0.25 N.A. objective</i>	206
5.3.3 Optimising the increase in light transmission and GFP intensity by evaluating immersion times for the ECI protocol	210
5.3.4 Evaluating the depth of imaging after clearing	211
5.3.5 Evaluating the distorting effect of clearing protocols on tumour samples	214
5.3.6 Evaluation of microscopic appearance of cells with tumour sample after clearing.....	216
5.3.7 Imaging depth: comparison between CUBIC and ECI cleared tumour samples	218
5.3.8 Evaluating the change in sample fluorescence after storage in clearing solutions. ...	222
5.3.9 Optimising advanced imaging for 3D samples	224
5.3.10 Comparing the Dragonfly and 880MP imaging systems.....	229
5.3.11 Optimising immunostaining in wholemount tumours.	235

5.3.12 Detecting apoptosis in neuroblastoma tumours using a cleaved caspase-8 antibody.	244
5.3.13 Image quantification.....	246
5.3.14 Evaluating the utility of fluorescent retinoids for vasculature labelling and tracking drug delivery.....	257
5.4 Discussion	263
5.4.1 Choosing the most appropriate clearing method	263
5.4.2 Challenges of immunolabelling in the 3D sample	264
5.4.3 Selecting the most suitable imaging tool and parameters	266
5.4.4 Handling large data sets	267
5.4.5 Tracking cells and compounds <i>in vivo</i>	268
5.4.6 Conclusion.....	269
Chapter 6 : General Discussion	270
6.1 The overall aims of the thesis	271
6.1.1 Chick Embryo model.....	271
6.1.2 CDK inhibitors in neuroblastoma	276
6.1.3 Hypoxia, HIF-2 α inhibition and neuroblastoma	279
6.1.4 Developing advanced microscopy for cancer research	280
6.2 Future Considerations.....	282
6.3 Conclusions.....	283
References	285
Appendix.....	322

List of Abbreviations

ADAMTS1	A disintegrin and metalloproteinase with thrombospondin motifs 1
ALK	Anaplastic lymphoma kinase
Anti-GD2	Anti-GD2 monoclonal antibodies
ASCL1	Achaete-Schute homolog
ATRX	ATP-dependent RNA helicase
BMP	Bone morphogenic factors
BNIP3	BCL-2 adenovirus E1B 19kDa-interacting protein
BSA	Bovine Serum albumin
Ca-9	Carbonic anhydrase 9
CAM	Chorioallantoic membrane
CGHS	Congenital central hypoventilation syndrome
CCRC	Clear cell renal carcinoma
CDH-1	E-cadherin
CDK	Cyclin-dependant kinase
COG	Children's Oncology Group
CSC	Cancer stem cells
CTNNB1	Catenin
CUBIC	Clear, unobstructed brain/body imaging cocktails and computational analysis
CXCR4	C-X-C chemokine receptor type 4
DeepMACT	Deep learning-enabled metastasis analysis in cleared tissue
DISCO	3D imaging of solvent-cleared organs

DMOG	Dimethyloxaloylglycine
DMSO	Dimethylsulfoxide
ECI	Ethyl cinnamate
EMT	Epithelial-to-mesenchymal transition
FCS	Fetal calf serum
FDG	¹⁸ F-fluorodeoxyglucose
FIH-1	Factor inhibiting HIF
FN1	Fibronectin-1
FOXD3-AS1	Forkhead box D3 antisense RNA 1
Frizzled 6	Frizzled class receptor 6
GEMM	Genetically engineered mouse models
GLUT1	Glucose transporter type 1
GN	Ganglioneuroma
HIF	Hypoxia Inducible Factor
HRE	Hypoxia response elements
HVA	Homovanillic acid
IDRF	Image-defined risk factors
IND	Investigational new drug
INPC	International Neuroblastoma Pathology Committee
INRG	International Neuroblastoma Risk Group
INSS	International Neuroblastoma Staging System
ITCC	Innovative Therapies for Children with Cancer
ITG	Integrin

KLF4	Kruppel-like factor 4
LSFM	Light sheet fluorescence microscopy
MCP-1/CCL2	Monocyte chemoattractant protein-1/CC chemokine ligand 2
MCS	Multicellular tumour spheroid
MIBG	Metaiodobenzylguanidine
MRI	Magnetic resonance imaging
MTT	3-(4,5-dimethylthiazol-2-yl)-2,5-diphenyl-2H-tetrazolium bromide
NANT	New Approaches to Neuroblastoma Therapy
NCAM	Neural cell adhesion molecule
NCC	Neural crest cell
NDDS	Neuroblastoma New Drug Development Strategy
NEPENTHE	Next-Generation Personalized Neuroblastoma Therapy
NF-KB	Nuclear factor kappa-light-chain-enhancer of activated B cells
NPARMS	Non-polyalanine repeat expansion mutations
NRT	No reverse transcriptase
NTC	No template control
ODD	Oxygen-dependant domain
PBS	Phosphate Buffered Saline
PDAC	Pancreatic ductal adenocarcinoma
PDTC	Pyrrolidine dithiocarbamate
PDX	Patient-derived xenografts
PET	Positive emission tomography
PFA	Paraformaldehyde

PFS	Progression-free survival
PHOX2B	Paired-like homeobox 2B
qPCR	Quantitative Polymerase Chain Reaction
RB	Retinoblastoma protein
RI	Refractive index
RIMS	Refractive index matching solution
ROBO2	Roundabout, axon guidance receptor, homolog 2
RTK	Receptor tyrosine kinase
SCLC	Small cell lung cancer
SIOPEN	International Society of Paediatric Oncology European Neuroblastoma
β-ME	β-mercaptoethanol
STMN4	Stathmin-like 4
TERT	Telomerase reverse transcriptase
TGF-1	Transforming growth factor-1
TIMP4	Metalloprotease-4 inhibitor
TPCK	L-1-tosylamido-2-phenylethyl chloromethyl ketone
UDISCO	Ultimate 3D imaging of solvent-cleared organs
VCAN	Versican
vDISCO	Nanobody(VHH)- boosted 3D imaging of solvent-cleared organs
VEGF	Vascular endothelial growth factor
vHL	Von Hippel–Lindau
VIP	Vasoactive intestinal polypeptide
VMA	Vanillylmandelic acid

α -SMA

α -smooth muscle actin

List of Figures

Figure 1.1 Hallmarks of cancer and enabling characteristic acquired by cancer cells during the process of tumorigenesis, described by Hanahan and Weinberg (2022).	23
Figure 1.2 Neuroblastoma development from the neural crest.	28
Figure 1.3 A simplified tree diagram of the International Neuroblastoma Pathology Classification	40
Figure 1.4 Timeline of major events contributing to risk classification for neuroblastoma.	41
Figure 1.5 Schematic of cell cycle regulation highlighting the major functions of CDKs in cell cycle, adapted from Zhang et al 2021	50
Figure 1.6 Regulation of the cell cycle G1/S transition	51
Figure 1.7 Chemical structure of Palbociclib	53
Figure 1.8 Regulation of hypoxia inducible factor α subunits in normoxia and hypoxia.	58
Figure 1.9 Distinct effects of HIF-1 α and HIF-2 α on MYC complex formation.	61
Figure 1.10 Schematic illustrations of fluorescence imaging techniques	82
Figure 2.1 Visual display of the steps in chick embryo experiment.	92
Figure 2.2 Tumour growing under the CAM shown in ovo as A) Brightfield Image B) Fluorescent image.	95
Figure 2.3 Dissected Chick Neuroblastoma A) Brightfield Image B) Fluorescent image.	96
Figure 2.4 Fluorescent metastatic neuroblastoma tumours shown in ovo in NB A) intestines B) Feathers.	97
Figure 2.5 Workflow of clearing of tumours	104
Figure 2.6 Example plate layout for qPCR. NTC, no template control.	113
Figure 3.1 Sensitivity of MYC-N amplified (SK-N-BE(2)C) and MYC-N non amplified (SK-N-AS) cell lines to Palbociclib after 48 hours of treatment.	Error! Bookmark not defined.
Figure 3.2 Cell Cycle Analysis of neuroblastoma cells treated with Palbociclib	Error! Bookmark not defined.
Figure 3.3 Sensitivity of MYC-N amplified (SK-N-BE(2)C) and MYC-N non amplified (SK-N-AS) cell lines to RO 3306 after 48 hours of treatment.	Error! Bookmark not defined.
Figure 3.4 Cell Cycle Analysis of neuroblastoma cells treated with RO 3306	128
Figure 3.5 Sensitivity of (SK-N-BE(2)C) (SK-N-AS) cell lines to BAY-11-7082 after 48 hours of treatment.	131
Figure 3.6 Cell Cycle Analysis of neuroblastoma cells treated with Bay-11-7082.	132
Figure 3.7 The formation of neuroblastoma tumours preconditioned in normoxia and hypoxia on the chorioallantoic membrane of the chick embryo model.	135
Figure 3.8 The effect of drug treatment on chick survival and somatic development.	137
Figure 3.9 The effect of drug treatment on tumour presence, number of tumours formed per egg and the weight of tumours.	142
Figure 3.10 Brightfield images of SK-N-BE(2)C (top) and SK-N-AS (bottom) tumour sections at 40x magnification.	145
Figure 4.1 Trends of Hypoxia inducible factor inhibitors from 1985 – 2021. Number of publications per year with 'HIF inhibitor' within the title. Data taken from PubMed (pubmed.ncbi.nlm.nih.gov) on 14.01.2022.	Error! Bookmark not defined.
Figure 4.2 Kaplan Meier survival plots to show the impact of overexpression of HIF1 and HIF-2 genes on overall survival.	158
Figure 4.3 HIF-1 α and HIF-2 α protein expression in normoxia and hypoxia	159
Figure 4.4 Dose response curves of SK-N-AS and SK-N-BE(2)C treated with PT2385 alone.	161
Figure 4.5 Dose-response curves of SK-N-BE(2)C and SK-N-AS treated with PT2385 and Palbociclib	162

Figure 4.6 Cell Cycle Analysis of neuroblastoma cells treated with PT2385 and Palbociclib. _	164
Figure 4.7 The impact of genes associated with hypoxic genetic signature on the overall survival in MYCN non-amplified and MYCN amplified neuroblastoma cells. _____	167
Figure 4.8 The impact of hypoxia and drug treatment on genes associated invasion and metastasis in SK-N-BE(2)C and SK-N-AS neuroblastoma cells in vitro. _____	171
Figure 4.9 The impact of hypoxia and drugs on genes associated with cell cycle and cell differentiation in MYCN non-amplified and MYCN amplified neuroblastoma cells. _____	176
Figure 4.10 The percentage of chick survival after treatment with HIF inhibitor and combination drug protocol. _____	179
Figure 4.11 SK-N-BE(2)C or SK-N-AS cells were implanted as described in methods and materials on embryonic day 7. _____	180
Figure 4.12 The effect of drug treatment on number of tumours formed per egg. _____	181
Figure 4.13 The percentage of live embryos with metastasis. _____	183
Figure 4.14 Expression of genes associated with hypoxia within SK-N-BE(2)C and SK-N-AS tumours grown in the chick embryo. _____	185
Figure 4.15 Expression of genes associated with invasion and metastasis within SK-N-BE(2)C and SK-N-AS tumours grown in the chick embryo. _____	187
Figure 4.16 Expression of genes associated with differentiation within SK-N-BE(2)C and SK-N-AS tumours grown in the chick embryo. _____	190
Figure 5.1 Biology occurs in three dimensions. _____	197
Figure 5.2 Traditional tissue analysis and the principles of two photon microscopy. _____	199
Figure 5.3 The principals of clearing. _____	200
Figure 5.4 Examples of workflow for A) CUBIC Cancer and B) ECI clearing. _____	204
Figure 5.5 Calculating the increase in light transmission in pre- and post- clearing tumours. _	206
Figure 5.6 The brightfield and GFP signal intensity of samples before clearing. _____	207
Figure 5.7 The fold change in light change and GFP intensity over time with CUBIC Clearing. _____	209
Figure 5.8 The fold change in light transmission and GFP intensity over time with ECI clearing. _____	211
Figure 5.9 Comparing the mean intensity of fluorescent signal over depth in samples before and after clearing _____	213
Figure 5.10 Assessing gross change in area and weight of tumours after clearing. A) Example of tumour measurements before and after the clearing steps _____	215
Figure 5.11 Preservation of cellular morphology upon clearing. _____	217
Figure 5.12 Imaging at depth before and after CUBIC clearing. _____	219
Figure 5.13 Imaging at depth before and after ECI clearing _____	221
Figure 5.14 Comparison of fluorescence preservation during long-term storage of tumours. _	223
Figure 5.15 Imaging whole mount tissues with light sheet microscope. _____	225
Figure 5.16 Differences in image quality when using an imaging well compared to embedding in agarose. _____	227
Figure 5.17 Comparing Dragonfly and 880MP microscopes. _____	230
Figure 5.18 Comparing Dragonfly and 880MP image quality at depth. _____	232
Figure 5.19 Tile scan functions for lsm880MP and Dragonfly microscopes. _____	234
Figure 5.20 Ki67 antibody testing on fixed SK-N-AS cells. _____	236
Figure 5.21 Tumour sections labelled with GFP, Hoechst and KI67. _____	241
Figure 5.22 Cleared and immunolabelled neuroblastoma tumour. _____	243
Figure 5.23 Cross sectional images of tumour to demonstrate sandwiching of antibody. _____	244
Figure 5.24 Cleaved caspase-8 staining on neuroblastoma cells. _____	245
Figure 5.25 Cleaved caspase-8 staining on neuroblastoma sections. _____	246
Figure 5.26 Using Imaris Spot function to segment nuclei. _____	248

Figure 5.27 Nuclear segmentation of 3D images using Imaris workflow. _____	249
Figure 5.28 Workflow for nuclear segmentation in 2D images using STARDIST. _____	252
Figure 5.29 Smooth muscle actin immunolabelling of cleared whole neuroblastoma tumours.	254
Figure 5.30 Workflow for vessel segmentation in 3D rendered images. _____	256
Figure 5.31 Increasing cell concentration of DC271, to establish detection threshold. _____	258
Figure 5.32 The intensity of DC271 fluorescence retained by cells over time. _____	259
Figure 5.33 The fluorescence intensity of DC271 before and after fixation with PFA. _____	260
<i>Figure 5.34 The distribution of DC271 through the chick embryo vasculature upon injection.</i>	262
<i>Figure 5.35 The distribution of DC271 through the chick embryo vasculature upon injection.</i>	262

List of Tables

Table 1.1 The International Neuroblastoma Staging System (1988)	42
Table 1.2 International Neuroblastoma Risk Group (INRG) Pre-treatment classification system (2005)	43
Table 1.3 Image Defined Risk Factors (IDRF) (2005)	44
Table 1.4 General advantages/disadvantages of the CAM assay	70
Table 1.5 Comparison of 3D Tissue Clearing Techniques	76
Table 2.1 Cell lines used in this work and the media for cell culture	85
Table 2.2 Information on the origins and characteristics of the cell lines used in this project	85
Table 2.3 Therapeutic compounds used	88
Table 2.4 Drug compounds and concentrations used in different experimental groups	90
Table 2.5 Materials used in cryofixation and sectioning of tissue	99
Table 2.6 Objective information for Andor Dragonfly	100
Table 2.7 Objective information for Zeiss Axio Examiner (Ism880 MP)	101
Table 2.8 Excitation laser lines for fluorescently labelled proteins and antibodies	101
Table 2.9 Reagent used in CUBIC-Cancer clearing	102
Table 2.10 Formulation of clearing solutions	102
Table 2.11 Optimised clearing times for tumour samples in CUBIC	104
Table 2.12 Reagents used in Ethyl cinnamate clearing	105
Table 2.13 Ethyl cinnamate clearing protocol	105
Table 2.14 Antibody details	106
Table 2.15 Formulation of polyacrylamide gels	108
Table 2.16 Formulation of buffers for Western Blotting	108
Table 2.17 Antibody details for Western Blotting	109
Table 2.18 Primer pairs	112
Table 2.19 Step conditions	114
Table 5.1 Comparison of acquisition times and dataset sizes for single images, single point z stacks, tiled image and tiled z stack images.	235
Table 5.2 The optimisation steps for cleared tumour sections.	238

Chapter 1 : Introduction

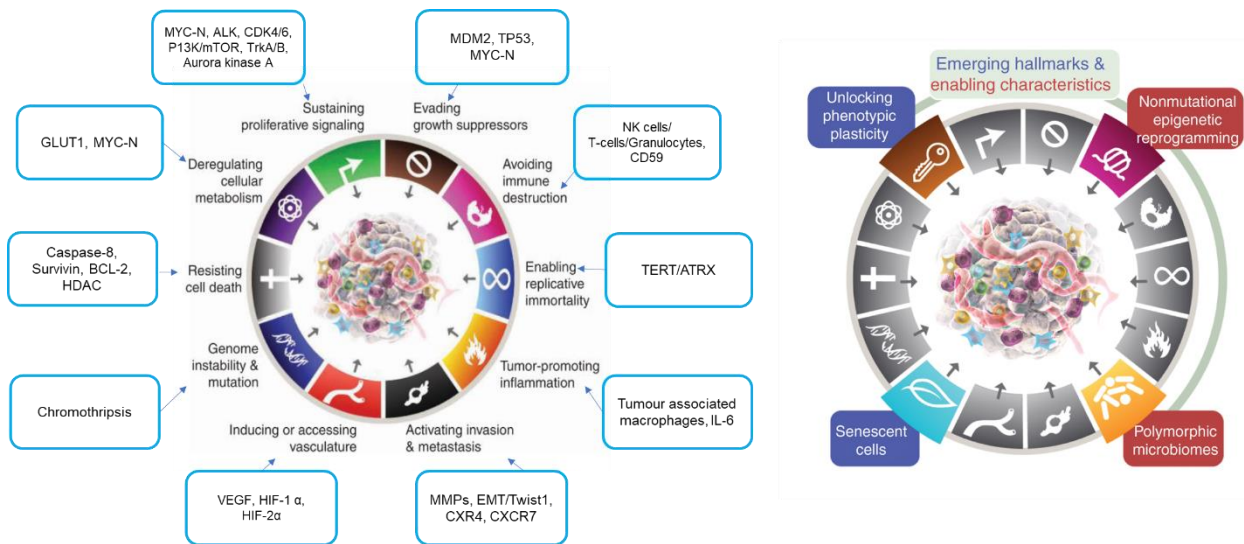
1.1 Cancer

Cancer is not a single disease but a collection of disease processes originating through the complex interactions of genetic and environmental factors. As one of the most lethal diseases, cancer is responsible for 10 million cancer-related deaths worldwide. (Ferlay *et al.*, 2021)

Although cancer is a heterogeneous group of diseases, they are characterised by disruption to normal cellular functions as a collective. (Hanahan and Weinberg, 2000) (Kreeger and Lauffenburger, 2010) An accumulation of multiple genetic mutations can deregulate the signalling governing the cell's most critical pathways. These include pathways that control cell growth, cell death, and DNA repair. When these pathways are no longer tightly regulated, the cell can proliferate and grow with no restrictions – and cancer develops.

Cancer research in the last 50 years has highlighted specific characteristics in almost all cancerous cells. Hanahan and Weinberg named these critical features in the landmark paper 'Hallmarks of Cancer' in 2000. (Hanahan and Weinberg, 2000) This work discusses the importance of two specific gene classes – oncogenes and tumour suppressor genes. The cumulative effect of genetic mutations causes the upregulation of oncogenes and inactivation of tumour suppressor genes, leading to uncontrolled cell proliferation and survival. In addition to cell survival, the paper also discusses the importance of metastasis and angiogenesis in cancer growth. As we understood more about cancer biology, the list of fundamental cancer traits expanded from 6 to 10 in 2011; the new additions included deregulated cellular energetics, avoiding immune destruction, and enabling characteristics of tumour-promoting inflammation and genome instability. (Hanahan and Weinberg, 2011a) (**Figure 1.1**) The latest iteration, published in 2022, includes four further 'emerging hallmarks and enabling characteristics', exploring the importance of phenotype plasticity and cell senescence to cancer cell survival. (Hanahan, 2022)

Figure 1.1 Hallmarks of cancer and enabling characteristic acquired by cancer cells during the process of tumorigenesis, described by Hanahan and Weinberg (2022).



Blue boxes illustrate the genes and genetic events which contribute to the development of neuroblastoma at each hallmark. Image adapted from Hanahan and Weinburg for neuroblastoma.

Although cancer models seek to categorise better and define cancer, cancer is still a heterogeneous disease. Key oncogenes and tumour suppressor genes are seen in multiple cancer types but are not ubiquitous in all cancers. A stark example of the differences in cancers can be seen when looking at cancers in children and those seen in adults.

Gene changes in cancer are attributed to many factors, including carcinogens, viruses, radiation exposures, ageing and epigenetic signals. Large-scale genomic sequencing of paediatric cancers has shown that the somatic mutational load is often low, on average 9.6 mutations per cancer, compared to adult cancers, where on average, 33-66 somatic mutations are identified per cancer. (Vogelstein *et al.*, 2013) The lower mutation burden in paediatric cancers has been attributed to the embryonal origin of many of these cancers, dysregulation of developmental pathways and the comparatively lesser contribution of environmental carcinogens. (Tomlinson, Novelli and Bodmer, 1996) In addition, it cannot be assumed that all paediatric cancers are secondary to inherited genetic mutations. Only 1-2% of patients with neuroblastoma have a family history of the disease; on average, only 9% of paediatric cancers are familial. (Maris *et al.*, 2007; Mossé *et al.*, 2008; Zhang *et al.*, 2015)

The significance of this is that the lack of identifiable mutations can make identifying therapeutic targets much more challenging. The commercial availability of new technologies, such as massively parallel DNA and RNA sequencing, dramatically increases our understanding of the complexities of paediatric cancers. (Meyerson, Gabriel and Getz, 2010) (Hong *et al.*, 2020). In addition to providing meaningful insight, genotype sequencing can identify therapeutic targets for improving patient survival.

1.2 Neuroblastoma

Neuroblastoma is often used as an umbrella term to refer to a spectrum of neuroblastic tumours arising from the primitive sympathetic ganglion cells, including neuroblastomas, ganglioneuroblastomas, and ganglioneuromas. (Steliarova-Foucher *et al.*, 2005) The sympathetic ganglia and adrenal medulla are components of the autonomic nervous system responsible for the 'fight or flight response. The sympathetic ganglia, also known as paravertebral ganglia, run alongside the spinal cord from the neck to the pelvis and include the adrenal glands, which sit within the retroperitoneal space above the kidneys bilaterally. Therefore, it is unsurprising that 65% of all neuroblastoma tumours are found in the abdomen and half of those within the adrenal medulla. (Brodeur, 2003; Mueller and Matthay, 2009) However, neuroblastoma can develop at any of the ganglia within the sympathetic chain, and those occurring within the thoracic regions have a more favourable outcome. (Kleihues, Cavenee and International Agency for Research on Cancer., 2000) Neuroblastoma is predominantly a cancer of childhood with a median age at diagnosis of 17 months. With over 100 cases diagnosed annually in the UK, it is the 2nd most common extracranial solid tumour of childhood and currently accounts for 15% of all paediatric oncology-related mortalities. (Stiller, 2007)

Neuroblastomas are remarkably heterogeneous tumours, varying in their primary tumour site, patient demographics, symptomology, histology and prognosis. For example, the prognosis can range from spontaneous regression in perinatal cases to refractory metastatic disease in older children leading to death. This heterogeneity arises from the diversity of cell types in this tumour and the genetic aberrations that drive tumour formation. (Louis and Shohet, 2015)

1.2.1 Epidemiology

Neuroblastoma is predominantly a cancer of infancy and early childhood, with 40% occurring in infancy and 10% seen in neonates. Unsurprisingly the highest incidence of neuroblastoma is seen

in countries with the highest surveillance, including North America, Japan, Western Europe and Australia. (Berthold *et al.*, 2017) However, the actual incidence rate is likely skewed by underreporting from low- and middle-income countries, where differences in diagnosis and registration may occur. (Kamihara *et al.*, 2017) In areas with diverse racial populations and better diagnostic facilities, such as the USA, there are minimal differences between children of black and Caucasian descent. (Steliarova-Foucher *et al.*, 2017)

Although tumours arise all along the paravertebral chain, the most common neuroblastomas site is the adrenal gland (50%), 20% are seen in the abdomen, and 15% within the thoracic cavity—the stage and type of neuroblastoma influence the incidence of metastasis at diagnosis. Most children under one at the time of diagnosis will have stage 4S disease, which presents with metastasis to skin, liver and bone marrow.

1.2.2 Aetiology

Most cases of neuroblastoma occur in isolation. However, about 1–2% of neuroblastoma is inherited in an autosomal dominant fashion within families. (Tolbert *et al.*, 2017). Patients with familial neuroblastoma often present earlier, with multiple primary tumour sites. There is still a high degree of variability in families with neuroblastoma, with members of the same lineage exhibiting high and low-risk disease. (Hardy and Nesbit, 1972) The most common genetic mutations are in the anaplastic lymphoma kinase (ALK) gene and the paired-like homeobox 2B (PHOX2B) gene. Gene analysis has shown that around 80% of families with neuroblastoma demonstrate mutations in ALK, and ALK mutations are seen to be somatically acquired in 10% of all cases of neuroblastoma. (Carpenter and Mossé, 2012) PHOX2B is the first gene thought to predisposed to neuroblastoma seen originally in families with neuroblastoma, Hirschsprung's disease and congenital central hypoventilation syndrome. (Stovroff, Dykes and Teague, 1995) Genetic testing for both ALK and PHOX2B is currently available for families to identify susceptibility and aid in decisions about screening other family members. However, not all families exhibit ALK and PHOX2B mutations, so the heritability of neuroblastoma remains only partially elucidated. More work is needed to understand this disease's genetic and environmental influences.

Of the other 98% of non-familial neuroblastoma cases, studies have been undertaken to identify pre-and perinatal environmental factors which may have contributed. However, given the condition's rarity and the lack of a robust registry in much of the world, the studies often lack

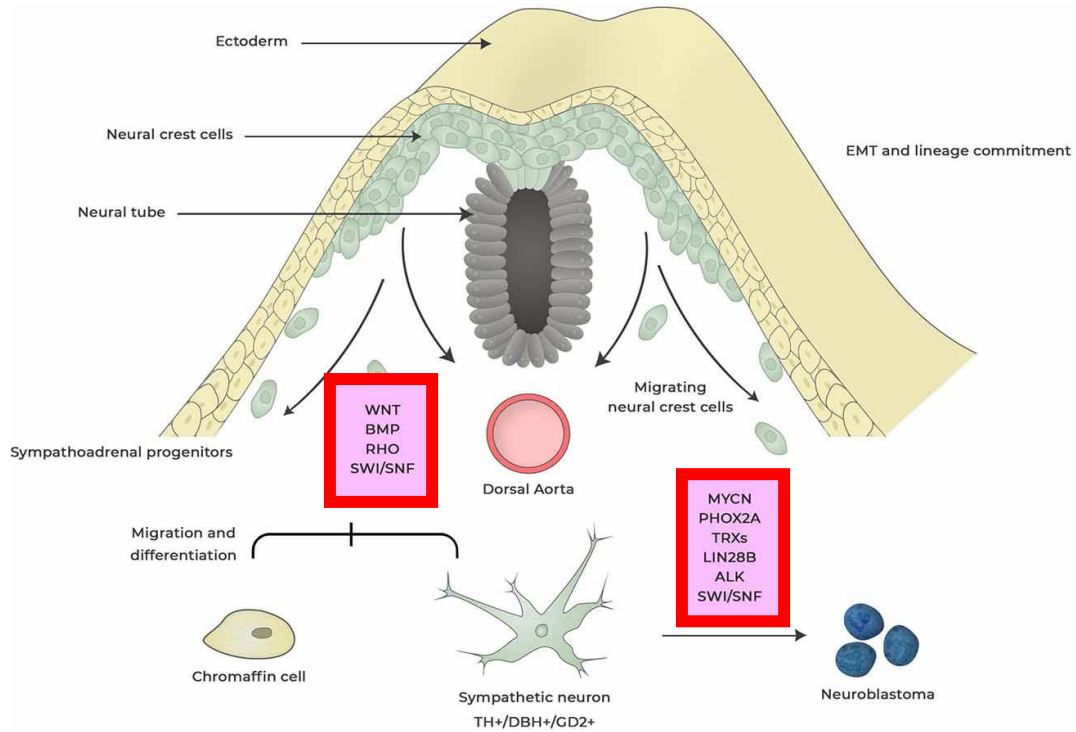
power. Several case-control studies have examined the relationship between gestation age, birth weight, maternal smoking and periconceptional folic acid supplementation. No conclusive evidence has been presented about birth weight contributing to neuroblastoma. Studies using maternal interviews demonstrated an inverse association between folic acid supplementation and neuroblastoma. (Olshan *et al.*, 2002; French *et al.*, 2003; Bluhm *et al.*, 2008) Two meta-analyses report an increase in neuroblastoma in children whose mothers smoked during pregnancy. (Müller-Schulte, Kurlemann and Harder, 2018; Rios *et al.*, 2019) Breastfeeding is reported to reduce the risk of neuroblastoma COG North-American study, with no association with the duration of breastfeeding. (Daniels *et al.*, 2002)

1.2.3 The neural crest and the development of neuroblastoma

The neural crest cells (NCCs) are a multipotent embryonic cell population from the embryonic ectoderm cell layer. Through the epithelial-to-mesenchymal transition (EMT), the NCCs can migrate to different sites within the developing embryo. (Theveneau and Mayor, 2012). Multiple networks of transcription factors aid the delamination and migration of these cells. Snai1/2, Slug and Twist promote the degradation of basement membranes and reduce cell adhesion molecules through the downregulation of N-CAM, N-cadherin and integrins. (Taneyhill, 2008) The cells can survive and proliferate and maintain their stemness through the action of multiple genes, including Sox10, Foxd3 and MYCN. (Johnsen, Dyberg and Wickström, 2019a) The four main types of NCCs are defined by their end location - cranial, cardiac, trunk, vagal and sacral. (Matthay *et al.*, 2016) The cells differentiate into an incredibly diverse population of cell types and contribute to numerous structures, including the branchial arches, thoracic and cardiac vessels, melanocytes, multiple structures of the head and neck and components of the sympathetic parasympathetic and sensory nervous systems. (Cheung and Dyer, 2013). The trunk NCCs form two populations; the dorsolaterally migrating cells form melanocytes, whereas the ventrolateral migration of NCCs forms the sympathetic ganglia and adrenal gland. Although closely linked, the sympathetic progenitor cells and the adrenal chromaffin progenitors are two distinct cell populations which may contribute to neuroblastoma's origin. (Furlan *et al.*, 2017) The intrinsic and extrinsic signalling factors are critical to the generation of the sympathoadrenal lineage. The main extrinsic factors involved in sympathoadrenal formation are the bone morphogenic factors (BMPs) secreted from the dorsal aorta. Achaete-Schute homolog 1 (ASCL1) expression is induced in response to BMP secretion (Schneider *et al.*, 1999). ASCL1 is the first marker of neuronal specification in humans. PHOX2A and PHOX2B, HAND2 and GATA2/3 drive the synthesis of

catecholamine synthesis through enzymes such as tyrosine hydroxylase and dopamine beta-hydroxylase, as well as through several generic neuronal markers such as SCG10 and NF160 (Ernsberger et al., 2000) (**Figure 1.2**) There are specific transcriptional programs governing the specification and differentiation of these cells. Errors herein can contribute to uncontrolled proliferation, survival and dedifferentiation of cells and malignant transformation of these cells leading to neuroblastoma formation. (Johnsen, Dyberg and Wickström, 2019b)

Figure 1.2 Neuroblastoma development from the neural crest.



Cells within the neural crest undergo epithelial-to-mesenchymal transition (EMT) allowing the cells to delaminate, migrate and differentiate into a variety of cell types. This process is tightly controlled by internal and external signalling pathways. Dysregulation of these pathways and transcription factors give rises to pre-oncogenic lesions which eventually result in neuroblastoma formation. Factors which have been identified as important contributors to neuroblastoma development are shown in the red boxes. MYC-N is the most powerful oncogenic driver for neuroblastoma. LIN28B control MYCN expression via regulating Let-7 miRNA. Anaplastic lymphoma kinase (ALK) and paired-like homeobox 2B (PHOX2B) are germline mutations found in neuroblastoma. Bone morphogenetic protein (BMP), initiates differentiation of the sympathoadrenal precursor. At this stage cells committed to becoming sympathetic ganglia acquire the catecholaminergic enzymes, dopamine- β hydroxylase (DBH) and tyrosine hydroxylase (TH). Rho signalling is crucial for the migration of neural crest cells by controlling contact inhibition of locomotion between neural crest cells. SWI/SNF complexes are tumour suppressors that for coordinate diverse chromatin alterations which influences the transcriptional output, DNA replication and repair. Figure adapted from Johnsen et al. 2019.

1.2.4 Genetic and Molecular biology of neuroblastoma

The molecular and genetic aberrations leading to the development and progression of neuroblastoma are a fundamental research interest. The clinical heterogeneity of the disease perhaps speaks to the lack of a single genetic or molecular dysfunction common to all neuroblastoma tumours. Significant progress has been made in understanding the heritability and genetic predisposition to neuroblastoma through analysis of families with neuroblastoma and genome-wide association studies of sporadic cases. Only 1-2% of neuroblastomas run in a familial context, with the rest occurring as sporadic mutations. Numerous recurrent somatic mutations have been discovered in neuroblastoma, most commonly with gains or losses in genetic material. (Tolbert *et al.*, 2017)

Below we will discuss some of the more well-researched hereditary and somatic mutations. (Pugh *et al.*, 2013)

Key genes:

1. PHOX Paired-like homeobox 2B
2. MYC
3. ALK Anaplastic Lymphoma Kinase
4. ATRX/TRK

1.2.4.1 PHOX2B

Mutated PHOX2B has been occasionally detected in sporadic neuroblastoma (Van Limpt *et al.*, 2004), while overexpression of both mutated PHOX2A and PHOX2B is frequently detected in both neuroblastoma cell lines and primary tumours. (Longo *et al.*, 2008) PHOX2B gene encodes a homeobox transcription factor containing a homeodomain and two polyalanine repeat domains. The transcription factor promotes cell cycle exit and neuronal differentiation and is critical in developing the autonomic nervous system.

Germline mutations within the two polyalanine repeats of 9 and 20 residues are associated with familial forms of neuroblastoma associated with congenital central hypoventilation syndrome (CCHS) and neuroblastoma-Hirschsprung's disease-CCHS association. The functional effect of mutations of PHOX2B has been investigated in several models. Concurrent overexpression of mutated PHOX2B and reduced levels of wild-type PHOX2B showed increased proliferation and reduced differentiation of neuroblasts within the chick model, indicating that PHOX2B mutations

may be a gain of function mutations. (Reiff *et al.*, 2010) When non-polyalanine repeat expansion mutations (NPARMS), seen in neuroblastoma-Hirschsprung's-CCHS, were introduced into an endogenous PHOX2B allele in a mouse model, the features of Hirschsprung's and CCHS were observed, but not in neuroblastoma (Cheung and Dyer, 2013). Therefore, the model cannot recapitulate the germline NPARM mutations leading to congenital neuroblastoma, so the exact mechanism of increased susceptibility remains unknown. However, the overall view is that PHOX2B mutations promote the maintenance of stemness within neuroblastoma, which increases the likelihood of malignant transformation of neural crest cells.

1.2.4.2 MYC-N

MYC-N belongs to the 'MYC' family of proto-oncogenes. The MYC family plays a fundamental role in controlling cell proliferation, growth, metabolism, differentiation, and apoptosis. It functions as a transcription factor composed of a DNA binding helix-loop-helix/leucine zipper protein that forms an obligate heterodimer with a partner protein termed Max, causing transcriptional activation of target genes. (Kamijo and Nakagawara, 2012) (Gherardi *et al.*, 2013) MYC-N, in particular, is highly expressed in neural and cerebral embryogenesis, with reduced expression in adulthood, indicating a pivotal role in the differentiation and development of the nervous system. (Henriksson and Lüscher, 1996). Disrupting MYC-N during embryogenesis is lethal in mouse embryos due to the prevalence of cardiac anomalies and lack of cranial and spinal ganglia. (Knoepfler, Cheng and Eisenman, 2002)

First identified in 1983, gene amplification of MYC-N (defined as more than ten copies for a diploid genome) is one of the earliest genetic markers found in neuroblastoma and remains the strongest predictor of poor prognosis. (Rössler *et al.*, 2001a; Huang and William A Weiss, 2013) Data from the International Neuroblastoma Risk Group, reviewing over 2500 patients with neuroblastoma, found that the survival of patients with stage 1 disease was significantly worse in those with MYC-N amplification than those without (53% vs 90%). (Bagatell *et al.*, 2009). Interestingly, MYC-N amplification is often seen in patients with high-risk neuroblastoma, and those with the low-risk disease at diagnosis do not 'acquire' gene amplification as their disease progresses. (Maris *et al.*, 2007; Huang and William A. Weiss, 2013) The implication is that MYC-N gene amplification is an early event, key in driving neuroblastoma development.

Genome-wide analysis of gene expression of neuroblastoma cell lines with and without MYC-N amplification has identified multiple pathways associated with MYC-N expression. These pathways are predominantly related to neuronal differentiation, cell proliferation and cell survival.

1.2.4.2.1 Cell Survival

The most characterised function of MYC-N is the promotion of cell proliferation and survival. Neuroblastomas with MYC-N amplified genotype show continued cell progression through usual cell cycle checkpoints despite irradiation and DNA damage. The mechanisms for this are numerous: through downregulation of tumour suppressor, p53 and upregulation of cyclin D-dependent kinases (CDK4, CDK2). (Gogolin *et al.*, 2013)(Huang and William A. Weiss, 2013). There is also active suppression of anti-proliferative proteins such as Dickkopf-1, a pro-inflammatory ligand that antagonises the WNT/ β catenin signalling pathway, regulating cell proliferation. (Koppen *et al.*, 2007) Aurora A kinase gene is required for the growth of MYC-N-amplified neuroblastoma as aurora A has a critical function in regulating turnover of the MYC-N protein. (Otto *et al.*, 2009) Knockdown of MYCN expression in murine models of neuroblastoma demonstrated increased cellular differentiation and cell proliferation reduction. (Chesler and Weiss, 2011)

1.2.4.2.2 Evasion of Apoptosis

Alongside increased proliferation, MYC-N amplification facilitates cancer cell survival by escaping programmed cell death. Cell type and the genetic environment determine the balance between proliferation and apoptosis. Mutations of the tumour suppressor gene, Tp53, which is seen in many cancer types, are strangely rarely seen in neuroblastoma. However, MYC-N-mediated regulation of Tp53 may play a role. MYC-N regulates key suppressors of p53 signalling such as H-twist, CUL7 and MDM2. (Swarbrick *et al.*, 2010; Huang and William A. Weiss, 2013). MDM2, in particular, promotes the degradation of p53 and is upregulated by MYC-N. (Barone *et al.*, 2014) Conversely, there is evidence that MYCN can promote the transcription of Tp53, so the balance between the two antagonising functions further highlights the heterogeneity in neuroblastoma disease. (Slack *et al.*, 2005). Interestingly, p53 mutations are acquired in cases of relapsing neuroblastoma, indicating a role in therapy in inducing relapse and chemoresistance. Caspase 8, a monomer protein known to propagate the apoptotic signal, is also lost in MYC-N amplified neuroblastoma. (Teitz *et al.*, 2013) Other pro-survival signalling cascades are upregulated in MYC-N amplified neuroblastoma, but less so in non-amplified tumours is tropomyosin receptor

kinase b (RTKB) protein (Kamijo and Nakagawara, 2012). This protein is also abundantly seen in patients with chemo-resistant neuroblastoma. (Brodeur *et al.*, 2009; Dewitt *et al.*, 2014)

1.2.4.2.3 Cell dissemination and metastasis

MYC-N amplification is associated with metastatic disease. Metastatic disease in neuroblastoma is often seen in the bone marrow, lymph nodes, liver and brain. (DuBois *et al.*, 1999). The process of metastasis is multistep, including cell detachment, motility, degradation of the extracellular matrix, adhesion and invasion to a distant site. (Van Zijl, Krupitza and Mikulits, 2011) Multiple genes exist within numerous networks, and MYC-N can differentially influence several genes. For example, during the initial stage of metastasis – detachment from the primary tumour – MYC-N can downregulate the integrins $\alpha 1$ and $\beta 1$. Integrins are cell surface receptors that promote the cell's adherence to the extracellular matrix. (Tanaka and Fukuzawa, 2008) In addition, through co-expression with BCL2, MYC-N increases the secretion of matrix metalloproteinases such as MMP2, which are endopeptidases that degrade a wide range of basement membrane components, a process necessary for tumour invasion (Noujaim *et al.*, 2002) Indeed in SHEP neuroblastoma cells, the application of an MMP2 inhibitor reduced the invasive potential of the cell.

1.2.4.2.4 Immune Surveillance

The role of immune surveillance in cancer is now crucial in understanding and treating many malignancies. (Swann and Smyth, 2007) Recognising cancer cells as 'other' stimulates an immune-mediated cascade to attract natural killer cells and generate antigen-specific T cells to target and destroy the tumour. Once again, the role of MYC-N in this area has been explored. MYC-N has been shown to modulate the antigens expressed on the surface of tumour cells, such as the repression of monocyte chemoattractant protein-1/CC chemokine ligand 2(MCP-1/CCL2), thus allowing cells to escape surveillance. (Song *et al.*, 2007) Clinically this is seen in patients with MYC-N amplified disease with bone marrow metastasis, demonstrating only a quarter of natural killer cells as patients with non-amplified metastatic disease.

1.2.4.2.5 Angiogenesis

Another critical hallmark of cancer is the ability for neo-angiogenesis, allowing continued sustenance and growth of a tumour. High vascularity is associated with poor outcomes in many cancers, and neuroblastoma is no exception. Specifically, high vascularity and poor neuroblastoma outcomes are seen in those with amplification of MYC-N. (Ribatti *et al.*, 2002; Ozer *et al.*, 2007) MYC-N increases the expression of proangiogenic factors such as vascular endothelial growth factor (VEGF) and downregulates endothelial growth inhibitors' expression. (Kang *et al.*, 2008)

1.2.4.3 Anaplastic Lymphoma Kinase - ALK

The Anaplastic Lymphoma Kinase gene was identified as a significant player in neuroblastoma pathogenesis after discovering germline and somatic mutations in a group of familial and sporadic cases. (Chen *et al.*, 2008; Mossé *et al.*, 2008). This gene belongs to the insulin receptor family and encodes a tyrosine kinase receptor. The function of the gene was further characterised using the chick embryo model. *In vitro* and *in vivo* knockout of ALK within the model showed reduced proliferation of sympathetic neuroblasts, indicating its role in developing the sympathetic nervous system. (Reiff *et al.*, 2011) The role of ALK-activating mutations in neuroblastoma is still not fully clear. *In vitro*, ALK overexpression induced proliferation and survival even without MYC signalling. (Schulte *et al.*, 2013). Interestingly, ALK has also been shown to induce MYC transcription in neuroblastoma, which may explain the poor outcomes in patients with ALK mutation and MYC-N amplification. (Zhu *et al.*, 2012). Although ALK mutations are seen in all grades of neuroblastoma, analysis of 1596 diagnostic NB samples found that ALK mutations were associated with poorer survival in high- and intermediate-risk diseases. (Bresler *et al.*, 2014)

The somatic mutations of ALK seen in sporadic neuroblastoma cases seem to differ from those in germline mutations in familial cases. Mutations in three positions—R1275, F1174, and F1245—account for around 85% of ALK mutations in neuroblastoma, with R1275Q the most common mutation present in 45% of familial cases and a third of sporadic cases. (Bresler *et al.*, 2014) F1174 and F1245 mutants are exclusively found in sporadic disease at around 30% and 12% and are not seen in familial cases. (Mossé *et al.*, 2008).

ALK is an ideal target for drug inhibition as it is rarely seen at high levels in normal tissue but is frequently overexpressed in neuroblastoma. Unlike MYC-N, ALK is amenable to pharmacological inhibition with small-molecule, ATP-competitive inhibitors of the tyrosine kinase domain. Crizotinib was the first ALK inhibitor to undergo clinical assessment and showed encouraging results in

early trials for non-small cell lung cancer. After discovering the role of ALK in neuroblastoma in 2008, the Children's Oncology Group (COG) initiated the trial of Crizotinib in paediatric patients with relapsed or refractory solid tumours. Combination therapy trials with Crizotinib are now also underway (NCT01606878). (Clinicaltrials.gov, no date). The NEPENTHE (Next-Generation Personalized Neuroblastoma Therapy) clinical study (NCT02780128) commenced in 2016 and is currently recruiting patients with relapsed or refractory NB into treatment arms based on actionable genetic alterations. Patients with ALK mutations are treated with the synergistic combination of a tyrosine kinase inhibitor and cyclin-dependent kinases 4 and 6: Ceritinib and Ribociclib. Recently, the NANT (New Approaches to Neuroblastoma Therapy) consortium opened a phase I trial of second-generation tyrosine kinase inhibitor Lorlatinib in combination with chemotherapy (cyclophosphamide and topotecan) in patients with high-risk NB (NCT03107988). The discovery of ALK mutations in neuroblastoma is a blueprint for a successful bench-to-bedside therapy progression.

1.2.4.4 Telomerase Pathway Alterations: ATRX and TERT

Telomeres are repetitive nucleotide sequences on the ends of chromosomes. In non-cancerous cells, the telomeres are progressively shortened with each cell replication leading to cell senescence or cell death, thus ensuring each cell has a finite survival. (Allsopp *et al.*, 1995) The ATP-dependent RNA helicase (ATRX) and Telomerase reverse transcriptase (TERT) genes control telomere length. Mutations leading to the loss of function of ATRX and the overexpression of TERT have been seen in whole-genome sequencing of neuroblastoma. Overexpression of TERT increases telomerase's enzymatic activity, enabling cells to sustain proliferation capacity. There is also a strong correlation between MYC-N amplification and TERT overexpression. In a cohort of tumours where neither MYC-N amplification nor TERT overexpression is present, ATRX mutations have been observed. ATRX mutations are seen in up to 10% of patients; most are older children with neuroblastoma (>5 years of age at diagnosis) with a very poor prognosis. (Kurihara *et al.*, 2014)

1.2.4.5 Non-Coding RNAs

Noncoding RNA is the term given to RNA (microRNAs, lncRNAs, and piRNAs), which does not code a protein, but may contain information or serve a function within the cell. Noncoding RNAs are thought to have an important role in cancer pathogenesis. (Mattick and Makunin, 2006). Their role in neuroblastoma was first postulated when patients stratified into risk groups showed

different miRNA expression profiles. (Chen and Stallings, 2007). Mestdagh et al. have shown the correlation between specific noncoding RNAs and overexpression of MYC-N and suggested that the expression profile might be able to serve as a predictor of survival in high-risk neuroblastoma. (Mestdagh *et al.*, 2010). The role of all noncoding RNAs in neuroblastoma pathogenesis and progression is not fully understood. Several microRNAs have been linked with good or poor outcomes in neuroblastoma patients. miR-542-3p downregulation is associated with poor outcomes. Its expression is associated with increased apoptosis, likely through its regulation of anti-apoptotic protein survivin. Expression of survivin in tumours correlates with inhibition of apoptosis, resistance to chemotherapy, and aggressiveness of tumours. Targeting this pathway through miR-542-3p expression is, therefore, an attractive venture. (Kristina Althoff *et al.*, 2015) Through microarray analysis, Zhao et al. identified five lncRNAs which were consistently associated with the progression and aggressiveness of NB. (Zhao *et al.*, 2018) Forkhead box D3 antisense RNA 1 (FOXD3-AS1) is an independent prognostic marker for a positive outcome in NBs. FOXD3-AS1 is down-regulated in advanced neuroblastoma. Zhao et al. also showed that the treatment with FOXD3-AS1 construct reduces tumour growth and extends mice xenografts' survival. The deregulation of noncoding RNAs is a promising target for developing novel therapies. Anticancer therapies can alter the noncoding RNA expression, impacting drug response and chemoresistance. One example is targeting inhibition of oncogenic circular RNA circ-CUX1. Inhibition of circ-CUX1 blocks interaction with EWSR1 reduces tumour growth, and decreases ATP levels in mice xenograft tumours. (Li *et al.*, 2019)

1.2.4.6 LIN28 Mutations

LIN28A/B proteins are RNA-binding proteins highly present in early embryogenesis and are involved in maintaining progenitor cells by blocking differentiation. *In vitro* LIN28A/B is seen to be essential for sympathetic neuroblast proliferation. Polymorphic alleles within the LIN28B locus are associated with the development of high-risk neuroblastoma, and overexpression is often seen in tumours—the overexpression of LIN28A is correlated with high levels of MYC-N. (Molenaar, Domingo-Fernández, *et al.*, 2012) In addition, LIN28 has been shown to induce high levels of phosphorylated Aurora A, leading to further kinase activation. (Schnepp *et al.*, 2015)

1.2.4.7 Somatic mutations: 11q

Chromosomal aberrations such as loss of chromosome 1p, 3p, or 11q and the unbalanced gain of chromosome 17q appear to be associated with poor prognosis and increased neuroblastoma aggressiveness. However, only 11q has been formally included in the staging classifications for neuroblastoma.

Neuroblastoma tumours with 11q loss of heterozygosity seem to be a unique entity, occurring almost exclusively in MYC-N non-amplified tumours. Deletions of 11q in a consensus region at 11q23 are seen in approximately 40% of all cases and represent a high-risk patient cohort characterised by advanced stage, older age, and a higher genomic instability. Caren et al. analysed 165 neuroblastoma tumours using microarray with MYC-N amplification and 11q deletion genotypes. The median age at diagnosis was significantly higher in the 11q-del group than MYC-N amplified (42 months vs 21 months, respectively). Adolescents with neuroblastoma represent less than 5% of the cases, and the prevalence of 11q deletion in this group is between 30 to 60%. (Mlakar *et al.*, 2017) The precise timing of 11q deletion is not yet fully known, but the increasing frequency with stage and older age of NB onset could suggest a late-stage event. After diagnosis, the median survival time was 16 months for MYC-N amplified tumours and 40 months for 11q deletion. However, overall survival was similar. The 11q deletion group harboured 12 segmental aberrations on average, compared to the 4 of the MYC-N amplified group.

The pattern of the chromosomal breaks is also more unpredictable in the 11q group, described as a 'shotgun pattern'. They postulate that the loss of critical regulatory genes on chromosome 11q may be responsible for this chromosomal instability. One such gene could be the H2AFX gene, which resides in the chromosome region 11q23.2-q23.3. The loss of this gene increases errors in chromosomal double-strand break repairs and increases susceptibility to cancer in the absence of the p53 tumour suppressor gene. (Carén *et al.*, 2010).

11q is never lost on both chromosomes, suggesting that essential genes are present on the remaining 11q copy; however, haploinsufficiency must occur in other lost genes. The mechanism by which deletion in 11q causes high-risk disease is unknown, and therapies targeting this alteration have not been developed.

1.2.5 Spontaneous regression and Screening

4S neuroblastoma is a unique stage of aggressive disseminated tumour growth with metastasis to the liver, skin and bone marrow, usually seen in children under 18 months. 4S tumours are unique as they often spontaneously regress with little or no treatment. (Brodeur and Bagatell,

2014) Spontaneous regression describes a phenomenon when a cancerous disease is reduced in size until it disappears without any treatment. The prevalence of regression in neuroblastoma is unknown, as a proportion of these tumours will have regressed before diagnosis. To quantify prevalence, mass screening studies have been conducted. Surveillance of urine catecholamines has been used in Japan, Europe and Canada. (Sawada *et al.*, 2009) (Erttmann *et al.*, 1998), and the incidence of neuroblastoma increased from 1: 7000 to 1: 2000. However, the natural progression of this disease means that it does regress without any morbidity and mortality, so despite the screening programs to identify neuroblastoma, there has been no change in overall mortality. The surveillance programs have therefore been abandoned.

The cause of spontaneous regression is still unknown. It is thought to be modulated by several pathways, but immune system involvement is the most well-established hypothesis. Interactions between pathogen-associated molecular patterns and receptors on immune cells have produced a pro-inflammatory response. (Speeckaert *et al.*, 2011) This response may be responsible for the regression seen in spontaneously regressing neuroblastoma. Opsoclonus Myoclonus syndrome is a paraneoplastic manifestation of neuroblastoma disease. It occurs due to anti-neuronal serum antibodies triggered by the presence of the tumour. This condition also points towards the role played by the immune system in neuroblastoma and highlights the potential to harness this response in treating the disease.

1.2.6 Clinical Presentation

Neuroblastoma is predominantly an early childhood cancer, with the median age of diagnosis at 18 months. Nearly half of all disease is diagnosed in infancy. (London *et al.*, 2005) Older children with neuroblastoma, in general, exhibit a more aggressive and treatment-resistant disease. (Cohn *et al.*, 2009a)

Although tumours can occur anywhere along with the paraspinal sympathetic ganglia, the most common site is within the abdomen and the adrenal glands (>50%). The symptoms and signs at presentation will vary depending on the location of the primary tumour and the progression of the disease.

Neuroblastoma tumours may present with symptoms of abdominal mass, abdominal pain, bowel or bladder outlet obstruction, early satiety or oedema secondary to obstruction of venous drainage. Tumours within the thoracic cavity can lead to airway or vascular obstruction, which

may present difficulty breathing or venous engorgement of the head and neck. Involvement of the cervical sympathetic chain in high mediastinal/neck tumours may cause ipsilateral miosis, ptosis and anhidrosis – known as Horner's syndrome. (Berthold and Simon, 2005)

Two paraneoplastic syndromes are associated with neuroblastoma with local tumours. Opsoclonus-myoclonus syndrome occurs in up to 3% of children with neuroblastoma, presenting as rapid eye movements (opsoclonus) and jerking body movements (myoclonus). A vasoactive intestinal polypeptide (VIP) secretion is also associated with localised neuroblastoma. Symptoms of autologous VIP secretion include severe diarrhoea, leading to hypokalaemia. (Bourdeaut *et al.*, 2009) Patients with opsoclonus-myoclonus syndrome often have localised disease with good outcomes; however, neurological deficits can persist in 70% of cases. (Brunklaus *et al.*, 2012) Symptoms of excessive VIP often resolve after resection of the VIPoma. (Monclair *et al.*, 2009b)

The most common sites of metastasis are the lymph nodes and bone marrow, although liver and skin lesions are seen in 4S disease. Less frequently and in end-stage disease, the spread may also occur to the lung and brain. Manifestation of metastatic disease includes bone pain, weight loss, fatigue, skin nodules, coagulopathy and distinctive periorbital ecchymosis secondary to an unexplained predilection to infiltrate into the periorbital bones, commonly known as raccoon eyes. (Timmerman, 2003)

1.2.7 Diagnostic workup

Where there is suspicion of neuroblastoma, laboratory tests and imaging can help diagnose it. Once a diagnosis is made, tissue sampling allows patients' staging and risk stratification before treatment.

Secretion of catecholamines or catecholamine metabolites, such as dopamine, homovanillic acid (HVA) and vanillylmandelic acid (VMA), can be detected in the urine of 90% of all patients with neuroblastoma. Urinary catecholamine levels can also be prognostic, with increased dopamine levels or HVA/VMA ratio associated with aggressive disease. (Strenger *et al.*, 2007) Increased serum levels of normetadrenaline, metadrenaline, and methoxytyramine secreted by the tumour can also be measured. (Franscini *et al.*, 2015) At the initial presentation, ultrasonography is often the first used imaging modality. Positive findings on ultrasound would incur further imaging with computed tomography or magnetic resonance imaging. A complete radiological workup of the primary tumour and assessment of any metastatic disease is required for accurate staging of the

disease. The INRG classification used the presence of image-defined risk factors (IDRF) to stage the tumour and plan the course of treatment.

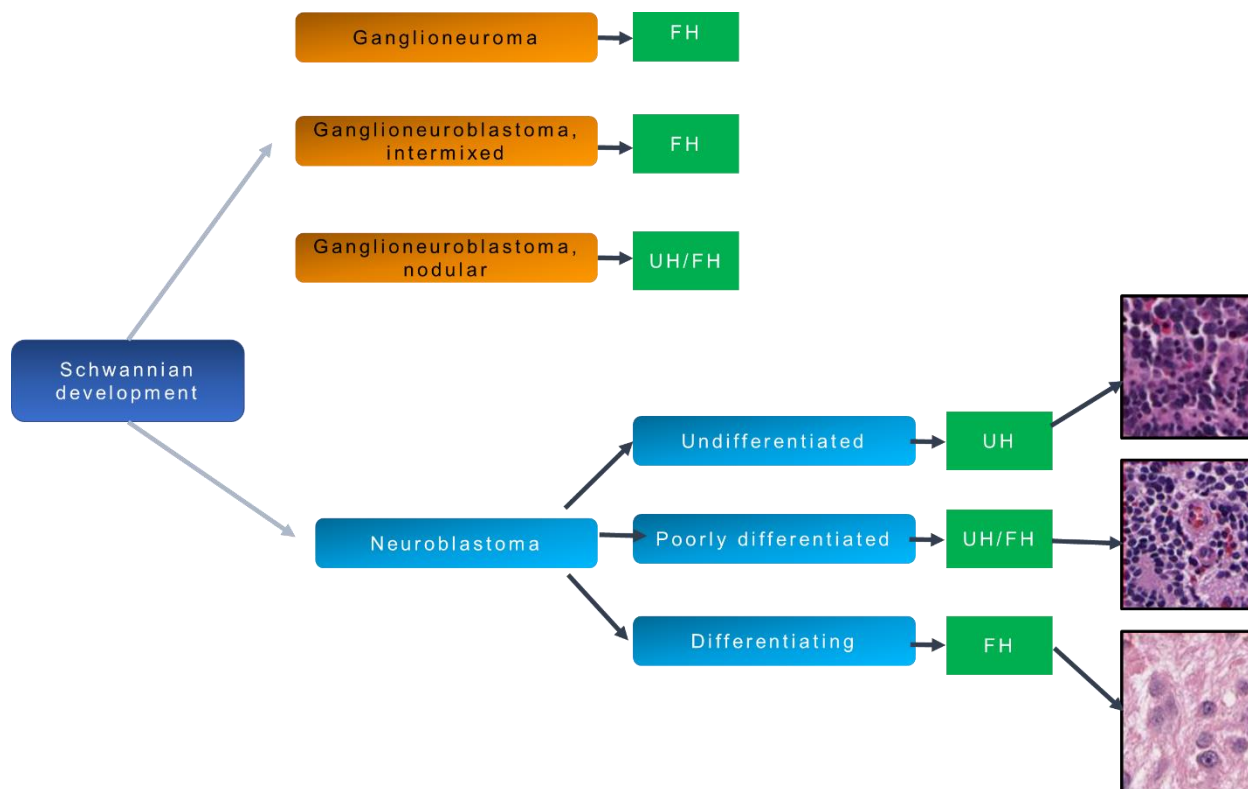
Metaiodobenzylguanidine (mIBG) is a radioisotope taken up by 90% of neuroblastoma cells via a noradrenaline transporter. It is commonly used to delineate the extent of metastatic disease, with a sensitivity of 90% and a specificity of 99%. (DuBois *et al.*, 2012) The COG is currently evaluating the use of mIBG-based scoring systems as part of the staging process. (Yanik *et al.*, 2013). In the 10% of patients who do not have mIBG avidity, ¹⁸F-fluorodeoxyglucose (FDG) PET-CT, or similar, is used to assess the metastatic disease. (Sharp *et al.*, 2009)

Fine needle aspiration or image-guided biopsy of tumour tissue and bone marrow aspirates or bone marrow biopsies are used to provide histological information for staging. Tumour molecular analysis techniques, such as fluorescent *in situ* hybridisation, assess the MYC-N amplification status (greater than 4x the reference value). (Ambros *et al.*, 2014) The use of flow cytometry to identify diploid cells is another feature of poor prognosis. (Ambros *et al.*, 2009) Single nucleotide polymorphism array can identify loss of heterozygosity or numerical chromosomal alterations, such as loss of 11q. (Kryh *et al.*, 2011) As new biomarkers and prognostic mutations, such as RAS pathway proteins (Eleveld *et al.*, 2015), are being discovered, more sophisticated genome and RNA sequencing methods are being used.

1.2.8 Staging

Abnormal migration and differentiation of the neural crest lead to the development of a spectrum of tumour types, including neuroblastomas, ganglioneuroblastomas and ganglioneuromas, histologically progressing from immature small blue cells to differentiated mature ganglion cells within Schwannian stroma, respectively. Ganglioneuroma (GN) consists of mature ganglion cells that form clusters and are surrounded by dense Schwannian stroma. GN often presents in older children and is less common than neuroblastoma. (Lonergan *et al.*, 2002) Ganglioneuroblastoma comprises a mixture of undifferentiated neuroblasts and mature or maturing ganglion cells and comprises nodular and intermixed tumours. A distinguishing feature in NB tumours is the presence of pseudorosettes (small round cells arranged in nests) surrounded by neuropil (eosinophilic neuritic material). (Lonergan *et al.*, 2002) **(Figure 1.3)**

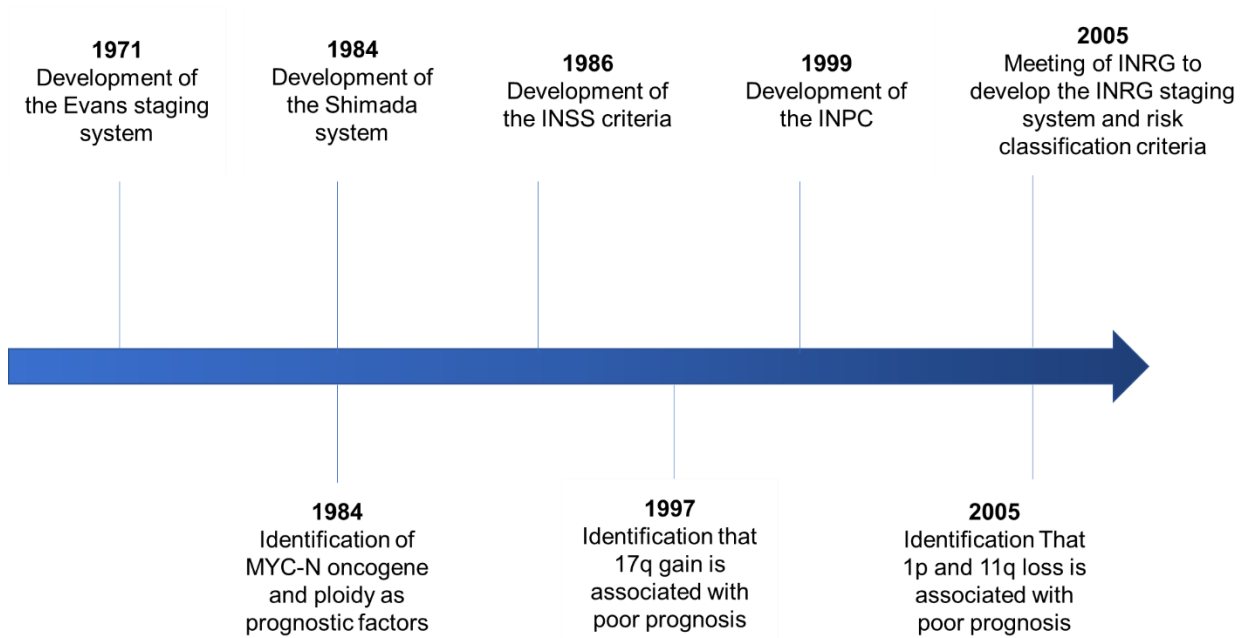
Figure 1.3 A simplified tree diagram of the International Neuroblastoma Pathology Classification



UH represents “unfavourable histology” FH represents “favourable histology”.

The Shimada classification of neuroblastoma combined histopathological evaluation with patient biological characteristics and a cellular index of mitosis and karyorrhexis to stage neuroblastoma tumours (Shimada *et al.*, 1984). This was modified by the International Neuroblastoma Pathology Committee (INPC) to include the presence of stromal Schwannian cells. This allowed for neuroblastic tumours to be subcategorised into four categories of neuroblastoma (Schwannian stroma-poor), ganglioneuroblastoma intermixed (Schwannian stroma-rich), ganglioneuroma (Schwannian stroma-dominant) and ganglioneuroblastoma nodular (composite Schwannian stroma-rich/stroma-dominant and stroma-poor). Depending on the development of Schwannian stroma, neuroblastoma may be divided into undifferentiated, poorly differentiated and differentiating neuroblasts. (Peuchmaur *et al.*, 2003) **Figure 1.4**

Figure 1.4 Timeline of major events contributing to risk classification for neuroblastoma.



INSS—International Neuroblastoma Staging System; INPC—International Neuroblastoma Pathology Classification; INRG—International Neuroblastoma Risk Group.

The International Neuroblastoma Staging System (INSS) developed the first internationally accepted surgical/pathological staging system in 1988. (Brodeur *et al.*, 1988). The response criteria are known as the International Neuroblastoma Response Criteria. Although widely adopted, the system was not without issues. **(Table 1.1)**

The same tumour could be staged differently in the INSS system, depending on the extent of surgical resection. (Kushner *et al.*, 1996). There was also no accurate staging for patients whose disease was expected to regress and were therefore managed conservatively. (Hero *et al.*, 2008)

Table 1.1 The International Neuroblastoma Staging System (1988)

1	Localised tumour with complete gross excision, with or without microscopic residual disease; representative ipsilateral lymph nodes negative for tumour microscopically.
2A	Localised tumour with incomplete gross excision; representative ipsilateral non-adherent lymph nodes negative for tumour microscopically*.
2B	Localised tumour with or without complete gross excision, with ipsilateral non-adherent lymph nodes positive for tumour. Enlarged contralateral lymph nodes must be negative microscopically.
3	Unresectable unilateral tumour infiltrating across the midline, with or without regional lymph node involvement; Or localised unilateral tumour with contralateral regional lymph node involvement; Or midline tumour with bilateral extension by infiltration (unresectable) or by lymph node involvement**.
4	Any primary tumour with dissemination to distant lymph nodes, bone, bone marrow, liver, skin, and/or other organs, except as defined for stage 4S.
4S	Localised primary tumour (as defined for stage 1, 2A or 2B), with dissemination limited to skin, liver, and/or bone marrow ***. (limited to infants < 18 months of age)
<p>* lymph nodes attached to and removed with the primary tumour may be positive ** The midline is defined as the vertebral column. Tumours originating on one side and crossing the midline must infiltrate to or beyond the opposite side of the vertebral column. ** Marrow involvement in stage 4S should be minimal, ie, < 10% of total nucleated cells identified as malignant on bone marrow biopsy or aspirate. More extensive marrow involvement would be considered to be stage 4. The mIBG scan (if performed) should be negative in the marrow. (Brodeur et al., 1993).</p>	

The International Neuroblastoma Risk Group (INRG) staging system was developed considering this. (Monclair *et al.*, 2009b) Patients were stratified based on age, histology, *MYCN* gene amplification status, DNA ploidy status, and segmental chromosomal anomalies such as 11q aberration. (Cohn *et al.*, 2009c) **(Table 1.2)** The INRG staging system is based on pre-treatment tumour characteristics so patients can be risk-stratified before surgical resection. The stages consider the presence or absence of IDRF and metastatic disease from radiological investigations. The IDRF can aid planning in terms of surgical resectability. The IDRFs are designed for diagnosis but may also be used for reassessments during treatment. (Monclair *et al.*, 2009a) These risk factors (INRG stage, age, histology, *MYCN*, 11q aberration, and ploidy status) are used to stratify patients into the following pre-treatment risk groups: very low, low, intermediate, and high.

Table 1.2 International Neuroblastoma Risk Group (INRG) Pre-treatment classification system (2005)

INRG Stage	Age (months)	Histological Category	Grade of tumour differentiation	MYCN	11q Aberration	Ploidy	Pretreatment Risk group
L1/L2		GN maturing; GNB intermixed					Very low
L1		Any, except GN maturing or GNB intermixed		Non-Amp			Very low
				Amp			High
L2	<18	Any, except GN maturing or GNB intermixed		Non-Amp	No		Low
					Yes		Intermediate
	>18	GNB nodular; neuroblastoma	Differentiating	Non Amp	No		Low
					Yes		Intermediate
			Poorly differentiated or undifferentiated	Non Amp			Intermediate
					Amp		High
M	<18			Non Amp		Hyper-diploid	Low
	<12			Non Amp		Diploid	Intermediate
	12 to <18			Non Amp		Diploid	Intermediate
	<18			Amp			High
	>18						High
MS (4S)	<18			Non amp	No		Very low
					Yes		High
				Amp			High

This system was designed to provide overall risk stratification based on a wide variety of patient derived and disease based features. GN, ganglioneuroma; GNB, ganglioneuroblastoma; Non Amp, non-amplified; Amp, amplified. Modified from Cohn et al. (2009).

Table 1.3 Image Defined Risk Factors (IDRF) (2005)

Image-defined risk factors in neuroblastic tumors
<p>Ipsilateral tumor extension within two body compartments Neck-chest, chest-abdomen, abdomen-pelvis</p>
<p>NECK Tumor encasing carotid and/or vertebral artery and/or internal jugular vein Tumor extending to the base of skull Tumor compressing the trachea</p>
<p>CERVICOTHORACIC JUNCTION Tumor encasing brachial plexus roots Tumor encasing subclavian vessels and/or vertebral and/or carotid artery Tumor compressing the trachea</p>
<p>THORAX Tumor encasing the aorta and/or major branches Tumor compressing the trachea and/or principal bronchi Lower mediastinal tumor, infiltrating the costovertebral junction between T9 and T12</p>
<p>THORACOABDOMINAL Tumor encasing the aorta and/or vena cava</p>
<p>ABDOMEN/PELVIS Tumor infiltrating the porta hepatis and/or the hepatoduodenal ligament Tumor encasing branches of the superior mesenteric artery at the mesenteric root Tumor encasing the origin of the coeliac axis and/or the superior mesenteric artery Tumor invading one or both renal pedicles Tumor encasing the aorta and/or vena cava Tumor encasing the iliac vessels Pelvic tumor crossing the sciatic notch</p>
<p>INTRASPINAL TUMOR EXTENSION WHATEVER THE LOCATION PROVIDED THAT: More than one third of the spinal canal in the axial plane is invaded and/or the perimedullary leptomenigeal spaces are not visible and/or the spinal cord signal is abnormal</p>
<p>INFILTRATION OF ADJACENT ORGANS/STRUCTURES Pericardium, diaphragm, kidney, liver, duodeno-pancreatic block, and mesentery</p>
<p>CONDITIONS TO BE RECORDED, BUT NOT CONSIDERED IDRFS Multifocal primary tumors Pleural effusion, with or without malignant cells</p>

1.2.9 Treatment by risk group

The risk stratification groups from the INRG staging allow optimal treatment by reducing exposure to harmful treatments in low-risk patients and identifying patients likely to require intensive multimodal therapies early on.

1.2.9.1 Very Low Risk

Very low-risk tumours are seen to undergo spontaneous regression. As such, in patients with International Neuroblastoma Risk Group Staging System (INRGSS) L1 and MS tumours without disease-related symptoms, observation is often sufficient. Infants (<12 months of age) with L1 adrenal tumours presumed to be neuroblastomas can probably be observed without biopsy sampling or the need for evaluation of possible metastases, given the low-risk nature of this group. (Nuchtern *et al.*, 2012) In patients with L1 tumours who are over 12 months of age, gross total resection should be considered. However, patients with incomplete resection and an absence of *MYCN* amplifications can probably be observed safely without the need for further intervention owing to a low risk of disease relapse. (Strother *et al.*, 2012). In asymptomatic patients with MS disease, biopsy sampling should be performed for risk stratification. Observation is appropriate if all favourable features are present because tumours with these characteristics usually spontaneously regress. More than 95% of patients with low-risk tumours by INRG risk stratification have survival durations of >5 years. (Irwin *et al.*, 2021)

1.2.9.2 Intermediate

Intermediate disease describes a heterogeneous population representing 9% of the total neuroblastoma patients, with an expected 5-year event-free survival between 50-75%. (Cohn *et al.*, 2009b) Patients less than one year of age with INSS stage 3, 4 or 4s disease with no *MYCN* amplification or INRG stage L1, L2 tumours without *MYC-N* amplification are generally regarded as intermediate risk. In those with L2 tumours at any site, biopsy sampling and metastatic work-up is necessary for risk stratification. Those with entirely favourable disease characteristics and a lack of clinical symptoms of disease can also be observed if <18 months of age. This approach is being tested in prospective trials led by the Children's Oncology Group (COG) (NCT02176967) and SIOP European Neuroblastoma Group (SIOPEN) (NCT01728155). Those with tumours not

meeting the size requirements for observation can be offered surgical resection in the first instance, with or without post-resection chemotherapy, based on the tumour biology. Overall there has been a move to less invasive and less aggressive treatment in intermediate-risk patients. In general, tumours with favourable biology are more likely to regress spontaneously. (Hero *et al.*, 2008)

1.2.9.3 High-Risk and Minimal residual disease

High-risk neuroblastoma comprises nearly half of all neuroblastoma and continues to have long-term survival of <50%. (Matthay *et al.*, 2016) The definition of high-risk disease has evolved over the years, which must be considered when comparing study outcomes. The definition varies between the North American COG and the International Society of Paediatric Oncology European Neuroblastoma (SIOPEN). Patients over 18 months with INSS stage 4 disease and those with INSS greater than 1 with MYCN amplification are considered high risk. Patients with stage 4 disease between 12-18 months are only considered high risk in SIOPEN if segmental abnormalities are also present. For patients with high-risk diseases, the first step in management after tissue diagnosis is initiating chemotherapy and stem cell collection. Regimes can vary but are typically composed of platinum, alkylating, and topoisomerase-inhibitor agents. Patients with MIBG avid tumours may undergo targeted radiotherapy with ¹³¹I-metaiodobenzylguanidine (¹³¹I-MIBG) as initial therapy. (Kraal *et al.*, 2015) Surgical resection following chemotherapy aims for 90% resection, although there is controversy over the importance of aggressive resection. Extensive studies from St Jude's Children's Research Hospital (McGregor *et al.*, 2005), the NB97 trial from Germany (Simon *et al.*, 2013) and a meta-analysis from Mullassery *et al.* (Mullassery, Farrelly and Losty, 2014) have demonstrated no increase in overall patient survival based on the extent of surgical resection in stage 4 patients. Conversely Holmes *et al.* compared over 1500 patients with stage 4 or 4S with MYCN amplification who had surgeon assessed complete macroscopic excision (CME) and incomplete macroscopic excision (IME). They showed an increase in overall survival (CME compared with IME: 5-year EFS, 0.33 ± 0.03 ; 5-year OS, 0.37 ± 0.03 ; $P < .001$ and $P = .004$) and a lower incidence of local progression with CME (0.17 ± 0.01 compared with IME 0.30 ± 0.02 ; $P < .001$). (Holmes *et al.*, 2020)

After surgical resection of high-risk tumours, further chemotherapy is administered. The consolidation phase of the treatment consists of high-dose chemotherapy and autologous stem

cell transplant alongside radiotherapy. The maintenance phase of therapy follows to prevent relapse. Approximately 30–50% of patients relapse despite induction chemotherapy, surgery, radiation, and myeloablative therapy. The minimal residual disease is treated with isotretinoin, a drug that induces neuroblastoma cell differentiation *in vitro*. The event-free survival for the isotretinoin arm was significantly better than no further therapy. (Matthay *et al.*, 1999) GD2 is a disialoganglioside found on the surface of all neuroblastoma cells, whilst rarely found in normal tissue. The relative tumour-specific occurrence of GD2 makes it a target for immunotherapy with monoclonal antibodies. Humanised anti-GD2 monoclonal antibodies (anti-GD2 mAb) have been effectively administered to patients with minimal residual disease. (Castel, Segura and Berlanga, 2013; Federico *et al.*, 2017) Clinical studies with targeted anti-GD2 antibodies showed efficacy in relapsed neuroblastoma: The 2-year event-free survival for the treatment arm was 66% compared to 46% for the isotretinoin alone ($p = 0,01$), and the overall survival was 86% vs 75% ($p = 0.02$). (Yu *et al.*, 2010)

1.2.9.4 4S/MS disease:

INRG stage MS or INSS stage 4S disease describes a unique subset of neuroblastoma patients, who are usually below 18 months of age, with localised tumours, favourable histology and genetic features and metastasis limited to skin, liver and bone marrow. For these patients, observation is the mainstay of therapy. Intervention with chemotherapy or surgical resection is, for the most part, reserved for those stage 4S patients with life-threatening symptoms.

1.3 Development of new therapies

Children with low/intermediate-risk neuroblastoma have good outcomes. Those with high-risk neuroblastoma, however, have a poor prognosis. Despite intensive multimodal therapies, including standard chemotherapy, surgery, radiotherapy, high-dose chemotherapy, differentiation therapy and immunotherapy with GD2-targeted monoclonal antibodies, over 50% of patients will relapse. The 5-year survival is dismal at only 10% survival rate. (Ladenstein *et al.*, 2017; Park *et al.*, 2019) New therapies targeting this aggressive phenotype with reduced long-term complications in developing children are desperately needed.

The pharmaceutical development of safe and efficacious new drugs must proceed through several key stages: (1) drug candidate discovery, (2) molecule characterisation, (3) formulation

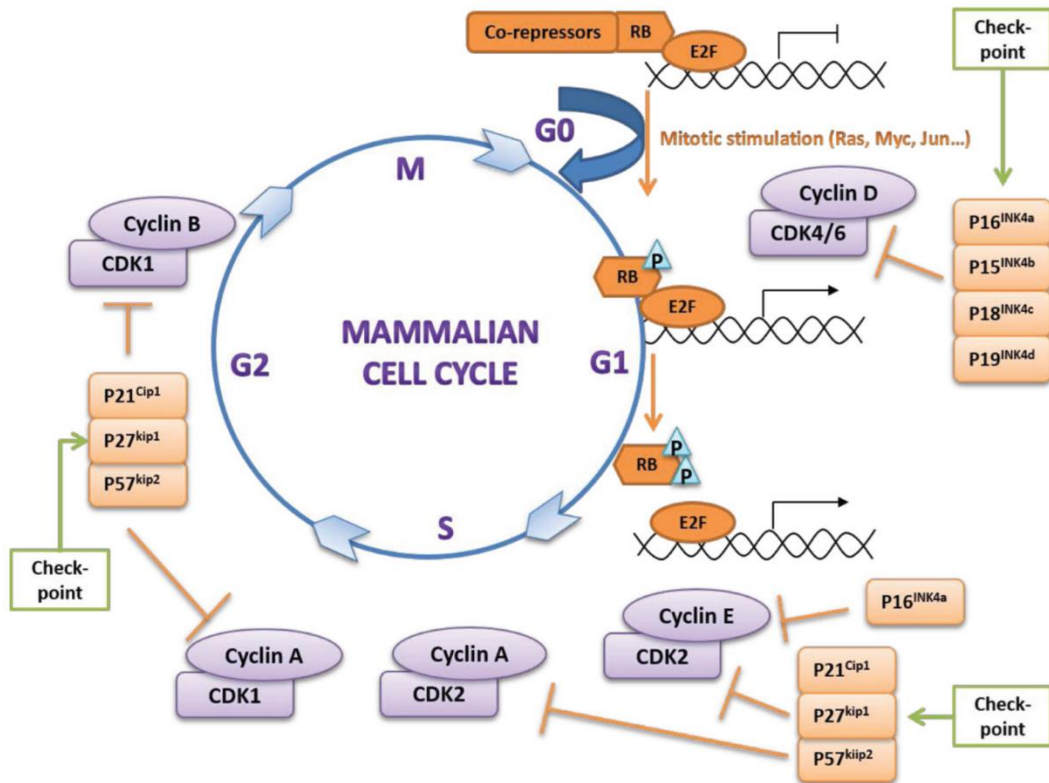
for delivery, (4) pharmacokinetics and biodistribution, (5) efficacy and toxicology testing, (6) investigational new drug (IND) application, (7) bioanalytical testing and (8) Phase I–IV clinical trials. There are many potential druggable targets and new therapies identified in preclinical research. Even though the number progressing to early clinical trials in neuroblastoma has increased, the success of these therapies being part of new clinical trials and incorporated into clinical treatment protocols is still low. There are several reasons for this attrition of therapies as they progress through drug development and testing. Drug development for paediatric use still primarily originates in adult pharmacological research. In solid tumour cancers, such as neuroblastoma, which are so inherently unique to the paediatric population, this does not serve to treat the biology of the malignancy. Neuroblastoma is also a rare condition and lacks the large numbers needed for meaningful clinical trial recruitment. The Orphan Drug Act was passed in 1983 in the United States to facilitate the development of drugs for rare conditions such as neuroblastoma. (Herder, 2017) The law seeks to incentivise the development of therapies for these conditions through benefits from the Federal Government, such as market exclusivity and reduced taxes. Following pharmaceutical company success and active involvement, Japan and the European Union adopted similar legislation. Twenty years on, a published evaluation of the orphan drug reform reported that by the end of 2017, 142 new orphan medicines had been authorised in the EU for 107 unique conditions. The issues now faced in Europe are the gross inequality in the availability and access to these novel therapies across the continent. (Zamora *et al.*, 2019) Another issue in rare disease research is the lack of collaboration and communication between academia, regulators and pharmaceutical industries. ACCELERATE, a multi-stakeholder forum aims to tackle this problem by encouraging dialogue between clinicians, academics, patient groups, pharmaceutical companies and drug regulatory authorities. (Vassal *et al.*, 2014) Specific to neuroblastoma, the Neuroblastoma New Drug Development Strategy (NDDS) was launched by the Innovative Therapies for Children with Cancer (ITCC) consortium together with the European Network for Cancer Research in Children and Adolescents and SIOPEN in 2012. The objectives of this group were to prioritise targets and druggable pathways in neuroblastoma, which should be advanced into clinical trials (Moreno *et al.*, 2017)

This project seeks to build on the knowledge of upregulated pathways and proteins to introduce potential targeted therapies against neuroblastoma.

1.4 The Cell Cycle

Cell proliferation refers to an increase in the number of cells due to cell growth and division and is necessary not only for growth and normal tissue function but also tumorigenesis. The stages of cell division, known as the cell cycle, can be divided into the synthesis and mitotic segregation phases. Between the two stages occur two intervening phases known as G1: where the cell enlarges in preparation for DNA synthesis, and G2: the phase preceding mitosis when organelles and proteins necessary for cell division are produced. The control of the cell cycle is mainly in two processes: the accurate replication of genomic DNA and the division of the DNA between daughter cells. Cell cycle checkpoints serve to monitor these events and prevent genetic errors accumulating and being passed on through delaying the cell cycle, or inducing cell cycle exit and cell death. The cell cycle is regulated at checkpoints between G1/S, G2/M, and mitotic spindle checkpoints. **(Figure 1.5)** Whether a cell can enter the cell cycle is determined by intrinsic factors (such as protein synthesis) and extrinsic factors (such as growth factors). The absence of these essential factors causes the cell to end its cell cycle and enter into a dormancy period known as the G0 phase. (Vermeulen, Van Bockstaele and Berneman, 2003) In non-cancerous cells, the cell cycle is regulated at checkpoints by multiple protein families—cyclins, cyclin dependent kinases (CDKs), CDK inhibitors (CKIs), and tumour suppressors including P53 and RB. The cell cycle is primarily controlled by a cyclin-dependent kinases (CDKs) subfamily. CDKs are serine/threonine kinases that control cell cycle progression, and their activity is controlled by activators (cyclins) and inhibitors (Ink4 and Cip and Kip inhibitors). Tumours are groups of cells which can divide continuously and aggressively in an unchecked manner because of cancer related mutations which disrupt cell cycle control mechanisms.

Figure 1.5 Schematic of cell cycle regulation highlighting the major functions of CDKs in cell cycle, adapted from Zhang et al 2021



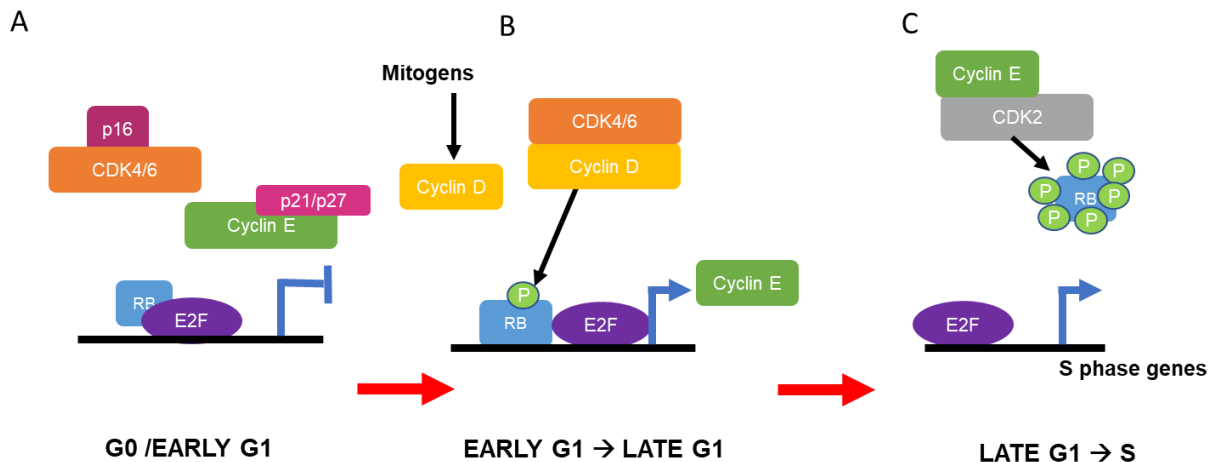
The cell cycle is split into four phases: gap phase 1(G1), DNA synthesis (S phase), gap phase 2(G2), and mitosis(M). Regulation of the cell cycle (activation and inhibition) is dependent upon several cell cycle checkpoints. These checkpoints are controlled by cyclin-dependent protein kinases (CDKs); including CDK4/6+cyclin D, RB1/E2F, CDK2+cyclin E, CDK2+cyclin A, CDK1+cyclin A, CDK1+cyclin B. CDK-Cyclin complex can phosphorylate RB protein and regulate cell cycle positively, whereas CDK-Inhibitors (CKIs) will inhibit part of the cell cycle process and play a negative regulatory role. After the cell has been stimulated by mitotic signals, it then enters the G1 phase. Before it further enters the next phase, RB protein would be first phosphorylated by CDK4/6-CyclinD and CDK2-CyclinE complexes, thereby releasing E2F protein, promoting downstream cell cycle factors and transcription-related gene expression. P16^{INK4a}, P21^{Cip1}, P27^{Kip1} and P57^{Kip2} are CKIs. P16^{INK4a} inhibits the activity of CDK4, prevent the phosphorylation of RB protein and the release of E2F, thereby inhibit the cell cycle in G1 phase. P21^{Cip1}, P27^{Kip1} and P57^{Kip2} inhibit the activity of CDKs and Cyclins more extensively and block cells at different stages of the cycle.

1.5 Cell cycle inhibitors

At the start of G1, the tumour suppressor retinoblastoma protein (RB) is hypo-phosphorylated and sequesters E2F transcription factors. (Nevins, 1992) This interaction blocks the active domain of members such as E2F1 and prevents the expression of S phase genes needed for cell cycle progression. (Flemington, Speck and Kaelin, 1993) In response to mitogenic signals, cyclin D levels rise. (Sherr and Roberts, 1999) Cyclin D binds to and activates CDK4/6. Activated cyclin D-CDK4/6 then phosphorylate RB, weakening its interaction with E2F transcription factors. (Kato, Matsushime, Hiebert, Ewen, & Sherr, 1993; Meyerson2 & Harlow, 1994; J. R. Nevins, 2001)

Figure 1.6)

Figure 1.6 Regulation of the cell cycle G1/S transition



A: In resting cells, CDK4/6 and CDK2 are inactive. D-type cyclin levels are low due to the lack of mitogenic stimulus, limiting CDK4/6 activity. Moreover, CDKs 4 and 6 are bound by INK4 family members (e.g. p16), establishing binary complexes that lack kinase activity. CDK2 complexes are inhibited by the CIP/KIP proteins p21 and p27. Collectively, the suppression of CDK4/6 and CDK2 leads to RB hypo-phosphorylation, and hence repressed expression of E2F target genes. This repression is mediated by direct blockade of the E2F transactivation domain by RB, and by recruitment of histone modifiers to RB that further silence E2F target gene expression.

B: Levels of D-type cyclins increase in response to mitogenic stimuli, due to both enhancement of cyclin D gene expression and an increase in cyclin D protein stability. D-type cyclins bind to CDK4/6, forming complexes that are stabilized by p21 or p27. Cyclin D:CDK4/6 complexes then enter the nucleus and phosphorylate RB. This partially de-represses expression of E2F target genes, including those for the E-type cyclins. The partial phosphorylation of RB facilitates progression through G1.

C: As the levels of E-type cyclins rise in late G1, CDK2 is activated resulting in RB hyperphosphorylation and inactivation. Hyperphosphorylated RB is released from E2F, enabling increased transcription of E2F target genes necessary for the cell to proceed into S phase. Figure adapted from Goel et al. 2019

CDK1 was the first CDK identified. It is conserved in all organisms, and its activity is a significant determinant of cell cycle progression. (Santamaría *et al.*, 2007) Cyclin A and cyclin B binds CDK1 during the late S/G2 phase. This leads to the activation of the transcription factors FOXM1 and FOXK2, which promote the expression of genes involved in mitotic progression. (Laoukili *et al.*, 2008; Marais *et al.*, 2010; Sadasivam, Duan and DeCaprio, 2012) In addition, the CDK1/cyclin B complex has several nuclear substrates, which phosphorylate lamin, leading to nuclear envelope breakdown (Peter *et al.*, 1990a, 1990b), and nucleolin which regulates nuclear fragmentation and organisation. (Belenguer *et al.*, 1990) CDKs are involved in the cell cycle and other critical cellular processes, such as gene transcription, insulin secretion, glycogen synthesis, and neuronal functions. (Lim and Kaldis, 2013)

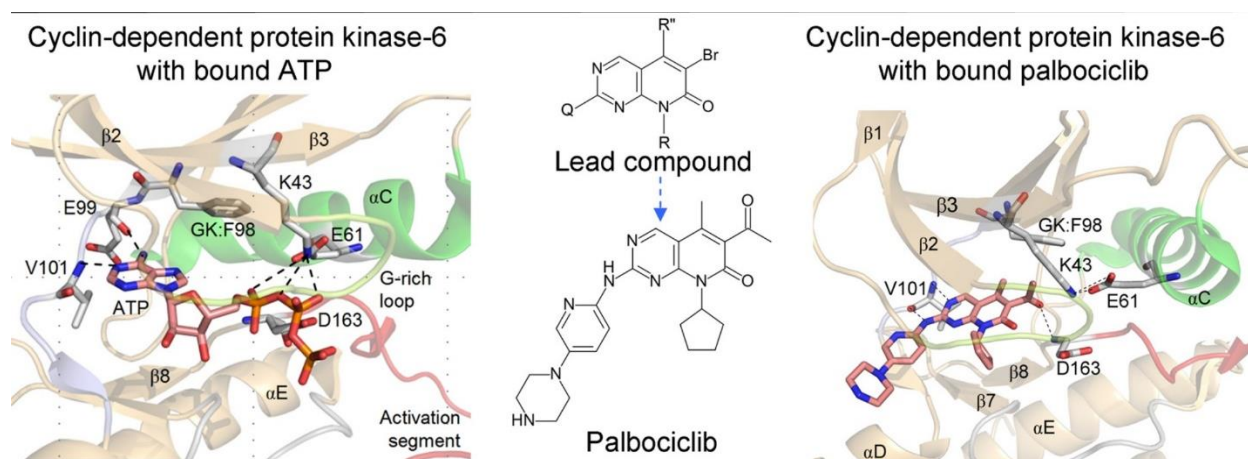
1.5.1 CDK4/6 inhibition in cancer therapy

Many human cancers harbour genomic or transcriptional aberrations that activate CDK4/6 through various mechanisms described. (Finn *et al.*, 2009) Amplification of genes encoding D-type cyclins is commonly observed in human cancer and is correlated with increased levels of cyclin D protein. In addition, liposarcoma and glioblastoma exhibit amplification of CDK4, whereas neuroendocrine cancer of the prostate has shown higher expression of CDK6. (Cerami *et al.*, 2012). *CCND1*, *CDK4*, and *CDK6* are highly expressed in neuroblastoma. Genomic amplification of *CCND1* (cyclin D1 tumours) and *CDK4* and deletion of *CDKN2A* are associated with reduced survival, and around 30% of neuroblastomas exhibit aberrations in genes which regulate the G₁ checkpoint (Molenaar, Koster, *et al.*, 2012; Peyressatre *et al.*, 2015). From NDDS, first-round cyclin-dependent kinase (CDK4/6) was identified as a potential therapeutic target to be advanced into trials. Ribociclib (LEE011) is an orally bioavailable, highly specific inhibitor of CDK4/6. Ribociclib completed phase I single-agent and demonstrated stable disease as a frequent outcome in neuroblastoma patients (7/15; 47%). (Geoerger *et al.*, 2017) LEE011 is being tested in combination in ESMART ([NCT02813135](#)) and NEPENTHE ([NCT02780128](#)). Three CDK4/6 inhibitors are currently approved for clinical use – Palbociclib, Ribociclib, and Abemaciclib. Palbociclib and Ribociclib are similar in chemical structure, while Abemaciclib differs and has a higher CDK4/6 binding power than the other two CDK4/6i. (Schettini *et al.*, 2018)

Palbociclib (Figure 1.7) has been tested in several clinical trials and phase two trials as a monotherapy and combination therapy in a wide variety of solid tumours, namely well-differentiated or dedifferentiated liposarcoma (WD/DDLS). (Dickson *et al.*, 2013, 2016), epithelial ovarian cancer (Lee and Ho, 2020) and HR+ and triple-negative breast cancer (DeMichele *et al.*,

2013), with moderate success. Rihani et al. describe the utility of Palbociclib in neuroblastoma cell lines, showing that treatment of neuroblastoma cells *in vitro* with Palbociclib resulted in growth arrest in some cell lines, such as IMR-32, SH-SY5Y. (Rihani *et al.*, 2015) Moreover, work with the group shows that CDK inhibitors reduce cell proliferation and reverse hypoxia-induced metastasis of neuroblastoma tumours in a chick embryo model. (Swadi *et al.*, 2019). Currently, the phase II Pediatric MATCH Treatment Trial is ongoing, examining the efficacy of Palbociclib in treating patients with relapsed or refractory Rb-positive advanced tumours, including neuroblastoma.

Figure 1.7 Chemical structure of Palbociclib CDK4/6 inhibitor



Palbociclib is a member of the class of pyridopyrimidines that is 2-[[5-(piperazin-1-yl)pyridin-2-yl]amino]pyrido[2,3-d]pyrimidin-7-one bearing additional methyl, acetyl and cyclopentyl substituents at positions 5, 6 and 8 respectively. Figure adapted from Roskoski et al. 2016 (<https://doi.org/10.1016/j.phrs.2016.03.012>.)

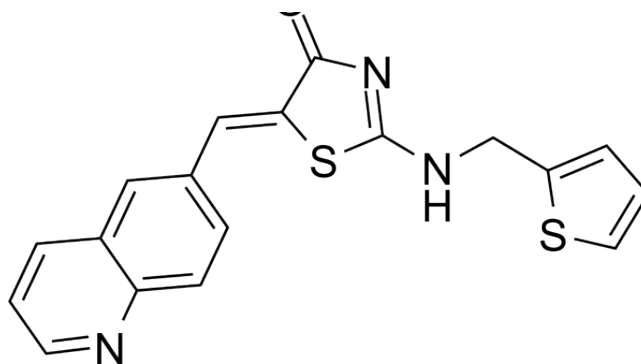
1.5.2 CDK1 inhibition in cancer therapy

Goga et al. postulated that CDK1 inhibition might have value in treating human malignancies that overexpress MYC, such as neuroblastoma. (Figure 1.8) Using an MYC-transgenic mouse that developed liver tumours resembling human hepatoblastoma, Goga showed that only half of the mice treated with CDK1 inhibitor purvalanol showed macroscopic tumours compared to all of the DMSO control group. The total number of macroscopic tumours in DMSO compared to purvalanol-treated transgenic mice decreased 3.2-fold after CDK inhibitor treatment. It is also

important to note that there was toxicity in mice treated for prolonged periods with CDK inhibitors compared to DMSO alone. (Goga *et al.*, 2007)

There is also a link between CDK1 activity and hypoxia-inducible factors (HIF) regulating the hypoxia response, which needs further exploration. Warfel showed that CDK1 directly phosphorylates HIF-1 α at Ser668, increasing its steady-state levels under both normoxia and hypoxic conditions to promote the transcription of HIF-1 α target genes. In inhibiting CDK1, they showed a reduction in HIF-1 α expression at the post-translational level. (Warfel *et al.*, 2013) Given the previously discussed hypoxia-driven phenotype of many neuroblastoma tumours, this is an exciting avenue of therapy to explore.

Figure 1.8 Chemical Structure of RO 3306 CDK1 inhibitor



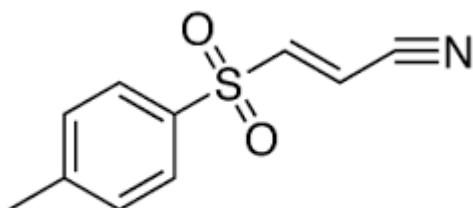
1.6 NF-KB

Transcription factor NF-KB (nuclear factor kappa-light-chain-enhancer of activated B cells) has been extensively studied for its roles in cancer development. We now understand that NF-KB plays a significant part in cancer, particularly those originating from immune cells. The contribution of NF-KB to cancer development is expansive; mutations can occur in the transcription factors or the upstream regulators of NF-KB. Aberrant NF-KB activity can affect cell survival, cell cycle progression, inflammation, metastasis, angiogenesis and regulatory T cell function.

In neuroblastoma, NF- κ B has been shown to have constitutive activity in SH-EP and SK-N-AS cells. Inhibition of NF- κ B using pyrrolidine dithiocarbamate (PDTC) and L-1-tosylamido-2-phenylethyl chloromethyl ketone (TPCK) in these cell lines has induced apoptotic cell death. (Bian *et al.*, 2002) Zhi *et al.* showed that the over-expression of NF- κ B in neuroblastoma cells promoted cell migration and invasion through the upregulation of CXCR4. (Zhi, Duan, Zhou, Yin, G. Guan, *et al.*, 2014). One of the proposed mechanisms in drug resistance, leading to treatment failure in high-grade neuroblastoma, is the activation of the NF- κ B pathway. (Wang *et al.*, 2017) However, the relationship between NF- κ B associated pathways and neuroblastoma is unclear and complex. (Mayo and Baldwin, 2000). NF- κ B can be pro-and antiapoptotic, depending on the external stress stimulus. (Dajee *et al.*, 2003; Lenz and Staudt, 2010).

NF- κ B is of particular interest given its cross-talk with pathways regulating hypoxia. HIF– NF- κ B cross-talk has been implicated in many conditions where chronic hypoxia and inflammation are prominent drivers of disease, including cancer. Members of the NF- κ B family interact with members of the PHD–HIF pathway in ways that link inflammation to hypoxia. (Eltzschig and Carmeliet, 2011) This interaction involves amplification of NF- κ B signalling through HIF binding Toll-like receptors. (Kuhlicke *et al.*, 2007) There is also greater HIF transcriptional activity through binding of the NF- κ B precursor I κ B α to factor inhibiting HIF (FIH)-1, which acts at residue 803 of HIF-1 α to block HIF coactivator binding. (Rius *et al.*, 2008) (Lando *et al.*, 2002) BAY 11-7082 (BAY 11-7821) is a NF- κ B inhibitor which inhibits TNF α -induced I κ B α phosphorylation thus preventing the release of active NF- κ B into the nucleus and subsequent transcription of target genes. Bay 11- 7082 has shown a reduction in active proliferation of neuroblastoma cell lines. (Carter *et al.*, 2012) (**Figure 1.9**)

Figure 1.9 Chemical structure of BAY11 7082



1.7 Hypoxia

Tissue normoxia is the level of oxygenation required for the survival of healthy cells and tissues. The oxygenation level can vary between tissue type, metabolic activity and function. Hypoxia refers to a primarily non-physiological level of oxygen tension below the demand of a cell/tissue. During embryonic development, before a circulatory system is established, mammalian development occurs in a relatively low oxygen environment (1-2% O₂) (Fathollahipour, Patil and Leipzig, 2018). Hypoxia drives and coordinates critical processes such as vascular and nervous system formation in this environment. (Simon and Keith, 2008) Beyond the embryological period, however, low pathophysiological availability of oxygen sets different responses on cellular and whole-organism levels in motion. (Ortmann, Druker and Rocha, 2014).

Hypoxia is seen in the majority of malignant tumours. As the demand for oxygen in a rapidly growing and expanding tumour outstrips its supply, a progressively increasing hypoxic environment is created. Hypoxic tumours typically exhibit oxygen tensions of <10mmHg, whereas normal tissues have O₂ 24-66 mmHg. (Vaupel, Kallinowski and Okunieff, 1990) Cancer cells respond differently than non-malignant cells to decreased oxygen levels. Dysfunctional and haphazard vascular neogenesis and epithelial to mesenchymal phenotype transition have all been described as part of cancer's response to hypoxia-related stress.

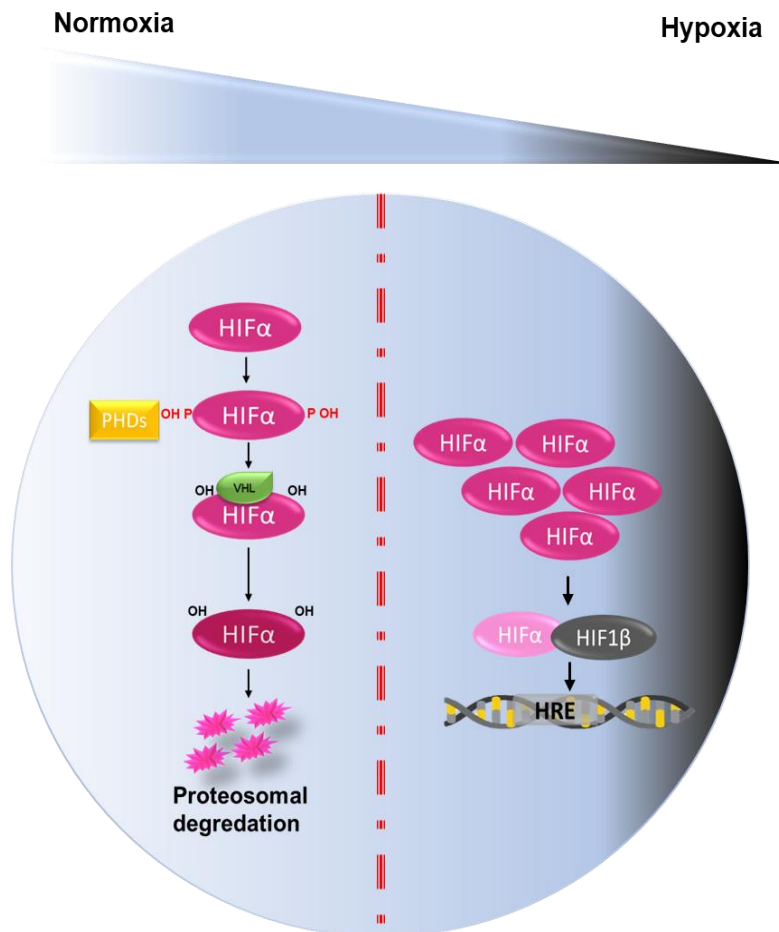
The chronicity of the hypoxia will also determine the type of response from tumour cells. Acute hypoxia is a short and reversible exposure to hypoxia, which can occur *in vivo*, for example, if a blood vessel is occluded. *In vitro*, these conditions are simulated by exposing cells to low oxygen gradients for up to 72 hours. (Bayer and Vaupel, 2012) The impact of chronic hypoxia on tumour growth propagation may depend on the duration and the level of hypoxia. The proposed mechanisms include alterations in gene expressions leading to changes in the proteome, changes in the genome, and clonal selection. (Graeber *et al.*, 1996; T. Y. Reynolds, 1996; J. Yuan, 2000; Semenza, 2003; P. Vaupel, 2004)

1.7.1.1 Regulation of Hypoxia (hypoxia-dependent cell signalling)

The hypoxic response in cancer and non-cancer cells is primarily controlled HIF pathway. (Semenza and Wang, 1992) The HIFs are a family of transcriptional regulators composed of a constitutively expressed HIF-1 β and an oxygen-sensitive HIF α subunit. When oxygen supply

meets the cells' metabolic requirement, the HIF- α subunits (HIF-1 α , HIF-2 α , and HIF-3 α) are hydroxylated within the oxygen-dependant domain (ODD) by prolyl hydroxylases (PHDs) – a group of oxygen-sensitive dioxygenase enzymes. (Bruick and McKnight, 2001) The hydroxylated HIF- α subunit then binds to the von Hippel–Lindau (VHL) tumour suppressor E3 ligase complex, leading to proteasomal degradation. However, oxygen-sensitive PHDs can no longer facilitate HIF degradation when the oxygen levels drop. The HIF- α subunits accumulate in the nucleus, where they dimerise with the HIF- β subunit. This complex accumulates in the nucleus and binds to hypoxia response elements (HREs), leading to transcriptional upregulation of target genes (Maxwell *et al.*, 1999). There are thousands of hypoxia-inducible genes with a broad spectrum of functions. (**Figure 1.10**) In addition to hydroxylation, HIF- α transcriptional activity and protein stability appear also to be dynamically regulated by other posttranslational modifications such as acetylation, S-nitrosylation, SUMOylation, and phosphorylation. Interestingly in HIF α the extent of phosphorylation seems to be dependent on the signal, cell-type, or tissue, and so the phosphorylation of HIF- α by different kinases or after modulation of signalling pathways may be a highly cell type-specific event. Much of the literature has identified post-translational modifications in HIF subunits through fragment-based strategies and modifying enzymes to identify PTMs *in vitro*, and replicate oxygen deprived environment through the use of hypoxia mimetics such as dimethylxalylglycine. Daly *et al.* have demonstrated both HIF-1 α and HIF-2 α are subject to extensive modification throughout the whole length of the two proteins. (Daly *et al.*, 2021)

Figure 1.10 Regulation of hypoxia inducible factor α subunits in normoxia and hypoxia.



In normoxia PHD enzymes hydroxylate HIF α . Hydroxylation within the ODD domain of HIF α mediates the binding of the VHL E3 ligase which polyubiquitinates HIF α and induces proteasomal degradation. In hypoxia, when oxygen levels are decreased PHDs activities are reduced. HIF α stabilization and dimerization with its transcriptional partner HIF1 β within the nucleus. HIF can then activate transcription of target genes

A non-hypoxia dependant pathway has also been described. HIF- α can also be stabilised through epigenetic changes, genetic mutations, and response to growth factors mediated by PI3K/AKT/mTOR and NF- κ B pathways. (Agani and Jiang, 2013)(Royds *et al.*, 1998)

The HIF pathway contributes to cancer growth and metastasis through many pathways. HIF can: enhance and promote cell survival and allow evasion of cell death, upregulate cell detachment, invasion and migration through regulation of cadherins and metalloproteinases, and promote neovascularisation around tumours to allow further growth spread through interaction with VEGF

and modulate cell metabolism through GLUT regulation. (Tafari *et al.*, 2013) (Semenza, 2013) (Na *et al.*, 2003)

Of the three HIF- α subunits described, HIF-1 α and HIF-2 α are the major isoforms mediating the HIF transcriptional pathway. Both isoforms have a highly conserved domain structure and exhibit many functional similarities. However, despite binding to the same HRE, it is becoming increasingly apparent that HIF-1 α and HIF-2 α also carry significant differences in their transcriptional activity in response to disease and hypoxia. (Keith, Johnson and Simon, 2011)

Due to the significant cross-over in their target genes, the differential roles of HIF-1 α and HIF-2 α are not always distinct. The most clearly defined case study is the vHL disease-associated clear cell renal carcinoma (CCRC). The VHL gene, which usually facilitates HIF degradation, is mutated in many clear cell carcinomas. There is constitutive activation of the HIF transcription pathway. However, clear cell tumours demonstrate a striking predominance of HIF-2 α expression over HIF-1 α . (Raval *et al.*, 2005) Furthermore, genome-wide analysis of HIF1- α and HIF2- α binding sites across >25000 human genes demonstrated a considerable overlap in the binding of the two HIF- α isoforms, but there are striking differences in gene regulation. (Mole *et al.*, 2009) HIF-1 α preferentially induces the glycolytic pathway (Li *et al.*, 2020), whereas HIF-2 α regulates tumour growth and stem cell pluripotency genes. (Gordan *et al.*, 2007b) (Covello *et al.*, 2006). HIF-1 α -mediated cancer pathways are mainly involved in tumour metabolism, proliferation and survival (Soni and Padwad, 2017), whereas studies suggest that HIF-2 α is mainly involved in metastasis and chemoresistance in advanced cancers. (Zhao *et al.*, 2015; Schöning, Monteiro and Gu, 2017; Hahne *et al.*, 2018)

1.7.1.2 Hypoxia and Neuroblastoma

Hypoxia has been linked to neural crest cell (NCCs) migration and differentiation. Genes controlling the delamination of neural crest cells, such as SNAIL2, are seen to be more highly expressed under hypoxic conditions. (Chen *et al.*, 2017a) In animal models, hypoxia regulates the number of migrating neural crest cells in the chick embryo (Scully *et al.*, 2016), and mice with HIF-1 knockout are seen to have neural tube deformities. (Barriga *et al.*, 2013) Therefore, oxygen tensions and HIF levels are carefully balanced for stable and accurate neural crest cell migration. Population studies examining risk factors for neuroblastoma have indicated that in-utero exposure to low oxygen levels, such as maternal anaemia or neonatal haemolytic disease, could predispose

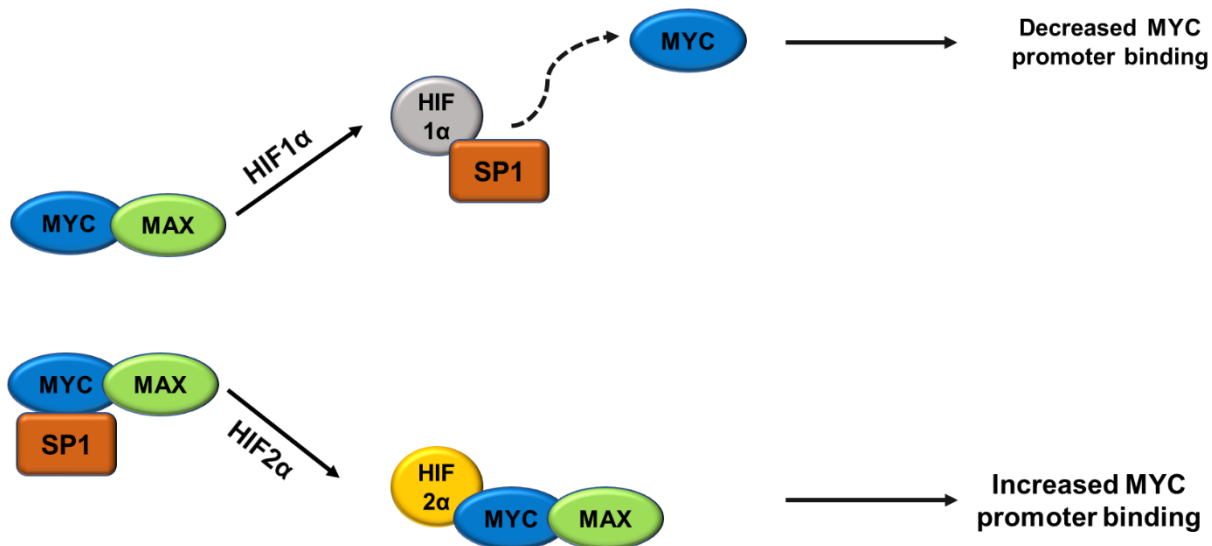
to neuroblastoma development. (Bluhm *et al.*, 2008) If this is the case, hypoxia also plays a role in developing neuroblastoma.

The importance of HIF-2 α in developing the sympathetic nervous system has been well described, with HIF-2 activating transcription in rat sympathoadrenal progenitors, resulting in a mature sympathoadrenal phenotype. (Bishop *et al.*, 2008). HIF-2 α also targets Oct-4, a transcription factor essential for maintaining stem cell pluripotency. (Covello *et al.*, 2006) Could dysfunction or overexpression of HIF-2 α , integral to sympathetic nervous system formation, play a part in the malignant transformation of neural crest cells to neuroblastoma tumours? The level of differentiation of a neuroblastoma tumour is part of the risk stratification for prognosis, and poorly differentiated histology has been correlated with worse outcomes. Studies strongly suggest that high levels of HIF-2 protein in neuroblastoma cells are associated with an immature and neural crest phenotype. (Pietras *et al.*, 2009a). Increased levels of HIF-2 α outline an immature neural-crest-like neuroblastoma cell subpopulation, characterised by the expression of NOTCH1, HES-1, c-Kit, vimentin and dHAND. (Pietras *et al.*, 2008) HIF2- α has been implicated in promoting an aggressive neuroblastoma phenotype with poor outcomes in patients with high expression of HIF2- α . (Jögi *et al.*, 2004) Knockdown of HIF-2 in tumour-initiating neuroblastoma cells results in an increased expression of several neural differentiation markers. In addition, tumours grown from knockdown HIF-2 α cells in xenograft models demonstrate a poor vasculature with large areas of necrosis, whereas the control cells with high HIF-2 α were well vascularised with rich stroma and poor differentiation. (Pietras *et al.*, 2009b) High HIF-2 α levels, therefore, appear to confer an immature phenotype with an unfavourable outcome. Hypoxia-independent functions of HIF have also been described as contributing to aggressive tumour behaviour. Proteomic analysis of neuroblastoma cells showed that high levels of HIF-2 α in normoxia conditions are associated with increased fatty storage seen in high-risk tumours. (Cimmino *et al.*, 2016). Not all studies are supportive of this, however. Work from Westerlund *et al.* suggests that HIF-2 α expression is associated with differentiated cells and low-risk MYC-N non-amplified tumours. (Westerlund, Shi and Holmberg, 2019). The opinion is controversial as it contradicts the general trend reported in the literature. It further highlights the heterogeneity of neuroblastoma and the impact of using differential transcriptomic datasets and analytical tools. Applebaum *et al.* analysed transcriptome data from diagnostic neuroblastoma tumours and hypoxic neuroblastoma cell lines to identify gene expression levels that correlate with poor patient outcomes and are involved in the hypoxia response. The signature included the expression of LCO4A1, ENO1, HK2, PGK1, MTFP1,

HILPDA, VKORC1, TPI1, and HIST1H1C. Identifying hypoxia-related gene signatures can potentially lead to using hypoxia-related pathways as targets for NB treatment. (Applebaum *et al.*, 2016; Cangelosi *et al.*, 2020).

In addition to neuroblastoma cell differentiation, hypoxia has also been associated with increased neuroblastoma tumour cell survival. When MYC-N amplified SK-N-BE(2)C neuroblastoma cells were cultured in hypoxia, a transient cell cycle arrest was detected, but no increase in cell death. HIF1 stabilisation has been shown to induce cell cycle arrest in clear cell renal carcinoma. MYC-N amplification is thought to stabilise HIF-1, so MYC-N amplified neuroblastoma cells may promote anti-apoptotic pathways through HIF-1a stabilisation. HIF-2 α appears to increase proliferation and reduce cell death through an MYC-independent pathway. (Yin *et al.*, 2015; Zaatiti *et al.*, 2018a)(Gordan *et al.*, 2007b). **(Figure 1.11)**

Figure 1.11 Distinct effects of HIF-1 α and HIF-2 α on MYC complex formation.



*Hypoxic cells exclusively expressing HIF-1 α exhibit decreased MYC activity due to reduced association with MAX and SP1, as well as reduced MYC stability. Cells expressing HIF-2 α exhibit increased MYC complex formation and target gene activation. Adapted from Johnson *et al* 2011.*

The link between hypoxia in neuroblastoma and metastatic tumours is less well described. Metastasis involves multiple pathways, and the influence of hypoxia in each step is not fully understood. In cell culture, hypoxic preconditioning of cells has shown reduced expression of

genes involved in the maintenance of cell-cell and cell-matrix interactions, such as metalloprotease-4 inhibitor (TIMP4), E-cadherin (CDH1), catenin (CTNNB1) and fibronectin-1 (FN1) and upregulation of pro-metastatic genes such as integrin 7 (ITGA7), vascular endothelial growth factors (VEGF), transforming growth factor-1 (TGF-1). Taken together, these promote cell detachment, invasion and vascular neogenesis. (Poomthavorn *et al.*, 2009). Herrmann *et al.* working with our lab group in Liverpool elegantly demonstrated the effect of hypoxia on neuroblastoma cells *in vivo* through live-cell imaging. Preconditioned neuroblastoma cells were more capable of migration toward blood vessels within the chick embryo model. These cells were also more readily able to slow their speed to extravasate into distant sites from the primary injection site and proliferate at the distant sites. In addition, the memory of hypoxic exposure held with these cells could influence neighbouring non-hypoxia cells to behave in a similar metastatic manner. (A. Herrmann *et al.*, 2015)

Hypoxia has been linked to the formation of metastatic disease. The downstream expression of hypoxia proteins initiates and supports metastatic spread via tumour cell motility and invasion, intravasation, extravasation, and metastatic colonization. In addition, tumour hypoxia exacerbates chemotherapy resistance through physiological and genomic mechanisms. (Teicher, 1994; Tannock, 1998). The detection and assessment of tumour hypoxia plays a critical role in both the validation and development of cancer therapies for their eventual adoption into routine clinical practice, and for this work, I have tested all compounds in hypoxia (1%) and normoxia (21%)

1.7.1.3 Targeting HIF

Hypoxia and hypoxia-inducible factors are fundamental in neuroblastoma development, progression, and metastasis. It stands to reason that targeting these factors and their downstream targets would be an attractive therapeutic avenue in treating neuroblastoma. There are many different strategies for inhibiting the HIF pathway. Small molecules have been shown to inhibit HIF activity through various mechanisms, including HIF protein synthesis, protein stabilization, HIF-1 α -HIF-1 β dimerization and DNA binding. However, due to the multitude of complex pathways which converge on HIF, it can be challenging to separate the desired effects on one pathway from another.

Angiogenesis is key to the growth and spread of cancer, and HIF is known to upregulate the key angiogenesis promotor - VEGF. HIF-2 α is known to upregulate VEGF in neuroblastoma. (Lee *et*

et al., 2019). Anti-angiogenesis therapies such as receptor tyrosine kinase (RTK) inhibitor Sunitinib have shown effectiveness in neuroblastoma cell treatment. Sunitinib has been combined in another study with Evofosfamide, a cytotoxic drug activated in a hypoxic environment, showing tumour growth suppression (Kumar *et al.*, 2018). More research must identify novel and specific inhibitors targeting clearly defined points in the HIF pathway. Such new agents could be used in combination therapy and may overcome the resistance that can develop during the initial treatment. Several VEGF inhibitors have been approved for clinical use; for example, the anti-VEGF monoclonal antibody bevacizumab has been approved for treating colorectal cancer and non-squamous non-small cell lung cancer, glioblastoma and renal cell carcinoma. (Hurwitz *et al.*, 2004; Arora *et al.*, 2021) However, monotherapy with VEGF inhibitors may yield limited results. This is because tumours use multiple pathways for recruiting vessels, and blocking VEGF alone has incomplete effects on tumour vasculature, and tumours may switch from one mechanism to another. (Gardner, Madu and Lu, 2017) Prolonged treatment of anti-angiogenic therapies has been known to exacerbate hypoxia, resulting in subsequent treatment failures (Carmeliet and Jain, 2011; Gaustad *et al.*, 2012). Therefore, inhibition of the upregulating HIF signals may be more practical than targeting the downstream VEGF.

1.8 Models for neuroblastoma research

Establishing clinically relevant models for studying tumour biology, metastasis, and drug testing is a significant challenge in cancer research, especially in paediatric cancer research. Neuroblastoma is a clinically heterogeneous cancer. There is a lack of consistent genetic markers and a range of possible outcomes based on genetic and histological variation, so developing new therapies relies on understanding the disease's biology.

1.8.1 *In vitro* models

In vitro, cellular models encompass many systems, including 2-dimensional adherent monolayers of cells, 3D spheroids, and scaffolding/tissue-engineered constructs.

1.8.1.1 2D

Two-dimensional cell culture techniques have a key place in cancer research. The studies are often high throughput, relatively low cost and usually easy to reproduce. Many cell lines have been commercially characterised explicitly for *in vitro* neuroblastoma research. (Thiele, 1998) However, it is increasingly accepted that although these methods are used, the monolayer of cells

does not recapitulate complex interactions with a 3D tumour microenvironment and cannot fully depict some key cellular behaviours and interactions. (Asghar *et al.*, 2015)

1.8.1.2 3D spheroids

The multicellular tumour spheroid (MCS) model is currently one of the most popular and well-characterised 3D cell culture platforms. (Katt *et al.*, 2016) The spheroid model can be formed through the hanging drop, forced flotation and rotational culture. The spheroids can provide important information about cell-to-cell interactions in a 3D environment alongside mimicking *in vivo* tumour diffusion gradients and oxygen and nutrient transfer. Similar to 2D models, they are high throughput and easy to replicate without specialist equipment in most circumstances. Studies using MCS in neuroblastoma research have modelled the 3D architecture of the cells, with a central necrotic core surrounded by proliferating cells at the periphery. (Stock *et al.*, 2016) Furthermore, the spheroids can reproduce the drug resistance seen in clinical practice more closely than that observed in 2D studies alone. (Besançon *et al.*, 2012).

Further finetuning spheroids has led to the development of scaffold-based platforms and hydrogel embedding models. Unlike matrix-free spheroids, these models use supportive polymers to mimic the microenvironment of tumours and the biomechanical stresses of the extracellular matrix. (Yeung *et al.*, 2015)

1.8.2 *In vivo* models

1.8.2.1 Murine models

In vivo animal models most commonly used in neuroblastoma research are transgenic, xenograft, syngeneic and humanised animal systems. As demonstrated in the variety of models used, no single model can accurately fully capitulate the disease progression in neuroblastoma.

1.8.2.2 Syngeneic mouse models.

Syngeneic mouse models or allograft mouse models were first used in neuroblastoma research around 50 years ago. Immortalised mouse cancer cell lines are engrafted into the same inbred immunocompetent mouse strain. This allowed tumour formation in an immunocompetent host without rejection. The C1300-NB model demonstrated spontaneously arising tumours from the spinal cord. The TBJ-NB is a spontaneously developing clone from C1300-NB, which can grow rapidly and invasively with metastatic invasion. (Beltinger and Debatin, 2001) However, C1300-NB and other models do not genetically recapitulate human disease as no genetic alterations

identified in humans are present in these models. (Seitz *et al.*, 2012) Also, they do not replicate neuroblastoma development in embryos like the human disease.

1.8.2.3 Transgenic mouse models

Transgenic mouse models or genetically engineered mouse models (GEMMs) can be engineered to knock in or knock out genes of interest. These are the MYCN overexpressing mice that reproduce MYCN amplification seen in many aggressive neuroblastoma tumours. These models have overcome some of the disadvantages associated with syngeneic models. TH-MYCN and LSL-MYCN; Dbh-iCre are transgenic neuroblastoma murine models engineered to overexpress MYCN in neural crest cells. (Althoff and Schramm, 2017) In neuroblastoma, the most widely used GEMM is the TH-MYCN model. (Weiss *et al.*, 1997). Many studies have shown the validity of this model, including in the MYCN expression of the tumours produced and the similarity in the histopathology between tumours grown in the model and human tumours. (Chesler *et al.*, 2007)

The advantage of this model is that it can be used to test chemotherapies targeting MYC-N and its downstream targets. The success of *in vitro* chemotherapies targeting the MYC-N pathway, such as BET-bromodomain protein inhibitors, has been replicated within the model. (Henssen *et al.*, 2016). The model is not without its limitations, however. The model cannot wholly replicate the distant metastasis often seen in aggressive MYC-N amplified neuroblastoma. In addition, the neuroblastoma development and spread pattern are different from the one seen in clinical practice: none of the murine neuroblastoma tumours originated in the adrenal medulla in a study by Teitz *et al.* seen in the sympathetic ganglia. In comparison, in around 40% of human patients, tumours are first seen here. (Teitz *et al.*, 2011). In addition, the only chromosomal aberration in this model is MYC-N amplification, unlike human disease, where multiple concurrent mutations are seen.

Althoff *et al.* generated transgenic mice, termed *LSL-MYCN; Dbh-iCre*, with Cre-conditional induction of *MYCN* in *Dbh*-expressing cells to address some of the drawbacks of the Th-MYCN model. (K. Althoff *et al.*, 2015) Tumours in the *LSL-MYCN; Dbh-iCre* model arise in multiple anatomical locations, such as the superior cervical ganglion and the adrenal glands. They also express neuroblastoma-specific genes such as paired-*Phox2b*, *Dbh* and *Th* alongside increased levels of MYC-N expression. The THMYCN mouse inserts into chromosome 18, and the consequences have not yet been characterised.

In contrast, the LSLMYCN; Dbh-iCre mice insert into the ROSA26 locus on chromosome 6, a more commonly used locus for constitutive, ubiquitous gene expression in mice. The LSLMYCN; Dbh-iCre models also reproduce the histology and MYCN expression in THMYCN models and respond similarly to MYCN antagonists. Finally, the tumours from *LSL-MYCN; Dbh-iCre* mice exhibit a partial gain of chromosome 11, syntenic to human chromosome 17q. Therefore, this model resembles the genetic aberrations observed in human neuroblastomas more closely than the *Th-MYCN* model.

Although developing new transgenic models is refining *in vivo* research of neuroblastoma, GEMMS still harbour disadvantages. They are restricted by high husbandry costs and long development time (an average of 65 days), making rapid, high-throughput testing difficult. They still do not show a perfect match to human pathways and exhibit differential responses from what is seen in clinical practice. (Waterston *et al.*, 2002)(Perel *et al.*, 2007)

1.8.2.4 Xenograft models

Xenograft models have been used extensively in preclinical neuroblastoma research, where human cells have been engrafted into mice. Subcutaneous or orthotopic injections of neuroblastoma cells can develop into tumours that are more homologous to human disease and, in general, more accessible to generate than tumours in transgenic models. (Teitz *et al.*, 2011) However, the mouse has to be immunocompromised to engraft a different cell species into the murine host. As a result, this model cannot be used to study the effect of immunotherapies or accurately depict the tumour microenvironment shaped by the host immune response. Despite this, orthotopic and subcutaneous tumours have been used extensively for preclinical testing of therapeutics, including chemotherapy, small interfering RNA, and drug delivery methods such as nanoparticles. (Byrne *et al.*, 2014; Iyer *et al.*, 2015; Guan *et al.*, 2016) In addition to immortalised cells, patient-derived xenografts (PDX) are taken directly from patients and implanted into mice by implantation or injection of tumour cells. Studies show that PDX tumours grown in mouse models share molecular characteristics with primary NB cells and can spontaneously metastasise in murine models. (Braekeveldt *et al.*, 2015; Stewart *et al.*, 2015). PDX and xenograft models still take time to establish tumours, limiting their use for high throughput large-scale studies. The interactions between human cells and murine stroma are still not completely understood. The most significant drawback is the lack of a robust immune system to test immune-based therapies accurately. There has been a considerable effort to humanise the immune system of immunocompromised mice. Immuno-avatar murine models have transplanted human peripheral

blood mononuclear cells, and haemato-lymphoid humanised mice have transplanted CD34+ human haematopoietic stem cells. (Chen *et al.*, 2019) These hybrid models and PDX transplantation can advance the understanding between tumour development and the human immune system in a preclinical model. However, they are highly sophisticated and expensive models, and their availability for widespread use is limited. (Nguyen *et al.*, 2021) (Sanmamed *et al.*, 2016)

1.8.2.5 Zebrafish Model

The zebrafish model has gained wide popularity in modelling neuroblastoma in recent years. The advantage of this model is that it allows high throughput testing of drugs, which are relatively inexpensive to handle. The most recent model has shown histology comparable to human neuroblastoma (Her *et al.*, 2021). However, zebrafish's organ system and development differ vastly from human and murine systems. This difference in metabolic activity means that direct comparisons of neo-angiogenesis and cellular proliferation are unlikely to spread to human or murine systems. (Corallo *et al.*, 2016; Casey and Stewart, 2018; Li *et al.*, 2021)

1.8.3 The chick embryo model

Chick embryos have been instrumental to developmental biology and significant contributions to cancer biology, virology, immunology and cell biology research. (Kain *et al.*, 2014)

The first use of the chick embryo as an oncological animal model was described over a century ago. (Murphy and Rous, 1912; Kain *et al.*, 2014) Moreover, the chick embryo contributed to the discovery of the first oncogene, c-src. (Stehelin *et al.*, 1976)

For several reasons, the chick embryo is an attractive model for cancer, especially in neuroblastoma research. It has many anatomical, cellular and molecular similarities to the human as an embryonic model. Although the model is immunocompetent, this immune system only starts development around embryonic day nine and does not fully mature until embryonic day 18. Hence, an immunodeficient model in its early development stages is ideal for xenografting tumour cells. (Vargas *et al.*, 2007a)

The model is widely available, self-contained and requires minimal and relatively inexpensive husbandry equipment. According to European law (Directive 2010/63/EU of the European Parliament and of the Council of 22 September 2010 on the protection of animals used for scientific purposes), the Chorioallantoic membrane (CAM) chick model system does not raise any

ethical or legal concerns. Current UK legislation on the protection of animals for scientific purposes allows experimentation on chick embryos without authorisation up to the age of development day 14 (E14). This makes the model extremely feasible and conducts experimental work up to E14.

The chick model also satisfies the ethical principles of refining, reducing, and replacing (3Rs) for animal use in scientific experimentation. The chick model can reduce and replace the need for expensive rodent models in several preclinical tumour biology experiments. It also can refine the long list of potential drug therapies by acting as a screening tool for new chemotherapy agents.

1.8.3.1 CAM assay

The stages of chick embryo development were documented in great detail by Hamburger and Hamilton in 1951. (Hamburger and Hamilton, 1951) This has allowed researchers to take advantage of this *in vivo* system for biomedical research.

The cycle from fertilisation to hatching is 21 days. The chorioallantoic membrane is a highly vascular, semi-permeable membrane formed from the fusion of the mesodermal allantois and the chorion. This layer is vital for gas and nutrient exchange in the chick and forms a film over the developing embryo at around 4-5 incubation days. Upon this layer, Armstrong et al. reported the ability of several different types of tumour cells to invade and form tumours just beneath. (Armstrong, Quigley and Sidebottom, 1982)

The ability to reliably engraft and grow tumours using the CAM model is one of the reasons for its appeal. (**Table 1.4**) The low engraftment rates in expensive immunodeficient animal models have been well described: DeRose et al. describe an engraftment success rate of less than 25% in a murine breast cancer model. (Derose *et al.*, 2011) A review from Debord et al. shows a much higher success rate in multiple tumour types when using the CAM model, with a success rate approaching 100% demonstrated in glioma xenografts. (DeBord *et al.*, 2018)

The model's tumour growth and metastasis assessment have since been widely studied. (Shioda *et al.*, 1997; Cimpean, Ribatti and Raica, 2008; Deryugina and Quigley, 2008) Successful experiments using immortalised cancer cell lines and patient-derived tissue/cell xenografts have been described. The xenografts can be placed onto the surface of CAM (Klingenberg *et al.*, 2014) (Karnofsky, Ridgeway and Patterson, 1952; Gronau *et al.*, 2006; Huang *et al.*, 2017) or injected into the veins of CAM (Leong, Chambers and Lewis, 2012).

Notably, the tumours developing within the chick recapitulate the heterogeneity seen within clinical practice. In melanoma, tumours formed were morphologically similar to patient-derived tumours. (Durupt *et al.*, 2012) The patient-derived xenografts used within the model replicate the features of the original tumours with high fidelity. Rovithi *et al.* engrafted pancreatic ductal adenocarcinoma (PDAC) onto the CAM and showed through immunohistochemistry and genetic analysis the retention of PDAC markers such as mucin-1 and common PDAC gene mutations such as *SMAD4/DPC4*. (Rovithi *et al.*, 2017)

Table 1.4 General advantages/disadvantages of the CAM assay

	Advantages	Disadvantages
Technical	Short experimental duration	Short observation period
	Easy handling	High attrition of eggs – susceptible to infections and equipment failure
	Inexpensive	Can be technically difficult to access vasculature
	Allows high throughput screening	
	Allows multiple tests per individual CAM	
	High reproducibility	
	Allows continuous/direct visualization	
	In vivo imaging available	
	Animals need not to be restrained or narcotized	
Biological	Naturally immunodeficient	Unable to examine tumour-immune cell interaction
		Non-specific inflammatory reaction after chick immune system development
	Highly vascularized environment for tumour growth	Difficult in distinguishing neovascularization and existing vessels
	Closed system	Sensitive to environmental factors (e.g., changes in pH, osmolarity and oxygen)
	High feasibility on primary human cell lines	Limited antibodies and cytokines for chicken tissue characterisation
	Well-known biology and physiology	Differences in drug metabolism and immune system with mammals
	Various drug treatment routes	Oral route cannot be tested – allantoic sac is proxy only
Ethical	No administration consent needed	

1.8.3.2 Metastasis in the chick embryo

The mortality and morbidity associated with any cancer metastasis are significant. *In vivo* models need to fully recapitulate the tumour biology and interactions with the tumour microenvironment, which leads to cell migration and secondary site tumour formation. The chick embryo has been used to study both spontaneous and induced metastasis. Spontaneous metastasis can be used to study invasion in specific tumour types with simple engraftment onto the CAM, whereas injection of tumour cells into the allantoic sac or allantoic vein can show the behaviour of cells within the circulation. (Chu *et al.*, 2022) Studies have demonstrated that squamous cell carcinoma

implanted on the surface of CAM metastasised to the chick embryo's eye, brain, liver, and myocardium. (Ribatti, 2016) Sites of metastasis are often very cancer-specific, and metastatic models showing similar metastasis patterns as seen in clinical disease are desirable. Human leukaemia cells have been shown to metastasise to the chick brain, displaying a more similar phenotype to human leukaemia progression than some murine models. (Taizi *et al.*, 2006a)

1.8.3.3 Drug delivery in the chick embryo

A key advantage to any model is accurately and reliably testing compounds. The development of a model for drug testing can be challenging as all physiological barriers and metabolic interactions which can govern drug bioavailability and toxicity need to be considered. A chick embryo is a valuable tool for assessing different compounds and drug delivery systems. Numerous different compounds and delivery systems have already been evaluated in this model. Drugs applied to the CAM surface are absorbed through the membrane and circulate systemically. Similarly, compounds can be injected intravascularly or into the amnion. The latter is akin to oral administration in clinical practice. The activity and toxicity of the compound can also be assessed in the model. Fluorescently labelled compounds can be tracked to the xenografted tumour tissue, and toxicity levels can be assessed by chick survival, chick growth or local inflammation on the CAM. (Ribatti, 2014a) Different drug delivery systems have also been tested successfully, including nanoparticles, nanoemulsions, liposomes, dendrimers, nanotubes, microparticles/microspheres, and hydrogels. (Swadi, Pizer, *et al.*, 2018; Victorelli *et al.*, 2020)

1.8.3.4 Imaging the chick embryo

Scientists have developed different methods to measure and quantify tumour growth, metastasis and drug efficacy in the chick embryo. The techniques can be classified into *ex ovo* culture and *in ovo* culture, and the outcomes measured may be qualitative, semi-quantitative and quantitative. (Ribatti *et al.*, 2010; Dunn *et al.*, 2013) Light microscopy has been used to examine the surface of the CAM, the growth of tumour xenografts and to measure the density of the vasculature as a proxy of inflammation or neoangiogenesis. (Ribatti, 2014b) For this, part of the shell must be removed to visualise the structures below. It is a destructive endpoint method of measurement. *Ex ovo* culture, where the chick is grown in a weighing boat or cling film hammock, allows unobscured examination of the CAM at multiple time points. (Yalcin *et al.*, 2010) The disadvantage of this method is high rates of chick death due to infection or loss of heat and

moisture. Fluorescent microscopy can also be used with labelled cells to visualise tumour growth and spread into nearby vascular structures. In 2013 the first use of computed tomography combined with positive emission tomography (PET) to visualise metastatic cells was reported. (Warnock *et al.*, 2013) Magnetic resonance imaging (MRI) has also been used to visualise tumour cells labelled with magnetic polymers in the embryo's organs. (Herrmann *et al.*, 2018) However, MRI image acquisition requires a special contrast agent, and many cells need to be implanted on the CAM due to the substantial loss of signal resulting from cell proliferation.

There is a high demand for reliable and accessible models of neuroblastoma to address the ethical implications and cost of large-scale 'top-down' animal models. Using the chick embryo as a biological platform that is cost-efficient, ethical, and well-researched is an exciting prospect.

1.9 Three-dimensional imaging

Biological specimens are three-dimensional units, but because of light scattered by cellular constituents, it is easier to image thin sections rather than thick volumes. Two-dimensional thin sections of tissue samples are used in research and clinical practice as a proxy for the whole 3D structure. However, this is an imperfect representation. Nerves, vessels, and the extracellular matrix extend beyond the scope of 2D sections in all directions. 3D spheroids or tumours may have different characteristics at the leading edge of the structure compared to the centre. 3D reconstruction of 2D sections has been attempted, but distortion or loss of sections is expected, so this information is lost. Current methods of histological grading of cancers are also susceptible to inaccuracies due to this lost information. For example, the Gleason grading of prostate cancer uses histological sections to evaluate prognosis. However, the reproducibility of the exact score is only seen in 50% of patients. (King and Long, 2000). Another example where volumetric imaging may be an advantage is for cancer cell-positive lymph nodes. Lymph node sampling is often used to approximate the level of distant metastasis. However, micro-metastasis may be missed if only a few sections per lymph node are analysed. There is a 33% false-negative rate when reviewing lymph node biopsies before starting chemotherapy (Brown *et al.*, 2010). With the advent of more sophisticated and powerful microscopes, the interest in imaging deeper into 3D tissue has grown inexorably. Microscopic imaging of samples without sectioning may negate some of these issues. However, another problem emerges: out-of-focus information from regions

above and below the area of interest can blur the image, and imaging at depth causes scattering of the light and increased signal: noise.

1.9.1 Light scattering and a tissue sample

Light travels in rays as a straight line. Any molecules, membranes, or structures in this path will cause the light to deviate. Light itself is composed of photons with an electrical and magnetic properties. The wavelength of light will determine its frequency – the speed at which it vibrates. As this vibrating wave interacts with another atom in its path – a cell membrane – it momentarily passes some of its energy to the atom. This energy is absorbed and released as a new, expanding spherical light wave. This new wave of light or wavelet does not travel in the same direction as the original and is therefore said to be scattered. Like its originator, this wave of light will also encounter membranes and are further scattered – and so on. An essential distinction between inert dense structures, such as glass, and biological samples must be made. Although dense, glass is a homogenous structure with many atoms to scatter light. Although light scattering exists in the glass, there is destructive interference between the many wavelets, cancelling themselves out, so the sum effect is zero. Light does not escape in lateral directions, and the material is thus transparent. In tissue structures, however, there is vast heterogeneity in the tissue, and light scattering is cumulative, not cancelling. There are multiple wavelets emitted perpendicular to the light source. There is also a relationship between the wavelength of light and the size of the heterogeneous particles. In a sample with multiple small particles, a short wavelength is more likely to be absorbed and re-emitted (Rayleigh scattering).

In contrast, longer wavelengths, such as those used in 2 photon microscopy, are less frequently absorbed and scattered. If the particle is greater than 1/10 of the organelle, reduced scattered is seen (Mie scattering). In addition to light scattering, there is also light absorption. Haemoglobin, myoglobin and melanin are all molecules found within biological tissues which can absorb light. Removing these molecules from the sample can aid in deep tissue imaging – however, it is not always possible. In animal models, the perfusion of a clear buffer through the vasculature can remove haem particles. When this is not possible, bleaching compounds such as hydrogen peroxide can be used to decolourise the molecules – although the sample may be damaged through exposure to harsh chemicals. (Richardson and Lichtman, 2015)

There is also a delay in the transmission of light caused by particles in its path. This interruption, although only femtoseconds, causes a delay in the wavelength of the new wave of light. Over its

entire journey, the ray of light will encounter many molecules; at each one, there is a scattering of light and a speed reduction. This speed reduction is known as the refractive index. The refractive index depicted as an equation is a ratio between the speed of light with no delay (in a vacuum) and the speed of light in that particular medium. Many factors may influence the refractive index of a structure – the density and the composition. Hydrophobic molecules are more likely to absorb light energy than hydrophilic molecules, so the lipids within a cell membrane are more likely to cause a change in the speed of light than the water surrounding the cell. This cumulative difference in refractive indices and progressive scattering of light leads to an opaque sample.

1.9.2 Tissue clearing

Over 100 years, a German scientist, Werner Spalteholz, developed a method to make organs translucent. This first clearing technique employed multiple organic solvents that would dehydrate, bleach, decolourise, and clear the entire organ. This pioneering work allowed unprecedented views of biological samples and significantly advanced the field of anatomy. (Spalteholz, 1914) However, this intense chemical exposure damaged the tissue and was unsuitable for all samples. One hundred years on, tissue clearing and 3D imaging is a rapidly expanding field with multiple methods developed for deep imaging biological samples by reducing light scattering. Although clearing was first developed to study neuronal development, it has not escaped attention that high-resolution images of tumours may hold the key to unlocking how certain cancers grow and metastasise. 3D image has proven helpful in quantitatively visualising tumour architecture and the surrounding tumour microenvironment in models and patient samples. Whole organism quantitative metastatic counts have been performed using clearing and immunostaining in mice with glioma and pancreatic cancers (Garofalo *et al.*, 2015; Shimpei I Kubota *et al.*, 2017; Cai *et al.*, 2019a). The interactions of the tumour with the physical environment are an area of great research interest. The tumour architecture cannot be fully depicted by 2D histopathology.

1.9.2.1 Advances in tissue clearing

Tissue-clearing techniques have developed alongside advances in microscopy. There now exists over 60 different techniques for tissue clearing. The development and widespread use of fluorescence imaging has enabled scientists to observe structures of interest labelled with lectins, dyes and antibodies deep within the tissue.

Clearing techniques have fallen into three categories – solvent-based, aqueous-based, and hydrogel embedding. The table illustrates the most commonly used clearing methods below.
(Table 1.5)

Table 1.5 Comparison of 3D Tissue Clearing Techniques

Technique	Mechanism of action	Tissues cleared	Preserves endogenous fluorescence?	Molecular Phenotyping	Tissue Integrity	Complexity of method	Time investment	Comments	References
3DISCO (EtOH/BABB)	Dehydration with EtOH followed by RI homogenisation with BABB	Rodent CNS and embryos. D. Melanogaster	No	IHC confirmed. Must be performed before clearing	Tissue shrinkage.	Incubation in multiple solutions over variable periods of time	Several days for whole mouse brain or embryos. 1 day for small tissues.	Rapidly quenches endogenous fluorescence. Not effective in heavily myelinated tissue. Only minimal validation of IHC	Dodt et al 2007 Erturk et al 2011 Erturk and Bradke, 2013 Kuwajima et al. 2013
3DISCO (THF/DBE)	Dehydration with THF followed by RI homogenisation with DBE	Rodent CNS, embryos, kidney, heart, muscle, vasculature	Yes – but loses signal in 24-48 hours	IHC confirmed. Must be performed before clearing	Tissue shrinkage.	Incubation in multiple solutions over variable periods of time	Overnight for whole mouse brain or embryos. A few hours for small tissues	Less background fluorescence and faster/better clearing than EtOH/BABB. Extensive validation of IHC [4,5]	Becker et al 2012, Erturk et al 2011 Belle et al 2014, Renier et al. 2014 Erturk and Bradke 2013 Erturk et al 2012
ScaleA2/U2	RI homogenisation via aqueous urea and glycerol mixture. Results in lipid removal.	Mouse brain and embryos	Yes but does quench some signal	IHC confirmed in 30 um sections	Tissue shrinkage.	Incubation in multiple solutions over variable periods of time	Weeks to months	Not effective in heavily myelinated tissue	Renier et al 2014 Hama et al 2011 Ke, Fujimoto and Imai, 2013 Kuwajima et al 2013 Tainaka et al 2014
ScaleS	RI homogenisation via aqueous urea, sorbitol and glycerol mixture	Mouse and human brain	Yes	IHC, lipophilic dyes and chemical stains confirmed	No significant change in size. Compatible with EM.	Incubation in multiple solutions over variable periods of time	Several days	Major improvements over ScaleA2/U2. Heavily myelinated regions still cause problems	Hama et al 2015
ClearT/T2	RI homogenisation using formamide (ClearT) or formamide/PEG mixture (ClearT2)	Rodent brain and embryos, intestine, muscle	Yes	IHC confirmed with ClearT2 to a depth of 120 um	No significant change in size for ClearT. Slight swelling in ClearT2. Clearing is reversible	Incubation in multiple solutions over variable periods of time	Overnight for whole mouse brain or embryos. Minutes/hours for small tissues sections	Only brain sections up to 1mm thickness tested. Very high 1 st Ab conc. used. Compatible with lipophilic dyes	Renier et al 2014 Kuwajima et al 2013
SeeDB	RI homogenisation with aqueous fructose solution	Rodent brain and embryos	Yes	IHC confirmed	No significant change in size. Clearing is reversible	Incubation in multiple solutions over variable periods of time	Several days	Compatible with lipophilic dyes. Optical transparency is limited compared to other techniques	Renier et al 2014 Ke, Fujimoto and Imai, 2013 Tainaka et al 2014
CUBIC	RI homogenisation via urea and amino alcohol based chemical cocktails. Results in lipid removal. Unbinds heme, increasing transparency in tissue.	Mouse brain, lung, kidney, liver, spleen, heart, pancreas, muscle, skin, intestine	Yes	IHC confirmed. Performed during clearing process	No significant change in size	Incubation in multiple solutions over variable periods of time	Approx. 2 weeks for whole mouse brain	Whole-body clearing is possible via transcardial perfusion with CUBIC reagents. Elution of the endogenous chromophore, heme, results in excellent transparency.	Renier et al 2014, Susake et al 2014 Tainaka et al 2014 Susaki et al 2015
CUBIC Cancer	RI homogenisation via urea and amino alcohol based chemical cocktails. Results in lipid removal. Unbinds heme, increasing transparency in tissue.		Yes	IHC confirmed. Performed during clearing process	No significant change in size	Incubation in multiple solutions over variable periods of time	8 days for whole mouse 5 days for mouse organs	Analysis can profile cancer metastasis at a single-cell level in a whole-animal context.	Kubota et al 2017
CLARITY (active)	Formation of tissue hydrogel hybrid followed by lipid removal via electrophoresis and SDS. RI matching in imaging medium	Mouse brain, spinal cord, spleen, pancreas, intestine, kidney, lung, testis, muscle	Yes	IHC and in situ hybridisation confirmed. Performed after clearing process	Some tissue swelling after clearing.	Polymerisation followed by complex electrophoresis step and mounting in imaging medium	Several days for small tissues. Approx. 2 weeks for whole mouse brain, or 3 days with stochastic Electro-transport	Requires complicated and expensive ETC set up. Variable results with standard ETC chamber. Marked improvements described with stochastic Electro-transport. Variability reported with IHC.	Renier et al 2014 Chung et al 2013 Tomer et al 2014 Epp et al 2015 Lee et al 2014 Kim et al 2015
CLARITY (passive)	Formation of tissue hydrogel hybrid followed by lipid removal with SDS. RI matching in imaging medium	Rodent brain, spinal cord, intestine, kidney, lung, liver, pancreas, human brain, zebrafish.	Yes	IHC and in situ hybridisation confirmed. Performed after clearing process	Some tissue swelling after clearing.	Polymerisation followed by clearing in a single solution and mounting in imaging medium.	Several days for small tissues. Several weeks for whole mouse brain.	No ETC chamber required. Simple 'low maintenance' procedure	Yang et al 2014 Tomer et al 2014 Zheng and Rinaman 2016 Palmer et al 2015 Trewick et al 2015 Liu et al 2016 Cronan et al 2015

1.9.2.2 Solvent-based clearing

Solvent-based clearing involved the solvation of lipids through dehydration, followed by a refractive index matching step. The solvent used in the dehydration step is commonly an alcohol-based substance such as methanol. This first acts to remove water and some of the lipids to leave a homogenous and dense sample. The next step is the matching step, whereby samples are immersed in agents such as methyl salicylate, benzyl alcohol or benzyl benzoate with high refractive indexes to make the sample clear. (Dodt *et al.*, 2007a; Becker *et al.*, 2012a; Ertürk *et al.*, 2012)

The removal of water in the initial dehydration step prevents most fluorophores from emitting a signal, so this method was, in its conception, unsuitable for fluorescently labelled samples. The original solvent-based DISCO (3D imaging of solvent-cleared organs) protocol has spawned many more refined protocols: 3Disco, iDISCO, UDISCO (ultimate 3D imaging of solvent-cleared organs), and F-DISCO (DISCO with the superior fluorescence-preserving capability) are all more recent methods which have been proposed to combat this. They work by replacing the methanol with another solvent, such as tetrahydrofuran or an aqueous solution, such as phosphate buffered saline, allowing the fluorescent signal to be reserved for a few days or months. (Ertürk *et al.*, 2011, 2012; Renier *et al.*, 2014; Qi *et al.*, 2019). Solvent-based techniques reportedly prove excellent tissue transparency and can clear large organ systems or even whole animals in a short time, with relatively little specialist equipment. However, when samples are immersed in the solvent for microscopy, the glues used in the objectives may be affected. This reduced the utility of these solutions with specific microscopy techniques. (Becker *et al.*, 2012a)

1.9.2.3 Aqueous based clearing

The aqueous-based clearing was born out of the need to preserve fluorescence and reduce the changes to tissue architecture caused by dehydration in solvent methods. Aqueous clearing can be done through passive or active immersion in a solution followed by a refractive index matching medium immersion step.

Most simple immersion techniques do not remove lipids and try to match the *average* refractive index of tissue by replacing the liquid in and around a tissue with a high refractive index solution. Passive or simple immersion steps are suitable for small samples, where the overall clearing time

is short. The sample is placed in an aqueous solution with a high refractive index, such as fructose or sucrose (Tsai *et al.*, 2009) (Costantini *et al.*, 2015), and it is left to become clear gradually. As highly refractive solutions are also highly viscous and can be challenging to handle, new solutions such as Focusclear (Moy *et al.*, 2015) and Histodenz (Yang *et al.*, 2014) have been specifically developed with a lower viscosity. This method is simple, with low instrumental costs; however, clearing can take a long time, is not as effective as solvent methods and is mainly restricted to small samples.

1.9.2.4 Hydrogel embedding

In 2013 Chung *et al.* presented a new method to clear mouse brains called CLARITY. (Chung *et al.*, 2013a) CLARITY uses electrophoretic tissue clearing to remove lipids. The tissue was first incubated in a solution of acrylamide and bisacrylamide monomers that formed polyacrylamide in the tissue after polymerization. This scaffold of acrylamide stabilised the tissue after removing the lipid bilayer within the cell membranes. In a specially designed chamber, samples are submerged in a clearing solution of boric acid, sodium dodecyl sulfate, sodium hydroxide and distilled water. An electric current allows more efficient circulation and penetration of the clearing solution and reduces the clearing time. A final step of immersion in either FocusClear, the Histodenz-based clearing solution RIMs, TDE, or 80% glycerol produces a sample that is well cleared. The time taken to clear an adult mouse brain is approximately eight days.

Compared with other clearing methods, CLARITY causes 8% protein loss from tissues during clearing compared to 41% loss in Scale clearing. (Scardigli *et al.*, 2021). However, CLARITY is not without its disadvantages: specific and expensive equipment is needed, and the clearing timeline is slow. (Kim, Chung and Deisseroth, 2013)

1.9.2.5 Hyperhydration

An alternative approach to simple immersion is to remove lipids and reduce the refractive index of tissue samples during the clearing process. *Scale* (Hama *et al.*, 2011) was the first method to try this, using detergent-based lipid removal alongside urea and glycerol-mediated hydration as a refractive index matching solution. The significant advantage of clearing in a hydrophilic environment is that the fluorescence is preserved (Yushchenko and Schultz, 2013). In addition, it was a simple method, which, unlike CLARITY, did not require expensive equipment. Also, the refractive index of urea-containing aqueous solutions is similar to the RI of water, so imaging with

water-immersion objectives was possible, unlike solvent-based clearing methods. However, this method is slow, sometimes taking months (Keller and Dodt, 2012). Attempts to use Scale to clear mouse brain and muscle tissue showed that it did not effectively clear areas with high myelin content. (Becker *et al.*, 2012b)

Clear, unobstructed brain/body imaging cocktails and computational analysis (CUBIC) is similar to hyperhydration clearing methods. The first reagent consists of N, N, N', N'-tetrakis(2-hydroxypropyl)ethylenediamine, urea and Triton X-100. Triton X-100 improves diffusion into the tissue (Tsai *et al.*, 2009). The second reagent consisted of sucrose, urea, 2,2',2' -nitrilotriethanol and Triton X-100. The high triton levels were used to improve diffusion into the tissue and remove lipids not removed in the first step. The high refractive index of sucrose aids the refractive index matching and clearing further. Another advantage is that immunolabelling could be performed between the two steps and was shown to be preserved at imaging. Fluorescence imaging was possible up to a depth of >750µm, mainly because the permeability of tissues increased after lipid removal. However, the high levels of triton needed to maximise the lipid removal were also seen to result in a high degree of protein loss (24-41%) which lowers epitope concentrations and potentially weakens immunostaining (Chung *et al.*, 2013b)

1.9.2.6 CUBIC CANCER

In 2017 Kubota *et al.* described a further advance on the original CUBIC protocol with the CUBIC-Cancer analysis. (Shimpei I Kubota *et al.*, 2017) CUBIC-Cancer uses refractive index (RI)-optimized protocol to comprehensively profile cancer cells in murine models' organs and whole bodies. The protocol and analysis showed cancer progression at single-cell resolution and assessed the response to anti-cancer drugs. The two immersion solutions were simple and effective: CUBIC-L for decolourization and delipidation was prepared as a mixture of polyethylene glycol mono-p-isooctylphenyl ether/TritonX-100 and N-buthyldiethanolamine). CUBIC-R for RI matching was prepared as a mixture of 2,3-dimethyl-1-phenyl-5-pyrazolone/antipyrine and nicotinamide.

Most importantly, the protocol was compatible with immunostaining. Kubota *et al.* counterstained nuclear structures with RedDot2 or propodium iodide and smooth muscle with anti- α -smooth muscle actin (α -SMA) antibody. By using fluorescently labelled cancer cells alongside, they could track the tumours within the whole mouse. Using the light sheet microscope to image the models

and organs, they demonstrated the spatial distribution of smooth muscle cells, vascular endothelial growth factor receptors and cancer cells. The RI values of tissue and cell structures can range from 1.34 to 1.59, and the refractive index medium of CUBIC Cancer is 1.52.

1.9.2.7 Tissue clearing in cancer research

FLASH clearing of pancreatic cancer has shown the tumour cell and microenvironment factors that can predict tumour cell dissemination. (Messal *et al.*, 2019). The quantification of metastasis after dissemination is also vital for understanding disease patterns. So, the metastasis burden will often dictate the patients' overall prognosis. Kubota *et al.* used the CUBIC Cancer protocol to examine metastatic disease in 13 mouse models with various primary cancers. This powerful single-cell resolution spatiotemporal imaging is the beginning of understanding how cancer spreads and potential targets to prevent the spread. (Shimpei I Kubota *et al.*, 2017). The innovation in analytical tools alongside imaging has also proven to be vital. vDISCO (nanobody(VHH)- boosted 3D imaging of solvent- cleared organs) cleared tissue was analysed using machine learning-based DeepMACT (deep learning-enabled metastasis analysis in cleared tissue) to map the metastatic patterns and quantify the responses to therapy. (Cai *et al.*, 2019b; Pan *et al.*, 2019) Another study was able to predict the uptake of nanoparticles, and the success of targeted drug delivery, in breast cancer by calculating the proximity of the metastasis to the vasculature (Kingston *et al.*, 2019a). Understanding the tumour vasculature can aid in targeting neo-vasculogenesis to starve the tumour of nutrients and oxygen. 3D mapping of tumour vasculature has demonstrated cancer vessel formation's tortuous and sometimes haphazard nature. (Lagerweij *et al.*, 2017) Taking it one step further, research in ovarian cancer showed that tumour vessel radius directly impacted the level of platinum chemotherapy sensitivity. Understanding this could help tailor patients' treatment to their cancer type. (Tanaka *et al.*, 2017). 2D histopathology remains the gold standard of tumour analysis. Although 3D imaging is powerful in quantifying and characterising cancers, 2D histology can still demonstrate a more granular depiction of the cytological characteristics. This, in part, is due to the longevity and widespread use of this technique, and so more tools for immunolabelling and analysis have been developed. Several papers have sought to combine clearing and 3D imaging with paraffin or frozen sectioning—these aids in validating the 3D imaging protocol. Lymph nodes resected from patients with colorectal cancer have been cleared using CUBIC and imaged to detect micro metastasis. (Nojima *et al.*, 2017). Following the 3D imaging, the samples were then embedded into paraffin for traditional histopathological analysis. iDISCO clearing protocol has also been

used to phenotype fixed and paraffin-embedded tumours in 3D. Tanaka et al. showed that clearing sections and reconstructing the 3D image could better demonstrate patterns in the spatial distribution of cells in the whole tumour. (Tanaka *et al.*, 2017)

1.9.2.8 Clearing and microscopy

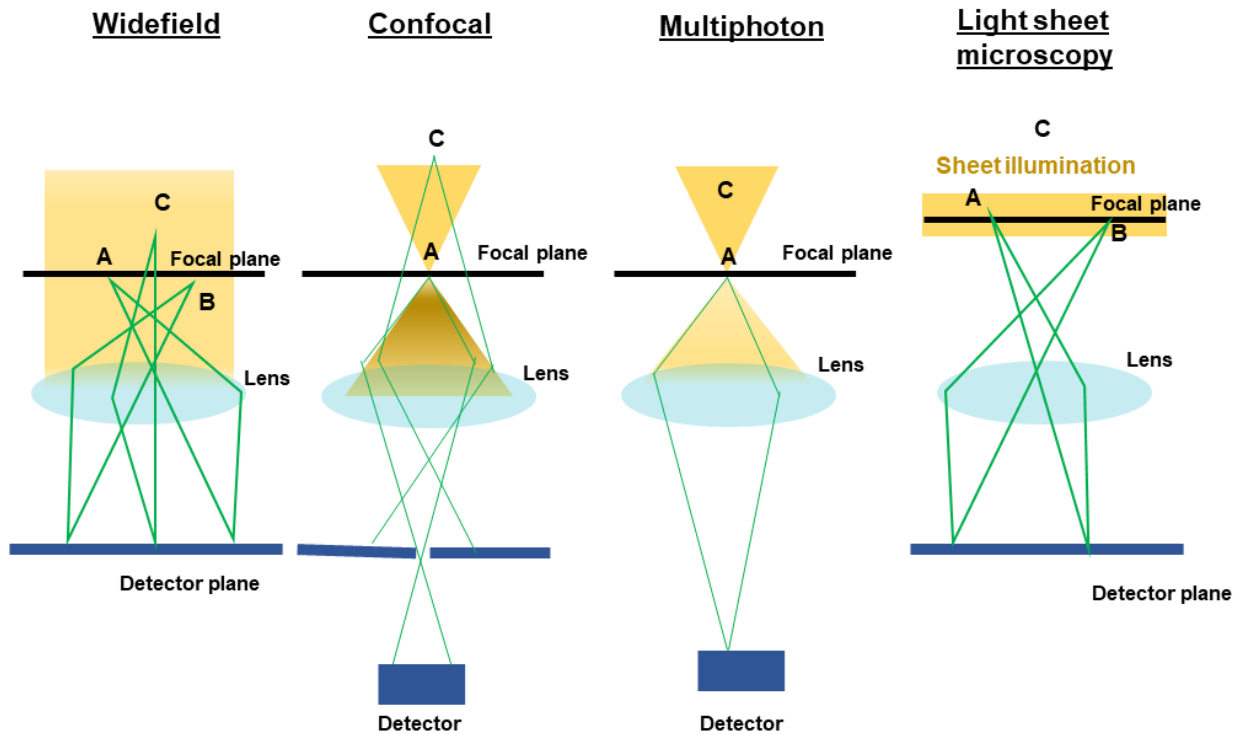
The quest to produce ever more transparent and clear biological tissues must be accompanied by progress in microscopy modalities and equipment to image them. Innovation in light microscopy is happening at a startling rate. Several optical sectioning methods for imaging cleared tissue are commercially available, including confocal, 2-Photon, and lightsheet fluorescence microscopy. (**Figure 1.12**)

Confocal microscopy produces fluorescence images by omitting out-of-focus light with a pinhole or series of pinholes to generate high-resolution imaging of cellular and subcellular structures. (Jonkman and Brown, 2015)(Jonkman *et al.*, 2020) 2Photon or multiphoton microscopy develops on this principle: two or more long-wavelength photons are combined to excite the fluorophore. The powerful and focused beam ensures that only photons within the focal plane are excited, reducing the out-of-focus signal. The long wavelengths used are also better suited to deeper penetrating tissues, making this modality ideal for deep tissue imaging. (Helmchen and Denk, 2005). A commonly cited disadvantage of this method however is that the focussed scanning of small areas one by one makes image acquisition extremely slow. Therefore, they are only suited for high-resolution imaging of localized regions within cleared tissues (Richardson and Lichtman, 2015).

Light sheet fluorescence microscopy (LSFM) illuminates a selected x-y plane of interest from the side of samples with a thin light sheet, while out-of-focal plane regions are not excited. This not only reduces photobleaching and background signal. (Susaki and Ueda, 2016) (Hillman *et al.*, 2019) but is also significantly quicker at imaging large samples than confocal methods. In many studies developing clearing protocols, light sheet microscopy is the preferred modality for imaging for studying developmental biology, neuroscience and cancer biology. (Dodt *et al.*, 2007b; Weber and Huisken, 2011)(Herbert *et al.*, 2009; Power and Huisken, 2017; Sabyusheva Litschauer *et al.*, 2020). The disadvantage of a light sheet microscope is its resolution limitations due to the low numerical aperture often used. Like any specialised equipment, the utility of these microscopes

is dictated by cost and availability – which is to say their use is still limited to specialist imaging centres.

Figure 1.12 Schematic illustrations of fluorescence imaging techniques



(A) wide-field, (B) point scanning confocal, (C) multi-photon, and (D) light sheet microscopy. In all diagrams, points A and B lie in the focal plane of the lens while point C lies outside the focal plane. Optical sectioning in light sheet microscopy works by creating a plane of excitation light that is coincident with the focal plane of an imaging objective. Since the sectioning occurs during excitation, the emitted light from the whole field of view can be gathered as a two-dimensional image with a standard camera. Image adapted from Taormina et al 2012

1.10 Project Aims & Objectives

Robust drug screening and development methods from *in vitro* to *in vivo* models are necessary to identify novel neuroblastoma therapies. Overexpression of Cyclin D and HIF-2 α is correlated with poor clinical outcomes in neuroblastoma. (Gordan *et al.*, 2007a) Cell cycle inhibitors and therapies targeting the hypoxia-inducible pathways are promising avenues for exploration and driving new treatments. This thesis seeks to outline the workflow of drug screening from the laboratory bench into dynamic 'living biology' *in vivo* models whilst also analysing the efficacy of these novel drug compounds using advanced 3D microscopy techniques.

The following objectives will be addressed to achieve this:

1) Test the efficacy of CDK inhibitors *in vitro* and *in vivo* in neuroblastoma cell lines.

CDK4/6 inhibitor Palbociclib and CDK 1 inhibitor RO3306 have been selected. *In vitro* testing includes cell survival and cell cycle assays. *In vivo* experimentation will be using the chick embryo model as a novel drug screening tool. The effect of the compounds on chick growth, survival and tumour formation will be assessed.

2) Assess the potential of HIF-2 α inhibitors targeting neuroblastoma growth and metastasis *in vitro* and *in vivo*, alone or in combination with CDK inhibitors. HIF-2 α inhibitor PT2385 will be tested on MYC-N amplified and 11q deleted neuroblastoma cell lines. The expression of HIF regulated genes with and without HIF-2 α inhibition will be quantified using qPCR. The effect of the compounds on chick growth, survival and tumour formation and tumour metastasis will be assessed.

3) Explore the usefulness of clearing technology and 3D advanced microscopy to quantify the effects of drug therapy(s).

Chapter 2 : Materials & Methods

2.1 Tissue culture

2.1.1 Cell lines

Neuroblastoma cell lines used in this PhD project work are detailed in **Table 2.1** below. Cells were labelled with enhanced green fluorescent protein (EGFP)

Table 2.1 Cell lines used in this work and the media for cell culture

Cell line	Source	Media
SK-N-AS	ECACC 94092302	MEM + 10% FCS + 1% NEAA
SK-N-BE(2)C	CRL-2268	DMEM + 10% FCS +1% NEAA

The details regarding the patient data from which the neuroblastoma cell lines were derived are summarised in **Table 2.2**

Table 2.2 Information on the origins and characteristics of the cell lines used in this project

Cell line	Patient history	Primary site	Metastatic site	Origin	Genetic characteristics	Cell type	Stage
SK-N-AS	Metastatic site: bone marrow biopsy of a six-year-old child.	Adrenal gland	BM	BM	Single copy MYCN Chromosome 1p deletion Chromosome 11q deletion	S	4
SK-N-BE(2)C	A sub-clone of SK-N-BE(2), a neuroblastoma cell line established from a bone marrow	Unknown	BM	BM	MYCN amplified Chromosome 1p deletion	I	4

	biopsy taken from a two-year-old child with disseminated neuroblastoma after repeated chemotherapy and radiotherapy.				Chromosome 17 translocation.		
--	--	--	--	--	------------------------------	--	--

2.1.2 Cell culture

Cells were cultured as monolayers in a humidified incubator with 25cm² or 75cm² cell-culture flasks (Corning, UK) at 37°C in 5% CO₂.

Cells were passaged upon reaching 70-80 % confluence; this was typically 2/3 days after thawing. At this stage, media was removed, and cells were washed with room temperature calcium and magnesium-free Phosphate Buffered Saline (PBS). Flasks were then incubated at 37°C with 1 ml 1xTrypsin/EDTA for 2 minutes or until all the cells had detached. After detachment, 9 ml of fresh media was added to halt the trypsin reaction. Cell density was calculated using Bio-Rad TC20 automated cell counter. Cells were reseeded into 175cm² at a density of 3 million cells in 25 ml of media. Both neuroblastoma cell lines were cultured and passaged in the same way. For hypoxic experiments, cells were pre-incubated for three days in a Don Whitley Scientific (UK) H35 Hypoxystation in a humidified 1% O₂/5% CO₂/ 94% N₂ environment and maintained at 37°C. The chamber was calibrated every two weeks.

2.1.3 Long-term cryogenic cell storage

Cells were frozen as cell stock at the lowest possible passage number. Upon reaching 90% confluence in 25cm³ flasks, cells were washed with PBS and trypsinised as described above. Cells were resuspended in 10 ml of the appropriate media (**Table 2.1**) and transferred to a sterile 30 ml universal (Starlab, UK). Cells were counted using Bio-Rad TC20 automated cell counter, and the total number of cells in the 10 ml suspension was calculated. The cell suspension was centrifuged at 1000x rpm for 5 minutes. The supernatant was removed, and the cell pellet was resuspended in a freezing solution of 10% dimethylsulfoxide (DMSO) and 90% FCS (Fetal Bovine serum) to obtain 1 million cells per millilitre. DMSO was used to draw water away from the cells and reduce the formation of water crystals within cells. One millilitre of resuspended cells was

aliquoted per every 1.5 ml externally threaded cryovial (Starlab, UK). The cryovials were placed in a cryo-freezing container (Nalgene, UK) containing 100% isopropanol for 24 hours at -80° C. This allowed a controlled cooling of cell suspensions at approximately -1°C/minute. Frozen cryovials were placed for long-term storage in a cell storage tank cooled by vapour phase liquid nitrogen at -135° C.

2.1.4 Thawing of stored cell lines

Frozen cells from liquid nitrogen stores were thawed as follows. Once removed from the liquid nitrogen store, the contents of the cryovial were carefully resuspended with a warm culture medium. Once thawed, the culture medium and cells were transferred into 10 ml of the medium in a 25cm² culture flask and moved into an incubator.

2.2 Therapeutic compounds

The stock concentration and storage of the therapeutic compounds used are outlined in **Table 2.3** listed below. All compounds were stored at -80°C in powder form until required. Liquid stocks were aliquoted and stored at -20°C for no longer than four months, per manufacturers' guidelines.

Except for RO3306, the other two compounds were soluble in PBS and media at the required concentrations at room temperature as per manufacturer instructions. On gross examination there was no evidence of solid components within the solutions. RO3306 was reconstituted using DMSO and PBS/Media, with the highest DMSO concentration at 0.1%, to prevent cell damage. All vehicle controls for RO3306 also contained the same concentration of DMSO.

Table 2.3 Therapeutic compounds used

Drug	Manufacturer Details	Solvent	Stock	Storage	Solvent to make therapeutic concentration
Palbociclib	Sellekchem, USA	DMSO	108 mM	-20°C	PBS
RO3306	Sigma-Alrich	DMSO	100 mM	-20°C	PBS/DMSO
Bay-11-7082	Selleckchem, USA	DMSO	100 mM	-20°C	PBS
PT2385	Arcus, USA	DMSO	10 mM	-20°C	PBS/DMSO

2.3 Functional Assays

2.3.1 MTT (3-(4,5-dimethylthiazol-2-yl)-2,5-diphenyltetrazolium bromide) assay

This assay relies on the reduction by intracellular NAD(P)H-dependent dehydrogenases of viable cells, of the soluble and pale-yellow tetrazolium salt, MTT, into insoluble and purple formazan crystals, thus reflecting the number of metabolically active cells present in a sample (Berridge et al., 2005).

Cell density over 72 hours in a 96-well plate was optimised before the assay. Both neuroblastoma cell lines had an optimal density of 10,000 cells per well at the end of 72 hours of incubation. SK-N-AS and SK-N-SK-N-BE(2)C cells were washed and trypsinised for passaging. The trypsinised cells were resuspended in the new medium, and 10µl was used to calculate cell density using an automated cell counter. The cells were reconstituted with a fresh medium to give an overall volume of 10×10^3 cells per 100µl. Cells were pipetted into a 96-well plate to give an overall concentration of 10000 cells per well. The wells bordering the edge of the plate were filled with 100µl media to reduce evaporation in cell-containing wells at the periphery. Cells were incubated

at 37°C in 5% CO₂ for 24 hours. After 24 hours of incubation, the drugs were added to the wells in ½ log serial dilution alongside a DMSO control. Each drug concentration was tested in triplicate. The cells were incubated with the treatment for 48 hours. MTT reagent (Sigma M2128) was dissolved in PBS (5 mg/mL) and filtered. After 48 hours of drug treatment, 10µl of the MTT solution was added to each well, including medium only, which was used as the negative control. After further incubation at 37°C for 4 hours, the reaction was terminated by adding 100µl 10%SDS/0.01M HCl in sterile water(solubilising reagent). The plates were then incubated at 37°C overnight to solubilise the crystals fully. The plates were read at 570nm on a spectrometer plate reader. The raw values were then processed by subtracting the average background signal (average of media only containing wells). This value was then calculated as a percentage normalised to the DMSO control average.

The 50% inhibitory concentration (IC₅₀) was defined as the concentration that caused a 50% decrease in the absorbance of treated cells compared to medium-grown cells. The data was plotted, and IC₅₀ was calculated using GraphPad Prism.

2.3.2 Trypan Blue Exclusion Assay

Cells were seeded into 6cm cell culture treated dishes, with 1.5x10⁵ cells plated in hypoxia for the assay and 1x10⁵ plated in normoxia. Cells were then incubated for 96 hours before collection. Cells were washed in PBS, trypsinised and counted using trypan blue 1:1 with cell suspension on a Bio-Rad TC20 cell counter. Live cell count and percentage viability were plotted for cell lines and incubation conditions.

2.3.3 Cell Cycle Analysis

2.3.3.1 Cell preparation

The optimal seeding density to allow around 60% confluency after 96 hours in a 6cm dish was evaluated before assay. 1.5x10⁵ cells were plated in hypoxia for the assay, and 1x10⁵ were plated in normoxia. Cells in both conditions were incubated for three days to allow cells to form a monolayer. After three days of incubation, the drug compounds were added to the dishes to make a total volume of 4ml per dish. Drug concentrations were calculated as half of the IC₅₀ from MTT experiments to observe drug effects with minimal toxicity. (**Table 2.4**

Table 2.4 Drug compounds and concentrations used in different experimental groups

Drug	SK-N-AS (NORMOXIA)	SK-N-AS (HYPOXIA)	SK-N-BE(2)C (NORMOXIA)	SK-N-BE(2)C (HYPOXIA)
Dose (μM)				
Palbociclib	15	20	5	10
RO3306	2.5	2.5	3	2.5
Bay-11-7082	5	5	2.5	0.5

Each compound, therefore, was evaluated in SK-N-BE(2)C and SK-N-AS in normoxia and hypoxia for each replicate.

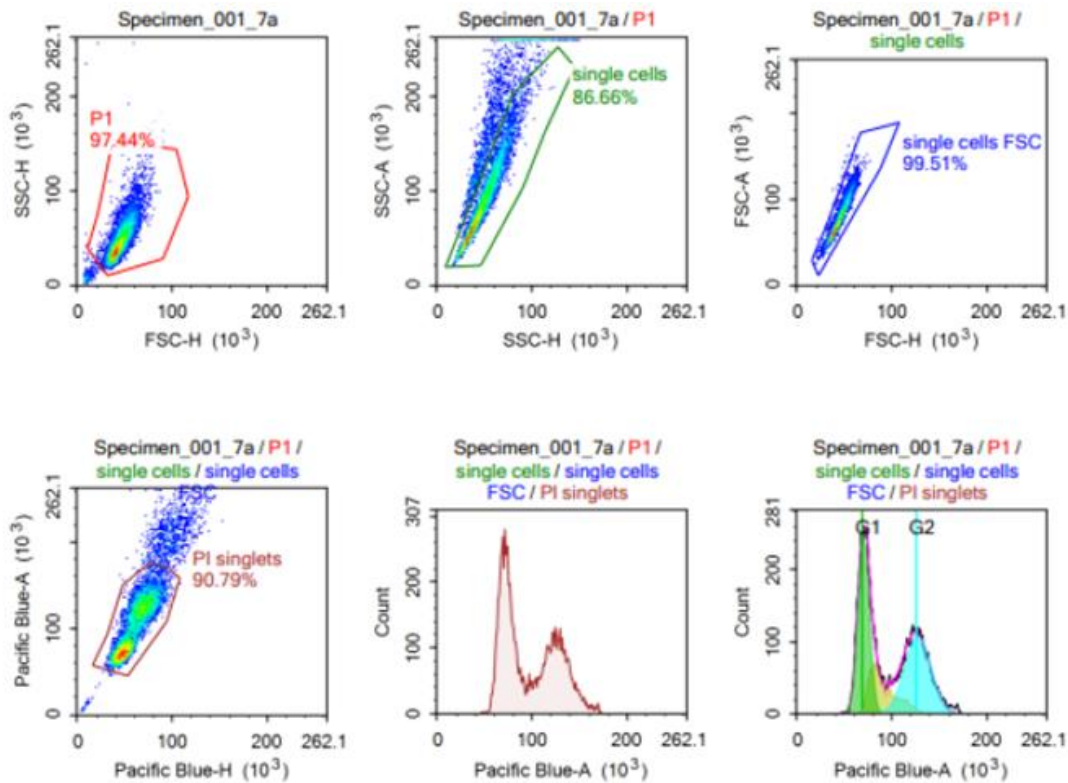
2.3.3.2 Flow Cytometry

After 24 hours of drug treatment, the dishes were washed with PBS and trypsinised as for cell passage. The cell suspension in media was centrifuged at 300xg for 3 minutes. The media was discarded, and the pellet was resuspended and washed with 500 μ l PBS. The resuspended cells were added dropwise to 4.5ml of ice-cold 70% ethanol whilst gently vortexing to fix them. Samples were cooled at 4°C for 30 minutes. The cells in ethanol were then centrifuged for 10 minutes at 300xg. The ethanol was discarded, and the cells were washed in ice-cold PBS twice. After the second wash, the cells were rehydrated in PBS for 2 minutes before centrifuging suspension again at 300x g for 3 minutes. The PBS was discarded, and 1 ml of 0.5% Tween 20 in PBS was added for 5 minutes to permeabilise the cells. The cells were centrifuged at 300x g for 3 minutes and washed twice with ice-cold PBS. After the second wash, the PBS was discarded, 1ml of Hoechst 33342 was added to each sample, and 1ml of PBS alone to the 'blank control' in each cell line. Cell cycle analysis was performed using a BD Bioscience FACSCanto II flow cytometry system using 488nm laser.

2.3.3.3 Data Analysis

NovoExpress 1.4.1 software was used to analyse flow cytometry data. The total population of cells were gated to isolate only live singlet cells. The NovoExpress analysis software then quantified the number of cells within each cell cycle phase: G0/G1, S and G2/M.

Figure 2.1 Example of FACS data analysis workflow



2.4 Chick embryo experiments

The steps involved in egg preparation, windowing, drug treatment and dissection are outlined in **Figure 2.2**

All chick embryo experiments were performed following Home Office guidance.

Figure 2.2 Visual display of the steps in chick embryo experiment.

E=0



Eggs are cleaned, numbered and placed in an incubator

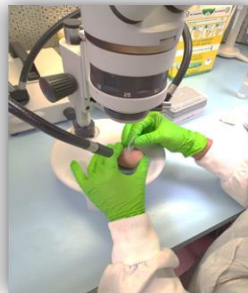
E=3 Window eggs



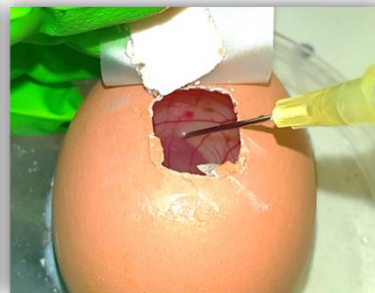
Eggs are rotated to free the CAM from the surface of the shell. Eggs are punctured and 5mls of albumin is removed and discarded using a syringe. A window is made through the egg shell to show the CAM below. Windows are taped carefully to ensure no leakage and placed back in the incubator



E=7 Implantation E=9-13 Treatment



Cells are implanted onto the CAM



After confirming presence of a tumour/viable cells drug compounds are injected into the allantoic sac

E=14 Dissection



Eggs are dissected at E14 using brightfield and fluorescent microscopy

2.4.1 Egg preparation for *in-ovo* experiments

White leghorn chicken eggs were sourced from Henry Stewart & Co (Norfolk) for the chick embryo experiments. Numbers per experiment ranged from 20 – 30 eggs. Upon arrival, the eggs were stored in a 4°C fridge until ready for use – most experiments were scheduled within two days of egg delivery. The eggs were gently cleaned using Brinsea solution and incubated horizontally at 37°C and 35% humidity on day 0. The chick embryo development is graded by Hamilton Hamburger staging. (Hamburger and Hamilton, 1951) By day 3 of incubation, the chicks are at Hamburger-Hamilton stage 12-18, and the extraembryonic membrane has not yet fused to the inner surface of the eggshell. 3-4ml of albumin was removed from the egg using a 19G needle, and a 5ml syringe was inserted at a 45° angle via a small hole made into the base of the egg. This reduction in *in ovo* volume drops the membrane away from the shell on the superior aspect of the egg. A 1.5cm² window was made in the eggshell: a strip of Sellotape was placed on the superior aspect of the egg to reduce eggshell cracking. A small hole was made using scissors or a circular saw, and an approximately 1.5cm circle or square was cut out of the eggshell. One side of the eggshell was kept intact – acting as a flap to allow access to the egg whilst acting as a barrier to moisture loss and infection. Another piece of Sellotape was placed on top of this window. The eggs were then re-incubated in a 37°C and 40% relative humidity incubator until cell placement at E7.

2.4.2 Cell Preparation and Implantation

There are many methods for introducing cells into the embryonic system, broadly divided into injection – (i) intravenously or (ii) intracorporeally or (iii) via placement on the CAM. The latter method has been used in this work. (Kue *et al.*, 2014) Cells were placed on the CAM of viable chick embryos after seven days of incubation. SK-N-BE(2)C and SK-N-AS cells were grown in 175cm³ flasks before implantation. In experiments where hypoxia cells preincubation was performed, the cells were preincubated for 3 days in 1% O₂ before implantation. Cells were washed in sterile PBS and incubated at 37°C with 2ml of trypsin for 3 minutes or until all the cells were detached. The cells were resuspended in 9ml of media per flask, and all the cell suspensions were transferred and combined into a single 50ml falcon. A cell count was performed, and the total number of cells was calculated. The cell suspension was then centrifuged at 1000 rpm for 5 minutes. The supernatant was discarded, and the cell pellet was resuspended in media to give 2x10⁶ cells per 400µl. The resuspended cells were then transferred into 1.5ml Eppendorf and

centrifuged for 5 minutes at 1000 x rpm. The supernatant was discarded, and the pellets were placed on ice until implantation.

Chick embryos were removed individually from the incubator to reduce heat and humidity loss. The taped windows were opened to expose the CAM, vasculature and the underlying chick embryo. After ensuring the chick was alive, sterilised lens tissue was used to abrade the surface of the CAM to increase permeability for the cells. The pelleted cells were resuspended in 5µL of media and pipetted onto the CAM. The window was re-sealed, and the chick returned to the incubator.

2.4.3 Drug injection into the chick allantoic sac

Our lab group has previously optimised the introduction of drug compounds into the chick embryo. (Swadi, Mather, *et al.*, 2018) The concentration of drug distributed to the tumour cells is similar for injections into the vasculature and injections into the allantoic sac. Injections into the allantoic sac were used in the drug screening experiments. The eggs were numbered sequentially to reduce bias based on position in the tray or order of injection. A random number generator was used to identify which eggs received control and treatment doses. The treatment was then recorded, and the chick's weight was recorded on the day of treatment. It was not possible to be blind to which treatment was given as Palbociclib and RO3306 have a distinct colour in the solution. On day 11 and day 13, the eggs were taken from the incubator, and the adhesive tape covering the window in the shell was removed. Drugs were injected into the allantoic sac under microscopy guidance using a sterile 21G needle and syringe. A new adhesive tape was again placed over the window, and the eggs were returned to the incubator. The dosing was calculated on the presumption that the average weight per chick is 50g. Ten per cent of this 50g was deducted as eggshell weight, leaving a weight of 45g. A density of one is assumed, giving the total volume per egg of 45ml. Drug concentrations were calculated by serial dosing of the chick model. The concentrations with the highest percentage survival after 2 doses were used. (n=50 per drug) Drug concentrations were used as outlined below:

1. Palbociclib was given in 2 doses of 20µM. 8 µl of 10 mM stock was made up to 200µL with sterile PBS per egg.
2. RO3306 was given in 2 doses of 10µM. 4µL of 10 mM stock was made up to 200µL with sterile PBS per egg.

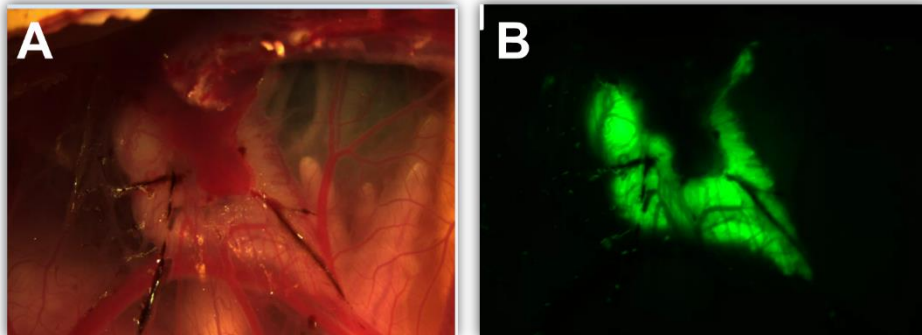
3. Bay-11-7082 was given in 2 doses of 10µM. 4µL of 10 mM stock was made up to 200µL with sterile PBS per egg.

Control groups were injected with 200µl of sterile PBS or 4µL DMSO in 196µL sterile PBS as control of RO3306.

2.4.4 Dissection of tumours

Home office guidance permits chick culture until E14 without an animal license. At E14 eggs, the viability of each chick was assessed and recorded using a Leica M165 FC stereo microscope. The eggshell was partly removed using flat forceps to examine the chick and CAM thoroughly. Using fluorescent light, the CAM was examined for the presence of tumour formation from GFP-labelled neuroblastoma cells. Tumour formation was detected at the site of cell placement or elsewhere on the CAM and was characteristically located beneath the surface of the CAM. **Figure 2.3).**

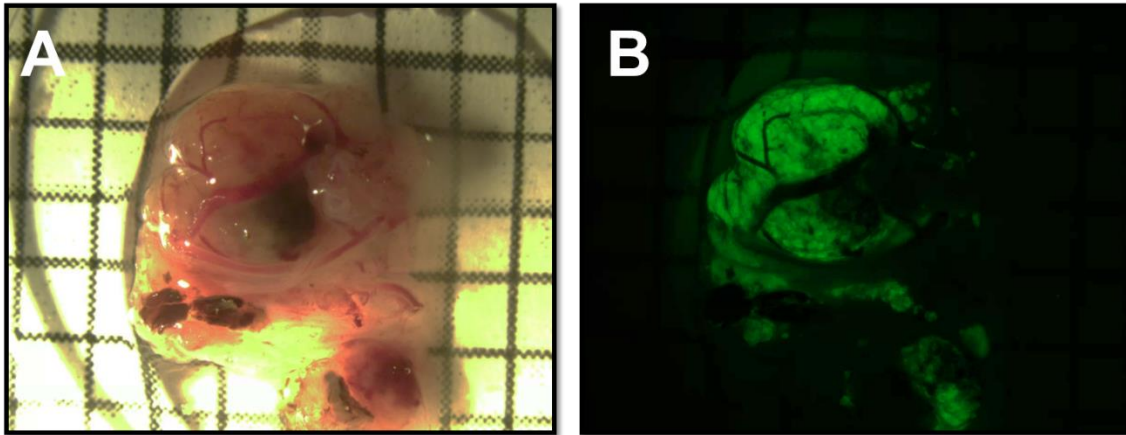
Figure 2.3 Tumour growing under the CAM shown in ovo as A) Brightfield Image B) Fluorescent image.



Fluorescently labelled SK-N-BE(2)C cells implanted on the CAM. Images taken in ovo on E14, immediately prior to dissection. Images demonstrate the growth of the tumour below the CAM and the ingrowth of chick vessels in and around the tumour. Images taken with Leica M165 FC stereo microscope

Tumours were dissected using clean forceps and scissors with a fluorescent dissection microscope. The number of tumours per egg was recorded, and dissected tumours were imaged individually. (Figure 2.4)

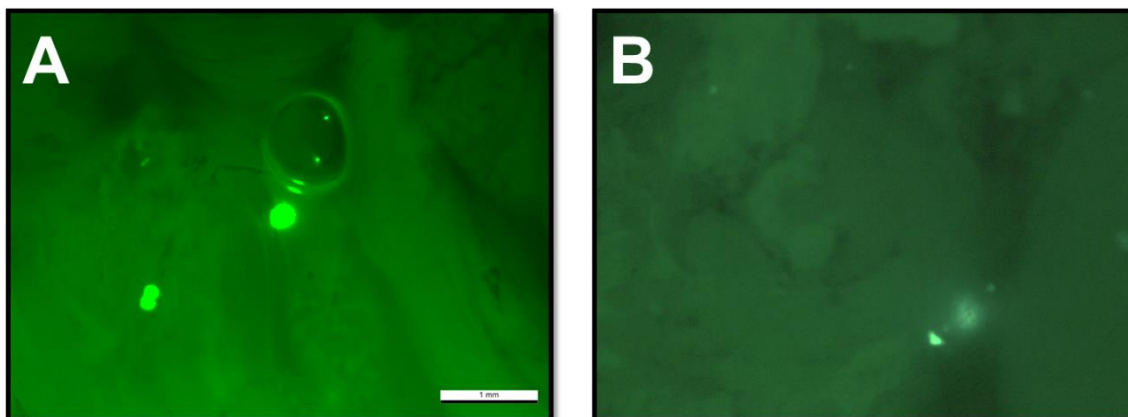
Figure 2.4 Dissected Chick Neuroblastoma A) Brightfield Image B) Fluorescent image.



Fluorescently labelled SK-N-BE(2)C cells implanted on the CAM. Images taken after dissection, before fixation in PFA. Images taken with Zeiss Axiovert S100 TV

The tumours were then weighed and placed into a 4% paraformaldehyde solution for fixation for up to 2-4 hours. The embryo was then culled through spinal cord separation. The embryos were dissected to assess for metastatic dissemination. This was achieved by dissecting the heart, lungs, intestines, kidneys, liver, brain and eye. Each organ was examined for fluorescent cells, and the remaining cavity was checked thoroughly. (Figure 2.5)

Figure 2.5 *Fluorescent metastatic neuroblastoma tumours shown in ovo in NB A) intestines B) Feathers.*



Fluorescently labelled SK-N-AS seen within the chick tissue. Images taken in ovo on E14, immediately prior to dissection. Images taken with Zeiss Axiovert S100 TV

Tumours were imaged before and after dissection using the Leica DFC425C camera using the LAS V4.0 software system. Tumours were then weighed and stored in RNAlater (QIAGEN) or fixed in PFA or formalin, depending on further utilisation.

2.5 Fixing, Sectioning and staining tissue

2.5.1 Cryofixing tissue

The materials used for cryofixation are listed in **Table 2.5**.

Firstly, tissues were fixed by submerging them in 4% PFA. Incubation time is roughly 2 hours per mm depth of tissue sample. After fixation, sample dehydration was performed. This is done using serial sucrose dilutions. The samples were submerged sequentially in 6%, 12% and 20% sucrose for 24 hours or until the sample sank to the bottom of the vessel. The samples were then placed in tear-away plastic cassettes using sterile tweezers. The samples were covered with cryomatrix resin – this is done slowly to avoid any sample movement or bubble formation. A labelled cork disc was then placed on top. The samples were then placed into the dry ice until solid. The samples were sectioned or stored long-term at - 80°C.

2.5.1.1 Sectioning Frozen Tissue

The frozen samples were sectioned using a Leica CM1950 cryostat set to -20°C. The microtome was set at 5µm. Once sectioned, mount onto Thermo Scientific SuperFrost slides. The slides containing cryostat sections were stored at -20 or -70 °C for up to 12 months.

2.5.1.2 Staining

Slides were thawed at room temperature, and the tissue area was marked using a hydrophobic pen. Once the pen was dry, the samples were washed twice in PBS before incubation for 5 hours using 5%(w/v) BSA (Bovine Serum albumin) in PBS as a blocking agent. The samples were submerged in 5% BSA and 0.2%(v/v) Triton-X100 overnight at room temperature for permeabilisation. The blocking buffer used was (5% (w/v) Bovine Serum Albumin in DPBS (Gibco); 0.1% (v/v) Triton X-100 (Sigma Aldrich); and 0.4% (v/v) Tween 20 (Sigma Aldrich). Then primary antibody dilutions in blocking buffer were prepared, and 100µL was added to each sample. The samples were incubated at 4°C for 12 hours in a humid chamber (empty pipette box with water). The primary antibody was removed, and the sample was washed three times in blocking buffer for 10-15 minutes each. The secondary antibody was added, diluted with blocking buffer, for 2 hours at 4°C. The samples are washed 3 times with a blocking buffer to remove unbound secondary antibodies. (**Table 2.14**) The nuclear stain Hoechst 33342 in DPBS solution was applied for 10 minutes. The slides were then washed twice in DPBS and rinsed in deionised water. Once dry, Anti-fade Medium (Dako) was added to the sample and sealed with coverslips (VWR International). The slides were left to dry overnight in a cool dark place and stored at 4°C in a slide holder, or for long-term storage, they were kept at -20°C.

Table 2.5 Materials used in cryofixation and sectioning of tissue

Material	Manufacturer
4% Paraformaldehyde Solution (PFA)	N/A
100% sucrose – dilutions down to 20%, 12% and 6%	N/A
Cryomatrix embedding solution	Thermofisher
Peel-a-Way disposable embedding moulds	Sigma-Aldrich
Superfrost slides	Thermo Scientific
SUPERPAP hydrophobic pen	Invitrogen
Anti-fade medium	DAKO
Coverslips	VWR International
Bovine serum albumin	Gibco
Triton X100	Sigma Aldrich
Tween 20	Sigma Aldrich

2.5.2 Histopathology and Immunohistochemistry

Chicks were euthanised on embryonic day 14 by cold exposure and then decapitation. Tumours and chick organs harvested were fixed in 4% PFA for 2-4 hours. Samples for histology were harvested and inserted into histology cassettes and stored in PFA. Samples were processed, and slides were made by Histology labs at the department of veterinary anatomy and physiology and pathology, University of Liverpool, Leahurst campus. The Leahurst facility has processed the samples by embedding them in paraffin and sectioning per their protocols. The samples were also stained with haematoxylin and eosin, and Ki67. Manual counting of histological sections using bright field microscopy was used to quantify the Ki67 proliferation index. For each section, five high-power fields were selected at 40x magnification. For each condition, five different slides were analysed. All the cells within the section were counted, and all the Ki67 positive nuclei –

stained brown- were counted. The index is presented as a percentage of Ki67 positive of the total. Chick tissue was differentiated from human neuroblastoma cells as it had a small nucleus, whereas neuroblastoma tumour tissue cells have a relatively larger nucleus with less visible cytoplasm.

2.6 Tumour Imaging

Tumour imaging after dissection was performed on the **Zeiss Axiovert S100 TV** microscope. The timings of CUBIC and ethyl cinnamate clearing steps were optimised on **Leica M165 FC**.

2.6.1 Advanced microscopy for 3D tumour imaging

Three microscopes were used to acquire 3D and deep images of tumours.

1. Andor Dragonfly + Leica DMIB
2. Zeiss Axio Examiner Z1 (Ism 880 Multiphoton)

Andor Dragonfly

The Andor Dragonfly is an upright spinning disc light microscope—the objectives used are as outlined below.

Table 2.6 Objective information for Andor Dragonfly

Magnification	Numerical Aperture	Immersion type
10x	0.45	Water
25x	0.95	Oil
40x	1.3	Glycerin

Zeiss Axio Examiner z1 (880 Multiphoton)

The Zeiss 880MP is an inverted multiphoton—the objectives used as outlined below.

Table 2.7 Objective information for Zeiss Axio Examiner (lsm880 MP)

Name.Type	Magnification	Numerical Aperture	Immersion type
EC-Plan-Neofluar	10x	0.3	Air
W Plan-Apochromat	20x	1.0	Water
W Plan Aporchromat	40x	1.3	Water

The laser lines are outlined below:

Table 2.8 Excitation laser lines for fluorescently labelled proteins and antibodies

Laser line used	Used for
405nm	Hoechst nuclear staining
488nm	Green fluorescent protein
594nm	Alexa 594 – Ki67 staining
605nm	Far-red – SMA staining

2.6.2 Image acquisition

For the high-resolution imaging acquisitions, chick tumours were either

- A) embedded in 1.5% low-melting agarose in a 35mm glass bottom imaging dish (Greiner bio-one, one compartment dish #81218-200).
- B) Placed in a designed-for-purpose imaging dish and submerged in the clearing liquid (CUBIC/Ethyl cinnamate). As outlined fully later in Chapter 5, **Figure 5.16**

Images/videos were then acquired using Dragonfly spinning disk confocal microscope (Andor) or Zeiss Axio Examiner Z1 (lsm880 Multiphoton). Acquisitions were performed using the Fusion software in the Andor system and the Zen system for the Zeiss 880 microscope. All image/video analysis was made using both IMARIS and ImageJ software.

2.7 Clearing protocols

2.7.1 CUBIC Cancer Clearing

CUBIC- Cancer Protocol for CUBIC cancer clearing adapted from Kubota et al. (Shimpei I. Kubota *et al.*, 2017a)

Table 2.9 Reagent used in CUBIC-Cancer clearing

Reagent	Manufacturer
N butyldiethanolamide	B0725 Tokyo Chemical Industry
Triton X100	Sigma
Antipyrine	Sigma
Nicotinamide	Sigma

Table 2.10 Formulation of clearing solutions

Solution	Constituents	Mass/Volume
CUBIC L2	N butyldiethanolamide	5 g
	Triton X100	5 g
	dH ₂ O	40 ml
CUBIC L1	CUBIC L solution	25 g
	dH ₂ O	25 g
CUBIC R2	antipyrine	22.5 g
	nicotinamide	15 g
	dH ₂ O	12.5 ml
CUBIC R1	CUBIC R2 solution	25 ml

dH ₂ O	25 ml
-------------------	-------

2.7.1.1 Preparation of Reagents

CUBIC-L reagent (50 ml) (pH < 11)

5 g of TritonX-100 was added into a 50ml tube or a beaker, followed by 5g of N-butyldiethanolamine (pH 10–11) and 40g of ultra-pure water. The solution was stirred gently and was stored in a sealed container at 18°C–26°C.

CUBIC-R (N) reagent (amber-coloured) (50ml) (Refractive index (RI) = 1.52, Temperature = 25°C)

15 g of nicotinamide was added into a 50ml tube or a beaker, followed by 22.5g of 2,3-dimethyl-1-phenyl-5-pyrazolone/antipyrine and 12.5ml of ultra-pure water and mix. Use a microwave or heating stirrer up to around 70°C to dissolve them and shake gently. Chill to 18°C–26°C and store at 18°C–26°C in a sealed container and protect from the light.

2.7.1.2 Clearing Protocol

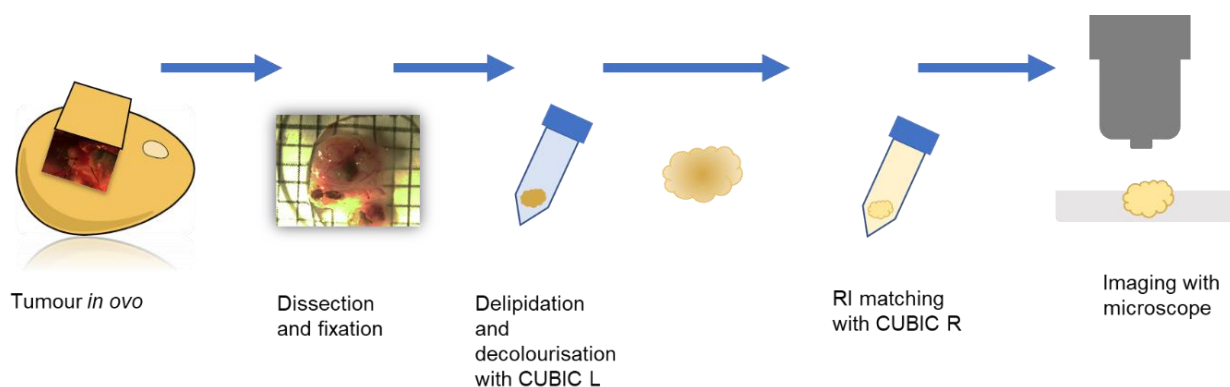
Tissue samples were fixed using 2ml of 4% PFA for 2 hours per mm depth of the sample. Prolonged incubation times (>24 hours) were avoided as this can lead to auto-fluorescence in the sample. After fixation, the samples were washed in an Eppendorf tube with sterile PBS on a rotating table for one hour. The wash step was repeated 3 times to remove residual PFA. All clearing steps were performed at room temperature on the lab bench. Samples were immersed in the clearing solutions stepwise: CUBIC L1, CUBIC L2, CUBIC R1 and CUBIC R2. The samples and clearing solutions were placed in a 1.5ml Eppendorf tube and then into a black 50ml Falcon tube to eliminate any bleaching of the sample from ambient light. The length of time the sample was immersed in each solution was optimised and is outlined in **Table 2.11** below:

Table 2.11 Optimised clearing times for tumour samples in CUBIC

Solution	Time (h)
CUBIC L1	1
CUBIC L2	1
CUBIC R1	5
CUBIC R2	3 hours minimum or until the sample appears clear. Suitable for long-term storage

As the immersion steps are reasonably short and most of the samples do not contain many blood clots, the solutions were not refreshed for each immersion step. However, if a sample was large or contained large blood clots, the immersion solution was changed if it became cloudy.

Figure 2.6 Workflow of clearing of tumours



2.7.2 Ethyl cinnamate clearing

Ethyl cinnamate is an FDA-approved solvent used in food preparation. ECI-based tissue clearing comprises two steps: (i) dehydration using ethanol; (ii) lipid extraction and clearing by matching RI to the remaining dehydrated tissue's index. Ethyl cinnamate can damage most plastics, so only specific plastic components were used. Glass-based materials are safe to use.

Table 2.12 Reagents used in Ethyl cinnamate clearing

Solution	Reagent	Quantity (ml)
50% Ethanol	Ethanol	25
	dH ₂ O	25
80% Ethanol	Ethanol	40
	dH ₂ O	10
100%	Ethanol	50
Ethyl cinnamate	Ready to use	10

Table 2.13 Ethyl cinnamate clearing protocol

Dehydration in 50% EtOH	30 minutes
Dehydration in 80% EtOH	30 minutes
Dehydration in 100% EtOH	30 minutes
Dehydration in 100% EtOH	30 minutes
ECI clearing	120 minutes (or overnight, as ECI is the storage solution as well)
Total time required	4 hours

2.7.3 Cleared sample immunostaining

As per published work, immunostaining with the CUBIC Cancer protocol was performed between delipidation (CUBIC L) and RI matching steps (CUBIC R). (Shimpei I Kubota *et al.*, 2017)

In brief, tumours were immersed in CUBIC L for 2 hours for delipidation. The tumours were then washed in PBS to remove any residual CUBIC L for 1 hour. Tumours were placed in 5% (w/v) BSA in PBS for 5 hours at room temperature for blocking. Following this, they were washed in 5% (w/v) BSA and Triton X100 0.2% (v/v) at room temperature overnight for permeabilisation and blocking. Primary antibody diluted 1:200 / 5% BSA was added for 3 days at 4°C under constant agitation. After primary incubation, tumours were washed in 5% BSA 3x 1 hour before incubation with the secondary Alexa Fluor antibody diluted 1:500 / 5% BSA for 2 days at 4°C under constant agitation. Tumours were then washed in 5% BSA 3x 1 hour before nuclear staining (Hoechst 1:500/PBS) for 5 hours. CUBIC R1 was added for 5 hours, followed by CUBIC R2 for a minimum of 3 hours before imaging.

Table 2.14 Antibody details

Antibody	Species	Dilution	Manufacturer
Anti-KI67	Rabbit anti- ms/human	1:200	Abcam AB15580
Anti-SMA	Mouse anti- human/chicken	1:200	Abcam MA1-06110
Anti - SMA	Rabbit anti-ms	1:200	Abcam ab5694
Anti-Caspase	Rabbit anti-human	1:50	Abcam ab32042
Alexa Fluor 594	Goat anti-RBT	1:500	Abcam A150080
Alexa Fluor 594	Goat anti-ms	1:500	Invitrogen A11032
Alexa Fluor 750	Goat anti-ms	1:500	Abcam A21037
Hoechst 33342	Nuclear stain	1:500	Thermofisher H3570

2.8 Western Blotting

2.8.1 Protein Extraction and quantification

Cells were seeded in 10 cm dishes at a density of 300,000 cells. They were then incubated in either normoxia (21% O₂) for 24 hours or hypoxia (1% O₂) for 8, 24, or 96 hours. At each experimental time point, cells were lysed. Cell lysis was done by washing cells twice with ice-cold PBS and using 300µL ice-cold lysis buffer (50 mM Tris-HCl pH8.0, 120 mM NaCl, 5 mM EDTA, 0.5% (v/v) NP-40 (IGEPAL CA-360), 1x EDTA-free protease Inhibitor (Roche)). For hypoxia samples, the lysis buffer was equilibrated for 1 hour at 1% O₂ before lysis in the hypoxic chamber. The samples were left on ice for 20 minutes, after which the cells were detached and collected using a cell scraper and transferred to Eppendorf tubes. Samples were centrifuged for 15 minutes at 12 000xg and pre-cooled to 4°C. The supernatant was then transferred to new Eppendorf tubes, and protein concentration was determined by BCA Assay Kit (Thermo Scientific) according to the manufacturer's protocol.

In brief, a standard curve was produced using a BSA solution standard diluted in lysis buffer, as described by the manufacturer. Protein samples were diluted 5µl into 15µl of water. 20µl BSA protein standard or protein sample was pipetted in triplicate into a 96-well plate. 175µl BCA reagent and 3.5µl of copper blue were added using a multi-channel pipette, briefly mixed using a plate shaker and then covered and incubated at 37°C for 30 minutes. After this time, the plate absorbance was read at 570nm using a Spectramax plus384 (Molecular Devices) plate reader. The concentration of the individual protein samples was determined from their mean absorbance values, using a standard linear curve produced from the mean absorbance values of the BSA protein standards.

2.8.2 Sample Preparation

Protein samples were prepared at a 4:1 ratio with 4x Laemmli buffer (Tris HCl 250 mM pH 6.8, 10% SDS, 30% Glycerol, β-mercaptoethanol, 0.02% Bromophenol blue) and boiled for 10 minutes at 95°C. Samples were centrifuged for 1 minute at 12 000 rpm.

2.8.3 Preparation and running of polyacrylamide gels

Table 2.15 Formulation of polyacrylamide gels

Resolving Gel	Stacking gel
0.4 M Tris base pH 8.8	0.4 M Tris base pH6.8
0.1% SDS	4% acrylamide
10% acrylamide	0.65 ng/μl ammonium persulphate (APS)
0.25 ng/μl ammonium persulphate (APS)	0.325% Temed
0.125% Temed	

Table 2.16 Formulation of buffers for Western Blotting

Running buffer (10x)		Transfer buffer (10x)	
Tris base [250mM]	30.27g	Tris base (250mM)	30.27g
Glycine [1.92M]	144.1g	Glycine (1.92M)	144.1g
SDS 10%	10g	Water	1 Litre
Water	1 Litre	Ethanol	100ml

Acrylamide gels were poured into 1mm-thick glass plates in a vertical casting apparatus (Bio-Rad). Resolving gels were overlaid with 200μl isopropanol to flatten the gel surface and prevent drying out of the gel and left to polymerise at room temperature for 45 minutes. Isopropanol was washed away using dH₂O, and stacking gel was poured over the set, resolving the gel. 10- or 15-well combs were immediately inserted into the stacking gel, and gels were left to polymerise for 15 minutes at room temperature. Residual unpolymerised acrylamide was removed from the wells using dH₂O, and gels were placed in a vertical gel electrophoresis tank (Bio-Rad) and submerged in 1 x running buffer. The protein sample was resolved on a stacking cast with a mini-Protean 3 system (Bio-Rad). 10μL of protein ladder (Bio-Rad, Kaleidoscope pre-stained protein marker) was

used as a molecular weight reference. The SDS-PAGE was run for 120V for 1.5 hours in 1x running buffer until the bromophenol blue dye front reached the bottom of the gel. After SDS-PAGE, proteins were transferred onto nitrocellulose membrane (0.2µm, Bio-Rad) via wet transfer. Gels were removed from their casting plates and rinsed twice in RO water before being submerged in freshly prepared transfer buffer (25 mM Tris base, 192 mM Glycine, 1% SDS, 10% (v/v) ethanol) for 15 minutes at room temperature. The transfer apparatus was assembled whilst maintaining the whole apparatus submerged in a transfer buffer to prevent the generation of air bubbles. The apparatus was placed in a vertical electrophoresis tank and filled with transfer buffer and a -20°C freezer pack. The tank was placed in an ice tray, and electroblotting was performed at 300mA for 1 hour and 50 minutes at 4°C.

2.8.4 Protein Detection

After transfer, membranes were rinsed twice with RO water and stained with ATX Ponceau S stain (Fluka) to check the transfer efficiency. Membranes were then blocked with 5% fat-free milk in TBST (0.2 M Tris pH 7.6, 0.14 M NaCl, 0.1% Tween-20 for 30 minutes at room temperature, on an orbital shaker. Membranes were then placed in 50ml tubes and incubated with the primary antibody in blocking buffer overnight at 4°C on a rolling mixer. The following day, membranes were washed 3 x 10 minutes in 0.1% TBS-T at room temperature. They were then placed in 50ml tubes and incubated with secondary antibody - Goat Anti-Rabbit HRP (Cell Signaling #7074S) in blocking buffer for 2 hours at room temperature on a rolling mixer. Membranes were washed a further 3 x 10 minutes in TBS-T, and excess liquid was removed. The membranes were incubated with Clarity Max ECL Substrate Kit (Bio-Rad #170-5060) for protein detection at a 1:1 ratio Substrate A and B). They were incubated for 2 minutes and imaged using a Syngene Gel Imaging G-box (Geneflow, UK).

Table 2.17 Antibody details for Western Blotting

Antibody	Species	Dilution	Manufacturer
Anti- HIF-1α	Rbt	1:1000	Protein Tech (20960-1-AP)
Anti-HIF-2α	Rbt	1:1000	Bethyl Labs (A700-003)

2.9 Quantitative Polymerase Chain Reaction (qPCR)

2.9.1 RNA extraction in neuroblastoma cells

Seventy-five thousand cells were seeded into 60 mm dishes and preincubated for 72 hours in either normoxia (21% O₂) or hypoxia (1% O₂) at 37°C. After 72 hours, cells were dosed for 48 hours as follows (concentrations determined from MTT IC₅₀):

Hypoxia and normoxia in both neuroblastoma cell lines: 10 µM PT2385

SK-N-BE(2)C Normoxia: 10 µM PT2385/ 5 µM Palbociclib

SK-N-AS Normoxia: 10 µM PT2385/ 15 µM Palbociclib

SK-N-BE(2)C Hypoxia: 10 µM PT2385/ 10 µM Palbociclib

SK-N-AS Hypoxia: 10 µM PT2385/ 20µM Palbociclib

After treatment, cells were washed twice with PBS, 300µl RNA lysis buffer (Roche) was applied, and cells were collected into Eppendorf tubes using a cell scraper. RNA extraction was completed using a High Pure RNA Extraction Kit (Roche, Cat: 11828665001) following the manufacturer's instructions. All reagents were stored in a dedicated RNase-free area in the laboratory, and samples were kept on ice throughout to prevent degradation. The RNA was eluted to 50µl, and RNA concentration was determined via a NanoDrop 1000 Spectrophotometer (Thermo Scientific).

2.9.2 RNA extraction from tumour tissue

As per manufacturers' instructions, RNA extraction was completed using the Nucleospin RNA kit (MACHEREY-NAGEL). All reagents were stored in a dedicated RNase-free area in the lab. Tumours dissected from the chick CAM were placed in RNAlater (QIAGEN) and stored at 4°C for up to 2 weeks before RNA extraction. In most circumstances, tumour dissection and RNA extraction were ideally performed on the same day. The tissue was first removed from the RNAlater and transferred to a clean RNase-free falcon tube. The tissue was homogenised in the presence of lysis buffer RA1 during simultaneous mechanical disruption with a rotor-stator homogenizer. Lysis buffer with 3.5µL β-mercaptoethanol (β-ME) was added to the homogenised tissue to lyse the cells. β-mercaptoethanol was added to inactivate RNases. The ground tissue was then vortexed vigorously. The lysate was filtered, and 70% ethanol was added to adjust the RNA binding conditions. RNA was extracted using spin-column-based isolation using the buffers

provided within the kit. The RNA was eluted to 65µL. RNA quantification was performed using a NanoDrop spectrophotometer (Thermo Scientific, USA), and RNA was stored in aliquots at -80°C.

2.9.3 cDNA synthesis

Reverse transcription of 2µg of RNA to cDNA was achieved using Superscript Vilo reverse transcription master mix (Invitrogen, Cat: 11755050), following the manufacturer's instructions. cDNA was diluted at 1:20 with RNase/DNase-free H₂O and stored at -20°C.

2.9.4 Reference genes

Reference genes were selected to allow normalised relative quantification of genes of interest to be calculated. Previous work by the group showed that Cyclophilin A was stably expressed across neuroblastoma cell lines and was selected as a reference gene to assess the effects of drugs and hypoxia on neuroblastoma cells. (Bagnall *et al.*, 2014; A Herrmann *et al.*, 2015)

2.9.5 Target gene selection

The effect of hypoxia on gene expression in several neuroblastoma cell lines in culture has been described by our group. (A Herrmann *et al.*, 2015) We selected the target genes outlined in the paper, including those involved in intravasation (for example, cell-cell adhesion; matrix metalloproteases; epithelial-mesenchymal transition), extravasation (for example, epithelial cell adhesion; glycoproteins) and a classical hypoxic response (for example, VEGF, glucose transporter type 1 (GLUT1)). Genes involved in differentiation in neuroblastoma are highlighted by Sung *et al.* From this paper, we selected Kruppel-like factor 4 (KLF4), roundabout, axon guidance receptor, homolog 2 (ROBO2), stathmin-like 4 (STMN4) and Phox2B to examine the effects of hypoxia and drug treatment on differentiation gene expression. (Sung *et al.*, 2013) MYCN was also included due to its significance in neuroblastoma differentiation.

2.9.6 Primers

Primer sequences were identified from published papers using the same target or reference genes in the qPCR experiments (A Herrmann *et al.*, 2015); Sung *et al.*, 2013). Primer sequences were ordered from Sigma-Aldrich. Once the primers were received, they were reconstituted in

nuclease-free water (ThermoFisher Scientific, UK) and stored at -20°C in small 10 mM aliquots to avoid the freeze-thawing process.

Table 2.18 Lists details all the primer pairs used.

Table 2.18 *Primer pairs*

Gene	Forward 5'-3'	Reverse 5'-3'
A3B1	ATATGGGCGCGGTGTTCTTG	GTCCTGCCACCCATCATTGT
A6B1/4	AGCTGTGCTTGCTCTACCTG	GAGCAACAGCCGCTTGTCC
ACTIN	GTTTCTCTGCCGGTCGCAAT	CCCGACGATGGAAGGAAAC
ADAMST1	CCCTCACTCTGCGGAAC TTT	GGACCCACACAAGTCCTGTG
BNIP3	GCCATCGGATTGGGGATCTAT	GCCACCCCAGGATCTAACAG
CA-9	GGGTGTCATCTGGACTGTGTT	CTTCTGTGCTGCCTTCTCATC
CDKN1A	AGCTGCCGAAGTCAGTTCCTT	GTTCTGACATGGCGCCTCCT
CYCLOPHILIN	GCTTTGGGTCCAGGAATGG	GTTGTCCACAGTCAGCAATGGT
E2F1	CCGCCATCCAGGAAAAGGTG	GTGATGTCATAGATGCGCCG
Glut1	GAACTCTTCAGCCGGGTCC	ACCACACAGTTGCTCCACAT
ITGαV	CGCTTCTTCTCTCGGACTC	AGAAACATCCGGGAAGACGC
ITGβ5	GGGAGCCAGAGTGTGGAAAC	GGATCGCTCGCTCTGAAACT
KLF4	CGCCGCTCCATTACCAAGAGC	CGGTTCGATTTTTGGCACTG
MMP2	CCAGCTGGCCTAGTGATGAT	CAGGTATTGCATGTGCTAGGT
MMP9	AGCGAGAGACTCTACACCCA	CGGAGTAGGATTGGCCTTGG
MYCN	CACAAGGCCCTCAGTACCT	ACCACGTGATTTCTTCCTCT
NCAM	GCGAAGAAAAGACTCTGGATGGGCA	CCGATGGTGTGCTGGCGGT
PHOX2b	ACCCGATAAGGACCACTTTTGG	AAGAGTTTGTAAGGAACTGCGG
ROBO2	GATGTGGTGAAGCAACCAGC	TGGCAGCACATCTCCACG
STMN4	CCTAGCAGAGAAACGGGAACA	GGCGTGCTTGTCTTCTCTT
VCAM	TGTTTGCAGCTTCTCAAGCTTTTA	GTCACCTTCCCATTCAAGTGA
VCAN	ACCAGACAGGCTTCCCTCCCC	GGGTGATGCAGTTTCTGCGAGGA
VEGFA	CTCCACCATGCCAAGTGGTC	GCAGTAGCTGCGCTGATAGA

RT-PCR was carried out in 96-well white plates (Roche), and all samples were pipetted in triplicate. Target experimental values were normalised to 2 housekeeping genes (Cyclophilin A and β -actin) using the relative quantification method with 4 independent biological samples per condition. Each reaction consisted of the following: 10 μ l Light Cycler SYBR Green I Master (Roche), 6 μ l DNase/RNase-free H₂O, 2 μ l cDNA and 0.5 μ M of each primer.

2.9.7 Controls

A no template control (NTC) was included for all experiments to monitor genomic DNA contamination and primer-dimer formation. A no reverse transcriptase control (NRT) was also included whenever a new RNA preparation was used to monitor genomic DNA contamination.

2.9.8 Plate design

Reaction super-mixes were prepared in triplicates, and 15 μ l of reaction super-mix was carefully pipetted into a single well of a 96-well white plate (Roche). The plate was covered by a clear seal (MSB1001, BioRad, UK) and centrifuged briefly in a microplate centrifuge. An example plate design can be seen in **Figure 2.7**. qPCR was performed using a Light Cycler 480 using the parameters described in **Table 2.19**. The Light Cycler employed precise temperature control and rapid temperature changes for optimal cDNA amplification.

Figure 2.7 Example plate layout for qPCR. NTC, no template control.

PLATE 3		NO treatment			HIF			CDK			COMBO		
	mmp2												
	mmp9												
	myc n												
	ncam												
	phox 2b												
	CycloA												
	ACTIN												
		NTC MMP2	NTC MMP9	NTC MYCN	NTC NCAM	NTC PHOX2B	NTC CYCLOA	NTC ACTIN	H2O	H2O	H2O	H2O	H2O

Table 2.19 Step conditions

Step	Temp (°C)	Time [HH:MM: SS]	Cycles
Pre Incubation	50	00:02:00	1
Amplification	95	00:05:00	45
	95	00:00:10	
	60	00:00:15	
	72	00:00:15	
Melt Curve	95	00:00:05	1
	65	00:01:00	
Cooling	97	Continuous	1
	40	00:00:10	

2.9.9 Fold Gene Expression

All data were analysed using Light Cycler 480 SW 1.5 software. Fold change in target gene expression was calculated relative to the control values of the mean of two housekeeping genes, cyclophilin A and β -actin, for each respective experimental condition.

The mean Ct value for 3 technical replicates from a single biological replicate was calculated, followed by the mean Ct value for 3 independent biological replicates. A commonly used method for calculating relative gene expression using qPCR data is the $2^{-\Delta\Delta Ct}$ method. (Schmittgen and Livak, 2008) To conduct statistical analysis, NRQ data of 3 independent biological replicates were compared to the control to standardise the fold change.

$$\Delta Ct = Ct (TG) - Ct (RG)$$

$$\Delta Ct = \Delta Ct \text{ Treatment} - \Delta Ct \text{ control}$$

$$\text{Fold change due to treatment} = 2^{-\Delta\Delta Ct}$$

Ct, threshold cycle; TG, target gene; RG, reference gene.

Values were converted to a log scale for statistical analysis.

**Chapter 3 : Assessing the
potential of cell cycle inhibition
and NF-KB inhibition of primary
neuroblastoma tumour growth *in
vitro* and *in vivo***

3.1 Introduction

Despite advances in therapies, high-grade metastatic neuroblastoma has only a 50% survival rate at five years. One key characteristic of the high-grade disease is uncontrolled cell proliferation leading to the huge, widespread tumour burden. This proliferative phenotype can be explained through chromosomal abnormalities in pathways affecting cell growth, differentiation and development signals. In addition, numerous transcription factors have been implicated in the unregulated proliferation of neuroblastoma cells, such as NF-KB and PHOX2B. However, arguably the most seen abnormality is the amplification of MYC-N. The MYC-N oncogene encodes N-MYC, which can increase the expression of genes activating cell proliferation when bound to promoter sequences. (Schweigerer *et al.*, 1990) (Negrone *et al.*, 1991). MYC-N has been shown to interact with the function of cell cycle regulators such as CDKs and tumour suppressors (RB) to progress the cell cycle. (Golias, Charalabopoulos and Charalabopoulos, 2004). A therapeutic strategy targeting cell proliferation, specifically those proteins and enzymes known to be overexpressed and upregulated in neuroblastoma, has real potential.

3.1.1 Targeting Cell cycle progression and pathways involved in drug resistance in neuroblastoma.

We chose to target the uncontrolled proliferation of tumours in our drug testing. Cyclin-dependent kinases are critical regulators of orderly cell cycle progression in mammalian cells. Certain CDKs are also crucial in stabilising the phosphorylation of MYC. (Sjostrom *et al.*, 2005) Small molecule inhibition of these kinases may offer an alternative method of inhibiting the cell survival and pro-proliferation effects of MYC-N overexpression, alongside targeting MYC-N stability. I have chosen to target the CDK4/6 complex and CDK1 in neuroblastoma cells and tumours.

Cyclin D1 complexes with CDK4 and CDK6 to initiate cell cycle entry through the phosphorylation and inhibition of retinoblastoma protein (pRB). (Kato *et al.*, 1993b) Dysregulation of this G1 entry checkpoint is an essential promoter of neuroblastoma development. Similarly, Cyclin-dependent kinase 1 (CDK1) is critical to the survival of MYC-N overexpressing cancers. (Chen, Y.-H. Tsai and Tseng, 2013) Inhibition of CDK1 has demonstrated apoptosis in MYC-N overexpressed cells, and *in vivo* studies using mouse lymphoma and hepatoblastoma have shown reduced tumour growth and improved animal survival. (Goga *et al.*, 2007) The CDK inhibitor compounds used here have previously been tested in various tumour types, for example in breast cancer, where

Palbociclib, a CDK 4/6 inhibitor, has been approved for use in patients. (Goel *et al.*, 2018) The CDK1 inhibitor, RO-3306, has also been successfully tested *in vitro* in MYC-N-driven cancers. (Kang *et al.*, 2014).

Another key reason for the poor outcome in high-risk group neuroblastoma is the development of drug resistance. The machinations of treatment failure are still not fully understood, but one proposed mechanism involves the activation of NF- κ B controlled pathways. (Wang *et al.*, 2017) Biological inhibitors of the NF- κ B pathway have been used here to understand the role of the NF- κ B pathway in the progression of neuroblastoma. Bay-11-7082, used in this work, has been reported to selectively inhibit the phosphorylation of I κ B α , thus preventing the release of active NF- κ B into the nucleus and subsequent transcription of target genes. (Lee *et al.*, 2012)

3.1.2 Utilising metastatic ‘high risk’ (as per INRG staging) neuroblastoma cell lines for *in vitro* and *in vivo* drug testing.

The focus of this project was to investigate difficult to treat metastatic neuroblastoma. Multiple commercial cell lines reflect the genetic and clinical heterogeneity associated with the disease. The two cell lines used in this work represent the cohort of patients with MYC-N amplification (SK-N-BE(2)C) and those with a segmental chromosomal aberration 11q deletion (SK-N-AS), together making 2/3rds of the most common genetic hallmarks seen in high risks neuroblastoma.

SK-N-BE(2)C cells are derived from the bone marrow biopsy of a young male with treatment-resistant disseminated neuroblastoma disease. The cell line is known to have amplification of MYC-N oncogene, as well as chromosome 1p deletion and chromosome 17 translocations. This cell line was previously xenografted on the CAM of the chick embryo model and has successfully grown neuroblastoma tumours. SK-N-AS cell lines represent another large group of aggressive tumours which are treatment-resistant but not MYC-N amplified: 11q deleted neuroblastoma. (Barnes *et al.*, 1981; Thiele, 1998) Although both MYC-N amplification and 11q deletion strongly correlate with poor prognosis, the two are rarely seen in the same tumour. This represents two distinct clinical groups to target with novel therapies. (Mlakar *et al.*, 2017) MYC-N amplification has been well characterised in neuroblastoma progression. However, there is far less known about how 11q deletion affects the tumour's aggressiveness. Although the cell cycle proteins and checkpoints are common to both cell types, any differences in response to therapy might shed light on the influence each genetic aberration has on the cell cycle progression.

3.1.3 Developing the use of the chick embryo model as a tool for drug screening in neuroblastoma.

Preclinical *in vitro* cancer models have faced the drawback of being ineffective at reliably predicting patient outcomes. While *in vitro* testing in cell-based experiments has always been a fundamental part of cancer research, these preclinical studies have not always been successful at producing data that reflect the exact behaviour of malignancies in response to candidate drugs. *In vivo* models can address the major limitation of *in vitro* studies in that they can validate the impact of a compound on the organism as a whole rather than isolated cells. This allows *in vivo* studies to better identify potential interactions with the organism and the tumour microenvironment, improving its predictions of safety, toxicity, and efficacy. However, *In vivo* studies face significant ethical concerns.

The 'three R's promote replacement, reduction and refinement in the practice of animal-based testing. In this respect, a high throughput, high fidelity, the data-rich model would be the ideal screening tool to bridge between *in vitro* and animal models.

The chick embryo is an established biological model which has contributed significantly to understanding virology, immunology and embryology. There are several key characteristics of the chick model which make it useful in cancer research: it is phylogenetically closer to mammals than other models such as zebrafish, chicks have a short incubation time allowing a quick turnover of experiments for drug screening, it is an easily accessible model for imaging and surgical procedures, and the husbandry of the model is economical, requiring only a temperature and humidity controlled incubator.

Previous work from collaborations between D Moss (Institute of translational medicine, University of Liverpool) and V See (Institute of Integrative Biology, University of Liverpool) has refined the chick embryo as a metastatic model of neuroblastoma and explored its use as a drug-screening tool. Compared with mammalian models, where tumour growth often takes between 3 and 6 weeks, tumours on the chick embryos are visible in less than a week from the time of tumour inoculation. Whilst the cells do not spontaneously metastasise into the chick embryo, it is now known that preconditioning of neuroblastoma cells in hypoxia (1% O₂) is sufficient to trigger invasive metastasis from a primary tumour into the chick embryo (A Herrmann *et al.*, 2015). The chick model, therefore, constitutes a cost-effective and rapid *in vivo* assay to investigate new

therapeutic strategies. As per European law (Directive 2010/63/EU of the European Parliament and of the Council of 22 September 2010 on the protection of animals used for scientific purposes), the CAM model system does not raise any ethical or legal concerns, and so the use of the model also addresses the 3Rs, by providing replacement and reduction in animal use.

This chapter describes the attempts to establish and characterise the impact of cell cycle inhibitors on MYCN amplified and non-amplified neuroblastoma cell lines. In addition, we aim to assess the utility of the chick embryo to screen these drugs as an *in vivo* model for metastatic neuroblastoma. We will do this by testing the compounds *in vitro* – to assess their effect on the cell cycle of neuroblastoma cells and *in vivo* to assess the toxicity of the compounds on a developing embryo and the drug's efficacy on neuroblastoma tumours.

3.2 Results

3.2.1 Investigation of drug treatment on survival of MYC-N amplified (SK-N-BE(2)C) and 11q deleted (SK-N-AS) cell lines *in vitro*.

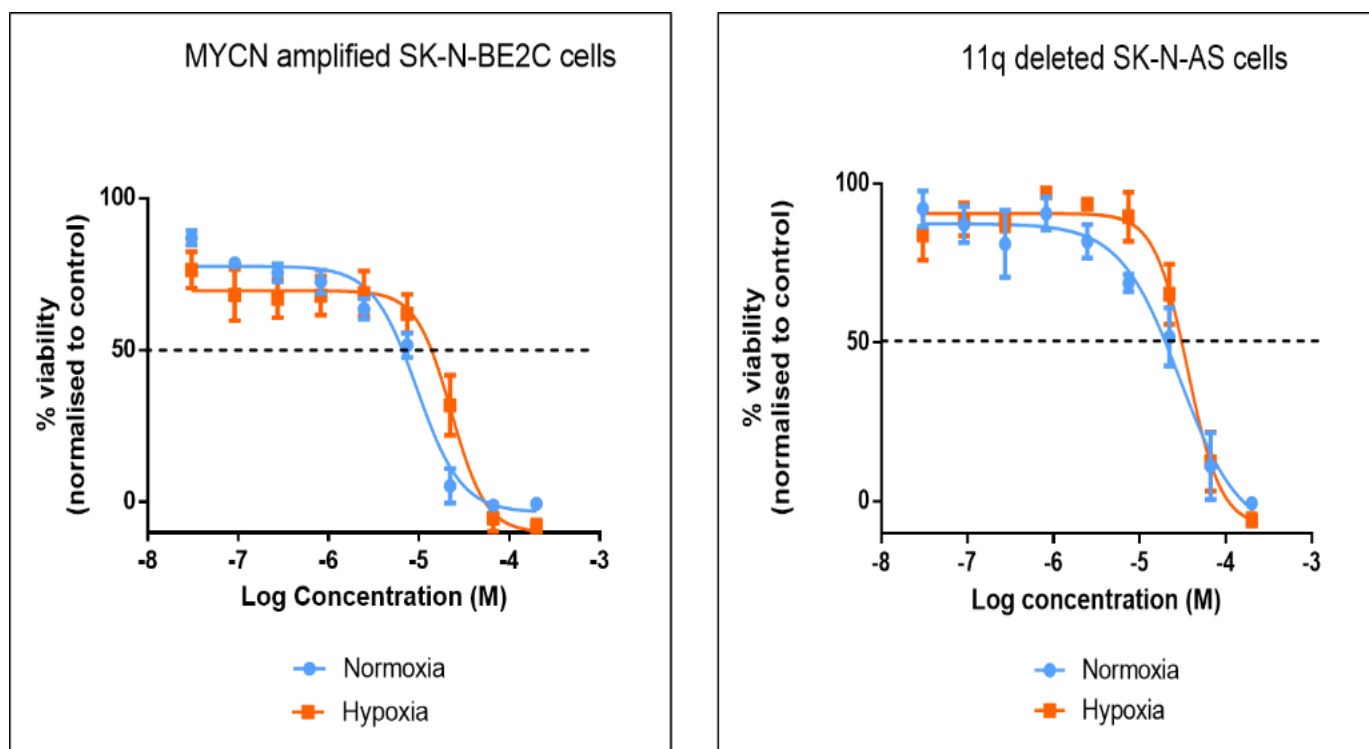
Our first objective was to quantify *in vitro* the effect of the three drugs in altering cell cycle progression and cell survival using an MTT assay. The drug dose causing 50% growth inhibition (IC₅₀ drug dose) was calculated to serve as a guide for *in vivo* dosing. For these experiments, SK-N-BE(2)C and SK-N-AS cells were used in cell culture conditions and treated with CDK1 inhibitor (RO 3306) and CDK 4/6 inhibitor (Palbociclib), NF-KB inhibitor (Bay-11-7082). Drugs were administered to cells in normoxia (21% O₂) and cells incubated in hypoxia (1% O₂) for 72 hours before dosing. Experiments were performed in both hypoxia and normoxia for two reasons: to assess the drug's efficacy in a hypoxic environment similar to within the chick embryo model (Al-Mutawa *et al.*, 2018) and to assess whether the cells behave more aggressively in hypoxia, thereby affecting the efficacy of the drug. The pharmacological inhibition of CDK4/6, CDK1 and NF-KB was performed across a wide concentration range (30nM to 200µM). Alongside the effect of increasing drug concentrations on cell survival, the impact of the three drugs on the cell cycle was tested here. The effect of each drug on cell survival and cell cycle progression is described in turn.

3.2.1.1 CDK4/6 inhibitor Palbociclib effect on SK-N-BE(2)C cells and SK-N-AS cells

CDK4/6 inhibitor, Palbociclib, treatment elicited dose-dependent cell death in both neuroblastoma cell lines (Error! Reference source not found.). MYC-N amplified SK-N-BE(2)C show that cell death is evident even at the lowest drug dose of 30nM when normalised to the control. The cell viability at 30nM was only 75% of the control. Cell death was also seen in the cells cultured in hypoxia, where the cell viability at 30nM was 25% lower than the control. Interestingly this was not seen in the SK-N-AS cells, where in both normoxia and hypoxic cells, the starting concentration of 30nM did not impact cell viability as strongly. The values of the IC₅₀s indicate how sensitive the neuroblastoma cell line is to a given drug. The SK-N-BE(2)C IC₅₀ values were lower than the SK-N-AS ones in both normoxia and hypoxia, indicating a greater sensitivity to Palbociclib in the SK-N-BE(2)C cell line compared to the SK-N-AS.

There was also a difference in the IC50 values between hypoxia and normoxia. SK-N-BE(2)C cells in hypoxia had a higher IC50 than the normoxia counterpart (9.6 μ M in normoxia compared with 22.8 μ M in hypoxia). Although there was also an increase in IC50 in the hypoxic SK-N-AS cells, the difference was less significant.

Figure 3.1 Sensitivity of MYC-N amplified (SK-N-BE(2)C) and MYC-N non amplified (SK-N-AS) cell lines to Palbociclib after 48 hours of treatment.



Cell line	21% Oxygen IC50 (μM)	1% Oxygen IC50 (μM)
SK-N-BE(2)C	9.6	22.8
SK-N-AS	29	36

Cells were plated in 96 well plate and treated as indicated in Materials and Methods. Cells grown in normoxia are depicted in blue and cells grown in hypoxia are shown in orange. Cells were treated in incremental ½ log dosages, from 30nM to 200μM, shown on the x axis. The y-axis represents the percentage of viable cells, measured by MTT, at each concentration compared to vehicle control. Each point shown depicts the mean value of 4 biological replicates, and error bars represent standard deviation. The dotted line shows the drug concentration when 50% cell death occurred – the IC50, which is then tabulated in the table below.

For cell cycle analysis, the two cell lines were cultured in hypoxia or normoxia. The effect on the cell cycle was performed better to characterise the drug's actions on the two cell lines. Rihani has demonstrated that different neuroblastoma cells have differential cell cycle responses to Palbociclib. (Rihani *et al.*, 2015) The drug concentration administered this time was half the IC50 value from the earlier cell survival experiments. A lower dose was chosen to enable cell cycle arrest without causing cell death. The cells were again treated for 48 hours.

The effect of drugs on the cell cycle was then assessed by flow cytometry.

A trypan blue exclusion assay to assess the percentage of live cells was performed before cell cycle sorting. The cell counts showed that in hypoxia, there were fewer living SK-N-BE(2)C cells in both control and treated groups. The cell death is depicted as the sub-G0 peak (black arrow) on the cell cycle graphs and indicates hypoxia-induced toxicity. The sub-G0 peak is not observed in normoxia conditions. It was only observed for SK-N-BE(2)C, and hypoxic preconditioning did not affect SK-N-AS cell survival. The implication is that the MYC-N amplified SK-N-BE(2)C cells are more sensitive to hypoxia. The sub G0 peak was seen for SK-N-BE(2)C hypoxia controls in all the flow cytometry experiments and all compounds.

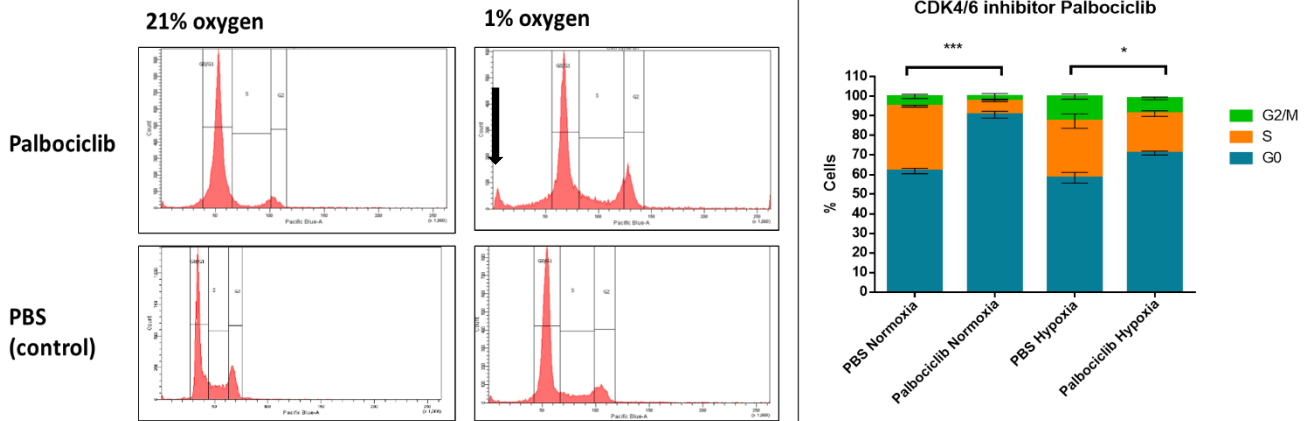
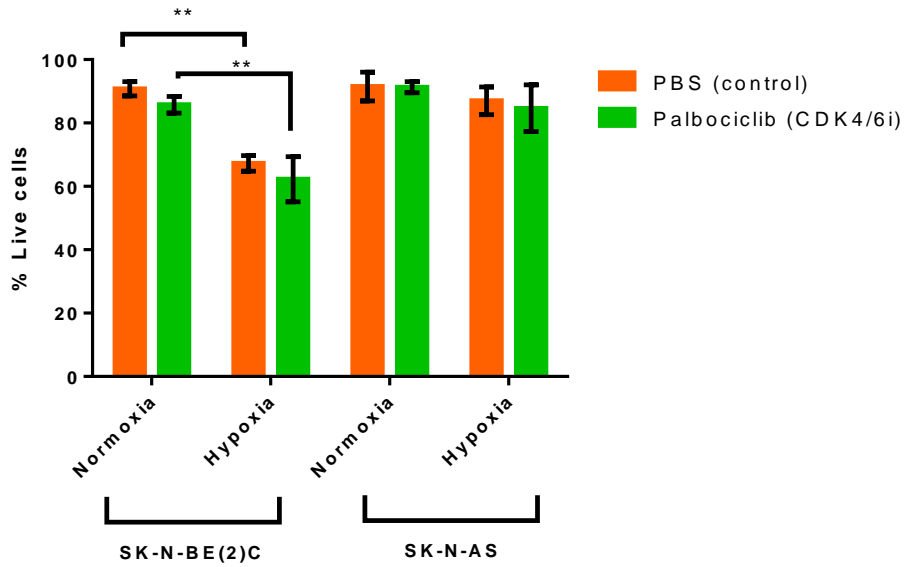
Error! Reference source not found. shows that Palbociclib induces G1 cell cycle arrest in SK-N-BE(2)C cells. The cell cycle arrest is shown by the marked increase in cells arrested in G0/G1 phase in the SK-N-BE(2)C normoxia treated group (mean = 90% SD=3%) compared to the PBS normoxia group (mean= 61 SD =2) ($p < 0.0003$). The same level of cell cycle arrest was not seen in the hypoxia-treated group, where the average percentage cell population in G0/G1 was 71% (SD= 1.5) and compared to the average in the PBS hypoxia group – mean = 58% (SD=5%) ($p = 0.0158$). The comparatively lower percentage of cells in G0/G1 in hypoxia indicates that the drug is less efficacious in hypoxic cells **Error! Reference source not found.**- B). The drug could function less well in the hypoxic environment, or the cells become more resistant to the compound after preincubation in hypoxic conditions. Interestingly SK-N-AS cells show no significant change in cell cycle progression with Palbociclib treatment. The relative resistance of the cells here echoes the higher IC50s measured previously.

These data highlight two important points: 1) that the efficacy of the drug may be altered in hypoxia when it is effective in normoxia and 2) that the fundamental genetic differences in MYC-N and 11q cells may make the SK-N-AS cell line more resistant. (**Error! Reference source not found.**)

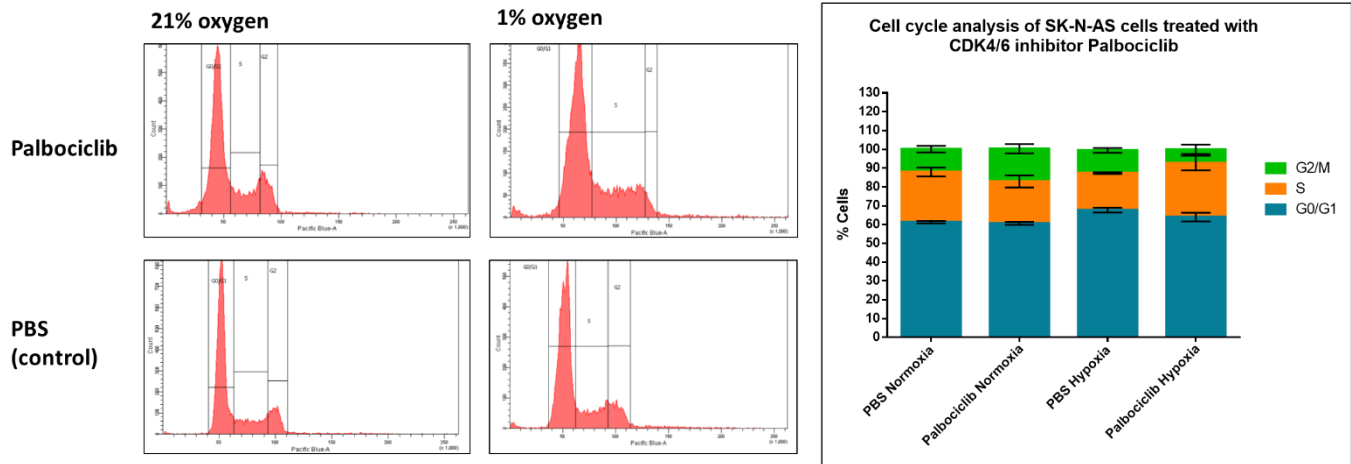
Figure 3.2 Cell Cycle Analysis of neuroblastoma cells treated with Palbociclib

A

Cell survival in neuroblastoma cell lines preconditioned in normoxia and hypoxia



B



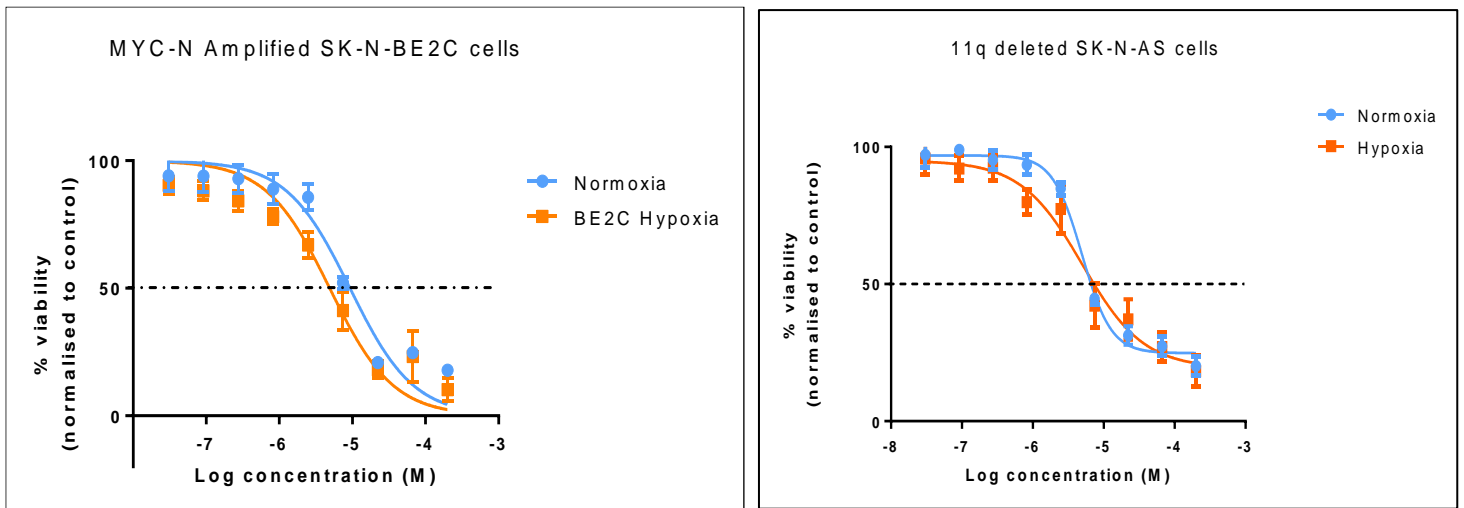
Cells were treated at half IC50 doses for 48 hours. Cells in hypoxia were preconditioned in hypoxia for 72 hours prior to treatment. A) Percentage of living cells after 48 hours of treatment in normoxia or hypoxia measured by trypan blue exclusion assay combined with cell counting B) Representative cell cycle graphs and percentage cells per cell cycle phase. Arrow depicts a sub G0 group within the differential cell populations. Unpaired t-test was performed to test for statistical significance. * $p < 0.05$, ** $p < 0.01$, *** $p = 0.001$, $p = 0.0001$

3.2.1.2 CDK1 inhibitor RO3306 efficiency in SK-N-BE(2)C cells and SK-N-AS cells

I then tested the efficiency of RO3306, a CDK1 inhibitor. MTT assay showed that both cell lines were sensitive to CDK1 inhibition in normoxia. No cell death was seen at the lowest concentrations of CDK1 inhibition in either cell line. (Figure 3.3)

In hypoxia, the SK-N-BE(2)C cell line, which had previously shown increased resistance in hypoxia with Palbociclib, had a similar IC50 compared to normoxia. The SK-N-AS cells, which had an IC50 of 36 μM to Palbociclib in hypoxia, have a lower IC50 of 4.9 μM . Therefore, we can conclude that both cell lines have comparable sensitivity for this compound, and hypoxia did not significantly alter the cell's response to this drug.

Figure 3.2 Sensitivity of MYC-N amplified (SK-N-BE(2)C) and MYC-N non amplified (SK-N-AS) cell lines to RO 3306 after 48 hours of treatment.

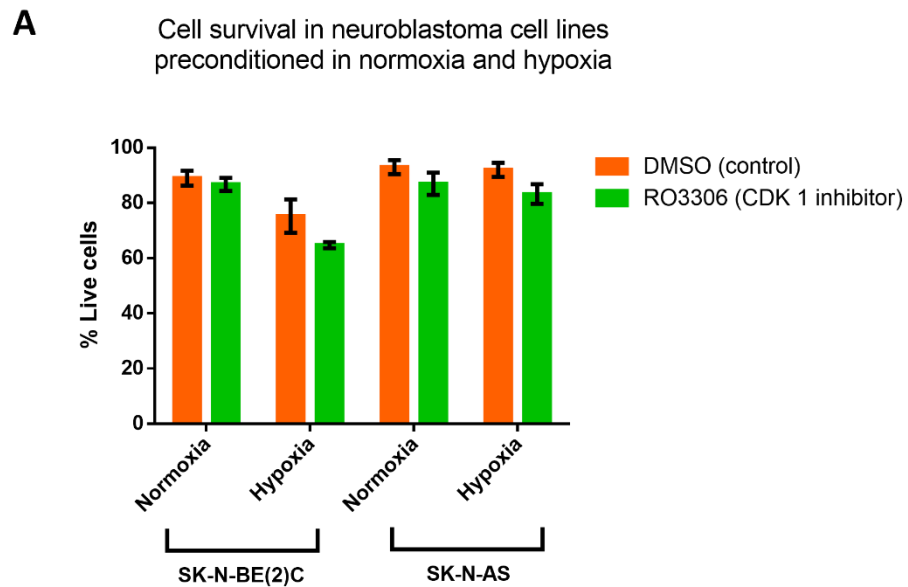


Cell line	21% Oxygen IC50 (μM)	1% Oxygen IC50 (μM)
SK-N-BE(2)C	6.6	4.7
SK-N-AS	4.9	4.9

Cells were plated in 96 well plate and treated as indicated in Materials and Methods. Cells grown in normoxia are depicted in blue and cells grown in hypoxia are shown in orange. Cells were treated in incremental $\frac{1}{2}$ log dosages, from 30nM to 200μM, shown on the x axis. The y-axis represents the percentage of viable cells, measured by MTT, at each concentration compared to vehicle control. Each point shown depicts the mean value of 4 biological replicates, and error bars represent SD. The dotted line shows the drug concentration when 50% cell death occurred – the IC50, which is then tabulated in the table below.

FACS analysis of live cell counts performed in normoxia and hypoxia confirmed the lower cell survival of SK-N-BE(2)C cells when preconditioned in hypoxia, as seen previously. For SK-N-BE(2)C cells and SK-N-AS cells, there was an increased number of cells in the G2 phase, as expected from CDK1 inhibition. This change in SK-N-BE(2)C cells was significant and comparable in both normoxia and hypoxic culture conditions. When assessing the effect of CDK1 on cell cycle progression in SK-N-AS cells, unlike for Palbociclib, the cells responded to CDK1 inhibition, with a significant difference in the number of cells arrested in G2. This difference was more pronounced in normoxia cultures. (**Figure 3.3**)

Figure 3.3 Cell Cycle Analysis of neuroblastoma cells treated with RO 3306



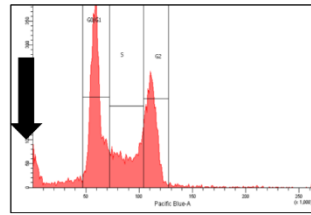
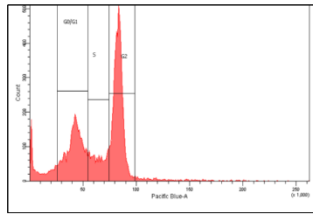
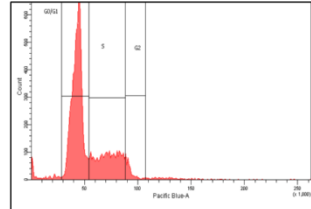
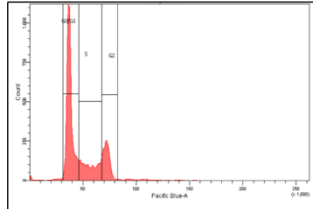
B

SK-N-BE(2)C

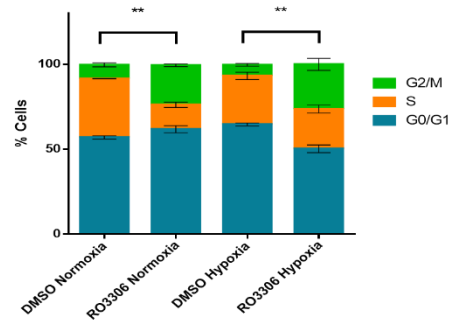
21% oxygen

1% oxygen

RO-3306

DMSO
(control)

Cell cycle analysis of SK-N-BE(2)C cells treated with CDK1 inhibitor RO3306

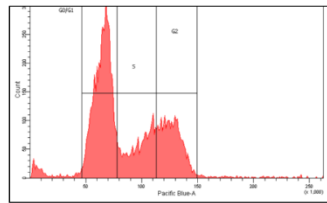
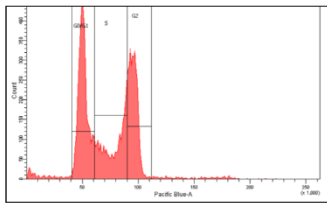
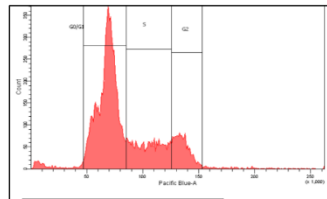
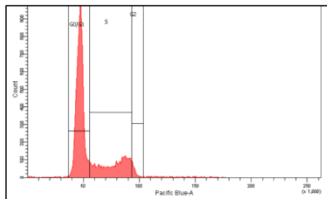


SK-N-AS

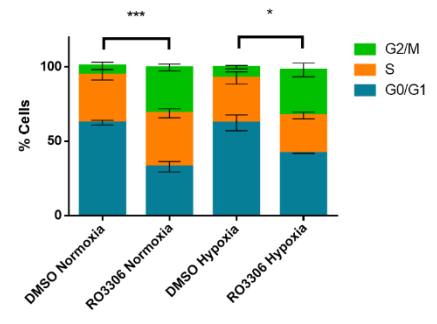
21% oxygen

1% oxygen

RO-3306

DMSO
(control)

Cell cycle analysis of SK-N-AS cells treated with CDK1 inhibitor - RO3306



Cells were treated at half IC50 doses for 48 hours. Cells in hypoxia were preconditioned in hypoxia for 72 hours prior to treatment. A) Percentage of living cells after 48 hours of treatment in normoxia or hypoxia measured by trypan blue exclusion assay combined with cell counting B) Representative cell cycle graphs and percentage cells per cell cycle phase. Arrow depicts a sub G0 group within the differential cell populations. Unpaired t-test was performed to test for statistical significance. * $p < 0.05$, ** $p < 0.01$, *** $p = 0.001$, $p = 0.0001$

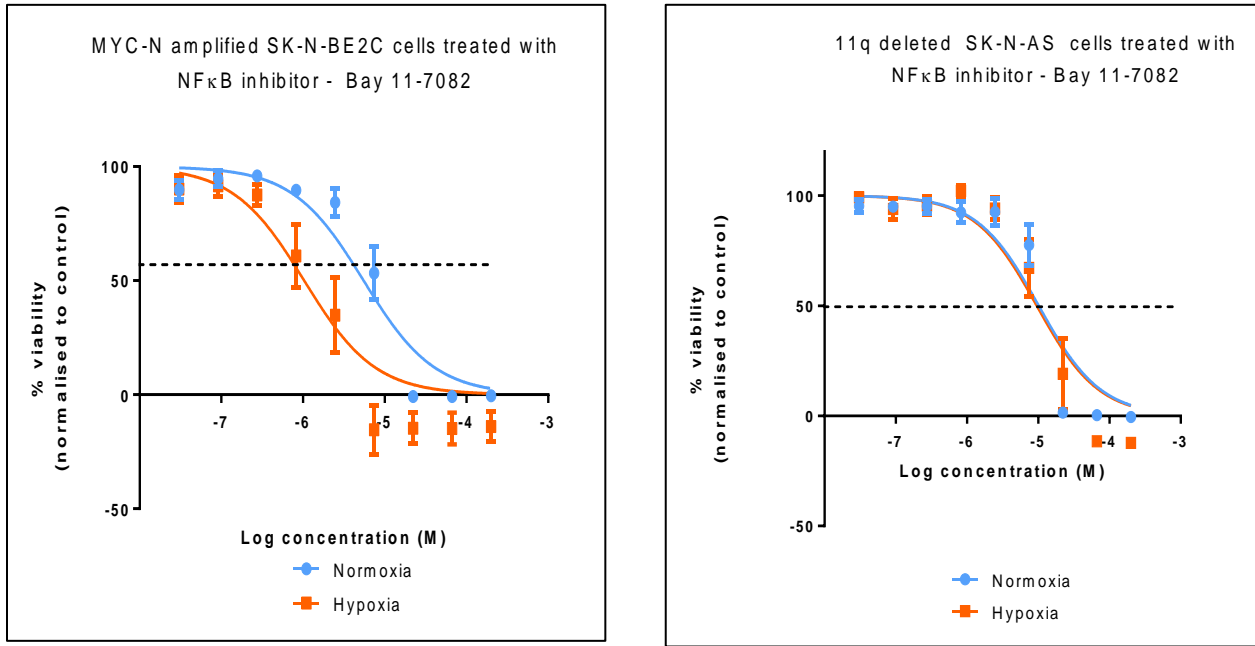
3.2.1.3 Assessing the efficacy of NF- κ B inhibitor BAY-11-7082 in SK-N-BE(2)C cells and SK-N-AS cells

Mullassery et al. showed that inhibiting the NF- κ B pathway caused neuroblastoma cell death. It was therefore hypothesised that inhibition of NF- κ B, using the Bay-11-7082 compound, may have a potential therapeutic role in neuroblastoma treatment.

Here we observed cell death in both lines after 48 hours of treatment, as measured by MTT assay (**Figure 3.4**). The IC₅₀s in both lines in normoxia were comparable at 5.5 μ M in SK-N-BE(2)C cells and 10 μ M in SK-N-AS.

In SK-N-BE(2)C cells, there was no evidence of cell death at lower concentrations of Bay-11-7082, unlike with Palbociclib. Preconditioning SK-N-BE(2)C cells in hypoxia appeared to sensitise them further to NF- κ B inhibition (5.5 μ M in normoxia and 1.0 μ M in hypoxia), whereas the IC₅₀ remained very similar between normoxia and hypoxia for the SK-N-AS cell line **Figure 3.5**. Overall, SK-N-BE(2)C cells appeared more sensitive to NF- κ B inhibition than SK-N-AS cells, as shown by the lower IC₅₀ in hypoxia. Bay-11-7082 is not known to have any impact on cell cycle progression. As expected, SK-N-BE(2)C and SK-N-AS cells treated with Bay-11-7082 had a broadly similar number of cells in each cell cycle phase as the control. In conclusion, the effects seen with the MTT assay were due to reducing the cell number by cell death rather than cell cycle arrest. Both cell lines were sensitive to Bay-11-7082, and the drug functions in a hypoxic environment.

Figure 3.4 Sensitivity of (SK-N-BE(2)C) (SK-N-AS) cell lines to BAY-11-7082 after 48 hours of treatment.



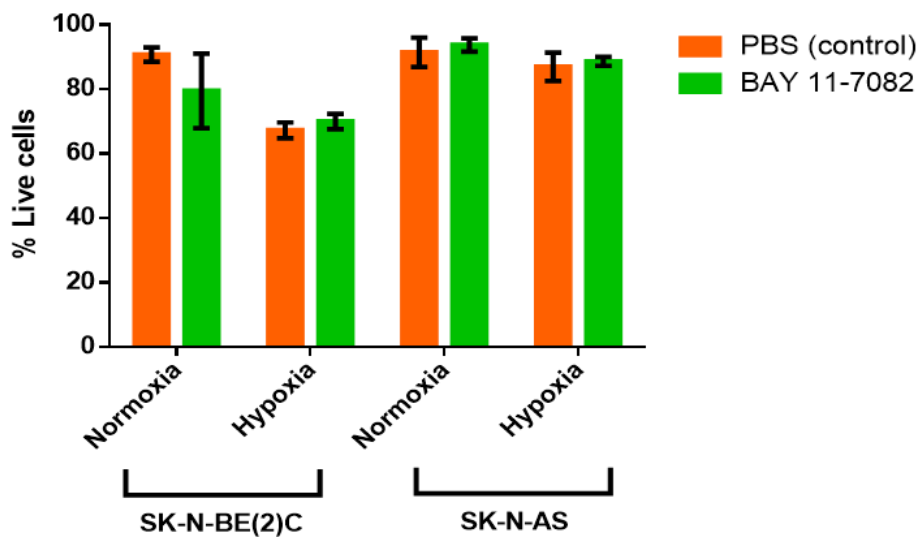
Cell line	21% Oxygen IC50 (μM)	1% Oxygen IC50 (μM)
SK-N-BE(2)C	5.5	1.0
SK-N-AS	10	9.5

Cells were plated in 96 well plate and treated as indicated in Materials and Methods. Cells grown in normoxia are depicted in blue and cells grown in hypoxia are shown in orange. Cells were treated in incremental $\frac{1}{2}$ log dosages, from 30nM to 200uM, shown on the x axis. The y-axis represents the percentage of viable cells at each concentration compared to vehicle control. Each point shown depicts the mean value of 4 biological replicates, and error bars represent SD. The dotted line shows the drug concentration when 50% cell death occurred – the IC50, which is then tabulated in the table below.

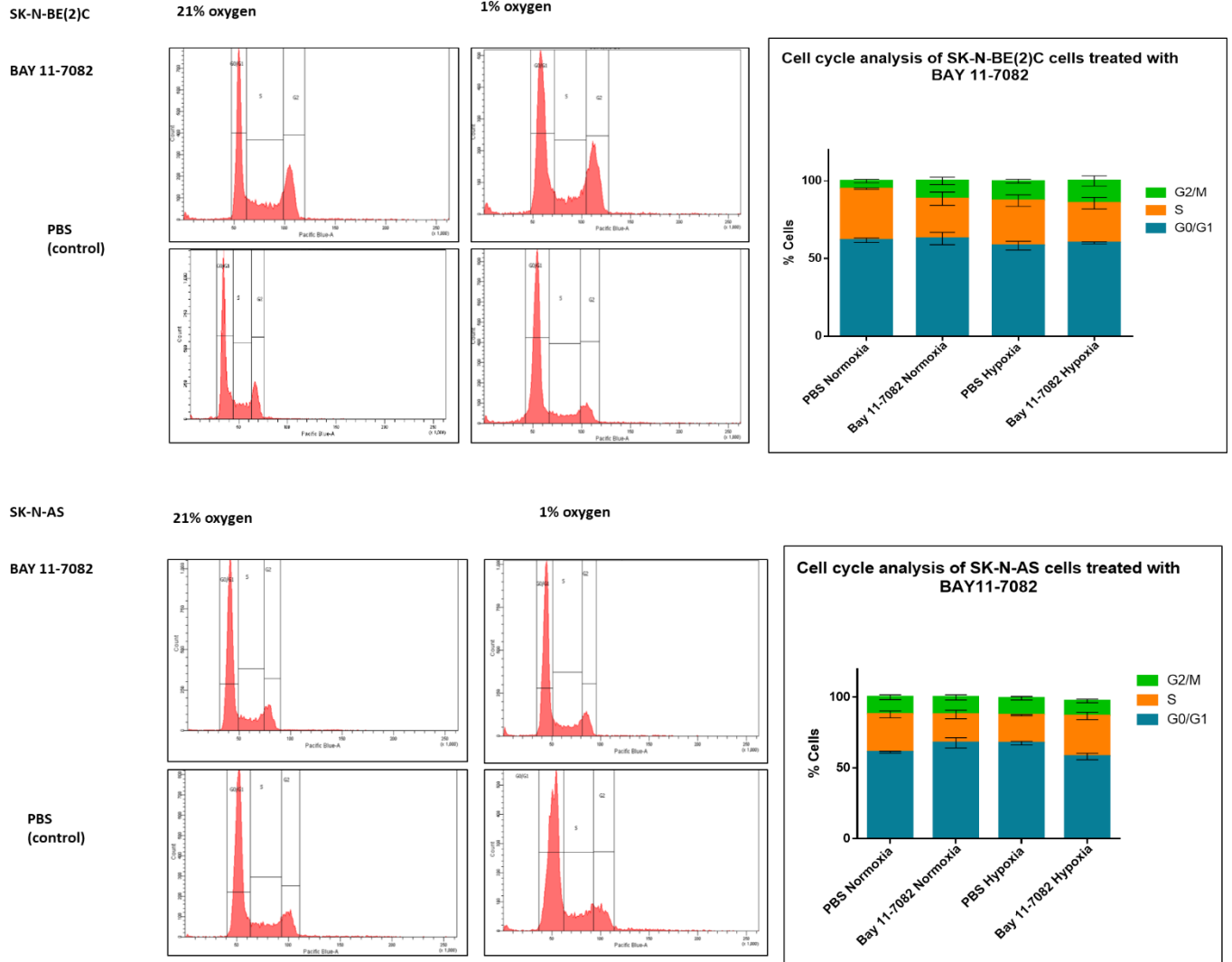
Figure 3.5 Cell Cycle Analysis of neuroblastoma cells treated with Bay-11-7082.

A

Cell survival in neuroblastoma cell lines preconditioned in normoxia and hypoxia



B



Cells were treated at half IC50 doses for 48 hours. Cells in hypoxia were preconditioned in hypoxia for 3 days prior to treatment. A) Percentage live cells after 48 hours of treatment in normoxia or hypoxia measured by trypan blue exclusion assay combined with cell counting. B) Representative cell cycle graphs and percentage cells per cell cycle phase. Unpaired t-test was performed to test for statistical significance.

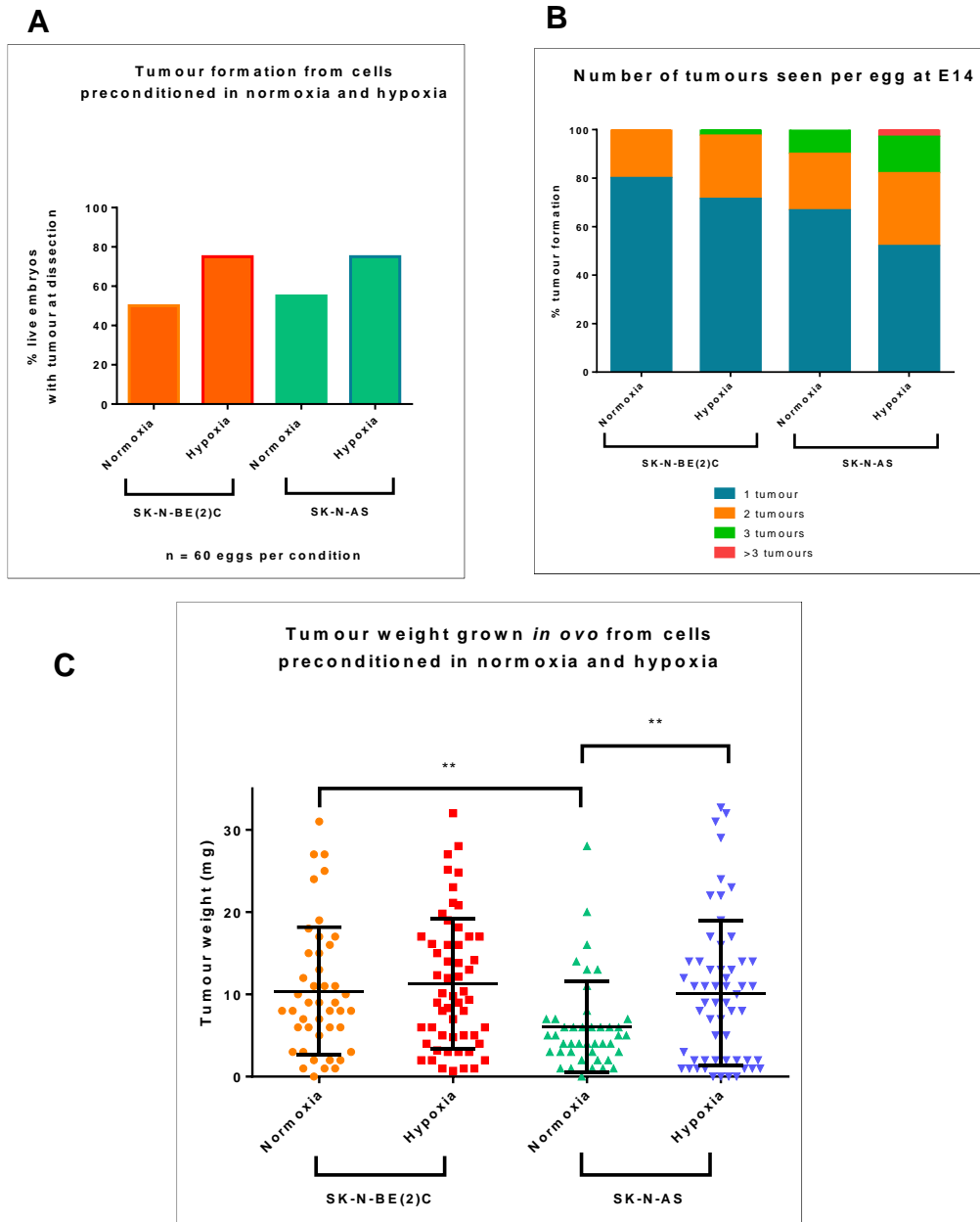
In conclusion, from these *in vitro* data, the most promising compound is CDK1 inhibitor RO3306. RO3306 demonstrated cell cycle arrest in both normoxia and hypoxia cultured cell lines. In addition, the IC50 of the drug is sufficiently low to allow small volumes for treatment, thereby avoiding high concentrations of DMSO for dilution, which will help to dose in the chick embryo. All drugs tested appeared to work in hypoxia but with different efficacies. CDK4/6 inhibitor Palbociclib showed a reduced efficacy in the cells incubated in hypoxia. MTT and FACS analysis showed apparent differences between SK-N-AS and SK-N-BE(2)C cells when treated with CDK4/6 inhibitor Palbociclib. Interestingly, RO3306 seemed to have the same effect on both cell lines and in normoxia and hypoxia.

The next step was to assess the efficacy of the drugs *in vivo* with the chick embryo model.

3.2.2 Assessing the efficiency of neuroblastoma tumour formation on the chorioallantoic membrane (CAM) in the chick embryo model.

The implantation of SK-N-BE(2)C and SK-N-AS cells on the chorioallantoic membrane has already been performed and optimised by Drs Diana Moss and Violaine See's groups in collaboration with Paediatric Surgery led by Professor Paul Losty. (A. Herrmann *et al.*, 2015; Swadi, Pizer, *et al.*, 2018) They also demonstrated a difference in metastatic potential between cells cultured in normoxia and hypoxia before implantation. Fluorescently labelled SK-N-AS cells were cultured under normoxia or hypoxia or treated with the hypoxia mimetic dimethylxaloylglycine (DMOG) before implantation onto the CAM. Cells grown in normoxia were capable of tumour formation at the primary site but not of metastatic invasion; whereas preconditioning in hypoxia for three days led to tumourigenesis as well as metastasis into the chick embryo organs. In this experiment, two million cells precultured in normoxia alone were implanted onto the CAM on embryonic day seven. The eggs were incubated for a further seven days, and the presence of primary tumour formation on the CAM, the number of tumours formed per egg, and the weight of each tumour were recorded (**Figure 3.6**).

Figure 3.6 The formation of neuroblastoma tumours preconditioned in normoxia and hypoxia on the chorioallantoic membrane of the chick embryo model.



Cells were implanted onto the CAM on embryonic day 7 as described in Materials and Methods. Tumours were harvested on embryonic day 14. Sixty eggs were used per condition. The percentage of eggs with tumour(s) were counted and shown in (A). Cells preconditioned in hypoxia are more likely to form tumours. Of the eggs with tumours, the number of tumours seen per egg is shown in (B). A tumour is described as a discrete aggregation of cells beneath the CAM, which when dissected retains its structural integrity. This data is shown as the proportion of eggs with 1, 2, 3, >3 tumours. Each dissected tumour was weighed (C). Unpaired t-test was used to assess for difference in weight between tumour groups. ** = $p < 0.01$.

Preconditioning in hypoxia increased the likelihood of tumour formation in both cell lines. Overall SK-N-AS tumours formed more readily than SK-N-BE(2)C tumours in both normoxia and hypoxia preconditioning groups, but this difference was not significant.

SK-N-AS cells preconditioned in hypoxia formed more tumours per egg and had a higher incidence of multiple tumours. SK-N-AS cells grown in hypoxia will form multiple tumours in almost half of all eggs implanted. Multiple tumours have been counted as more than one tumour growth in a discrete site. The maximum number of separate tumours was four individual tumours seen in 1 egg. In both cell lines, there were eggs where small groups of cells were seen in discrete sites but disintegrated on dissection. These may result from cells being spread across the CAM at the implantation, or these may have become distinct tumour sites with more time. These groups were not counted as formed tumours. The condition least likely to have multiple tumours was SK-N-BE(2)C cells grown in normoxia.

Another important characteristic of tumour formation is the weight of the tumour grown. The weight of tumours is highly heterogeneous. Tumour weights ranged from less than 1 mg to 30 mg. On average, the SK-N-BE(2)C cells grew heavier tumours than SK-N-AS in normoxia: SK-N-BE(2)C: mean=10 mg \pm 7, SK-N-AS: mean=6 mg \pm 5 ($p=0.01$). This difference in weight was not seen for cells precultured in hypoxia: SK-N-BE(2)C: mean=11 mg \pm 7, SK-N-AS: mean=10 mg \pm 8. The SK-N-AS hypoxia group of tumours appears to have two distinct tumour weight groups – a large number above 10 mg (the heaviest recorded is 32 mg) and a cluster of tumours weighing between 1-5 mg. When correlating the data between multiple tumours formed and the size of the tumours, it can be seen that when multiple tumours form within an egg, the overall weight of each tumour is smaller. The SK-N-AS cells appeared to migrate more readily than proliferating and increasing the tumour size in one location of the CAM.

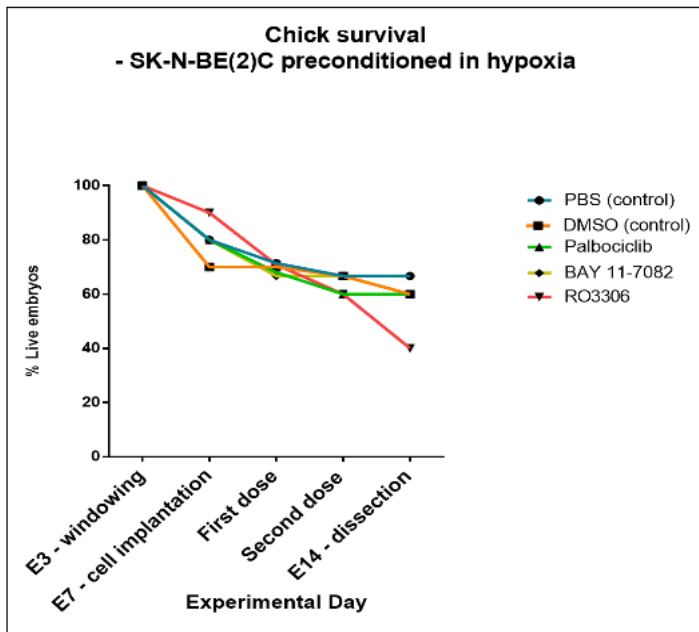
3.2.2.1 Monitoring the chick's survival and growth over time with drug treatment

The drug agents were administered in a two-dose regimen to the embryos. The first dose was given at embryonic day 11 (E11) and the second at E13. The rationale is for sufficient time for the tumour cells to adhere to the CAM and form tumour nodules whilst allowing a long enough duration for the drug therapy to take effect before termination of the experiment at embryonic day 14. The previous optimisation performed by R. Swadi (Swadi, 2018) demonstrated that tumour formation could be seen as early as three days after implantation (embryonic day 10). A two-dose regimen was chosen to reflect the best multiple dosages used in clinical practice. The total number of eggs surviving the two-dose treatment was recorded. The drug's effect on the somatic growth

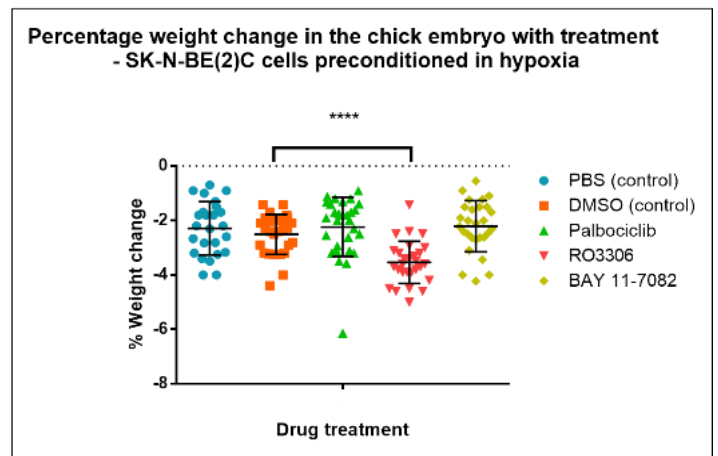
and the embryo's development was assessed through routine weighing of the egg. The difference in weight was calculated as a percentage change and is shown below. (Figure 3.7)

Figure 3.7 The effect of drug treatment on chick survival and somatic development.

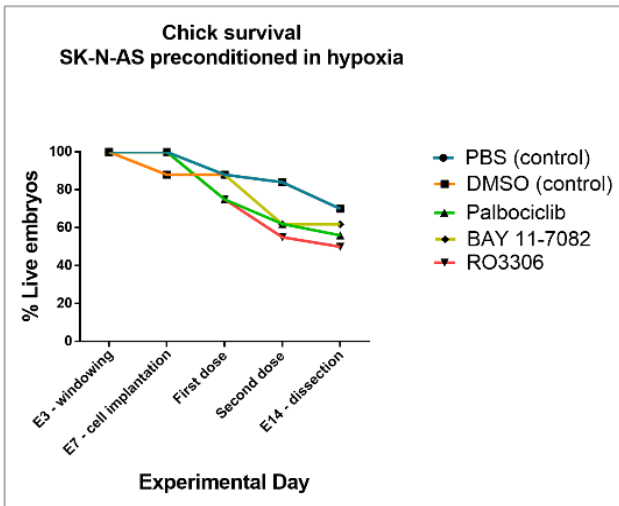
Ai



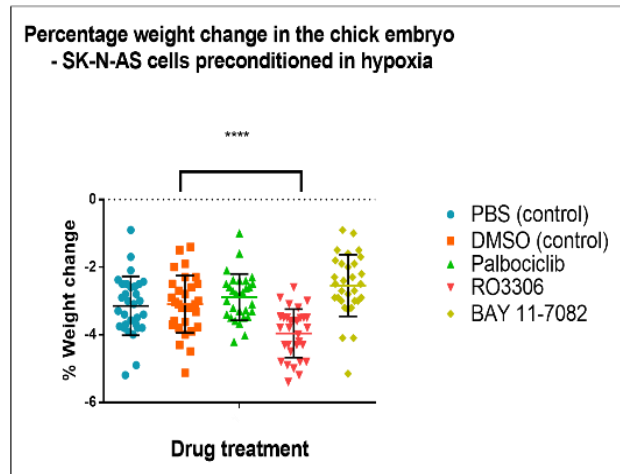
Aii



Bi



Bii



*SK-N-BE(2)C or SK-N-AS cells were implanted as described in methods on embryonic day 7. Drug treatment and the equivalent concentration of vehicle control was administered on embryonic day 11 and embryonic day 13. The chick survival was monitored from E3 onwards. The percentage of live embryos at each recording point is shown. (Ai and Bi) The somatic development was assessed through weight. The percentage change of the weight from before administration of first treatment to end of experiment is shown. (Aii and Bii) Statistical significance in weight was calculated using unpaired T test. Statistical significance is shown as **** = $p < 0.0001$*

There is a natural attrition of egg survival, as shown in **Figure 3.7**. The changes in the ambient temperature and humidity as eggs are removed from the incubator are known to increase chick embryo death. With both cell lines engrafted, the survival of Palbociclib- and BAY11-7082 treated eggs was comparable to the control groups. However, RO3306 showed toxicity and reduced egg survival. There was moisture evaporation from within the egg through the window created in the shell. In the control groups, this weight loss was usually in the order of 2-4% of the total weight of the chick. With Palbociclib and Bay-11-7082, a similar weight loss was measured. However, in the RO3306-treated embryos, the weight loss was more pronounced (3-6%), which was statistically significant compared to the DMSO control. Such weight loss with RO3306 treatment calls into question the suitability of this inhibitor for further testing.

The chick survival and weight loss trends were similar regardless of the cell line engrafted. However, there was a different weight loss upon engraftment of each cell line. The average weight loss for the SK-N-BE(2)C implanted PBS control was -2.2% of the original weight, whereas it was 3.1% for the SK-N-AS. This difference was actual for each experimental group's mean weight loss percentage. This may indicate that the implantation of SK-N-AS cells reduced the chick embryo's growth. As SK-N-AS cells are more likely to form multiple tumours – the cancer burden could be causing a 'cachexia effect' in the overall weight of the chick.

3.2.2.2 Effects of cell cycle and NF- κ B inhibitors on tumour formation of MYC-N amplified, and 11q deleted cells implanted in the chick embryo

There was an approximately 80% tumour formation with both control groups of SK-N-BE(2)C and SK-N-AS cells. As shown previously, SK-N-AS cells preconditioned in hypoxia were more likely to form multiple tumours in the eggs. All drug groups reduced tumour formation, albeit with varying success. (**Figure 3.8** Panel Bi) The presence of a tumour(s) was documented along with the percentage of chick embryos with multiple tumours and the weight of each tumour. **Figure 3.8**) The effect of each drug is now described in turn.

Palbociclib – CDK4/6inhibitor

Both tumour groups were very responsive to Palbociclib. The number of eggs with SK-N-BE(2)C tumours was reduced from, on average, 78% (± 3) to 51% (± 5.6) (**Figure 3.8**Panel Ai) and the

number of eggs with SK-N-AS tumours was similarly reduced from 76%(±3.6) to 55%(±6.1). **Figure 3.8** panel Bi) (SK-N-BE(2)C p=0.0001, SK-N-AS p= 0.0008)

The majority of eggs treated with Palbociclib had one tumour only. Thirty-nine per cent of SK-N-BE(2)C cell implanted eggs within the control arm had more than one tumour, compared to 20% of eggs treated with Palbociclib. (**Figure 3.8** Panel Aii) Similarly, 46% of SK-N-AS cell implanted eggs with control treatment had multiple tumours, compared to 30% of SK-N-AS implanted eggs treated with Palbociclib. (**Figure 3.8** Panel Bii)

In summary, Palbociclib reduced tumour formation in both SK-N-BE(2)C and SK-N-AS groups and reduced the ability of those primary cells to form multiple distant tumours.

Previously we observed that the lowest tumour weights were in the eggs with multiple tumours. In the Palbociclib SK-N-BE(2)C group, the weight of the single tumour was lower than the control, even though most eggs yielded a single tumour. The average weight of control tumours in SK-N-BE(2)C and SK-N-AS implanted eggs was 11mg(±7) and 10mg(±8.8), respectively. The average weight of tumours treated with Palbociclib in SK-N-BE(2)C and SK-N-AS implanted eggs was 7.1g(±5.7) and 10.43mg(±7.3), respectively. There is a statistically significant reduction in tumour weight with treatment with Palbociclib in (SK-N-BE(2)C (p=0.03) but not in SK-N-AS (**Figure 3.8** Panel Aiii and Biii)

RO3306 – CDK1 inhibitor

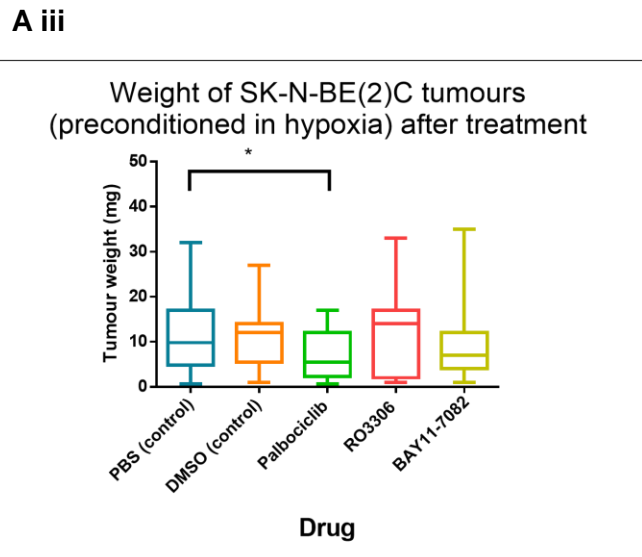
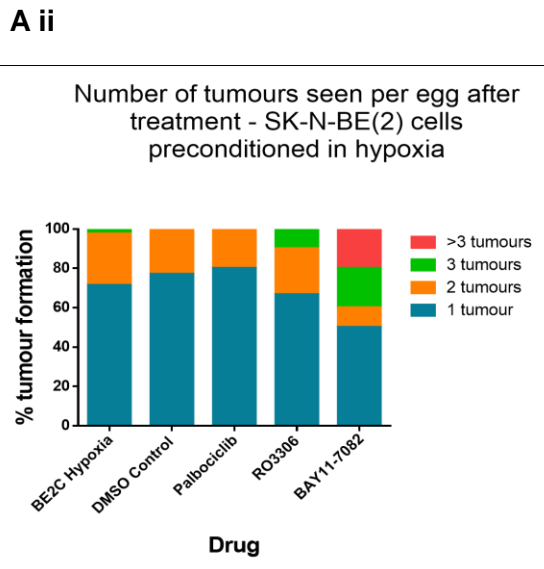
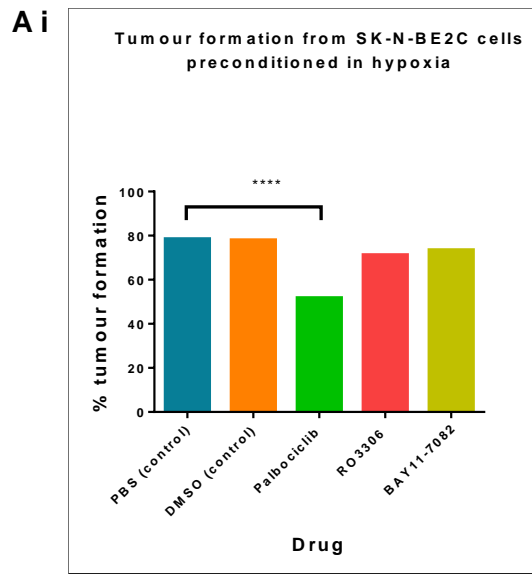
CDK1 inhibitor RO3306 treated eggs showed a reduction in the number of eggs with tumours in both cell lines. However, this reduction was only statistically significant with SK-N-AS cell lines engrafted eggs: SK-N-AS DMSO average tumour formation was 76% (±3.6), SK-N-AS RO3306 average tumour formation 66% (±2.9SD) (p=0.0051). (**Figure 3.8** Panel Bi) Despite reducing the number of eggs with tumours in the SK-N-AS group, there was no change in the weight of the tumours (DMSO mean weight = 15mg (±10) RO3306 mean weight = 12mg (±5) or the number of eggs with more than one tumour on the CAM. (**Figure 3.8** Panel Bii, iii).

Conversely, in the SK-N-BE(2)C tumours, RO3306 had no statistically significant effect on reducing the number of eggs with tumours. Twenty-three per cent of eggs treated with DMSO control had more than one tumour per egg, compared to 33% of eggs treated with RO3306. **Figure 3.8** panel Aii) Overall, it appears as though RO3306 can reduce the formation of tumours, but once formed, it has little impact on the size or the spread of the tumours.

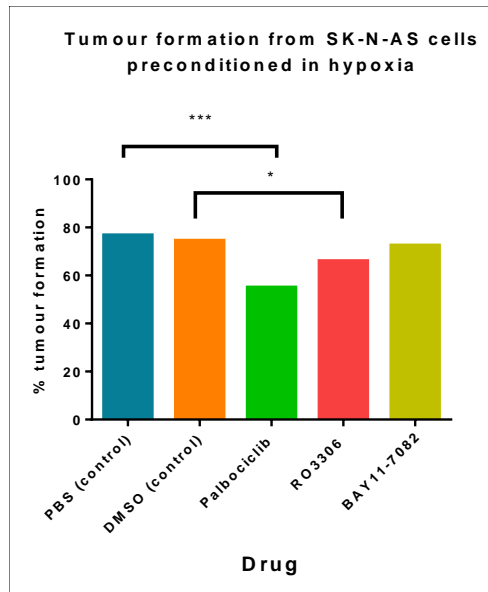
Bay-11-7082 - *NF-KB inhibitor*

NF-KB inhibition *in vivo* appeared to promote multiple tumour formation on the CAM. In SK-N-BE(2)C tumours, 50% of all eggs with tumours had multiple tumours (**Figure 3.8** Panel A ii), and in SK-N-AS tumours, 60% had multiple tumours (**Figure 3.8** Panel B ii). This is consequently reflected in the average weight of these tumours, which was lower in the treated group (SK-N-BE(2)C = 8.6 mg (± 7.8) SK-N-AS = 7.2 mg (± 5) than in the control group (SK-N-BE(2)C = 11 mg (± 8) SK-N-AS 10.2 mg (± 8.8)). The incidence of eggs with tumours remained unchanged between the control and Bay-11-7082 treated groups. (**Figure 3.8** Panel Ai and Panel Bi). Our results highlight the importance of considering multiple factors in assessing new therapeutics: a compound that reduces the size of a tumour but increases the total number of tumours will likely not be beneficial.

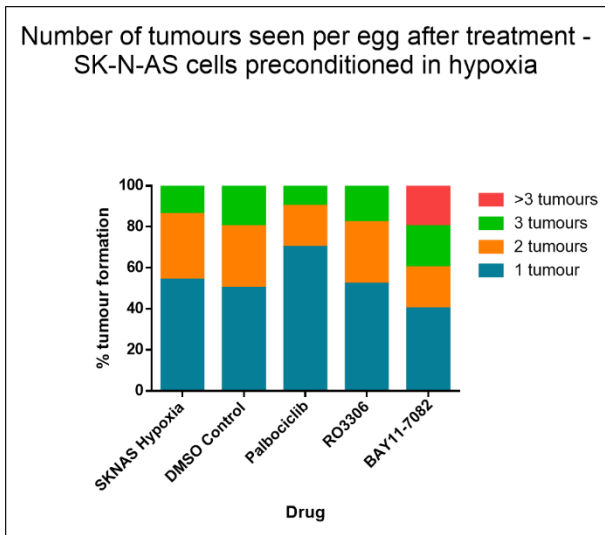
Figure 3.8 The effect of drug treatment on tumour presence, number of tumours formed per egg and the weight of tumours.



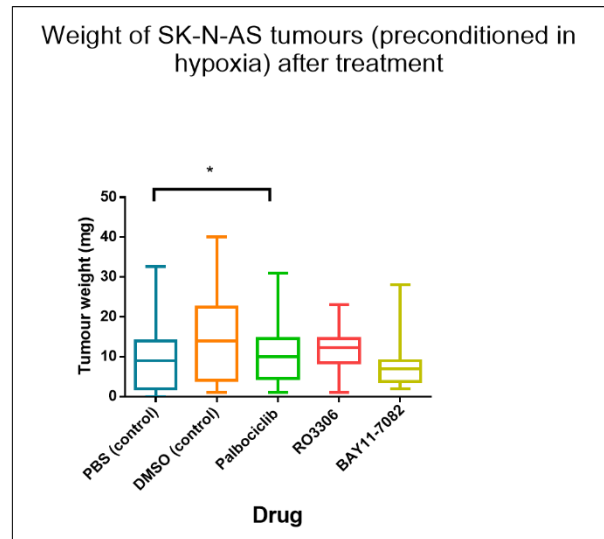
B i



B ii



B iii



The presence of SK-N-BE(2)C (panel A) and SK-N-AS (panel B) is shown as a percentage of eggs with tumours present (A i and B i). The experiment was repeated in 4 separate batches of eggs per cell line. Each batch had 10 eggs for each treatment arm. Of the eggs with tumours, the number of tumours per egg was then counted and is shown in A ii and B ii. The weight of tumours is shown in A iii and B iii. Two tailed unpaired t tests were used to calculate statistical significance. * p<0.05, ** p<0.01 ***p<0.001 ****p<0.0001

Overall, Palbociclib was the only compound which, for both cell lines, reduced tumour formation, number of tumours per egg and weight of tumours. This implied that the drug reduced the size of the primary tumour and the likelihood of satellite tumours forming on the CAM. Although RO3306 was promising *in vitro* compound, when tested *in vivo*, there was no real difference in tumour formation or weight of tumours from the control group. Bay-11-7082 increased the number of tumours formed; consequently, the overall weight per tumour was lower. Going forward, Palbociclib appears to be the best suited *in vivo*, despite not performing convincingly *in vitro*. This further highlights the importance of *in vivo* testing, the characterisation of compounds, and the need for a range of preclinical models for drug testing.

3.2.2.3 Quantifying the effect of CDK4/6 inhibition on the proliferation of neuroblastoma tumours.

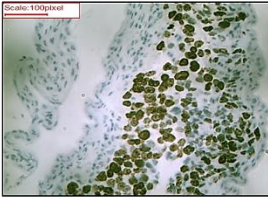
Tumours harvested from control and treated chick embryos were further characterised by immunohistochemistry and stained with haematoxylin and eosin (H&E), Ki67 – a cell proliferation marker. Cells positive for Ki67 staining were counted and are shown below. **(Figure 3.9)** In both SK-N-SK-N-BE (2)C and SK-N-AS cell lines, there was a reduction in cell number and a statistically significant reduction in the number of actively proliferating cells when treated with Palbociclib. (SK-N-BE (2)C 80% control vs 40% treatment and SK-N-AS: 80% control vs 48% treatment).

RO3306 treated tumours were very similar to the control group in terms of cell number and proliferating cells. Bay-11-7082 reduced the weight of the tumours **(Figure 3.8)**, which is reflected in the number of cells seen per high power field in both SK-N-AS and SK-N-BE(2)C cell lines. **(Figure 3.9**Panel A ii and iii, Panel B ii and iii) However, in both groups, although there was a reduction in the number of Ki67 positive cells, this reduction was not significant.

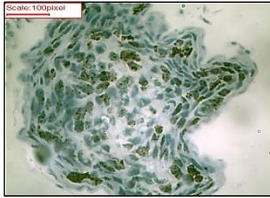
Figure 3.9 Brightfield images of SK-N-BE(2)C (top) and SK-N-AS (bottom) tumour sections at 40x magnification.

SK-N-BE(2)C

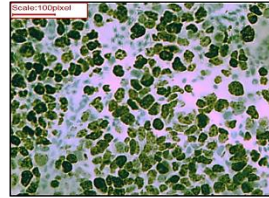
SK-N-BE2C
Control



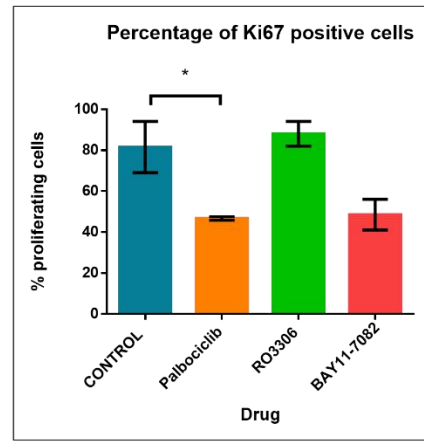
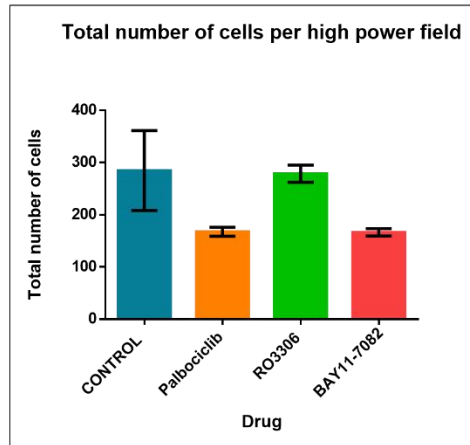
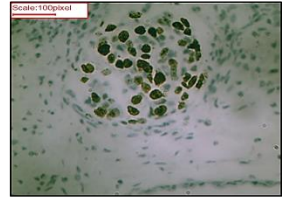
SK-N-BE2C
CDK4/6 inhibitor Palbociclib



SK-N-BE2C
CDK1 inhibitor RO3306

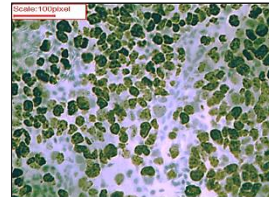


SK-N-BE2C
Nkfb inhibitor Bay11



SK-N-AS

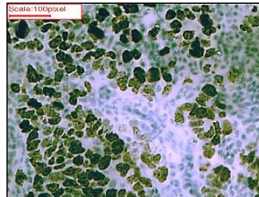
SK-N-AS
Control



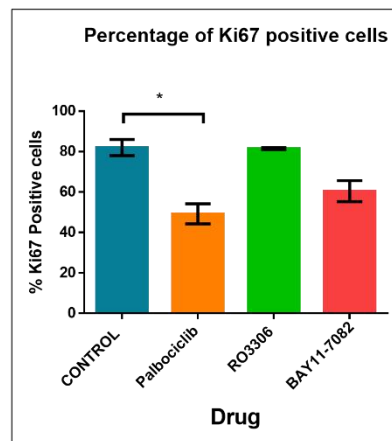
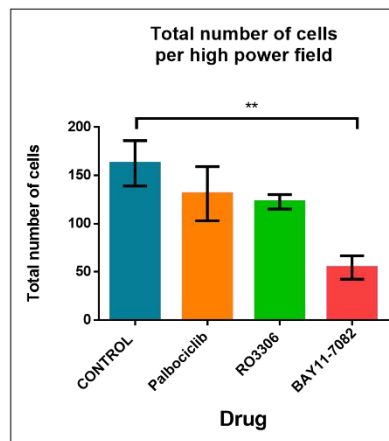
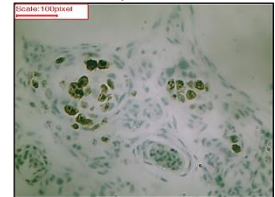
SK-N-AS
CDK4/6 inhibitor Palbociclib



SK-N-AS
CDK1 inhibitor RO3306



SK-N-AS
Nkfb inhibitor Bay11



*Tumours were harvested and fixed in 4% paraformaldehyde. Samples were then processed by Leahurst Veterinary Campus into paraffin sections and stained with haematoxylin and eosin (H&E), Ki67 – a marker of cell proliferation. Each treatment condition included at least two tumours harvested from different eggs as biological replicates. Three sections per tumour were analysed for Ki67 positive staining. Images of tumours were analysed for the total number of neuroblastoma cells present. These were differentiated from chick tissues through size and shape, with chick cells being smaller and more regular in shape. The percentage of Ki67 positive cells was calculated through cell counts. SK-N-BE(2)C (top panel - A) and SK-N-AS (bottom panel - B) results are shown. Ai and Bi) brightfield images of high power fields in each condition. Aii and Bii) Total number of cells per high power field shown. Aiii and Biii) Total number of Ki67 positive cells as a percentage of total cells shown. Statistical significance was calculated using unpaired t test. * $p < 0.05$, ** $p < 0.01$.*

3.3 Discussion

In this chapter, I have demonstrated the ability of cell cycle inhibitors to halt neuroblastoma cell growth and highlighted the differences in the efficacy of cancer therapy *in vitro* and *in vivo*.

3.3.1 The potential of CDK4/6 inhibition in NB

Around 30% of all neuroblastoma exhibit mutations in the genes which regulate the G1 checkpoint in the cell cycle. (Molenaar, Koster, *et al.*, 2012). Array-based data have shown that cyclin D1 expression is 3–8 times higher in neuroblastoma tumours than in libraries of 18 other common malignancies. Amplification of CDK4, CDK6 and deletion of CDKN2A is also commonly seen. (Molenaar *et al.*, 2008) For clinical correlation, patient tissue analysis has shown that high levels of CDK4 expression are associated with a poor prognosis, and CDK6 expression is correlated with undifferentiated histology, which in turn is associated with a poor prognosis. (Molenaar, Koster, *et al.*, 2012). Palbociclib is a selective CDK4/6 inhibitor that suppresses the cyclin D1-pRB pathway through the inhibition of phosphorylation of Rb and the downregulation of E2F target genes. As cyclin D activation is crucial to cell cycle progression, and most neuroblastoma cells are known to have higher expressions of cyclin D, we did not expect a difference in response to therapy between the two cell lines. However, the more sensitive line to Palbociclib was the MYC-N amplified SK-N-BE(2)C cells. In normoxia, these cells exhibited a dose-dependent cell death with IC50s comparable to other studies. (**Error! Reference source not found.**) (Rihani *et al.*, 2015). Similarly, when examining the drug's effect on the cell cycle, SK-N-BE(2)C cells responded more significantly, with a higher proportion of cells arrested in G0 after Palbociclib treatment

(Error! Reference source not found.). This has been shown previously in the literature. CDK4, CDK6 and CCND1 are all amplified or overexpressed in neuroblastoma cell lines. However, there are significantly higher levels of RB phosphorylation observed in MYC-N amplified cell lines than in non-MYC-N amplified cell lines. (Whittaker *et al.*, 2017) This difference may make SK-N-BE(2)C more sensitive to CDK4/6 inhibition than SK-N-AS. Others have also shown that 11q deleted cells, like SK-N-AS cells, do not respond to cell cycle inhibition through CDK4/6. Rihani *et al.* demonstrated this by examining the effect of cyclin D knockdown in several neuroblastoma cell lines. A great deal of heterogeneity in the impact of cyclin D knockdown on neuroblastoma cells was seen. SK-N-BE(2)C cells showed a 30% reduction in proliferation, and although SK-N-AS was not examined, other similar non-MYC-N amplified cell lines exhibited no change in cell proliferation. (Rihani *et al.*, 2015) Rader *et al.* have also shown that MYC-N amplified cell lines are more sensitive to CDK4/6 inhibition than MYC-N non-amplified lines, and interestingly there was no cell cycle arrest when SK-N-AS cells were treated with Ribociclib, another CDK4/6 inhibitor. (Rader *et al.*, 2013). This data demonstrates that pRB, CDK4, CDK6 or cyclin D status alone cannot be used to predict sensitivity to CDK4/6 inhibition, and perhaps in SK-N-AS cells, there is an alternative pathway of proliferation that does not rely solely on cyclin D activity. One possible explanation in sensitive cell lines is FOXM1-mediated cell senescence causing cytostasis in neuroblastoma. FOXM1 transcription factor promotes self-renewal and is a known target of CDK4/6 signalling. This dependence of FOX1M signalling for self-renewal is not seen in MYC-N non-amplified lines, where FOX1M levels remain unaltered with CDK4/6 inhibition. (Wierstra and Alves, 2006; Anders *et al.*, 2011; Wang *et al.*, 2011) An alternative pathway of symbiosis between cyclin D overexpression and MYC-N can be seen through MYC-N inhibition of glycogen synthase kinase 3b (GSK-3b) which in turn is involved in the degradation of cyclin D1 and other MYC-N proteins. (Huang and William A Weiss, 2013)

CDK4/6 inhibition in cancer is best characterised in breast cancer. Endocrine therapy was previously thought to be the gold standard in management, but the development of inhibitors of CDK4/6 has augmented its use. When CDK4/6 inhibitors are given in combination with ET, there is an approximate doubling of progression-free survival (PFS) associated with their use in advanced or metastatic hormone receptor-positive (HR+), human epidermal growth factor receptor-2 (HER2) negative breast cancers. Multiple large clinical trials have been performed with the three commercially available CDK4/6 inhibitors: Palbociclib, Ribociclib and Abemaciclib:

PALOMA-2 (Finn *et al.*, 2016) for Palbociclib plus letrozole; MONALEESA-2 (Hortobagyi *et al.*, 2016) for Ribociclib plus letrozole and MONARCH-3 (Goetz *et al.*, 2017) for Abemaciclib plus letrozole or anastrozole. Trilaciclib, a novel CDK4/6 inhibitor, has recently been approved in combination with chemotherapy for extensive-stage small cell lung cancer (SCLC). (FDA Approves Drug to Reduce Bone Marrow Suppression Caused by Chemotherapy, no date) However, what is emerging is *de novo* or acquired resistance to CDK4/6 inhibitors, with an, as yet, unknown mechanism of resistance. Hypothesis includes loss of retinoblastoma susceptibility gene product (Rb) Function. Understanding the long-term effects of CDK4/6 inhibition in well-established clinical practice is important before implementing its use in neuroblastoma.

3.3.2 CDK1 inhibition in NB

Another checkpoint that is altered by MYC-N amplification is CHK1. CHK1 phosphorylates WEE1, which inhibits the action of CDK1 at the G2/M level. It is postulated that this is one of the mechanisms through which neuroblastoma becomes resistant to chemotherapy. (Cole *et al.*, 2011) It was hypothesised that the inhibition of CDK1 directly may inhibit the unregulated progression through G2/M of MYC-N amplified neuroblastoma cells. Interestingly, both cell lines were sensitive to CDK1 with similar IC50 values, and the hypoxic environment did not affect this sensitivity. (SK-N-BE(2)C: 6.6 μ M, 4.7 μ M and SK-N-AS 4.9 μ M and 4.9 μ M in normoxia and hypoxia, respectively). SK-N-AS cells were also responsive to CDK1 cell cycle inhibition, as shown by the FACS experiments (**Figure 3.3**), with a significant change in cell number arrested in G2/M in both normoxia ($p < 0.001$) and hypoxia ($p = 0.05$) as compared to the control. Interestingly unlike with CDK4/6 inhibition, there was no difference in sensitivity between hypoxia and normoxia, nor a significant difference between the two cell lines.

Kang *et al.* investigated the differential sensitivity to CDK1 inhibition in breast cancer lines. They showed that sensitivity to the drug was not dependent on CDK1 levels in the cells, as this was similar across all cell lines, but instead on the interaction between lethal synthetic interaction MYC-N and CDK1. (Kang *et al.*, 2014) They postulate that as CDK1 is essential for cell division in all cell types, the inhibition of CDK1 causes increased mitotic stress, which induces MYC-N modulated replication stress resulting in cell death. (Goga *et al.*, 2007) Therefore cells with increased MYC-N activation may be more vulnerable to CDK1 inhibition. We can question why the non-MYC-N amplified SK-N-AS was so sensitive to CDK1 inhibition. Although SK-N-AS is not classed as an MYC-N amplified cell line, MYC-N is still overexpressed within the cells, which may

be enough to infer susceptibility. Chen et al. examined the effect of CDK1 inhibition on two neuroblastoma cell lines, one with increased MYC-N expression such as SK-N-AS and an SK-N-BE(2)C progeny with MYC-N amplification. The CDK1 inhibition resulted in complete loss of MYC-N expression within 4 hours in both neuroblastoma cells. (Chen, Y. H. Tsai and Tseng, 2013) This loss of MYC-N may make both cell lines equally susceptible and align with our results. Conversely, Schwermer et al. have shown that the sensitivity to RO3306 CDK1 inhibitor was not explained by the MYC-N status but by the p53 status of the cells. (Schwermer *et al.*, 2015) SK-N-AS cells are known to have aberrantly expressed p53, which may explain the cell's susceptibility to CDK1 inhibition, where CDK4/6 inhibition had little impact on cell cycle progression. (Nakamura *et al.*, 2007)

However, as promising as the *in vitro* results were, the most rigorous preclinical test of any targeted therapeutic strategy is the ability to block tumour growth *in vivo*. CDK1 inhibition in the chick embryo was not well tolerated by the developing embryo, with a statistically significant reduction in survival and weight. Santamaria et al. showed that although CDK1 has the potential to compensate for the loss of other CDKs when CDK1 itself was knocked out, there were no viable mice embryos seen. (Santamaría *et al.*, 2007). Goga et al. found no toxicity of RO3306 when testing in adult mice models, except for local inflammation at the injection site. (Goga *et al.*, 2007) This further highlights the need to test new compounds to treat paediatric conditions in models with high cell turnover. The high cell turnover within an embryonal system such as the chick embryo may be more sensitive to CDK1 inhibition, so although CDK1 is an attractive target as it is essential for tumour cell proliferation, *in vivo* inhibition displays a toxic effect which abrogates its clinical utility in paediatric cancer.

Currently, no inhibitors specific to only CDK1 are used in clinical practice. Pan CDK inhibitors such as TG02, a novel oral inhibitor of CDK1, CDK2, CDK7 and CDK9, and AT7519, a potent pan-CDK inhibitor of CDK1, 2, 4, 6 and 9, have shown promise in Phase I clinical trials against multiple myeloma (Ponder *et al.*, 2016), and refractory solid tumours (Chen *et al.*, 2014), respectively. This may reflect the lethality of selective CDK1 inhibitions, and combined pan inhibitors may provide a less toxic treatment strategy moving forward.

3.3.3 Tumour hypoxia and its role in NB development

Preconditioning neuroblastoma cells in hypoxia increases primary tumour formation and also the number of metastasis. (A Herrmann *et al.*, 2015) Here I have demonstrated that the preconditioning of neuroblastoma cells increases the likelihood of tumour formation on the CAM and the number of primary tumours within each egg. Hypoxia plays a role in multiple cancer cell lines' epithelial to mesenchymal transition. EMT upregulation increases collective cell migration and the formation of secondary tumour sites. (Saxena, Jolly and Balamurugan, 2020) There is a differential response to hypoxia preconditioning between the cell lines. SK-N-AS cells preconditioned in hypoxia are more likely to form multiple tumours on the CAM than the MYC-N amplified counterparts. Population studies have shown that the clinical course of 11q deleted neuroblastoma is longer, with multiple relapses and poor overall survival. Even when compared to MYC-N amplified tumours, known to have a poor prognosis, patients with 11q deleted tumours were seen to have higher rates of relapse and lower rates of event-free survival. (J Ribelles *et al.*, 2019). Although the primary tumours from both cell lines are of similar weight in both cell lines, in those eggs where multiple tumours were seen, the overall weight of the tumours was smaller. To extrapolate this into clinical practice, if there is a more undetected widespread disease that may escape the sensitivity of current imaging and diagnostic modalities, this could explain the recurrent relapses seen in 11q deleted neuroblastoma tumours. In addition, chick embryos with multiple tumours had a lower overall weight than those with single primary tumours, so multiple disseminated tumours are seen to have a more significant cancer burden and impact the overall growth and development of the chick embryo.

3.3.4 Cross-talk between hypoxia and CDK and NF- κ B signalling

Hypoxia is known to play a key role in the proliferation and metastasis of neuroblastoma. (Vega *et al.*, 2020a) As *intra-tumoral* oxygen tension is not regularly maintained at 21%, it was necessary to appropriately assess the efficacy of the drugs in a more physiologically representative environment. The cell survival and cycle progression experiments were repeated in 1% oxygen. Hypoxia induces a greater resistance to the CDK4/6 inhibitors in both cell lines, more markedly in SK-N-BE(2)C (IC₅₀ 9.6 μ M in normoxia compared to 22.8 μ M in hypoxia.) (Error! Reference source not found., Error! Reference source not found., Error! Reference source not found.). This could be explained by the reduced metabolic activity of cells in hypoxia, which in turn may lead to reduced uptake of the drugs through the surface transporters, so higher concentrations are needed for similar IC₅₀. (Donovan *et al.*, 2010). When Strese *et al.* screened 19 chemotherapeutics against different cell lines in normoxia and

hypoxia, it was seen that the sensitivity of the cells to the drugs varied greatly with oxygen levels. (Strese *et al.*, 2013) I have demonstrated a similar phenomenon here, so screening in different oxygen tension is essential when assessing the suitability of a drug.

When exposed to low oxygen conditions, FACS data reveals that SK-N-BE(2)C cells have lower live cell counts than SK-N-AS, and a greater number of cells are present in the sub-G0 phase of the cell cycle. (black arrow **Error! Reference source not found.** and **Figure 3.3**). This sub G0 is usually associated with DNA fragmentation secondary to apoptosis. This peak is seen only in SK-N-BE(2)C cells and not in the SK-N-AS cells and is not affected by the addition of Palbociclib, RO3306 or Bay-11-7082. The relationship between hypoxia, MYC-N amplification and neuroblastoma cell proliferation is unclear. Research suggests that MYC-N amplification stabilises hypoxia-inducible factor 1 (HIF-1), which drives the high proliferation of cells. (Zaatiti *et al.*, 2018b) If this is the case, then the increased number of sub-G0 cells, supposedly undergoing apoptosis, may be partly due to a sparsity of physical space, distribution of nutrients and removal of waste products (with a successful change in pH) caused by higher cell turnover. Several other studies have associated high levels of MYC-N with increased sensitivity to apoptosis in hypoxia. Proposed mechanisms have included interaction with interferon-gamma, increased TNF and TRAIL, and activation of the CD95 pathway. (Rössler *et al.*, 2001b)

As CDK4/6 inhibition in hypoxia seemed less effective in both cell types, we did not expect an improvement with treatment *in vivo*. Unexpectedly, however, when testing the chemotherapies *in vivo*, Palbociclib treated systems had the lowest rate of tumour formation and the smallest tumours. In addition, histology showed that the rate of actively proliferating cells, as measured by Ki67 positive cells, was also the lowest compared to control and other drugs. (**Figure 3.9**) This highlights the importance of different models for drug screening.

Most studies exploring the relationship between NF-KB and hypoxia in cancer cells show a reduction in apoptosis when NF-KB is activated. (Ortmann, Druker and Rocha, 2014). Our work here supports this as it demonstrates that cells are more sensitive to NF-KB inhibition in hypoxia – IC50 for SK-N-BE(2)C cells treated with Bay-11-7082 in normoxia is 5µM and in hypoxia is 1µM. However, at a lower dose, as was used in the cell cycle experiments, NF-KB did not affect cell cycle progression in either of the cell lines. Hypoxia-induced NF-KB activation has also increased the expression of proteins essential for angiogenesis and cell migration. (Zhi, Duan, Zhou, Yin, Ge Guan, *et al.*, 2014)(Yin *et al.*, 2013)(Li *et al.*, 2013) Inhibition of NF-KB in the chick embryo

demonstrated the opposite, displaying increasing numbers of tumours at distant CAM sites compared to the control.

Together these findings highlight the importance of multimodal drug screening in treating heterogenous cancer such as neuroblastoma. The differences in response from cell line to cell line and the impact of hypoxia on the cells' sensitivity are all factors that must be considered to identify successful therapies. The results from this study demonstrate that Palbociclib has an acceptable safety profile and efficacy in treating primary neuroblastoma tumours. Given the significant effect of hypoxia on these cell types, further studies of Palbociclib in combination with other agents, such as HIF inhibitors, may yield promising results and will be explored in the next chapter.

Chapter 4 : Assessing the effect of HIF-2 α inhibitor, PT2385, on neuroblastoma metastasis, alone and in combination with CDK4/6 inhibition

4.1 Introduction

4.1.1 The role of HIF-2 in neuroblastoma

Pahlman et al. found that when human neuroblastoma cell lines, SK-N-BE(2)C and SH-SY5Y, were exposed to hypoxia (defined as 1% O₂) for 72 hours, there was an induction of genes associated with cell growth, survival and resistance to treatment. (Jögi *et al.*, 2004) There is a differential response in the activation kinetics and the expression of the two most well-studied hypoxia-inducible factors. Whilst HIF-1 α stabilises rapidly in response to acute hypoxia, HIF-2 α is generally expressed after prolonged exposure to hypoxia. (Holmquist-Mengelbier *et al.*, 2006). HIF-1 α and HIF-2 α are also differentially recruited to target genes in neuroblastoma in response to hypoxia. (Khong and Malcomson, 2015). HIF-2 α is associated with a more aggressive and chemoresistant phenotype in neuroblastoma than HIF-1 α . There have been several examples of this; 1) HIF-2 α overexpression is closely correlated with stemness maintenance in the neuroblastoma cell population, a characteristic associated with poor outcomes. This has been confirmed as the knockdown of the *EPAS1/HIF2 α* gene results in a more differentiated tumour phenotype. (Pietras *et al.*, 2009a) Cancer stem cells (CSC) are more resistant to DNA damage through chemo- and radiotherapy, enabling them to better survive and proliferate despite treatment. 2) Co-localisation between areas of high HIF-2 α expression and VEGF within clinical neuroblastoma samples (Holmquist-Mengelbier *et al.*, 2006), suggesting a contribution of HIF-2 α in neuroblastoma angiogenesis.

Given this evidence in neuroblastoma and also other similar observations in different tumour types, HIF-2 α inhibitors have been developed and trialled for cancer treatment

4.1.2 Hypoxia, the neural crest and neuroblastoma

As cancer cells rapidly divide and grow into tumours, an oxygen gradient develops across the solid tumour. However, this is not a linear relationship, as most solid tumours demonstrate a heterogenous milieu of poorly oxygenated and better-oxygenated areas. The cellular response to the low oxygen conditions (hypoxia) has been linked to many cancers' development, progression, metastasis and resistance.

The neural crest, the precursor cells to neuroblastoma, is a population of multipotent embryonic cells with a vast migratory potential, which has been compared to that of malignant invasion of cancer cells. (Kulesa *et al.*, 2006)(Hendrix *et al.*, 2007; Kuriyama and Mayor, 2008) Even in the

earliest stages of physiological development, a hypoxic environment plays a crucial role in developing, migrating, and differentiation of the neural crest stem cells. In clinical studies, conditions that may exacerbate hypoxia in the foetus, such as maternal anaemia and fetal haemolytic disease, have also been postulated to increase the risk of neuroblastoma. (Bluhm *et al.*, 2008). Several studies have described the effect of exposure to low oxygen pressures *in vivo* models.

In the chick embryo, hypoxia has been shown to regulate the number of migrating neural crest cells early in embryogenesis. (Scully *et al.*, 2016) In rat neural crest stem cells, hypoxia promotes proliferation and the expression of genes involved in migration, such as SNAIL2, SOX10 and C-X-C chemokine receptor type 4 (CXCR4). (Chen *et al.*, 2017b) Neuroblastoma cells respond to low oxygen levels by triggering a transcription response controlled primarily by HIF-1 and HIF-2 α . Dysregulation of HIF-2 α has been linked with the malignant transformation of neural crest cells resulting in increased numbers of sympathetic cells and dysfunctional cells within the adrenal medullary and carotid bodies. (Bishop *et al.*, 2008). Another link between hypoxia, neural crest development and neuroblastoma is the frizzled class receptor 6 (frizzled-6) of the Wnt pathway, responsible for neural cell induction, which is also highly expressed within hypoxia areas in neuroblastoma tumours. (Cantilena *et al.*, 2011)

4.1.3 HIF-2 α inhibition.

Inhibition of HIF-2 α is, therefore, an attractive therapeutic venture for neuroblastoma. When the differentiation agent, all-trans-retinoic acid, is combined with HIF-2 α silencing, there is an increased expression of differentiation markers within glial cells. When HIF-2 α alone is silenced, increased cell senescence in glioma is also observed. (Cimmino *et al.*, 2015) Direct inhibition of HIF-2 α is now possible through the small molecule antagonist PT2385. Currently being tested in clinical trials against renal cell cancer and glioblastoma and demonstrating positive early results (Courtney *et al.*, 2020), The interest in small molecule inhibitors of the HIF pathway has increased over the past two decades.

PT2385 is also synergistically lethal against clear cell renal cancer when combined with a CDK4/6 inhibitor. (Nicholson *et al.*, 2019) Our previous work demonstrated that Palbociclib efficiently reduced primary tumour formation *in vivo*. We, therefore, explored in this chapter the potential for HIF-2 α inhibition with PT2385 alone and in combination with Palbociclib in reducing neuroblastoma growth, both as primary tumours and metastasis into the chick embryo. The PT2385 inhibitors were received thanks to a collaboration with Arcus Biosciences.

We specifically tested

- The effect of HIF-2 α inhibition on the growth and cell cycle of neuroblastoma cells *in vitro*
- The effect of HIF-2 α inhibition on genes regulated by hypoxia and promoting malignancy
- The ability of HIF-2 α inhibitors to reduce primary and metastatic tumour growth *in vivo*.

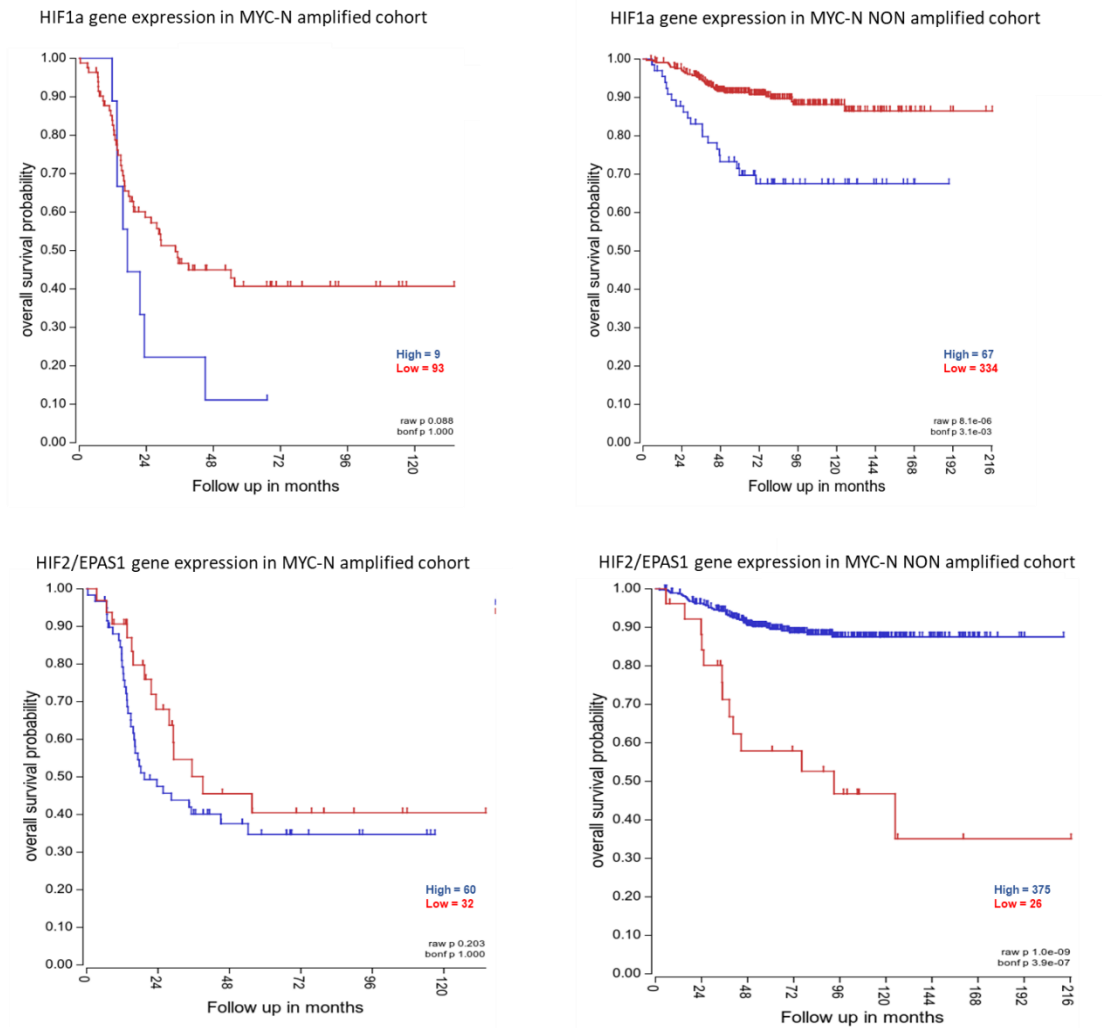
4.2 RESULTS

4.2.1 Correlation of *HIF-1α* and *HIF-2α* expression with clinical outcomes of neuroblastoma patients

To assess the impact of HIF expression on neuroblastoma patients' clinical outcomes, we used an online onco-genomic analysis platform: R2. R2 is an 'omic' database with interactive tools allowing analysis and visualisation, including correlation between genes, differential expression, generation of heatmaps of grouped samples and construction of Kaplan Meier graphs. It has been cited in over 850 peer-reviewed scientific publications.

Here we selected a single dataset – Cangelosi and 'Kaplan Meier by gene expression to assess the overall outcome for patients with overexpression of *HIF-1α* and *HIF-2α*. The Cangelosi database combines data from 1882 neuroblastoma human tumour specimens covering the entire spectrum of the disease from four publicly available data sets (RNA-seq498, Assymetrix413, Agilent709, and Agilent262. Previously large-scale expression data of neuroblastoma tumours were unavailable due to the differing technologies and proprietary annotations used to identify transcripts. This data seeks to merge to provide many gene expression profiles to allow risk stratification. The database has been validated in a peer-reviewed publication. (Cangelosi *et al.*, 2020). The expression data were further divided by MYC-N amplification/non-amplification, and the metric shown henceforth is 'overall survival.'**(Figure 4.1)** In patients with MYC-N amplified disease, *HIF-1α* and *HIF-2α* overexpression is associated with a lower overall survival probability. In MYC-N non-amplified disease, *HIF-1α* overexpression is associated with worse overall survival. However, *HIF-2α* overexpression confers a better overall survival in the MYC-N non-amplified cohort. The survival is longer in the MYC-N non-amplified group. The division of the patients into MYC-N amplified, and non-amplified may be simplistic. The non-amplified group will undoubtedly be heterogenous and include patients with the low-grade disease. This may be reflected in the expression data outcomes.

Figure 4.1 Kaplan Meier survival plots to show the impact of overexpression of HIF1 and HIF-2 genes on overall survival.

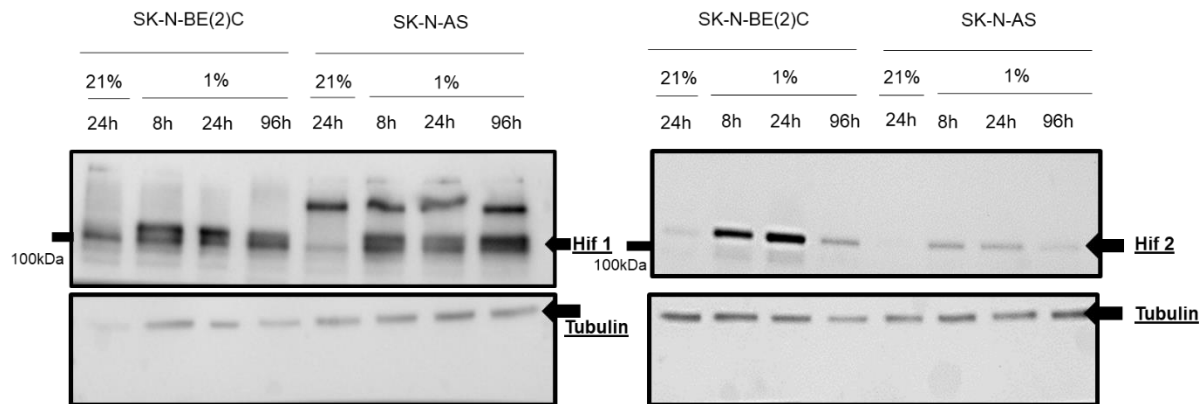


Using the neuroblastoma Cangelosi patient data-sets in the R2 Genomics Analysis and Visualisation platform (<http://r2.amc.nl>), patients were divided by high (blue) and low (red) HIF-1 and HIF-2/EPAS1 gene expression groups by median centred Log2 ratios and the survival curves were generated. With the exception of HIF-2 overexpression in non MYCN amplified tumours, HIF overexpression is associated with lower overall survival. The impact of HIF-1 and HIF-2 overexpression in MYCN amplified tumours is unclear, as although the raw p values are significant ($p < 0.05$), they are equal to 1 after a Bonferroni correction. HIF-2 overexpression is associated with better outcome in MYCN non-amplified cohort ($p = 1e-9$, bonf $3.9e-07$)

4.2.2 Evaluation of Hypoxia-Inducible Factors levels in SK-N-BE(2)C and SK-N-AS cell lines.

To assess the presence of HIF proteins in our cell lines of interest, before treatment, SK-N-BE(2)C and SK-N-AS cells were incubated in 21% O₂ (referred to as 'normoxia henceforth) and 1% O₂ (referred to as hypoxia henceforth) for 96 hours and HIF-1 α and HIF-2 α proteins were detected using a western blot assay. (Figure 4.2)

Figure 4.2 HIF-1 α and HIF-2 α protein expression in normoxia and hypoxia



Western blot analysis of HIF expression in SK-N-AS and SK-N-BE(2)C cells cultured for indicated times under hypoxia (1% O₂) and normoxia (21% O₂) oxygen conditions. Tubulin was used as a loading control. HIF-1 α is present in both cell lines in normoxia and hypoxia at all time points. Conversely, HIF-2 α is not seen in normoxia in either cell line after 24 hours. HIF-2 protein levels are shown to decrease over time in both SK-N-BE(2)C and SK-N-AS cell lines. The higher bands in HIF1 blot represent post-translational modifications.

HIF-2 α was not seen in normoxia in either cell line. In both neuroblastoma cell lines, HIF-2 α stabilisation was induced after 8 hours of hypoxia and maintained for 24 hours. However, SK-N-BE(2)C cells had notably increased expression compared to the SK-N-AS cells. After prolonged hypoxia (96 hours), HIF-2 α degraded in both cell lines. HIF-1 α was selectively stabilised in normoxia and was still present after prolonged exposure to chronic hypoxia. The induced HIF-1 α band in the SK-N-BE(2)C cells may be running lower than the SK-N-AS HIF-1 α band; in the SK-N-BE(2)C blot, two bands are running closely together in hypoxic conditions, whereas the induced band in SK-N-AS cells is running higher.

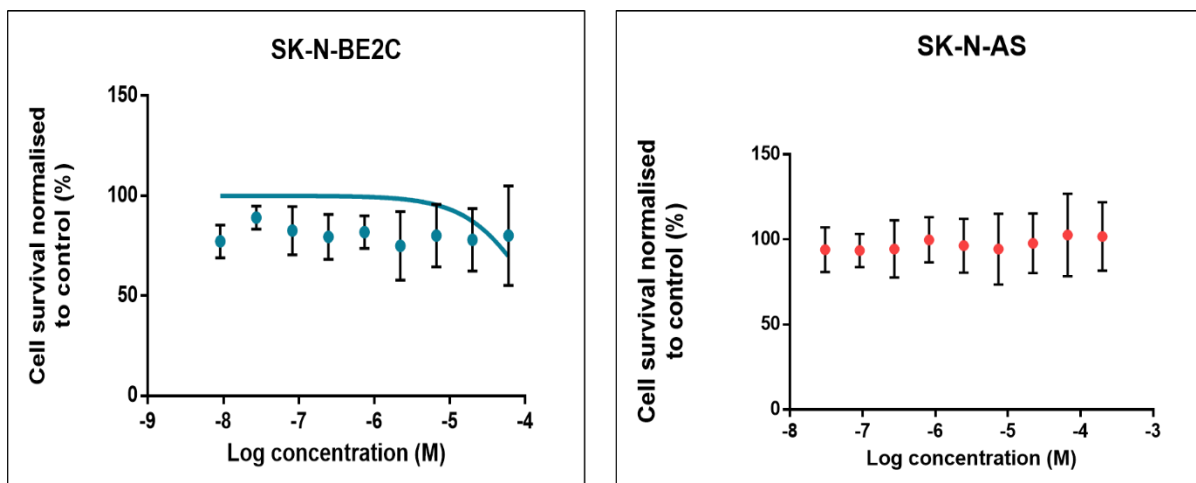
Qing et al. describe a differential expression of HIF proteins, conversely, with a greater expression of HIF in cells with a single copy of MYC-N. (Qing *et al.*, 2010) Mohlin et al. further investigating this claim echoed our results and showed that HIF-2 α was more highly expressed in MYC-N amplified tumours in neuroblastoma tumours. Contrary to other reports (Qing *et al.*, 2010), we found that HIF-2 α levels reduced between 24 and 96 hours. The 'prolonged' hypoxia was up to 72 hours in the papers reviewed, compared to 96 hours shown here. Therefore, this data may reflect what occurs after the 72-hour cut-off. There may also be variability in the cell lines and antibodies used in the experiments leading to differing conclusions.

After confirming the presence of inducible HIF-2 α within both cell lines in hypoxia, the effect of synthetic inhibition of HIF-2 α transcription was assessed.

4.2.3 The effect of PT2385 on neuroblastoma cell survival

Firstly, the viability of neuroblastoma cells in the presence of the HIF-2 α inhibitor PT2385 was examined using an MTT assay. Cells were preconditioned in hypoxia for 72 hours before drug application. They were incubated with the drug for 48 hours in hypoxia before assessing viability.

Figure 4.3 Dose response curves of SK-N-AS and SK-N-BE(2)C treated with PT2385 alone.



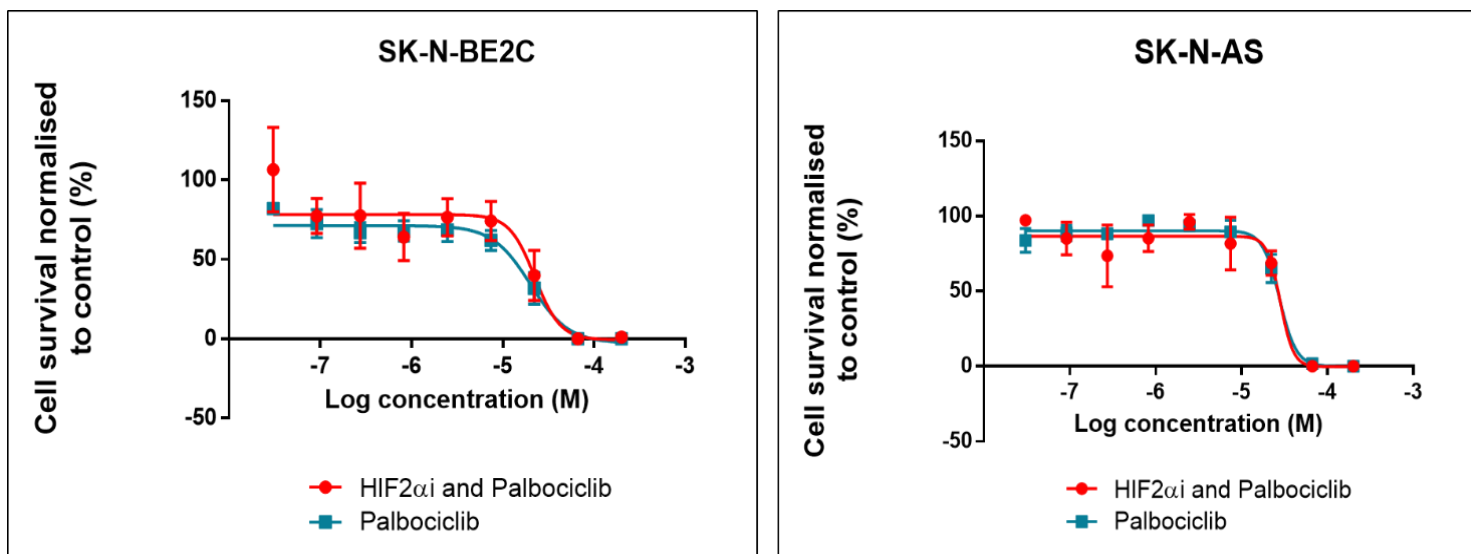
Half- log serial dilutions of HIF-2 α inhibitor PT2385, starting from 100 μ M were applied to SK-N-AS and SK-N-BE(2)C cells that had been preconditioned in hypoxia for 3 days. Data were normalised to DMSO control.

Figure 4.3 shows no significant difference in cell viability for any cell type when treated with PT2385 over 48 hours.

4.2.4 The effect of PT2385 and Palbociclib in combination

Next, I tested the combination of drugs targeting HIF-2 α and CDK4/6 on cell viability. As shown in **Error! Reference source not found.** cell survival decreased dose-dependent upon Palbociclib treatment. In combination with PT2385, we observed no synergistic effect, with the IC₅₀ of both drugs reflecting the inhibitory effect of Palbociclib alone. (**Figure 4.4**) The IC₅₀ of Palbociclib alone was 28 μ M and 23 μ M for SK-N-AS and SK-N-BE(2)C, respectively, and the IC₅₀ of both drugs together was 27 μ M and 20 μ M for SK-N-AS and SK-N-BE(2)C, respectively.

Figure 4.4 Dose-response curves of SK-N-BE(2)C and SK-N-AS treated with PT2385 and Palbociclib



Half- log serial dilutions of PT2385 alone and in combination with Palbociclib were applied to SK-N-AS and SK-N-BE(2)C cells that had been preconditioned hypoxia for 3 days. The drugs were administered and the cells and drug incubated for a further 2 days. Data was normalised to DMSO control.

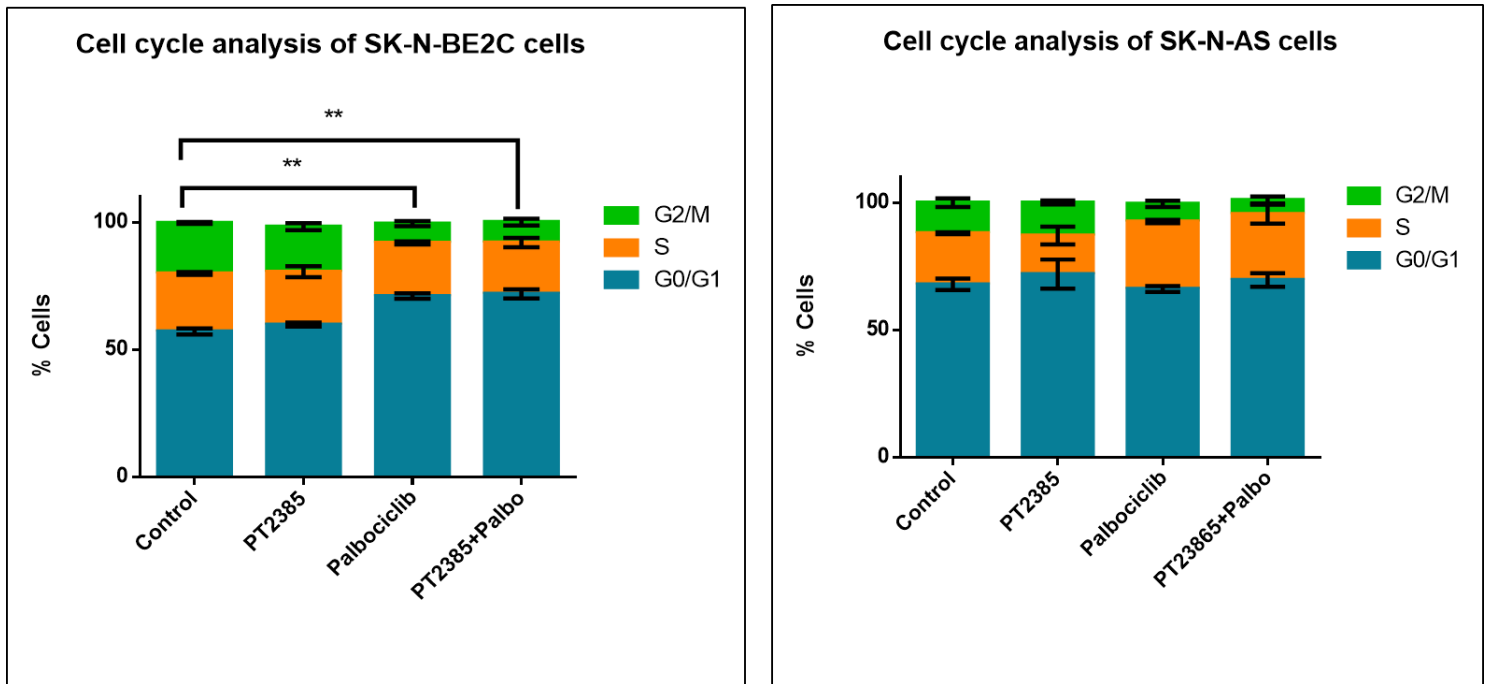
4.2.5 The effect of HIF-2 α inhibition on cell cycle

The role of hypoxia in non-cancer cell cycle progression has been well documented. (Hubbi and Semenza, 2015) (Ortmann, Druker and Rocha, 2014). Exposure to hypoxia would arrest cell proliferation in most cell types to reduce the cell numbers, thereby reducing the demand on limited resources. Flow cytometry analysis demonstrated an increase in the percentage of cells in the G1 phase and a reduction of cells in the S phase. (Krtolica, Krucher and Ludlow, 1998) There was also a decrease in CDK activity in hypoxia (0.5% oxygen) after 48 hours (Goda *et al.*, 2003). However, a hallmark of several cancer lines is the continued proliferation of cells despite a hypoxic environment or a reversal of the cell cycle arrest after prolonged hypoxia. (Krtolica, Krucher and Ludlow, 1998) (Richards *et al.*, 2016).

Our next aim was to assess whether PT2385, alone and in combination with Palbociclib, had an inhibitory effect on the cell cycle progression of neuroblastoma cells. Both cell lines were preconditioned in hypoxia for 72 hours before treatment with HIF-2 α inhibitor PT2385 or

Palbociclib or both drugs in combination. There was little lethality with PT2385, as shown by MTT assays. A concentration of 10 μ M of PT2385 was used to reflect recommended dosing from the manufacturers for *in vitro* investigations. (Communication from D Piovisan, ArcusBio) Palbociclib concentration reflects half the IC50 of the cells when conditioned in hypoxia. Cells were exposed to hypoxia for 48 hours. Then, the cell cycle stages were assessed using fluorescence-activated cell sorting. (**Figure 4.5**)

Figure 4.5 Cell Cycle Analysis of neuroblastoma cells treated with PT2385 and Palbociclib.



Cells were treated for 48 hours Cells were preconditioned in hypoxia for 3 days prior to treatment. Graphs depict cell cycle and percentage (%) cells per cell cycle phase. Unpaired t-test was performed to test for statistical significance . * $p < 0.05$, ** $p < 0.01$, *** $p = 0.001$, $p = 0.0001$

As shown previously, the SK-N-BE(2)C cells are more sensitive to the Palbociclib cell cycle arrest effect. In both solo and combination conditions, there is a statistically significant change from the control group in the proportion of cells arrested in G0/G1. However, there is no difference between the control and the PT2385-treated samples, nor between Palbociclib and the combination-treated samples. This indicated that no cell cycle inhibition was obtained by PT2385 treatment, and when combined with Palbociclib, it neither abrogates nor enhances the effect of the CDK4/6 inhibitor. There is no difference in the groups with SK-N-AS cells compared to the control. This relative insensitivity of the cell line to CDK4/6 inhibition was previously observed (Chapter 3: **Error! Reference source not found.**)

4.2.6 The effect of HIF-2 α inhibition on downstream target genes in cell culture.

Hypoxic preconditioning causes transcriptional activation of several genes associated with the cell cycle, invasion and metastasis and increased stemness of neuroblastoma cells. (Vega *et al.*, 2020b) PT2385 inhibition of HIF-2 α transcriptional activity in cells was evaluated by qPCR quantitation of known HIF target genes.

The genes selected were associated with a classical hypoxic response: Carbonic anhydrase 9 (*Ca-9*), *Glut1* and *Vegf*. In addition, to monitor the effects of the inhibitor on the neuroblastoma cell phenotype, we measured the level of gene expression associated with poor prognosis in neuroblastoma (*Glut1/Slc2a1*), cell migration and metastasis (metalloproteinases), cell proliferation (*E2f1*) and differentiation (*Phox2b*). Cells were cultured either in normoxia or hypoxia for 72 hours before treatment. PT2385 and PT2385/Palbociclib combination treatments were applied for 48 hours in hypoxia. The effect of hypoxia on the genes of interest was assessed, and the ability of PT2385, alone and in combination with Palbociclib, to reverse the hypoxic gene signature was measured. The log fold change values are shown normalised to normoxia controls.

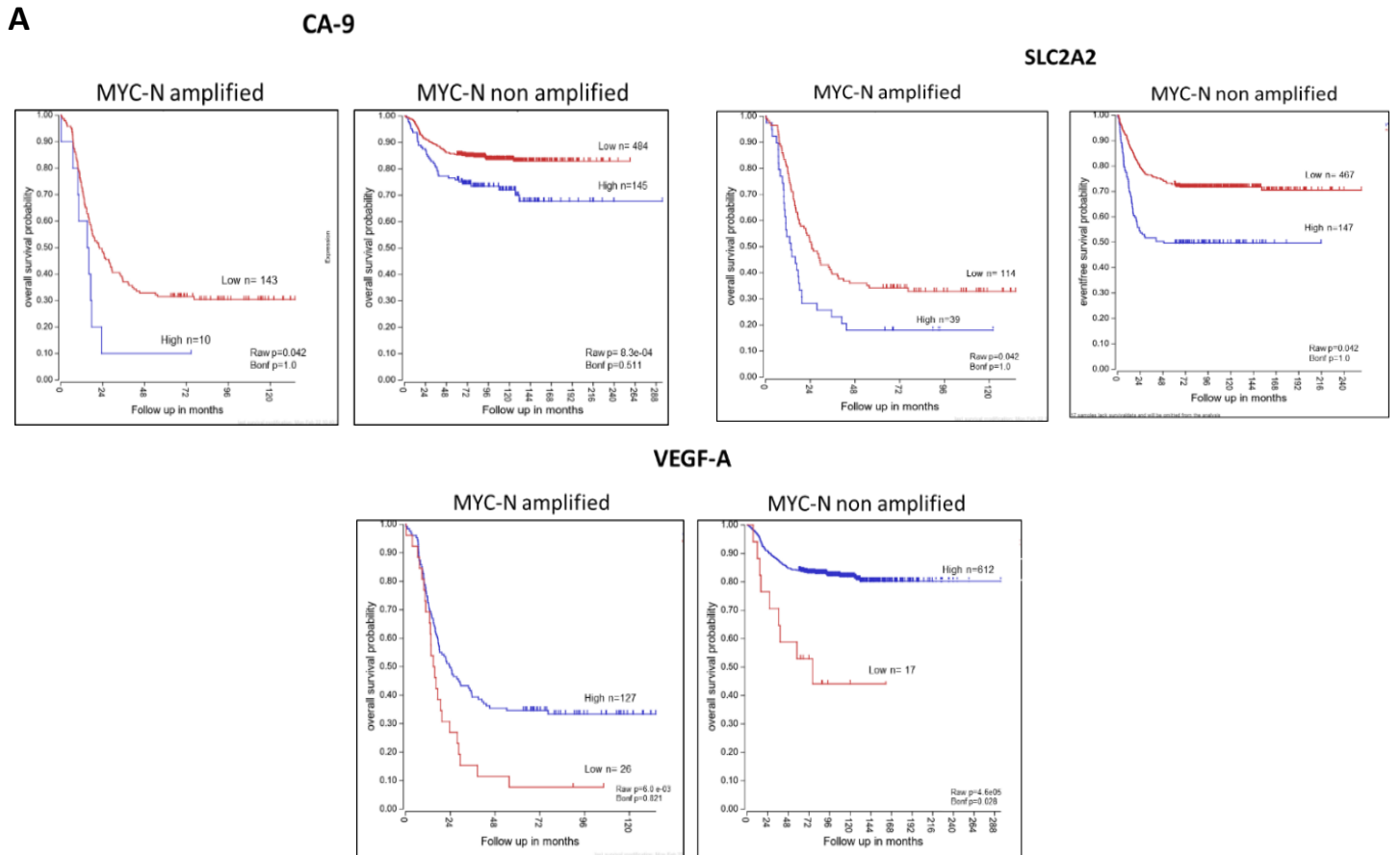
4.2.6.1 Genes associated with poor prognosis and hypoxic response in neuroblastoma

Ca-9, *Vegf* and *Glut1/Slc2a1* are all associated with the adaptive cellular response to a hypoxic environment. *Ca-9* is upregulated in numerous cancers and is associated with poor outcomes and retained stemness of cells. (Ilardi *et al.*, 2014) *Glut1* and *Vegf* are downstream targets of both *HIF1* and *HIF2*. High *Ca-9* and *Glut1/Slc2a1* expression are associated with shorter overall survival in patients with both MYC-N amplified and non-amplified neuroblastoma tumours. As expected, the overall prognosis in the MYC-N amplified cohort is worse. (**Figure 4.6**)

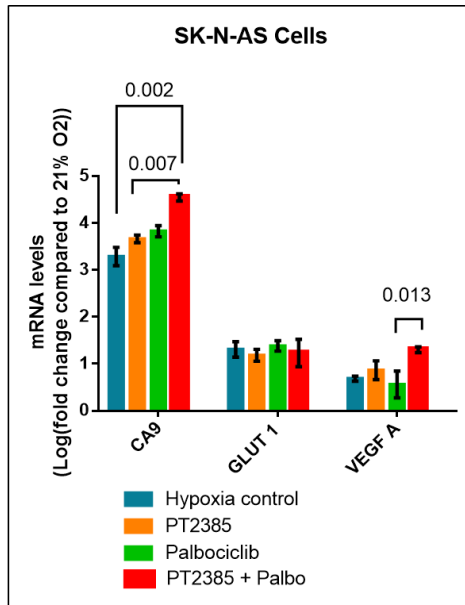
As expected, gene expression analysis in both cell lines showed a statistically significant upregulation in all three genes in a hypoxic environment. Across both cell lines, the most significant increase was the expression of *Ca-9*. The effect of hypoxia on SK-N-AS cells was more pronounced than in SK-N-BE(2)C, although there was no difference in statistical significance between the two cell lines. However, in any cell line, PT2385 did not reduce the hypoxia-induced expression of these three genes. Palbociclib and the combination of PT2385 and Palbociclib did not reduce any mRNA expression of the HIF-target genes. Although *Ca-9*, *Glut1* and *Vegf* are all downstream targets of hypoxia signalling pathways, none are exclusive *HIF2* targets. Whilst these results are surprising and indicate an absence of the targeted and expected effects of PT2385, we cannot exclude a compensation mechanism by *HIF1*.

Figure 4.6 The impact of genes associated with hypoxic genetic signature on the overall survival in MYCN non-amplified and MYCN amplified neuroblastoma cells.

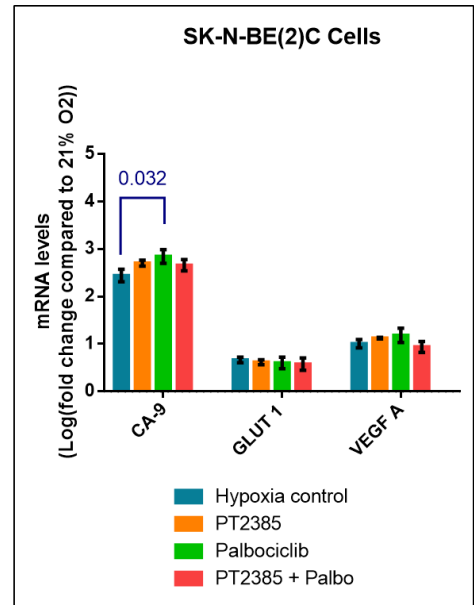
SLC2A1



B



	CA-9	GLUT1	VEGF-A
Log Fold change from 21% to 1% oxygen	4.5	1.2	1.3
Significance	****	****	****



	CA-9	GLUT1	VEGF-A
Log Fold change from 21% oxygen	2.4	0.7	1.0
Significance	****	****	****

A) Kaplan-Meier overall survival curves based on the expression level of CA-9, GLUT1 (SLC2A1) and VEGF-A in neuroblastoma patients using scan as cut off modus. High and low expression groups are indicated. The p values were corrected for multiple testing (Bonferroni correction). Dataset used from Cangelosi dataset from r2(<http://r2.amc.nl>) B) Relative mRNA levels of genes related to hypoxia and poor prognosis were measured through qPCR in cells cultured in normoxia and hypoxia. mRNA levels were measured relative to housekeeping genes cyclophilin A and β -actin and normalised to the relative gene expression levels of cells precultured in normoxia. Bars represent the logarithm of the normalised mean \pm standard error of mean of 4 independent experiments. Upregulated genes take positive values while repressed gene expressions are negative. * $P \leq 0.05$, ** $P \leq 0.01$ and *** $P \leq 0.001$ compared with normoxia.

4.2.6.2 Genes associated with increased cell invasion and metastasis

Matrix metalloproteinases are a large family of extracellular proteases that can modify the tumour microenvironment. However, their role in tumour progression and angiogenesis is still debated, with both tumour suppression and tumour growth potential (Conlon and Murray, 2019). Hypoxia adds further complexity. HIF-1 and HIF-2 have been shown to regulate specific metalloproteinases differentially. ADAMTS1 (a disintegrin and metalloproteinase with thrombospondin motifs 1) is a member of the matrix metalloproteinase family and an acute hypoxia-inducible gene promoting migration under hypoxic conditions. (Hatipoglu *et al.*, 2009). MMP2 and MMP9 are also proteases involved in tumour invasion and metastasis. MMP2 and MMP9, in particular, are known to degrade the basement membrane collagens, gelatin and elastin and are expressed at the protein level in neuroblastoma tumours. (Sugiura *et al.*, 1998). Sugiura *et al.* noted no relationship between MYC-N status and MMP2 levels, but higher-grade diseases expressed higher levels of MMP2. Hypoxia preconditioning of neuroblastoma cells is also sufficient to activate the long-lasting transcription of several prometastatic genes, including *MMP2*. (A Herrmann *et al.*, 2015)

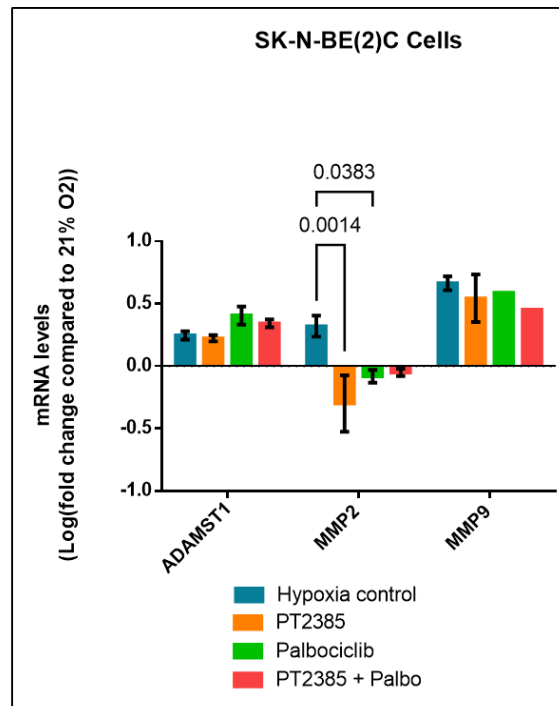
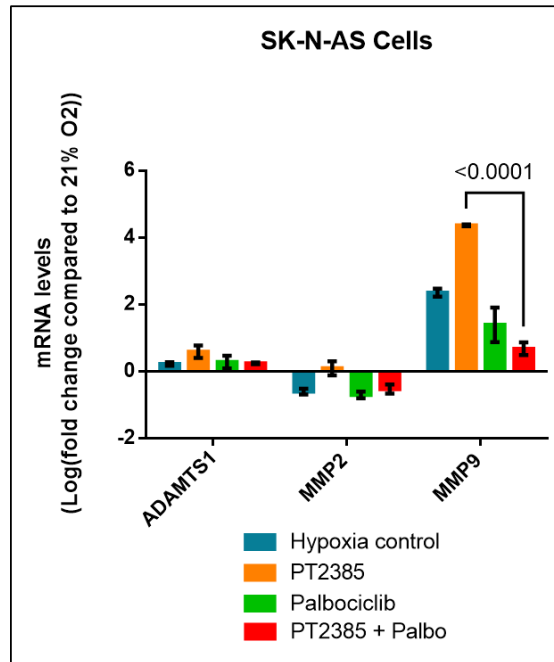
We observed little difference in *Adamts1* and *Mmp2* expression levels between hypoxic and normoxia conditions in both cell lines (**Figure 4.7**). However, in hypoxia, *Mmp9* levels were significantly increased in both cell lines ($p < 0.01$). This increase was again not affected by PT2385 (**Figure 4.7**). HIF-2 α inhibition with PT2385 significantly reduced *Mmp2* expression in SK-N-BE(2)C cells.

The process of metastasis is complex and multifactorial. Once the cells can detach and invade the surrounding tissue, they must be able to access and survive in the circulation, adhere at a distant site and adapt to grow in a new environment. A balance must also be struck, cell detachment is needed for the cell to migrate and metastasise, but cell adhesion is necessary for tumour development at a distant site. It has been shown that many adhesion molecules, including integrins, cadherins, selectins and CAMs, are involved in cancer metastasis. (Tang and Honn, 1994; Hanahan and Weinberg, 2011b). Based on previous genome studies in neuroblastoma tumours grown in the chick embryo, I have chosen to examine the effects of drugs on the expression of Neural cell adhesion molecule (NCAM), a cell surface glycoprotein, Versican (VCAN), which promotes metastasis through induction of transition from mesenchymal to epithelial cell types (Winkler *et al.*, 2020), and the cell-surface adhesion receptors - integrins: IGT 5, IGT V and $\alpha 6\beta 1/4$. (A Herrmann *et al.*, 2015)

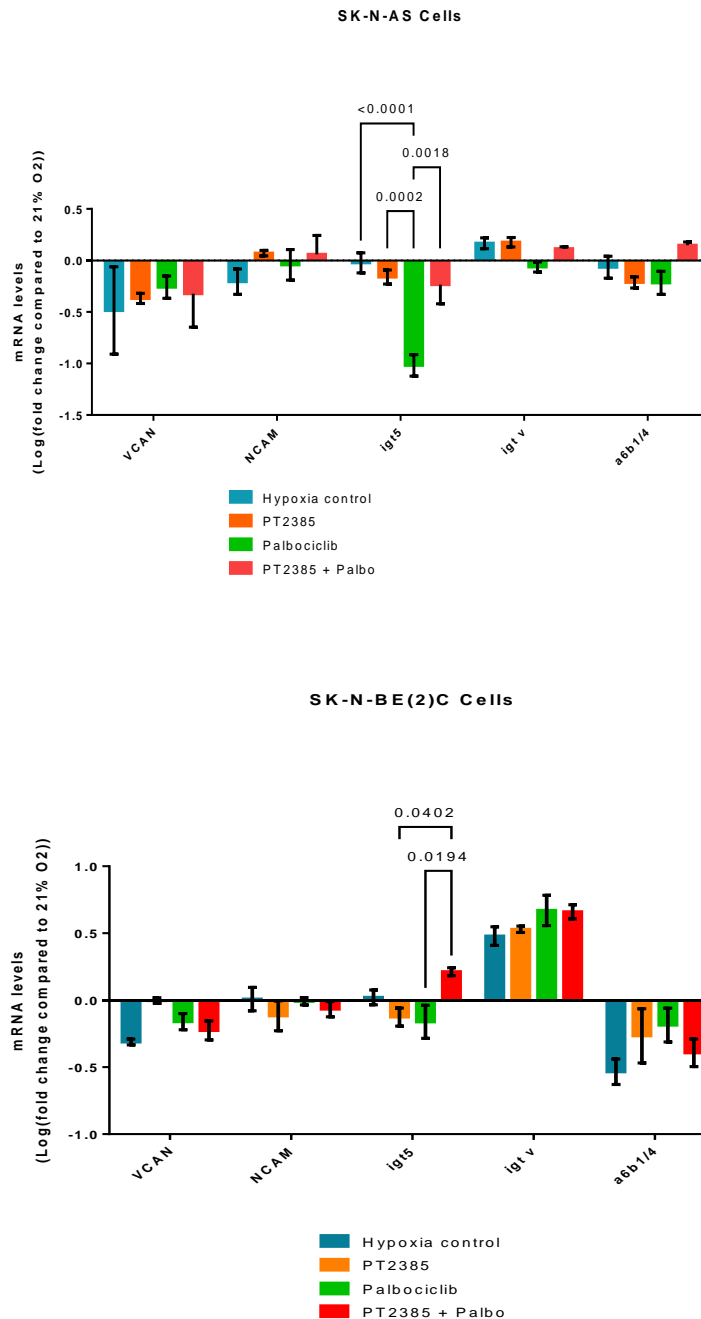
None of the adhesion genes tested was regulated by hypoxia in SK-N-AS cells or SK-N-BE(2)C cells. *Vcam* and *a6b1/4* were slightly down-regulated by hypoxia, yet because of the small change, it is hard to interpret any effect the drugs could have on this, and very few conditions reached statistical differences. The reduction in the *Vcan* gene induced by hypoxia in SK-N-SK-N-BE(2)C cells was reversed by PT2385 treatment, potentially exhibiting a protective effect. However, this effect on a single adhesion molecule is not convincing. Palbociclib did not show much more effect on adhesion gene expression. It caused a reduction in *Itg5* expression in both lines. This effect was lost when combined with PT2385. Altogether, monitoring the expression of the adhesion genes did not provide conclusive information. It is possible that because these experiments were performed *in vitro*, with a lack of extracellular matrix and tumour microenvironment, there was reduced expression of such genes.

Figure 4.7 The impact of hypoxia and drug treatment on genes associated invasion and metastasis in SK-N-BE(2)C and SK-N-AS neuroblastoma cells in vitro.

A



B



A) Genes relating to cell invasion. B) Genes relating to cell metastasis. Relative mRNA levels were measured through qPCR in cells cultured in hypoxia and normoxia. mRNA levels were measured relative to housekeeping genes cyclophilin A and β -actin and normalised to the relative gene expression levels of cells precultured in normoxia. Bars represent the logarithm of the normalised mean \pm standard error of mean of 4 independent experiments. Upregulated genes take positive values while repressed gene expressions are negative. * $P \leq 0.05$, ** $P \leq 0.01$ and *** $P \leq 0.001$ compared with normoxia.

4.2.6.3 Genes associated with cell cycle progression and differentiation

E2F1, E2F2 and E2F3 transcription factors induce MYCN transcription via binding to its proximal promoter *in vivo*, specifically in neuroblastoma cells. (Carcagno *et al.*, 2011) MYC-regulated genes enhance E2F1 expression, so MYC-N and HIF act in opposition. Various factors, not all known, can influence the crosstalk between these two pathways.

Appropriate cell death is also essential to regulate the cell cycle and cell proliferation. Autophagy is a phenomenon through which a cell can destroy misfolded proteins. BCL-2 adenovirus E1B 19kDa-interacting protein (BNIP3) is a pro-autophagy protein upregulated under hypoxia conditions in neuroblastoma cells. BNIP is a direct downstream target of HIF-1a (Bruick, 2000).

To understand the impact of MYC-N amplification and HIF-2 α inhibitors on the cell cycle, the levels of *p21*, *E2f1*, *Bnip3* and *Myc-n* were examined. When exposed to hypoxia, there was a significant upregulation of the *Bnip3* gene in SK-N-AS and SK-N-BE(2)C cell lines (**Figure 4.8 A**). Again, this was not altered by the PT2385 or Palbociclib, although in the SK-N-BE(2)C cell lines, there was a statistically significant reduction with the drug combination. This could suggest a pro-survival role achieved by the drug combination, which is the reverse of what was intended. However, this is only one gene and does not provide a clear picture of the mechanism of action of the drugs. We did not observe an induction of *Cdkn1a* by hypoxia. Neuroblastoma cells may be similar to glioblastoma cells, where hypoxia does not induce cell cycle arrest in most cell lines (Richards *et al.*; Kelly C, unpublished observation). There was no additional conclusive effect of the drugs on this gene.

E2f1 expression induced by hypoxia was more significant in SK-N-AS cells than in the SK-N-BE(2)C cells. The *E2f1* levels remained high in these cells despite the inhibition of CDK4/6. Conversely, in SK-N-BE(2)C cells, inhibition of CDK4/6 decreased E2F1 levels. This can explain previous data (Chapter 3: **Error! Reference source not found.**), where SK-N-AS cells continued cell cycle progression in the presence of Palbociclib, whereas SK-N-BE(2)C cells were arrested in G0.

Our data shows that MYC-N gene expression did not significantly change in the SK-N-BE(2)C cells exposed to hypoxia or PT2385. Upon HIF-2 α inhibition, there was an increase in MYC-N

levels in SK-N-AS. (**Figure 4.8**) The crosstalk between MYC family proteins and hypoxia is a complex relationship that varies depending on the cell type and the MYC protein levels. Qing et al. examined the effect of hypoxia on HIF-2 α expression in MYC-N amplified and non-amplified neuroblastoma cells. (Qing *et al.*, 2010) Interestingly, they showed that MYC-N amplified cells preferentially expressed HIF-1 α but not HIF-2 α . They hypothesised that MYC-N and HIF-1 α interactions are more prevalent in MYC-N amplified neuroblastoma, and HIF-2 α has a more prominent role in single copy tumours. In SK-N-BE(2)C, the most significant change in cell cycle progression was in the presence of Palbociclib (**Figure 4.4**), with no effect seen with PT2385. Palbociclib's effect on the SK-N-BE(2)C cell cycle may be acting through *E2f1* modulation more than *Cdkn1a*. We can observe in **Figure 4.8A** that Palbociclib causes a significant reduction in *E2f1* levels where *Cdkn1a* remain unchanged. Hypoxia also induced cell cycle arrest in SK-N-AS cells. (**Figure 4.4**). Examining the gene expression, *E2f1* expression is greatly increased in hypoxia and may indicate that hypoxia-induced G1/S transition is associated with the induction of *E2f1* in SK-N-AS cells.

We next investigated the expression of differentiation markers.

Genes that have been shown to change significantly were chosen to investigate the effect of hypoxia on differentiation. (Sung *et al.*, 2013). Kruppel-like factor 4 (KLF4), roundabout axon guidance receptor, homolog 2 (ROBO2), stathmin-like 4 (STMN4) and PHOX2B are the four 'differentiation' linked genes shown below. Overexpression of *Klf4* has reduced cell proliferation and inhibits angiogenesis and metastasis in neuroblastoma. STMN4 and ROBO2 are involved in neuronal differentiation. PHOX2B is a minimal residual disease marker of neuroblastoma, a marker of poor prognosis. Accordingly, high expression levels of *Phox2B* promote neuroblastoma cell proliferation and tumour growth. Hypoxia caused a significant change in most of the differentiation markers in both cell lines. *Klf4* and *Robo2* levels were increased with both cell lines. *Stmn4* levels increased in SK-N-AS but significantly reduced in SK-N-BE(2)C cells. *Phox2b* levels were not altered by hypoxic exposure. The inhibition of HIF-2 α affected *Robo* levels significantly – increasing them in SK-N-BE(2)C, associated with increased differentiation, and reducing SK-N-AS levels.

Hypoxia is associated with maintaining stemness in neuroblastoma cells. (Vega *et al.*, 2020a). Expression of both *Robo* and *Stmn* would be expected to reduce, and *Klf4* to increase in hypoxic

conditions. Both cells' *Klf4* levels have increased in hypoxia, implying a more undifferentiated cell type (**Figure 4.8**). Several studies have suggested a close link between stathmin expression and regulation of cellular proliferation in cancers. (Wang, Akhtar and Wang, 2015). Interestingly the Stathmin gene is transactivated by the E2F1 protein, and therefore high levels of *E2f1* expression in SK-N-AS cells may activate *Stmn* expression in hypoxia. (Chen *et al.*, 2013; Nie *et al.*, 2022)

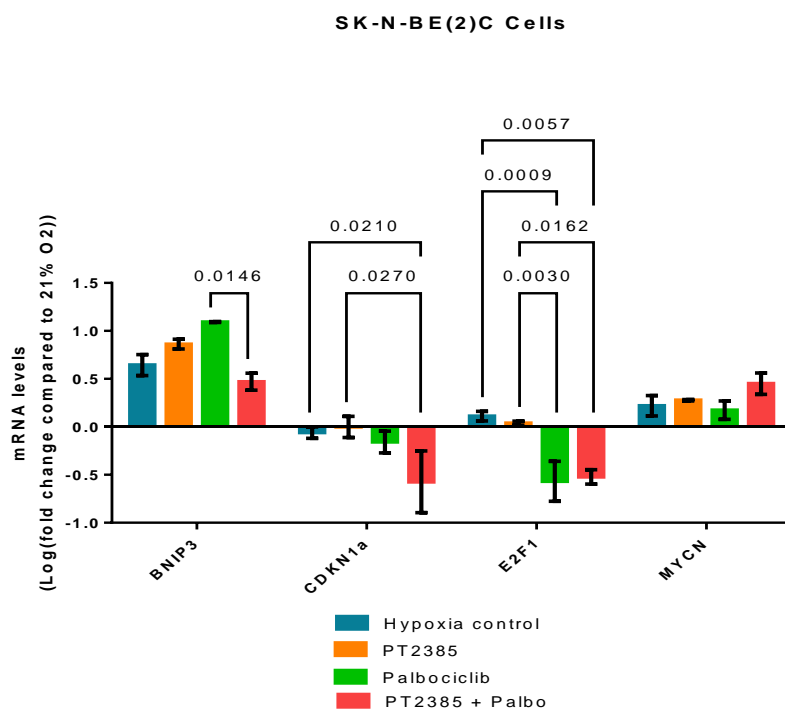
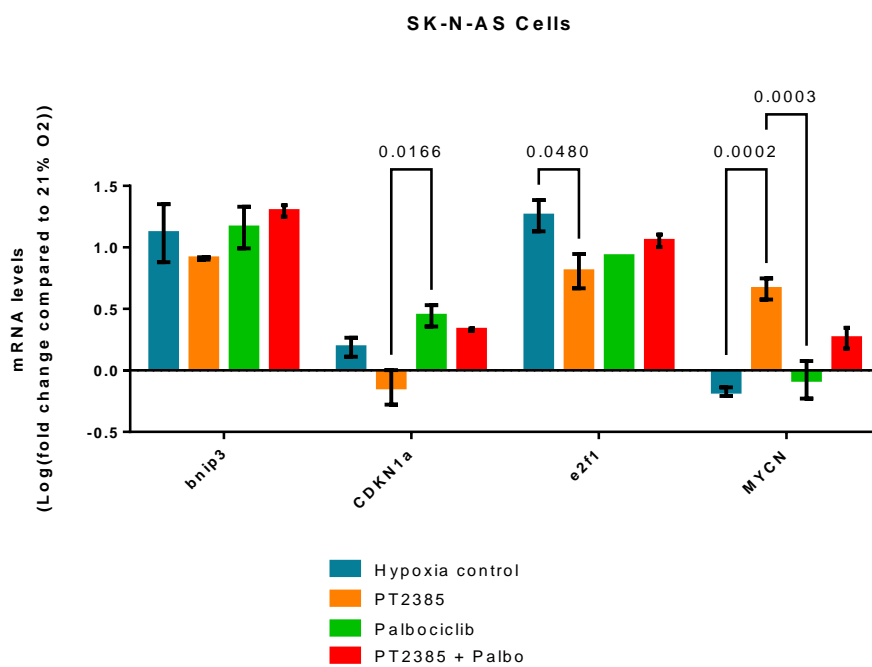
However, the other differentiation markers do not exhibit a clear pattern of behaviour. The genes chosen here are only a sample of potential differentiation markers and have other roles in proliferation and cell motility. A more comprehensive panel of genes needs to be investigated to characterise the effects on differentiation further.

No clear conclusion can be drawn from isolated genes regulated by the drugs; transcriptomic data would be required to obtain a clearer picture.

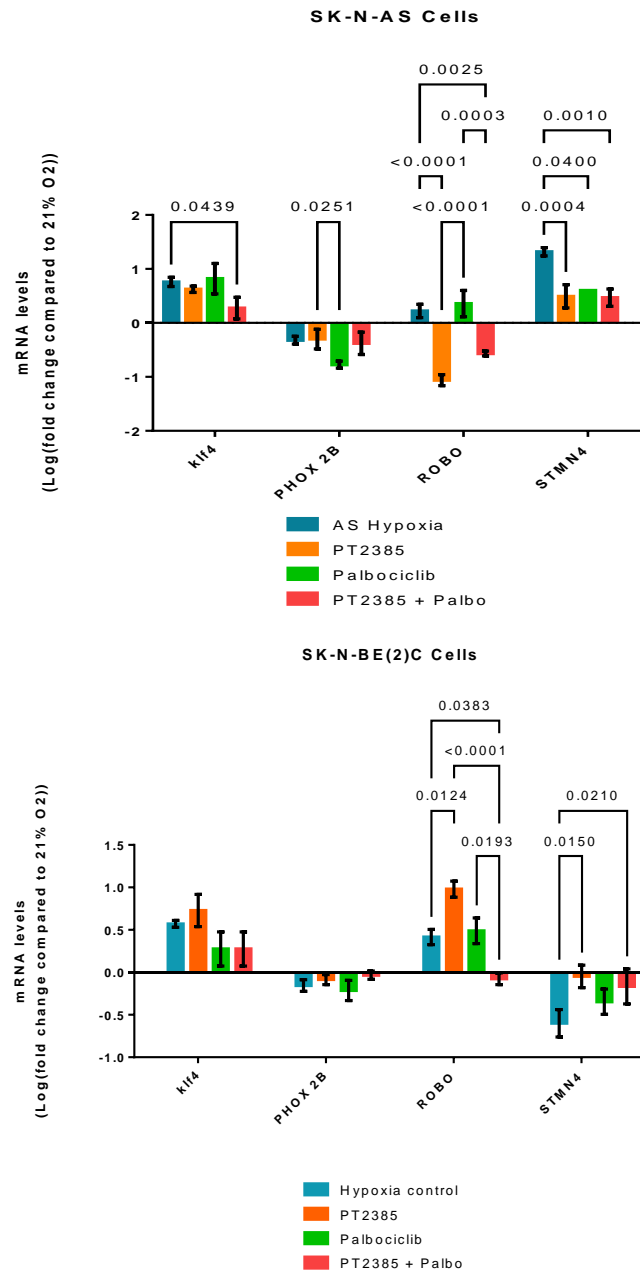
For a better understanding, the effects of the drug *in vivo* need to be examined. We can conclude from the data obtained *in vitro* that Palbociclib effectively blocks cell cycle progression in SK-N-BE(2)C cells, likely via inhibition of E2F-1 expression. Palbociclib does not seem to have any other effect on cell invasion or differentiation phenotype. We question the effectiveness of PT2385 in inhibiting HIF-2 α as it has no apparent effect on HIF target gene expression and had no other effects on cell cycle, differentiation or metastatic genes. However, since some inhibitors have very different effects *in vitro* and *in vivo*, we decided to evaluate further the potential of the HIF-2 α inhibitor alone or in combination with Palbociclib.

Figure 4.8 The impact of hypoxia and drugs on genes associated with cell cycle and cell differentiation in MYCN non-amplified and MYCN amplified neuroblastoma cells.

A



B



A) Genes associated with cell cycle: *Bnip3*, *Cdkn1a/p21*, *E2f1* and *Mycn*. B) Genes associated with cell differentiation: *Klf4*, *Phox2b*, *Robo*, *Stmn4*. Relative mRNA levels of genes related to hypoxia and poor prognosis were measured through qPCR in cells cultured in hypoxia and normoxia. mRNA levels were measured relative to housekeeping genes cyclophilin A and b-actin and normalised to the relative gene expression levels of cells precultured in normoxia. Bars represent the logarithm of the normalised mean \pm standard error of mean of 4 independent experiments. Upregulated genes take positive values while repressed gene expressions are negative. * $P \leq 0.05$, ** $P \leq 0.01$ and *** $P \leq 0.001$ compared with normoxia.

4.2.7 The effect of HIF-2 α inhibition on chick survival and growth *in vivo*

Despite the lack of conclusive effects of PT2835 *in vitro*, we decided to test its effect *in vivo*, as 1) the *in vivo* drug is provided with a different formulation for *in vivo* delivery and 2) the company also had little effects *in vitro*, but strong effects in preclinical models and encouraging results in clinical tests for clear cell renal carcinoma, 3) we hypothesised a specific effect on metastasis, which could not be seen *in vitro*. To assess the drug's effect *in vivo* and ascertain its suitability for use in the chick embryo model.

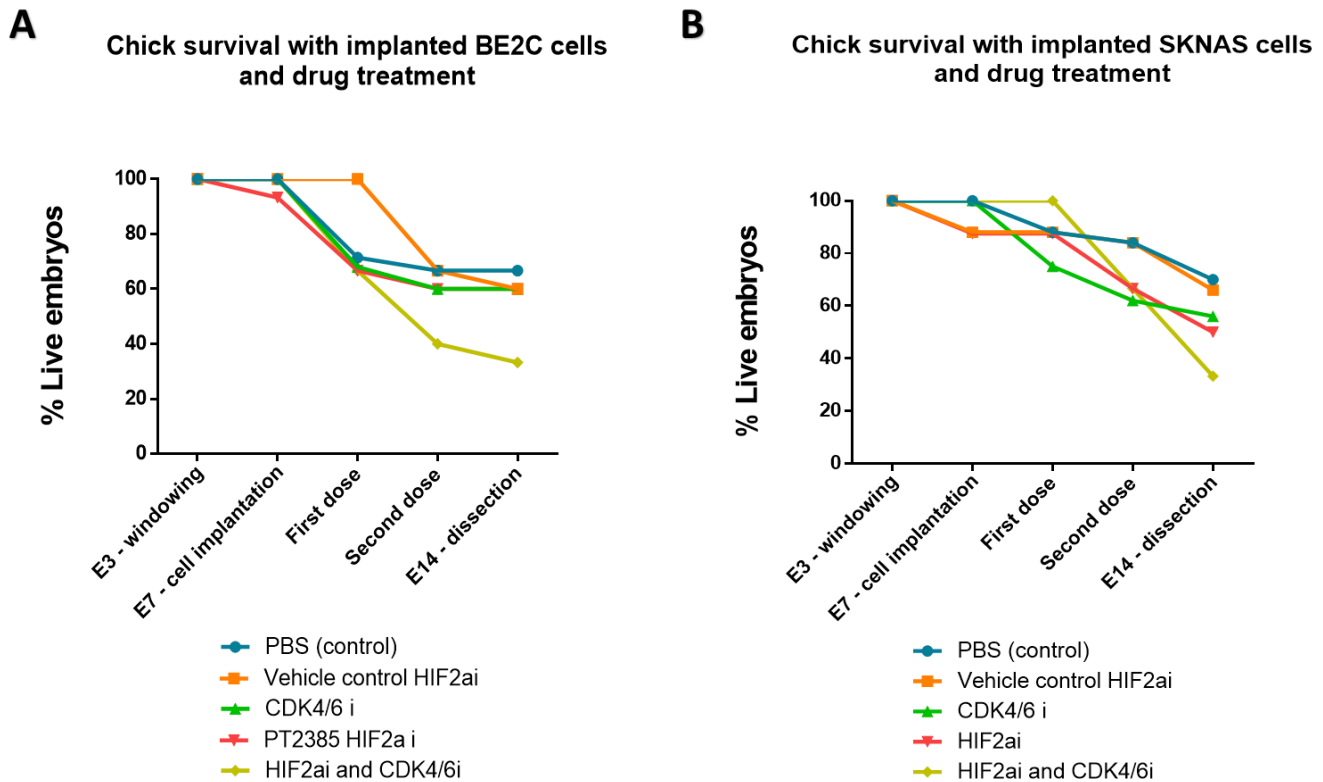
Two million fluorescently labelled neuroblastoma cells precultured in hypoxia for 72 hours were pipetted onto the chorioallantoic membrane on an embryonic day 7. On embryonic day 9, the first dose of the treatment was administered into the allantoic sac. The treatment arms were 10 μ M of PT2385, 10 μ M of PEG vehicle control, 10 μ M of PT2385 and 10 μ M of palbociclib, or 200 μ L of PBS. The second dose was administered on day 11. Previous experimentation by the drug manufacturer, ArcusBio, had used an equivalent dose in murine models, dosing four times a day. The treatment days were performed earlier than in previous experiments as we hypothesised that early treatments might better prevent early metastatic events. Whole eggs surviving treatment, the weight of the eggs surviving the treatment regime and the formation of primary and metastatic tumours were recorded.

Based on our existing dosing schedule and the *in vivo* dosing from ArcusBio, we assessed the chick survival after the first and second doses. (**Figure 4.9**) HIF-2 α inhibition did not negatively affect the chick embryo's survival or growth. There was little difference between the SK-N-AS and SK-N-BE(2)C cell lines on survival. Since we aim to assess the combination of Palbociclib and PT2835, we assessed the combination on chick survival. The combination decreased chick survival, with 30% survival compared to ~60% in the control group. The poor survival in combination suggests a synergistic lethality

The effect of the drugs on the somatic growth of the chick embryos was then evaluated. Chicks were weighed in a standard 10 cm culture dish before the first dose at E9 and before culling at E14. (**Figure 4.10**) There was no difference between the control and treatment groups in the somatic weight of the surviving embryos at E14. This implied that although the HIF inhibitor in combination with the CDK4/6 inhibitor in some eggs was lethal when tolerated, it did not affect the growth and development of the embryo. What is not clear is whether this is because the dosing was different in some chicks, although the methodology was the same, or if some chicks were

more susceptible to the drug combination. An identical drug concentration was given to all chicks based on average weight, although smaller, lighter chicks may have been overdosed.

Figure 4.9 The percentage of chick survival after treatment with HIF inhibitor and combination drug protocol.

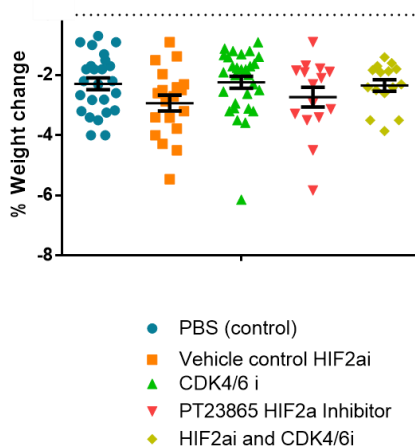


The number of chicks surviving each intervention was recorded and is shown as a percentage of the starting number at embryonic day 3. The data is divided by cell line to assess for any differences in the tumour burden between (A) SK-N-BE(2)C and (B)SK-N-AS cell implantation. As shown previously there is a natural attrition in survival corresponding to movement of the embryos and intervention in room air. PT2385 and Palbociclib together have the poorest survival in both groups, with only 30% surviving to E14 compared to 60-70% survival in the PBS groups.

Figure 4.10 SK-N-BE(2)C or SK-N-AS cells were implanted as described in methods and materials on embryonic day 7.

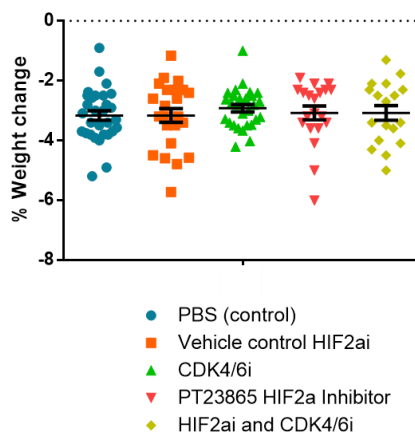
A

Chick weight change after treatment (BE2C cell line)



B

Chick weight change after treatment (SKNAS cell line)

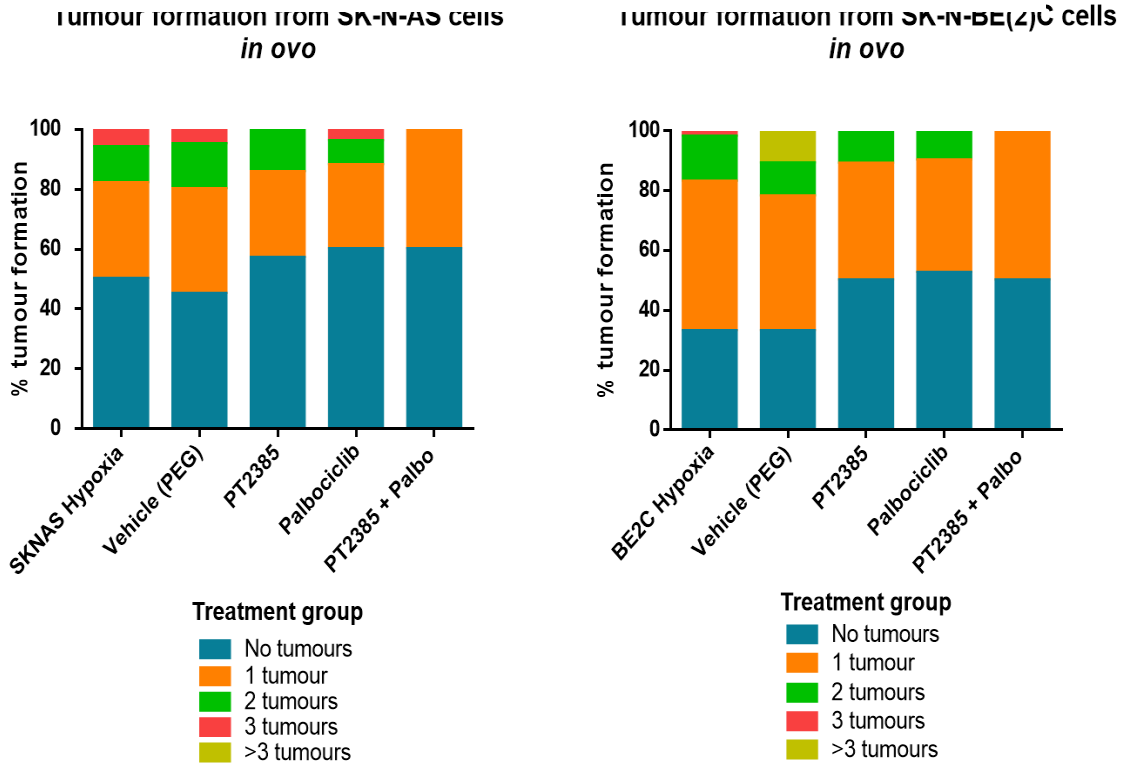


Drugs or the equivalent concentration of vehicle control were administered on embryonic day 9 and embryonic day 11. The somatic development was assessed through weight. The percentage change of the weight from before administration of first dose to end of experiment is shown. The error bars demonstrate the mean and the s.e.m. Statistical significance in weight was calculated using unpaired T test. There was no statistical difference between the treatment and control groups

4.2.8 The effect of HIF inhibition on tumour formation in the chick embryo.

The formation of SK-N-BE(2)C and SK-N-AS tumours with treatment was assessed as previously described (Chapter 3).

Figure 4.11 The effect of drug treatment on number of tumours formed per egg.



The presence of SK-N-BE(2)C and SK-N-AS tumours with each treatment condition is shown as a percentage of eggs viable at E14. A higher proportion of viable eggs were seen to have no primary tumours in the treatment groups in both SK-N-BE(2)C and SK-N-AS implanted eggs. 2-way ANOVA was used to assess the differences in tumour formation between each condition. Tukey's multiple comparisons correction was used. Alpha = 0.05 There was no statistical significance seen in the numbers of tumours formed with the different treatment conditions.

The number of tumours formed in chick embryos after treatment with PT2385, Palbociclib or combination therapy was lower than in the controls. (Figure 4.11) However, this was not a statistically significant difference. We also observed fewer eggs with multiple tumours forming in the presence of drugs. In either cell line, no eggs were growing more than three primary tumours in the combination therapy group. The caveat to this observation is that the overall numbers in this group were lower due to poor survival, so with a larger sample, this difference may not be seen.

4.2.9 Metastatic tumour formation in chick embryos after treatment with HIF-2 α inhibitor.

The primary goal of using HIF inhibitors in combination was to reduce the metastatic potential of both MYCN amplified and MYCN non-amplified neuroblastoma cell lines. Alongside dissecting the primary tumours, the chick organs were also dissected and examined for the presence of metastasis within each treatment group. The total number of metastasis was then recorded (Figure 4.12(B)). I have previously reported that in the absence of preculture in hypoxia, the neuroblastoma cells do not develop metastasis spontaneously within the chick embryo. (A Herrmann *et al.*, 2015; Herrmann, Moss and Sée, 2016) Pro-metastatic pathways are activated by this preincubation period. No metastasis was seen in the 'normoxia control' group in accordance with this. A high number of metastasis was seen in the eggs of both control groups (hypoxia alone and vehicle (PEG)). These two groups also carried the highest frequency of multiple metastases with both cell

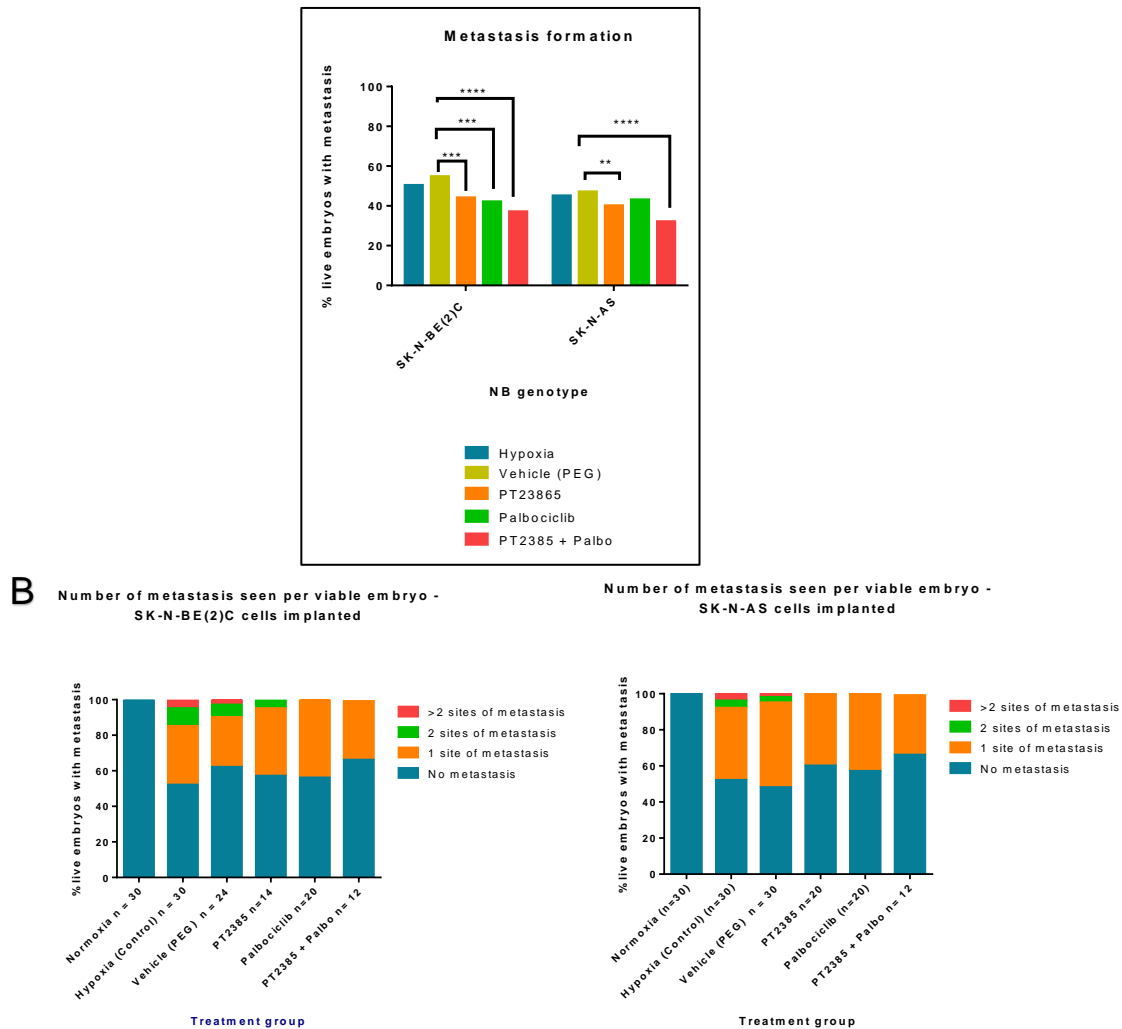
lines, with some chicks having over two separate sites of metastasis.

There was a statistically significant reduction in metastasis in the SK-N-BE(2)C tumours with all treatments and most significantly with the combination group. The combination therapy reduced the likelihood of single and multiple metastatic tumour formation. With the SK-N-AS tumours, the most significant reduction in metastasis observed was again with the combination treatment. Treatment with PT2385 reduces the metastasis formation in SK-N-AS tumours. (Figure 4.12A)

It has to be noted that some eggs had only one metastasis detected in a single site (liver, intestine, feathers), others had multiple metastases in a single site, and others had single metastasis in multiple sites. (Figure 4.12B). There was no predilection for specific distributions within each cell

line or treatment group. Administration of PT2385 showed a significant reduction in the number of distant metastasis seen in both cell lines compared to the vehicle group.

Figure 4.12 The percentage of live embryos with metastasis.



At E14 viable embryos were dissected to assess for primary tumours on the CAM and also for metastasis. A) The number of embryos seen with metastasis (single or multiple) were recorded as a percentage of all viable eggs. B) The bar chart shows the number of metastasis per treatment condition as a percentage of total viable eggs. As there was variable survival between groups the number of viable embryos per group are shown as n=Number of metastasis were categorised as distinct sites of metastasis. Common sites included within the intestines, feathers and the gizzard. There was no metastasis within the brain or the eyes.

The effect of HIF-2 α inhibition on downstream targets in the *in vivo* chick embryo model.

While the *in vitro* investigations of the PT2853 effects alone or combined did not indicate the molecular mechanism of action, given the effects on metastasis *in vivo*, we sought to depict some potential molecular mechanisms *in vivo*. Tumours were grown from cells cultured in either normoxia or hypoxia for 72 hours, as previously described (Materials and Methods 2.4.2). The data shown are normalised to the tumours grown in normoxia.

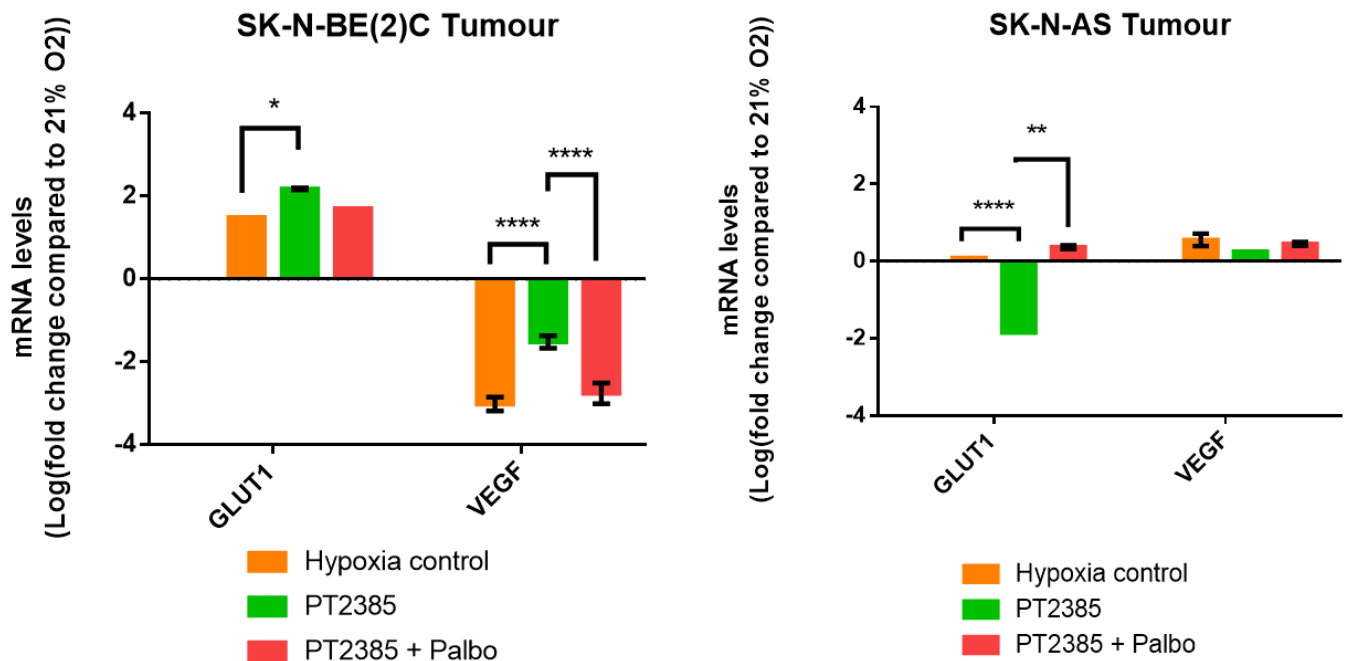
The data are divided into groups of genes within similar functional pathways as was done for the *in vitro* data. Gene expression data for Palbociclib alone is not shown as, due to time constraints, the experiments did not have a sufficient number of replicates.

4.2.9.1 Genes associated with poor prognosis and hypoxic response in neuroblastoma

In SK-N-BE(2)C tumours, HIF-2 α inhibition induced *Glut1* expression ($p=0.05$), whereas, in the SK-N-AS tumours, HIF-2 α inhibition reduced it ($p=0.0001$) (Figure 4.13). There was no difference in the *Glut1* expression in cell culture between the treated and control groups (Figure 4.13).

Whereas *Vegf* levels were increased in SK-N-BE(2)C cells in hypoxia, we observed a dramatic down-regulation *in vivo*. The tumours were harvested at embryonic day 14, and the qPCR analysis depicts a snapshot of the tumour at this time. It is possible for *Vegf*, as with all genes, that expression changes as the tumour is metabolically active and growing. Once the neo-angiogenesis is formed to supply the tumour sufficiently, the *Vegf* levels may reduce. This negative feedback would not occur in cell culture, as no angiogenesis is possible. HIF-2 α inhibition conversely appears to reduce this down-regulation. There is no significant change in *Vegf* levels in either SK-N-AS cells or tumours. Jogi et al. also found that when examining *Vegf* expression in neuroblastoma tumours, viable cells surrounding necrotic areas exhibited high *Vegf* expression, whereas most cells in other parts of the tumours were *Vegf*-negative. (Jögi et al., 2002) With this high level of heterogeneity across a tumour, it is not possible to conclude, through this methodology, the impact of PT3285 on VEGF activity. Data from *Ca-9* expression levels have not been included, as the qPCR primer could not be optimised for the *in vivo* samples.

Figure 4.13 Expression of genes associated with hypoxia within SK-N-BE(2)C and SK-N-AS tumours grown in the chick embryo.



	GLUT1		VEGF	
	SK-N-BE(2)C	SK-N-AS	SK-N-BE(2)C	SK-N-AS
Log Fold change from 21% to 1% oxygen	1.4	0.09	-3.0	0.7
Significance p=	0.001	ns	0.001	0.001

Relative mRNA levels of genes related to hypoxia and poor prognosis were measured through qPCR in tumours grown from cells cultured in hypoxia or normoxia before implantation. mRNA levels were measured relative to housekeeping genes cyclophilin A and β -actin and normalised to the relative gene expression levels of cells precultured in normoxia. Bars represent the logarithm of the normalised mean \pm standard error of mean of 3 independent experiments. Upregulated genes take positive values while repressed gene expressions are negative. 2 way ANOVA was performed, with a Tukey multiple comparisons test. $*P \leq 0.05$, $**P \leq 0.01$ and $***P \leq 0.001$ compared with normoxia. Table below shows mean change in gene expression of the target genes between tumours precultures in normoxia and those in hypoxia. Student's unpaired t test was used to assess for statistical significance. ((n=3). $*p < 0.05$, $**p < 0.01$, $***p < 0.001$)

4.2.9.2 Genes regulating cell invasion and metastasis

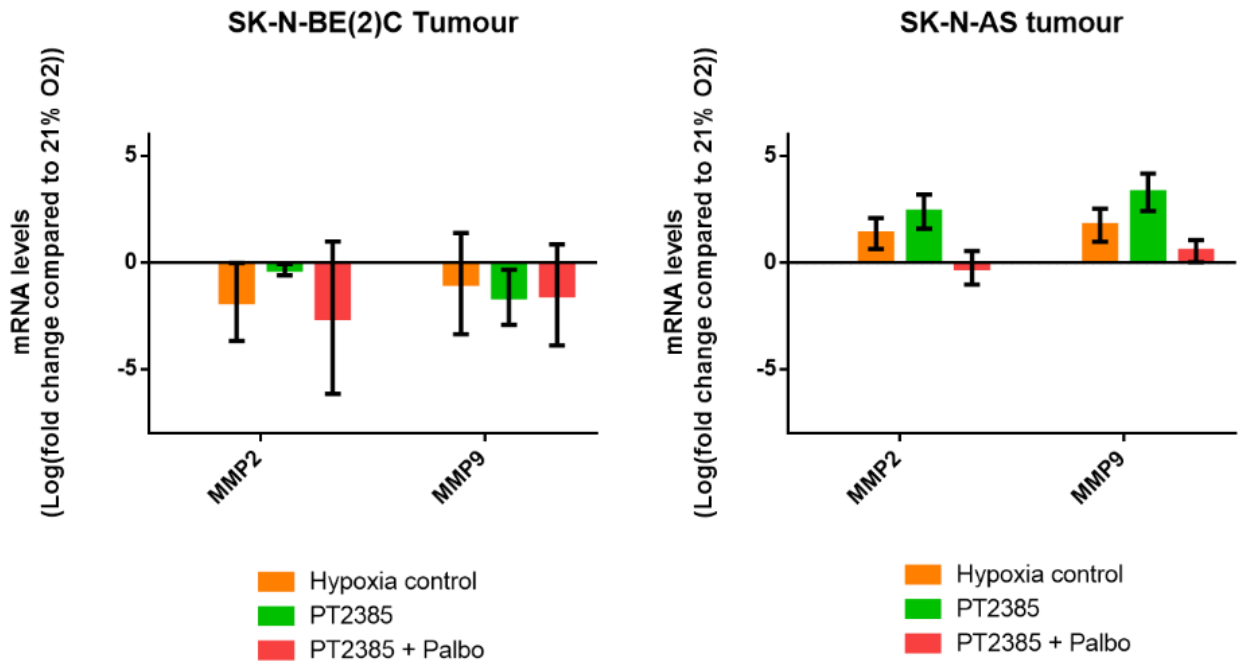
Overall, there was no significant expression change between normoxia and hypoxic tumours in both cell populations for *Mmp2* and *Mmp9*. Large variability between the replicates for these genes may reflect each tumour's invasion stage. This high variability makes it difficult to comment on the general trend with hypoxia and treatment. However, the trends in SK-N-AS cells show that in hypoxia, there was an increase in expression of *Mmp2* and *Mmp9*, and the inhibition of HIF-2 α further increased it, which was surprising considering the beneficial effects of PT2385 on the metastatic occurrence. (Figure 4.14)

There was no difference between cells cultured in normoxia and hypoxia for genes controlling cell migration and metastasis. (Figure 4.7, B) In the SK-N-BE(2)C tumours, PT2385 significantly reduced the expression of pro-metastatic genes such as *Vcan* and *Itg5*. The data for SK-N-AS tumours were inconclusive.

Given the multiple factors and varied, complex pathways involved in metastasis, it was not possible to accurately conclude the effects of PT2385 on metastasis using qPCR techniques.

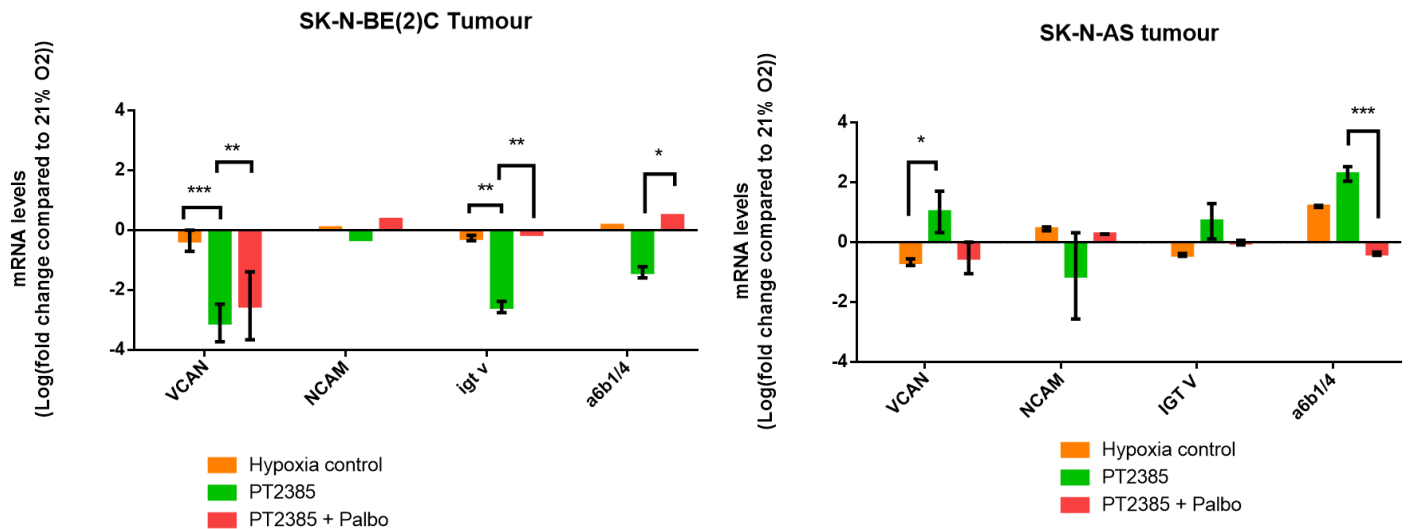
Figure 4.14 Expression of genes associated with invasion and metastasis within SK-N-BE(2)C and SK-N-AS tumours grown in the chick embryo.

A



	MMP2		MMP9	
	SK-N-BE(2)C	SK-N-AS	SK-N-BE(2)C	SK-N-AS
Log Fold change from 21% to 1% oxygen	-1.8	1.3	-0.9	1.7
Significance p=	ns	ns	ns	ns

B



	VCAN		NCAM		IGTV		A6b1/4	
	SK-N-BE(2)C	SK-N-AS	SK-N-BE(2)C	SK-N-AS	SK-N-BE(2)C	SK-N-AS	SK-N-BE(2)C	SK-N-AS
Log Fold change from 21% to 1% oxygen	--0.34	-0.66	0.07	0.45	-0.26	-0.40	0.15	1.20
Significance p=	ns	ns	ns	ns	ns	ns	ns	ns

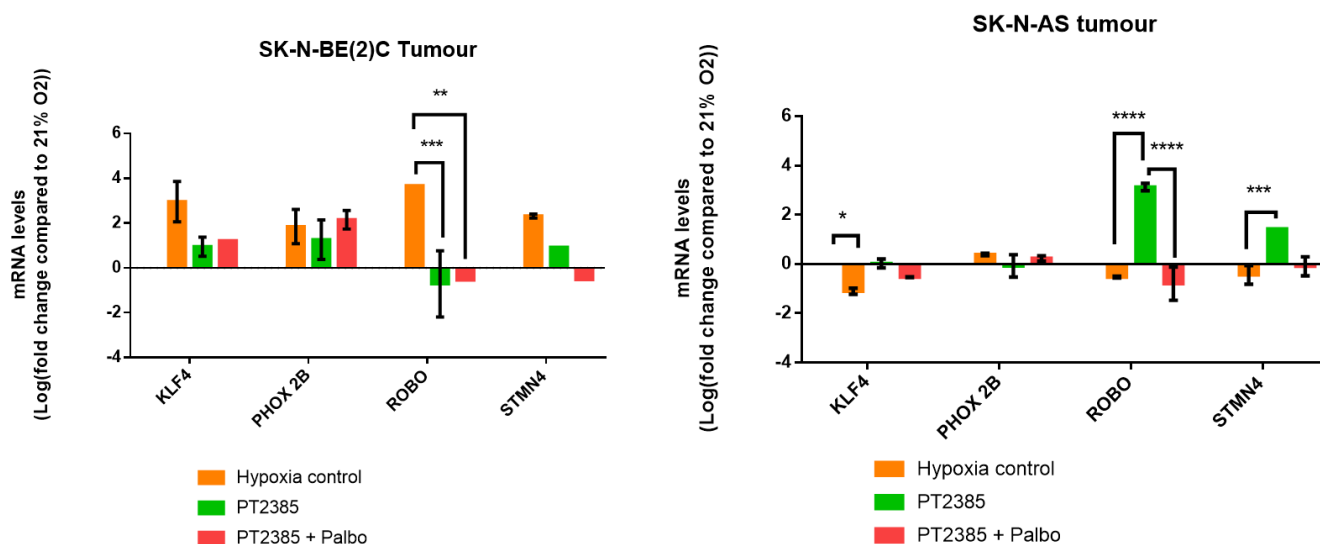
A) Genes regulating invasion; Mmp2 and Mmp9. B) Genes regulating metastasis: Vcan, Ncam, Itgv, A6b1/4, Relative mRNA levels of genes related to invasion were measured through qPCR in tumours grown from cells cultured in hypoxia or normoxia before implantation. mRNA levels were measured relative to housekeeping genes cyclophilin A and b-actin and normalised to the relative gene expression levels of cells precultured in normoxia Bars represent the logarithm of the normalised mean \pm standard error of mean of 3 independent experiments. Upregulated genes take positive values while repressed gene expression are negative. 2 way ANOVA was performed, with a Tukey's multiple comparisons test. * $P \leq 0.05$, ** $P \leq 0.01$ and * $P \leq 0.001$ compared with normoxia. Table below shows mean change in gene expression of the target genes between tumours precultures in normoxia and those in hypoxia. Students unpaired t test was used to assess for statistical significance. ((n=3). * $p < 0.05$, ** $p < 0.01$, *** $p < 0.001$)**

4.2.9.3 Genes regulating differentiation

The expression of key differentiation markers was measured to investigate the effect of the *in vivo* environment on the differentiation of cells. In the SK-N-BE(2)C cells, hypoxia caused an upregulation in *Klf4* (log fold increase of 2.96), and in the SK-N-AS, the same gene showed no real difference (log fold change -1.1) (**Figure 4.8**). With *Robo2*, there was a significant change with SK-N-AS tumours, but in SK-N-BE(2)C, it increased by almost 4-fold in hypoxia preconditioned cells. The other genes examined showed no change between the normoxia and hypoxia preculture. *Stmn4* levels were increased in hypoxic cell culture (**Figure 4.8**), but this was not observed in tumours. (**Figure 4.15**) Conversely, the levels of *Robo2* were increased in the tumours more than in the cells. These differences were observed for most genes investigated. It is evident that the tumour microenvironment dramatically influences the expression of specific genes and not at all in others. Interestingly there is a differential expression between groups of genes that have similar functions, with a preference for one pathway over another.

Overall it is not possible to draw any conclusions about the effectiveness of the PT2385 monotherapy and in combination with Palbociclib. The *in vivo* metastasis data indicates an inhibitory effect on metastasis formation. However, the gene expression analysis is not conclusive. A combination of tumour heterogeneity and limited gene selection likely means this data is not definitive. Greater numbers of samples with a broader range of pathway analysis would be more informative.

Figure 4.15 Expression of genes associated with differentiation within SK-N-BE(2)C and SK-N-AS tumours grown in the chick embryo.



	KLF4		PHOX2b		ROBO		STMN4	
	SK-N-BE(2)C	SK-N-AS	SK-N-BE(2)C	SK-N-AS	SK-N-BE(2)C	SK-N-AS	SK-N-BE(2)C	SK-N-AS
Log Fold change from 21% to 1% oxygen	2.96	--1.10	1.84	0.39	3.68	-0.53	2.32	-0.44
Significance p=	0.05	0.01	ns	ns	0.01	ns	ns	ns

Relative mRNA levels of genes related to differentiation were measured through qPCR in tumours grown from cells cultured in hypoxia and normoxia before implantation. mRNA levels were measured relative to housekeeping genes cyclophilin A and β -actin and normalised to the relative gene expression levels of cells precultured in normoxia O₂. Bars represent the logarithm of the normalised mean \pm standard error of mean of 3 independent experiments. Upregulated genes take positive values while repressed gene expression are negative. 2 way ANOVA was performed, with a Tukey multiple comparisons test. * $P \leq 0.05$, ** $P \leq 0.01$ and *** $P \leq 0.001$ compared with normoxia. Table below shows mean change in gene expression of the target genes between tumours precultures in normoxia and those in hypoxia. Students unpaired t test was used to assess for statistical significance. ((n=3). * $p < 0.05$, ** $p < 0.01$, *** $p < 0.001$)

4.3 Discussion

Neuroblastoma is a highly heterogeneous disease partly due to the cells' diverse genotypes. (Von Stedingk, Gisselsson and Bexell, 2019). This diversity and the possible effects of MYC-N on the mechanisms of proliferation, survival, and metastasis should be considered when examining hypoxia's effect on neuroblastoma growth.

Hypoxia itself has been strongly associated with neuroblastoma induction, dedifferentiation and propagation. HIF-1 and -2 have been shown to recruit target genes in response to hypoxia. (Vega *et al.*, 2020b) Although there is no clear consensus, in general, HIF-2 α promotes an aggressive phenotype. In addition, HIF deregulation may play a role in the malignant transformation of neural crest cells, which form neuroblastoma tumours. (Holmquist-Mengelbier *et al.*, 2006)

Our data reflects the variable effect of hypoxia on the two distinct cell populations. Some gene expressions are similar in both groups with the introduction of hypoxia – *Bnip*; for example, others show a significant discrepancy, e.g. *E2f1*, which is much more highly expressed in MYCN-non-amplified cells in hypoxia than the MYCN amplified counterparts. Although MYCN amplification may drive antiapoptotic pathways through HIF-1 stabilisation, the relationship between MYCN, HIF and hypoxia is still not established. (B. Zhang *et al.*, 2014). We accept that this is only true of the two cell lines examined. The variability of MYC-N influence across a greater number of cell lines with differing MYC-N levels would have been conclusive.

HIF-2 α inhibitor PT2385 showed a minimal effect *in vitro* in the cell cycle assays and downstream gene expression analysis. The lack of effect on the cell cycle is consistent with the observations that shRNA- or siRNA-mediated HIF-2 α knockdown does not affect either cell proliferation *in vitro*, whereas PT2385 administration in the renal cell population affects the cell cycle. (Wallace *et al.*, 2016a). Contrary to previous results published with PT2385 in renal cancer cells, there was no change in the expression levels of key HIF-2 α target genes *in vitro* or *in vivo*. This may reflect the drug's lack of efficacy in neuroblastoma, but it must also be considered that there is much crosstalk between HIF-1 and HIF-2 α signalling pathways. Although HIF-2 α may be abrogated, the HIF-1 pathway continues to drive the expression of these essential hypoxia genes.

The formulations of the drug may also have had an impact. The *in vitro* formulation was a powder made to be dissolved in solvent (DMSO), whereas the *in vivo* compound was already in liquid form with a different solvent (PEG) used as the vehicle control in these experiments.

Although PT2385 did not affect cell proliferation in culture, it showed an inhibitory effect on tumour growth and metastasis within the chick model. Overall there was a reduction in the frequency of primary and metastatic tumours when treated with the HIF-2 α inhibitor and combined with a CDK4/6 inhibitor. The synthetic lethality between HIF-2 α inhibitors and Palbociclib has been previously described. (Nicholson *et al.*, 2019) They described how the antiproliferative activity of CDK4/6 was synergistic with HIF-2 α inhibition in clear cell renal cancer with VHL loss. The lethality between CDK4/6 and VHL was not HIF-dependent. Although VHL mutation is not commonly described in neuroblastoma, in 11q deleted SK-N-AS cells, the area that encompasses the locus of the von Hippel-Lindau gene (VHL, 3p25) is lost. (Hoebeeck *et al.*, 2006)

Research has shown that moderate levels of hypoxia may inhibit cell cycle progression through HIF-1 mediated increase in cyclin-dependent kinase inhibitors. (Goda *et al.*, 2003) In opposition, HIF-2 α has been linked with an upregulation in cyclin D in clear cell renal cancer and neuroblastoma. (Gordan *et al.*, 2007b). As Palbociclib inhibits cell cycle progression through dissociation of CDK4 and CDK6 from cyclin D, it is expected that combined inhibition of HIF-2 α and Palbociclib alongside HIF-1 mediated cell cycle arrest may inhibit tumour growth. Combination therapy in the chick embryo had more significant toxicity than either drug alone. However, there was a statistically significant reduction in metastasis formation in those chicks that did survive. As discussed above, this may be due to the small sample size and this experiment warrants further investigation.

VEGF-A is key in the pathological neo-angiogenesis seen in neuroblastoma. (Bäckman, Svensson and Christofferson, 2002). Targeting *Vegf* and, by proxy, tumour growth is an attractive venture. Tyrosine kinase receptor inhibitor, Sunitinib, showed promise in early investigations against metastatic neuroblastoma. However, this did not translate into clinical studies. (Zhang *et al.*, 2009) Indeed antiangiogenic therapies have been seen to trigger metastasis in some models. (Ribatti, 2013). Hypoxia significantly increases *Vegf* expression in neuroblastoma cell lines. (Qing *et al.*, 2010) The *Hif2* expression has closely been linked with *Vegf*, with high *Hif2* expression in progenitor cell populations of neuroblastoma patient samples correlated and colocalised with *Vegf* expression. (Holmquist-Mengelbier *et al.*, 2006). Studies have also shown strong co-localisation of HIF-1 with VEGF. In addition, inhibition of *Hif2* through microRNA 145 (miR-145) also downregulates *Vegf*. (H. Zhang *et al.*, 2014). Targeting VEGF and angiogenesis through HIF-2 α as a therapeutic strategy has come to light. In our work, we demonstrate that the administration

of PT2385 did not affect *Vegf* expression *in vitro* or *in vivo*. This may indicate that the drug is ineffective against VEGF or that the sampling method is inaccurate. Previous works have shown a heterogeneous expression of *Vegf* within a tumour. (Jögi *et al.*, 2002) The expression levels and protein levels of VEGF are also seen to be different depending on the size of the tumour. (Steliarova-Foucher *et al.*, 2017) Q-PCR is an extremely sensitive assay, and the heterogeneity within each tumour and between tumours have likely introduced variances in the results HIF-1 is also closely linked to VEGF and is not inhibited in these experiments. B-cell leukaemia 2 (Bcl -2) and extracellular-signal-regulated kinase (ERK1/2) have been implicated in apoptosis resistance of neuroblastoma through stabilisation of *Hif* and upregulation of *Vegf* in hypoxia. (Baek *et al.*, 2000; Das *et al.*, 2005). In addition, when *Hif1* is inhibited through Nutlin-3a, an MDM2 inhibitor, concurrent p53-independent inhibition of VEGF is seen. (Patterson *et al.*, 2011). Another method to examine the success of *Vegf* repression through HIF-2 α inhibition would have been to perform immunohistochemical staining for CD31 – a protein present within the endothelium of capillary cells and a marker of vascularity - on the treated and control tumour samples.(Miettinen, Lindenmayer and Chaubal, 1994).

Neuroblastoma cells adapt to hypoxia by HIF-dependent and HIF-independent responses. HIF-1 and HIF-2 share regulation over 16% of the same genes of the HIF-dependent responses. (Downes *et al.*, 2018). Although HIF inhibition is a viable strategy, it is impossible to predict a HIF inhibitor's impact without understanding the differential impact of singly inhibiting HIF-1 or HIF-2 in a pathway. Protein quantification of HIF-1 in the presence of HIF-2 inhibitors and combination therapy may have provided this critical information. Persson *et al.* showed no difference in HIF-1 protein levels in patient-derived xenograft cells when treated with 1 μ M and 5 μ M PT2385. Interestingly, there was little change in HIF-2 α protein expression in normoxia, but the cells were more sensitive to treatment in hypoxia. (Persson *et al.*, 2020a)

Untangling the molecular mechanisms involved in neuroblastoma growth and metastasis is ongoing. The combined role of MYC-N, HIF and hypoxia is still controversial. The development of hypoxic 3D models will be vital in understanding these pathways in a translatable way. I have shown here that although there to no change in gene expression detected with treatment in cells or tumours, there is a difference in the number of tumours formed and the number of metastases seen in the chick. We concede that further experimentation with more significant numbers may negate this significance, but it does highlight the differences between *in vitro* and *in vivo* testing

and the utility of the chick embryo model to evaluate treatment response. The effects of PT2385 on neuroblastoma have only been, to our knowledge, published twice before. (Persson *et al.*, 2020a)(Westerlund *et al.*, 2017a) Our results also reflect those published within mouse models. Persson *et al.* treated orthotopically transplanted patient-derived neuroblastoma tumour cells into immunocompromised mice and monitored tumour growth with treatment with PT2385. After 14 days, they did not observe any difference in tumour growth between the control and treatment groups. (Persson *et al.*, 2020a) Westlund *et al.* examined the impact of PT2385 treatment in combination with differentiation agent retinoic acid. To this end, they found that the addition of PT2385 diminished the growth inhibitory effect of retinoic acid treatment. (Westerlund *et al.*, 2017b). Neither group examined the effect of HIF-2 α inhibition on the metastatic burden. The findings from our work and others raise questions about other mechanisms involved, as HIF-2 α has been demonstrated to maintain the undifferentiated state of neuroblastoma cells. (Pietras *et al.*, 2009a)

There are limitations to the chick model when studying the effects of hypoxia. The chick embryo is a self-contained model. The oxygenation status during avian embryogenesis is complex since O₂ continuously equilibrates across the porous eggshell. Our experiments incubate the chicks at atmospheric oxygen levels (21%). However, this does not reflect the oxygen tension within the chick. It is understood that the embryo develops in a hypoxic environment, with oxygen levels varying from 10% in the allantoic vein and 2% in the artery between days 10-16. (Hiroshi and Masaji, 1977) This variation in the oxygen tension within the embryo and between embryos is unavoidable and needs to be acknowledged when looking at changes due to hypoxia within the model.

Another potential source of error comes from the method of implantation of the cells. Although the cells are precultured in hypoxia, when they are prepared for implantation, this happens on the lab bench in atmospheric conditions. This process has been streamlined to avoid unnecessary exposure to normoxia conditions, but this may affect the hypoxia signalling within the cells. I have previously shown that the oxygen tensions within tumours grown from cells precultured in normoxia and hypoxia are different. (Al-Mutawa, 2017) The mean oxygen tension in tumours precultured in normoxia is 0.98% compared to 0.63% in hypoxic tumours. This work also showed the high tumour-to-tumour variability in oxygen levels, even within the same batch of eggs.

Immunohistochemistry-based analysis of tumour tissue labelled with protein markers may provide more accurate quantification and reflect the heterogeneity within the samples more faithfully.

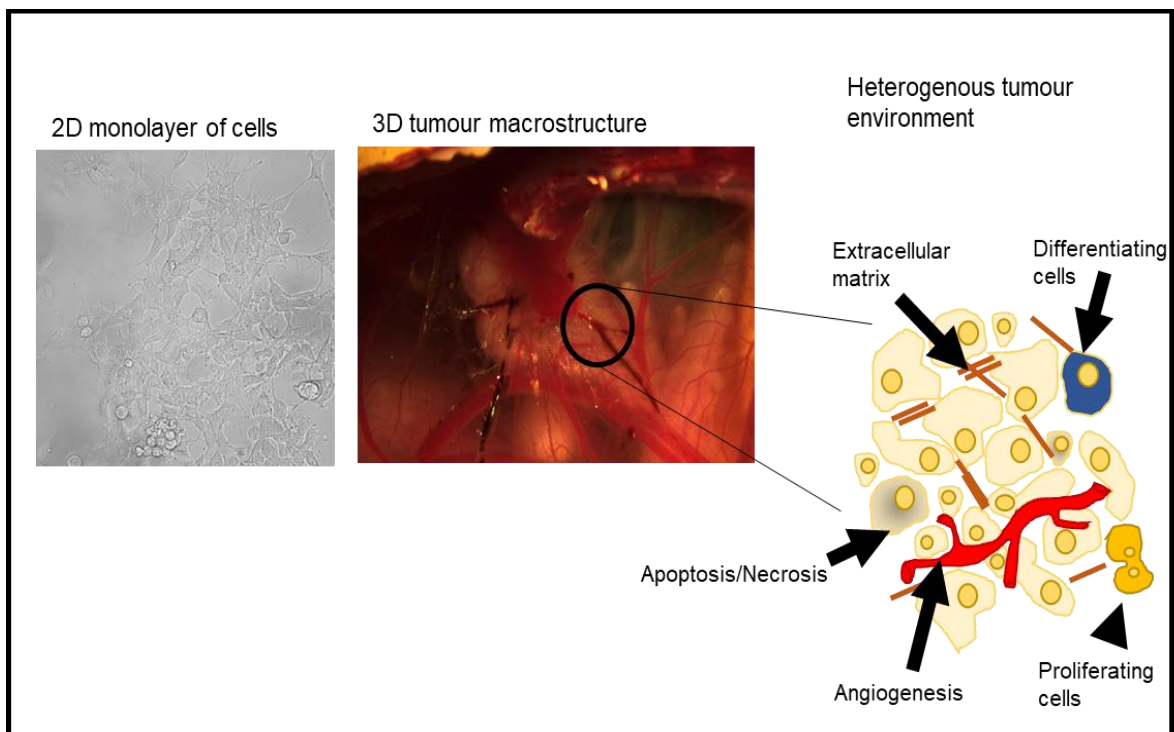
The potential of PT2385 as a therapy for neuroblastoma needs further evaluation. Although there have been positive results in ccRCC preclinical and clinical trials, there is no objective change in tumour burden with treatment within our cell population. The biological responses to PT2385 need more in-depth investigation as compensatory mechanisms by HIF-1 or other oncogenes may abrogate the drug's effect.

Chapter 5 : Utilising advanced microscopy techniques to monitor neuroblastoma growth and tumour response to therapy

5.1 Introduction

Whole tumours are three-dimensional structures containing multiple cell populations of different sizes, densities and genetic and phenotypic compositions (**Figure 5.1**). Advances in non-invasive *in vivo* 3D imaging, such as magnetic resonance imaging and computed tomography, can visualise the tumour and surrounding tissues. (Frangioni, 2008) These modalities have vastly improved the clinical assessment of cancers. However, the resolution is insufficient for cellular and subcellular visualisation, so accurate analysis of a solid tumour's microscopic characteristics cannot be ascertained with such approaches.

Figure 5.1 *Biology occurs in three dimensions.*

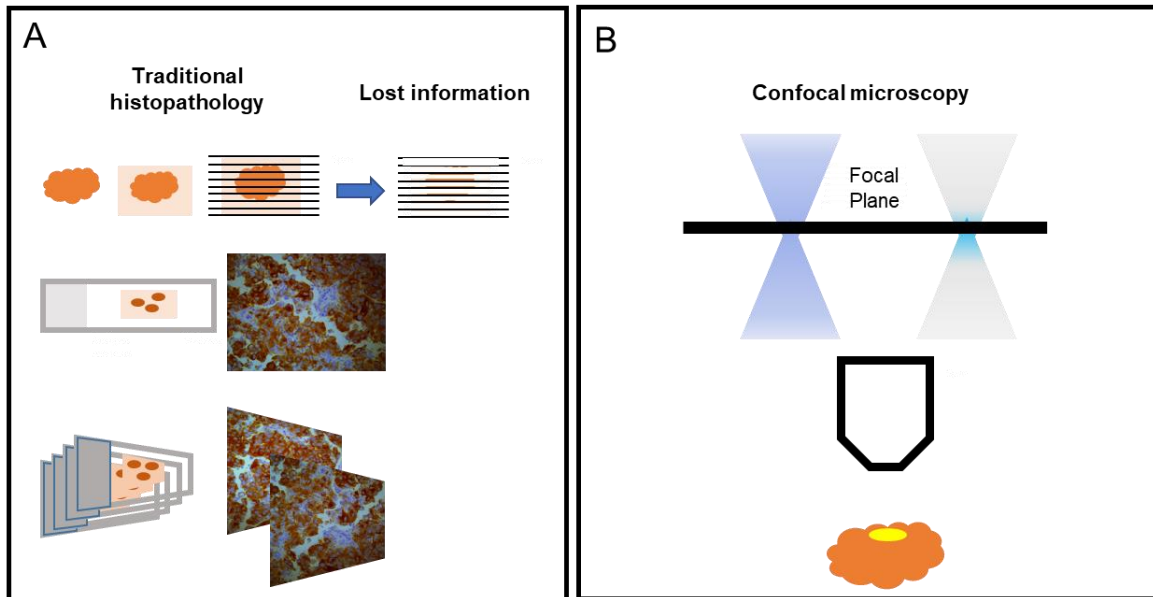


The analysis of cellular and tissue characteristics needs to occur in volumes rather than section. 2D analysis loses the inherent structure of cells and organs. Cells which are proliferating or differentiating outside the field of view may be lost to analysis. Structures such as nerves and vessels extend in many directions and their true nature cannot be completely understood by a thin section.

Histopathology is the 'traditional' field of interrogating whole tumour tissue's structural and pathological changes. Histology is invaluable in current cancer diagnosis, staging, and therapy evaluation. In practice, dissected tumour tissue is fixed, sectioned into 5-10 μm slices, and labelled using dyes or antibodies for specific markers of interest. The section is then examined under a widefield microscope. Such 2D sections visually represent the overall structure of a layer of tumour tissue. The process is repeated throughout the tumour at different locations to enable an assumed accurate depiction of the whole. Although this is the gold standard, it must be conceded that serial 2D sections cannot show the whole tumour and information between the chosen cross-sections is inevitably lost. **(Figure 5.2)** Imaging tumours in 3D offers a more physiological representation of their large-scale spatial organisation and cellular characteristics. By extension, the whole tumour analysis can provide quantifiable measurements of the effect of novel therapeutics on cellular features (proliferation, apoptosis and differentiation) and the associated extracellular environment (collagen, angiogenesis).

The advent of confocal microscopy heralded a new era of tissue imaging. Confocal imaging detected fluorescent signals from a single point of interest. The light from above and around this point was reduced, limiting the 'noise' within the image. Fluorescently labelled samples could be imaged without 'physical' sectioning by utilising 'optical' sectioning. This optical image can then be stacked with others from the same X and Y planes and rendered into a 3D image. Although confocal microscopy is still limited to imaging thin sections, the technology paved the way for the development of multiphoton, spinning disc and lightsheet microscopy, all of which can image more deeply into the tissue.

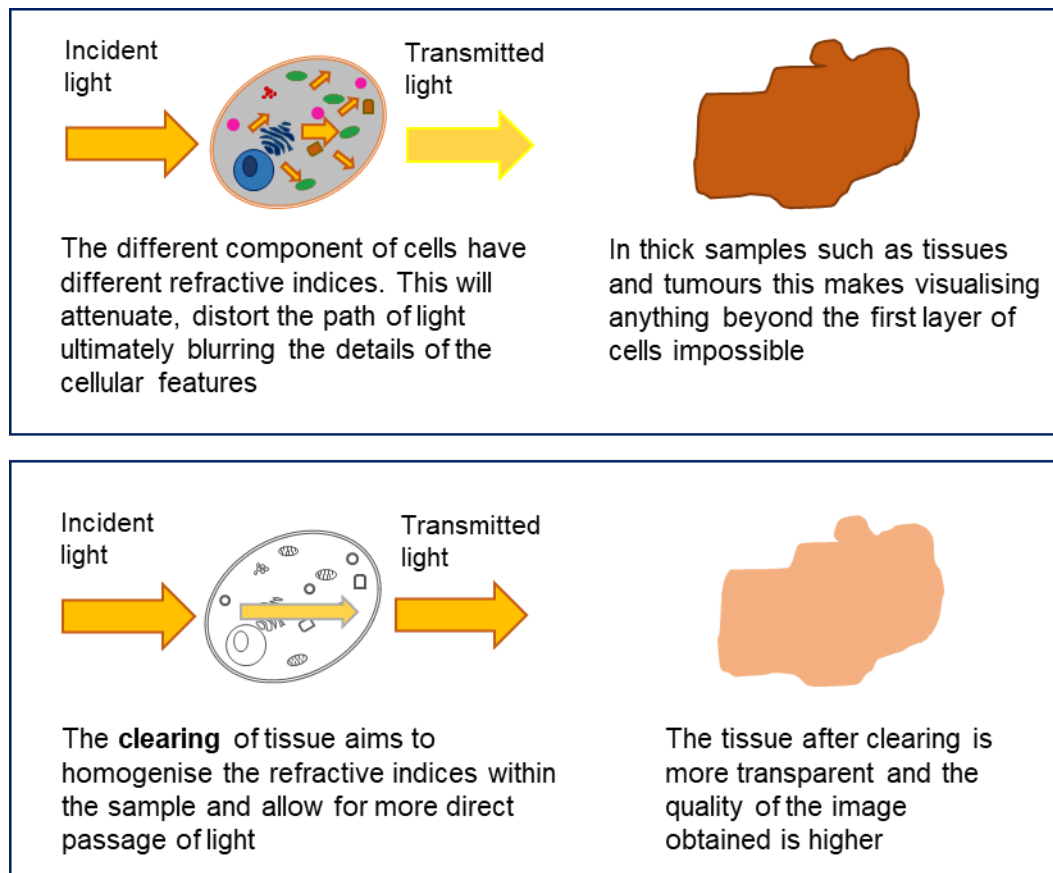
Figure 5.2 Traditional tissue analysis and the principles of two photon microscopy.



A) The sectioning of tissue can lead to loss of data. Physical sectioning cannot allow for scanning through tissue in the z-axis with ease. B) Confocal microscopy highlights single plane of view within tissue samples, thereby reducing noise from the planes above and below. These individual images can be compiled into a 'z stack' allowing rapid screening through the z axis.

One of the benefits of physically sectioning tissue for histology is to allow light transmission from the objective to the detector in the microscope. Optical sectioning is hindered by reduced light penetration through an opaque sample. Tissue opacity is predominantly due to refractive index mismatching between different tissue interfaces or scattering and absorption of light by lipids, collagen and heme groups. (Richardson and Lichtman, 2015) 'Clearing' is a method that aims to introduce homogeneity to the refractive indexes within the tissue, reduce light-absorbing and light scattering groups and ultimately improve light transmission. (**Figure 5.3**)

Figure 5.3 The principals of clearing.



Light scattering and absorption are the leading causes of tissue opacity, which blocks light transmission through a sample. Light scattering is caused by heterogeneous components such as lipids and proteins. Light absorption is due to endogenous light absorbers like heme. Tissue clearing technique makes tissue optically transparent by minimizing light scattering and light absorption

The steps involved in whole tissue imaging are generally: 1) to clear the opaque tissue so it is transparent for microscopy, 2) to immunolabel the sample for protein or cell type detection and 3) to image the tissue using confocal, multiphoton or light-sheet microscopy and to analyse the image data for required parameters. Multiple optimisations are required to tailor the process to the specific tissue and the data required within each step.

Numerous organic and aqueous-based tissue clearing techniques are outlined in the scientific literature, covered extensively in Chapter 1 - Introduction.

The ideal method should meet the following criteria:

- i) quick and straightforward to complete,
- ii) preserving the structural integrity of the tissue
- iii) effective sample clearing
- iv) retaining the endogenous fluorescent signal whilst limiting autofluorescence
- v) can be labelled using fluorescent labelled antibodies or nanoparticles
- vi) be compatible with imaging facilities available.

There is no one ideal clearing solution for all tissues. Each method and imaging modality presents its advantages and limitations. The quality and quantity of endogenous signals and the preservation of tissue structure must all be considered. No published literature outlines the utility of clearing and high-resolution microscopy in developing novel therapies for neuroblastoma.

5.2 Chapter objectives

The work described in this chapter aims to develop a high-fidelity workflow and method to assess neuroblastoma's cellular and structural characteristics. This will be done by:

1. Determining the best-suited clearing method for green fluorescent protein (GFP) labelled neuroblastoma tumours
2. Assessing the advantages and limitations of the imaging modalities available at the Centre for Cell Imaging, University of Liverpool
3. Using immunofluorescent labelling and imaging techniques to detect proteins of interest within the sample and obtain qualitative and quantitative data similar to traditional immunohistochemistry methods.

5.3 Results

5.3.1 Assessing the compatibility of clearing methods with neuroblastoma tumour samples grown in the chick embryo

The initial consideration when selecting a method of clearing is the sample type. It is essential for the clearing method to neither quench nor artificially enhance the endogenous fluorescent signal. Also, particular tissues may have a higher proportion of light-absorbing compounds such as heme, so a clearing method to eliminate this property whilst preserving the sample's integrity is needed. Neuroblastoma tumour samples are highly heterogeneous, unlike the brains often discussed in clearing protocols. The tumours vary from less than 1 mm to almost 1 cm in diameter. Some samples are highly vascularised and may also have blood trapped within the tumour. All the samples used within this work have grown from green fluorescent protein (GFP) transduced cells, so any clearing methods that may alter this endogenous fluorescent signal are, therefore, unsuitable.

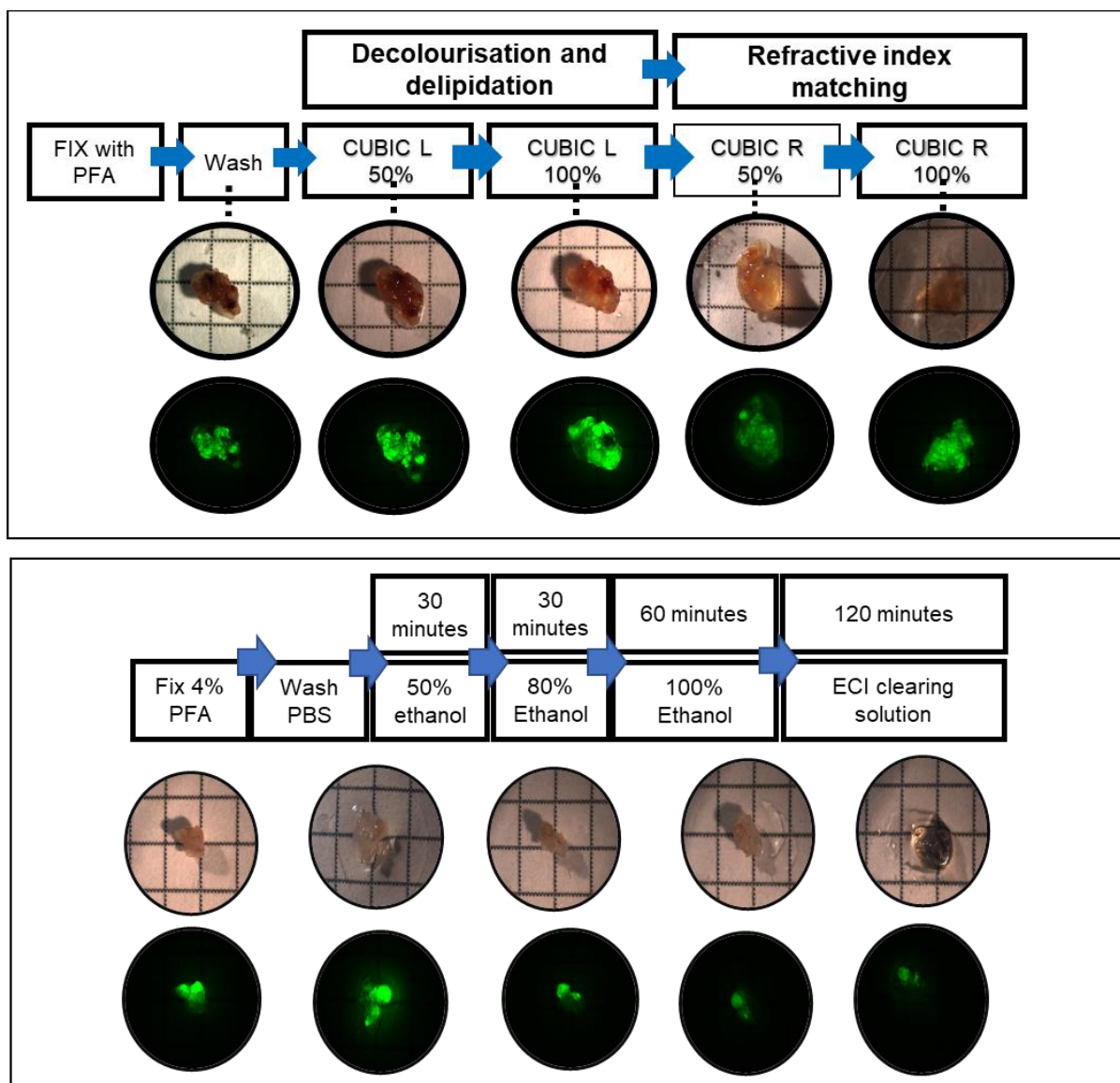
The Clear, Unobstructed Brain/Body Imaging Cocktails and Computational Analysis (CUBIC) clearing method was first described by Susaki *et al.* in 2014. (Susaki *et al.*, 2014a). CUBIC-CANCER is a modified method shown to clear a whole mouse whilst preserving the fluorescence of low densities of fluorescently labelled cells. (Shimpei I Kubota *et al.*, 2017) The protocol comprises immersion within four solutions, firstly in the delipidation steps followed by the refractive index matching steps. Kubota *et al.* also showed compatibility of immunolabelling within the CUBIC CANCER protocol. Overall, the protocol is straightforward, gentle to the sample, requires no special equipment, and quick for smaller specimens.

Ethyl-3-phenylprop-2-enoate or Ethyl cinnamate (ECI) is Food and Drug Administration-approved food flavour additive. (Wang *et al.*, 2016) It is a non-toxic organic solvent that can be used for clearing. (Masselink *et al.*, 2019) The successful use of ECI in clearing mouse kidneys – similar to heterogeneous tumours in the high heme content, fibrous tissue and size – was the leading proponent in choosing this method. (Klingberg *et al.*, 2017) ECI and CUBIC clearing protocols were chosen: Neither protocol required specialised equipment. They both involved simple immersion steps. ECI was reported to be effective in highly dense renal tissue, which we felt would be advantageous in clearing blood-filled tumours. CUBIC cancer has already been shown to be efficacious in tumour imaging. Notably, both methods are reported to preserve endogenous

signals and not damage tissue samples. Other organic solvent-based clearing methods, such as FDISCO have also been effective at clearing tumour tissues; however, the chemicals used can quench endogenous fluorescence and solvents can corrode/erode glues within microscope objectives.

All samples used for clearing and imaging are GFP-labelled neuroblastoma tumours grown in the chick embryo model unless otherwise stated. All samples were dissected on embryonic day 14. Samples were washed, weighed, and the dimensions measured and fixed in 4% PFA for 2 hours. We implemented CUBIC CANCER and ECI clearing methods on several tumour samples to examine the clearing capacity and endogenous GFP preservation. Samples were chosen to represent the diversity in size, heme content, and presence of the extracellular matrix. CUBIC and ECI achieved very similar results on gross examination. The clearing protocols both took less than 8 hours for the samples used. **(Figure 5.4)**.

Figure 5.4 Examples of workflow for A) CUBIC Cancer and B) ECI clearing.



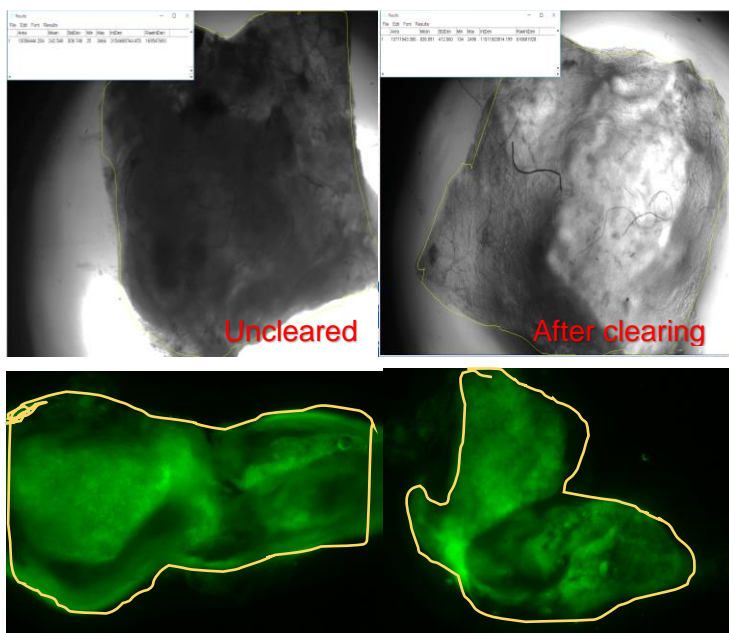
The brightfield and GFP images of tumours taken at each stage of the protocol are displayed. Clearing is broadly made of 3 stages: 1) Tissue fixation to preserve the structural information. This is done for both protocols using 4% paraformaldehyde. 2) Permeabilization using agents such as solvents or delipidising reagents to promote the diffusion of the refractive index matching medium and antibodies into the sample. In CUBIC Cancer this is done with buffer CUBIC L and in ECI clearing this is done with ethanol immersion. 3) The refractive index matching step to ensure an equilibration of the refractive index within the whole tissue. The timing of the immersion steps will vary depending on the composition and size of the tissue.

5.3.2 Optimising the increase in light transmission and GFP intensity as a function of incubation times for the CUBIC clearing protocol.

CUBIC-Cancer and ECI protocols could preserve the GFP signal expressed by the neuroblastoma tumours while rendering the sample macroscopically more 'transparent'. Published protocols for CUBIC Cancer do not outline immersion times for small tumour samples, and ECI protocols give time outlines for murine kidneys of a similar size, but again not tumour samples. CUBIC and ECI clearing immersion times were optimised for our samples to stop unnecessary exposure to chemicals. Samples were dissected from the chick embryo and fixed in PFA 4%. For normalised brightfield and fluorescence analysis, mean intensity signals from the tumours ($n = 2-5$) were recorded using Zeiss axiovert S100 TV. CUBIC-cleared sample images were taken at 1, 2, 3, and 5 hours after immersion in the four clearing solutions: L1, L2, R1, and R2.

The increase in the transparency of the samples was calculated as the 'increase in mean light intensity.' More transparent samples will allow white light to pass through to the camera so that the resulting imaging will have a higher mean light intensity. The GFP signal from samples after each immersion time was recorded for the fluorescence loss analysis. After subtracting background values, all signal values were normalised and plotted on the line diagram. The background signal was determined as the average signal from 4 areas of the image where no tumour signal was visible. (**Figure 5.5**) ImageJ was used to process raw images, and the selected background areas were adjacent to signal areas. Excel was used to execute the signal intensity analysis. All data are plotted as individual values to demonstrate intertumoral variability.

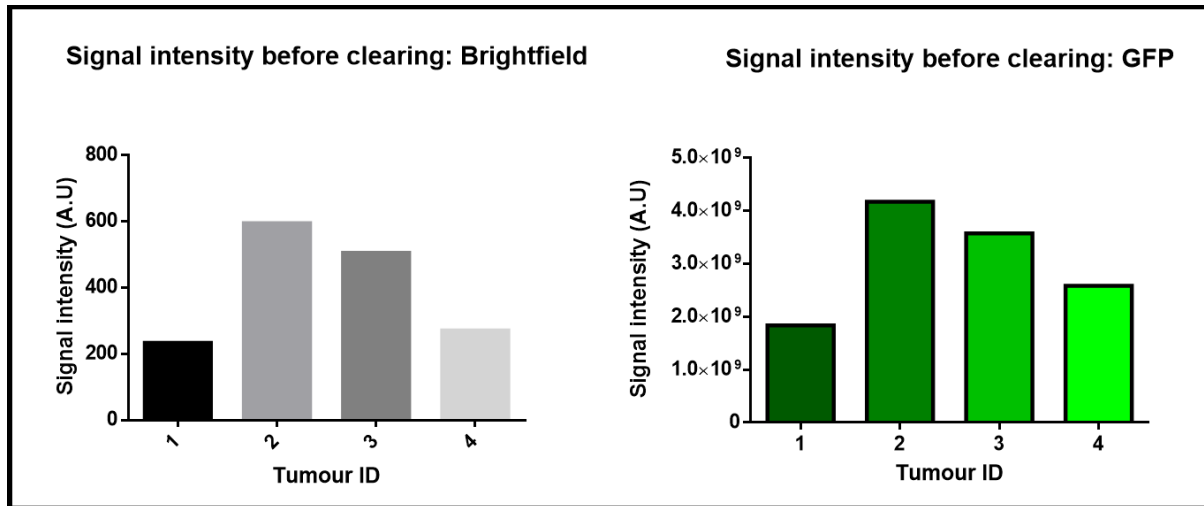
Figure 5.5 Calculating the increase in light transmission in pre- and post- clearing tumours.



Acquisition settings were kept constant between measurements. Samples were imaged 3 times in different orientations, and the difference in mean intensity calculated. Intensity was calculated using Fiji software. The tumours within the images were marked as a region of interest and the average signal intensity within that area was calculated by the software. This was done using 3 different images for each sample at each time point and the average value taken. Images taken using Zeiss Axiovert S100 TV Inverted Microscope with the: 5x, 0.25 N.A. objective

There was sample variability in size, cell density or amount of heme/blood within the tissue. **Figure 5.6** illustrates the samples' different brightfield and fluorescence intensity before clearing with CUBIC. In general, samples with low brightfield signal levels also exhibited low GFP signal levels.

Figure 5.6 The brightfield and GFP signal intensity of samples before clearing.



This figure illustrates the heterogeneity between the samples. The average signal density in brightfield and GFP channels were measured for 4 neuroblastoma tumours of similar size. Tumours allowing only low levels of light transmission in brightfield also had low levels of GFP signal before clearing.

The data shown in **Figure 5.7** is discussed below:

Step 1: L1 Immersion, timing optimisation

There was a statistically significant difference in brightfield signal intensity between all immersion times and the control as determined by a one-way ANOVA ($p=0.016$). As multiple time points were being compared, we conducted a Bonferroni posthoc test to identify which groups differed. This showed a difference between 1 hour and 2 hours immersion versus control ($p= 0.04$ and 0.05 , respectively). There was no significant change in the GFP signal between 0 hours and all immersion times ($p= 0.26$). Based on these findings, an immersion length of 1 hour was chosen for L1.

Step 2: L2 Immersion, timing optimisation:

There was a statistically significant difference between all immersion times and the control as determined by a one-way ANOVA ($p=<0.015$). A Bonferroni post hoc test showed a difference between 1 hour versus control. There was no statistically significant change between 2-5 hours of immersion for the brightfield signal. There was no significant change in the GFP signal between

0 hours and all immersion times ($p= 0.28$). Based on these findings, an immersion duration of 1 hour was chosen for L2.

Step 3: R1 Immersion, timing optimisation:

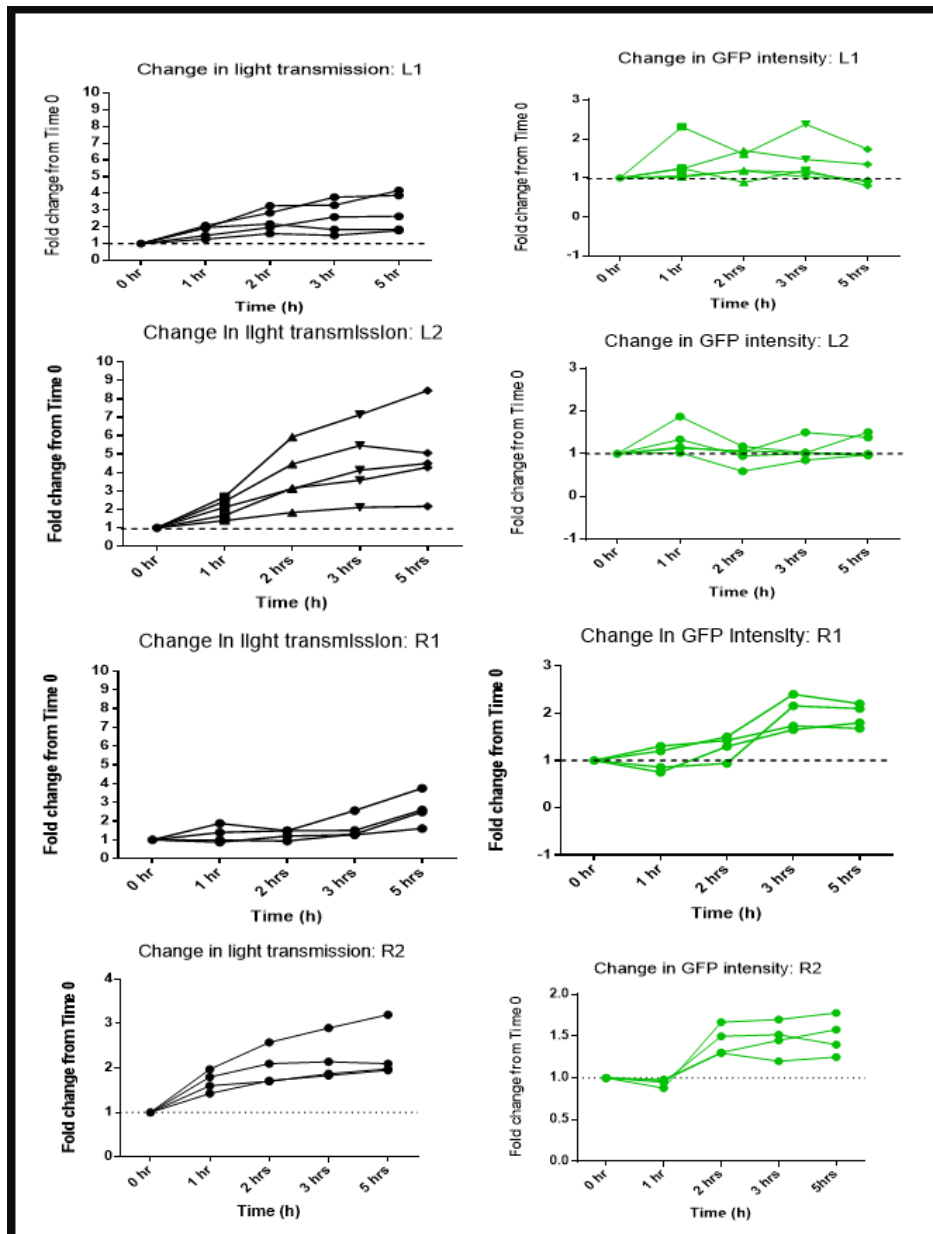
The refractive index matching steps (R1 and R2) allowed us to gain the most significant increase in transparency of the sample. This is reflected in the one-way ANOVA that showed a statistical difference between R1 immersion and after R1 immersion ($p=0.027$). There was a significant change up to the 5-hour endpoint ($p=0.04$). The GFP signal increase reached significance after 3 hours of immersion. As there is no loss of GFP signal with increased R1 immersion times, a time of 5 hours was chosen for R1, providing maximum transparency.

Step 4: R2 Immersion, timing optimisation

The R2 immersion solution is also the storage solution for CUBIC Cancer cleared samples. This experiment was stopped after 5 hours. A statistically significant increase in light transmission between 0 hours and 5 hours of R2 clearing ($p=0.015$) was seen. There was no statistically significant change in light transmission after 3 hours of R2 immersion. If samples were to be imaged immediately after the R2 step, an immersion time of a minimum of 3 hours should be used.

There was variability between the tumours, as highlighted in [Figure 5.6](#). As the tumours moved through the clearing stages, this inter-tumour heterogeneity in the transparency persisted: there was a statistical inter-tumour variability in light transmission between tumours after R2 clearing as calculated with ANOVA analysis. ($p=0.023$). This was in contrast to the GFP signal, where the differences in the intensities at the beginning of the clearing process were no longer measurable by the end stage, as assessed by ANOVA ($p= 0.3$). This is in keeping with biology – as the heterogeneous light-refracting elements are removed through the clearing process, leaving the neuroblastoma cells, which should have the same characteristics in each sample.

Figure 5.7 The fold change in light change and GFP intensity over time with CUBIC Clearing.



The imaging of tumours samples before and after each step of CUBIC clearing by Zeiss axiovert 8100 TV or Leica DFC450C under the same imaging conditions. Images were taken to show fold change in signal intensity in brightfield and fluorescence signals. Data is shown as individual tumour values (n=4). Statistical significance (* $P < .05$) was assessed by one-way ANOVA followed by Bonferroni's multiple comparison tests.

5.3.3 Optimising the increase in light transmission and GFP intensity by evaluating immersion times for the ECI protocol

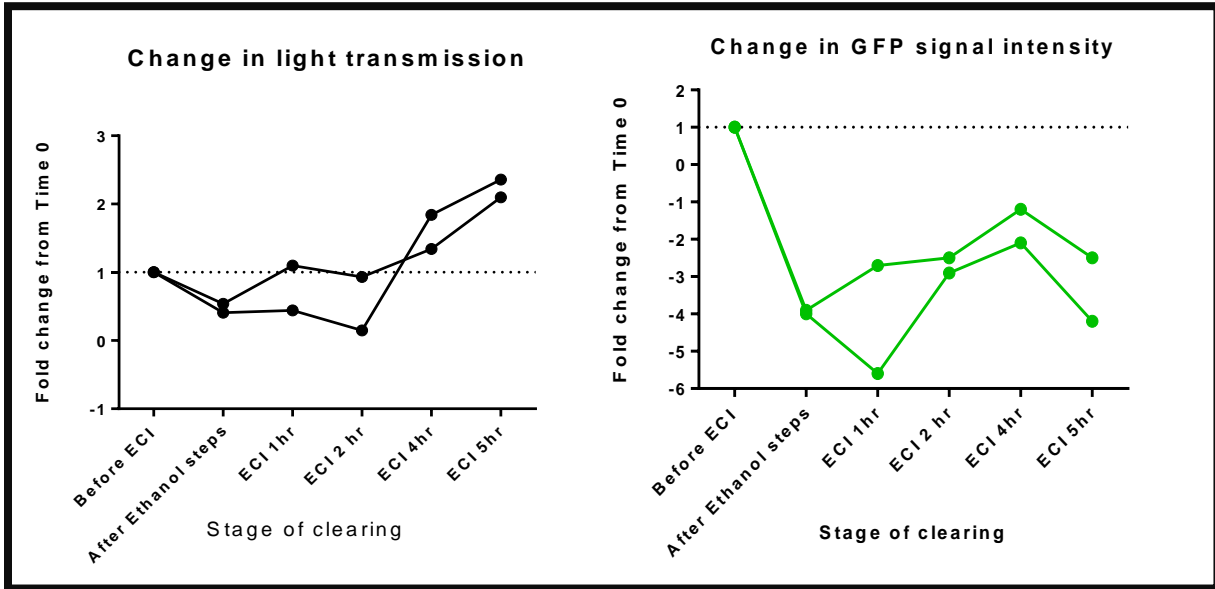
The ECI protocol contains the following steps:

1. Dehydration:
 - a. 30 minutes 50% ethanol
 - b. 30 minutes 80% ethanol
 - c. 1 hour 100% ethanol
 - d. 2 hours Ethyl cinnamate.

As this protocol was optimised for renal samples, serial imaging was performed to assess tumour samples' suitability. The dehydration steps are the same as outlined in the literature; however, increasing ECI immersion times were performed (**Figure 5.8**).

The dehydration steps are not expected to increase the sample's transparency, so the starting point for measuring light transmission was after the dehydration steps, before immersion into ECI. As only two tumours were imaged, no statistical analysis was performed. The light transmission line graph shows that the clearing steps with ECI increased the sample's transparency after 3 hours of immersion. In contrast, there was a loss of GFP signal within only 1 hour of ECI immersion. However, as the transparency increased after 2-3 hours of immersion, there was an upward trend in the GFP signal intensity, thanks to the clearing. Despite this, the relative GFP signal from the cleared ECI tumour sample was less than the original at the end of the clearing protocol. This pattern could reflect an initial increase in GFP as the sample is more transparent; therefore, more fluorescent signal is detected, followed by quenching of this signal over time in immersion solutions.

Figure 5.8 The fold change in light transmission and GFP intensity over time with ECI clearing.



The data demonstrates that ECI immersion increasing light transmission up to the end point of this experiment – 5 hours. Overall there was a fold reduction in GFP intensity – dropping to 4x less than the starting GFP intensity – dropping to 4x less than the starting GFP intensity at 2 hours, followed by an increase to 2-fold less at 4 hours. N=2.

5.3.4 Evaluating the depth of imaging after clearing

We used an Andor Dragonfly SPIM microscope to assess the impact of clearing on the depth penetration of laser light. For each clearing protocol, tumours of varying size and density were imaged before and after the clearing. Each tumour was imaged at random y and x positions in the sample four times. At each point, a z-stack was taken, with a 2µm depth between each frame. The Z-stack limits were set from the first point of the visible GFP signal and ended when no further signal was seen. The tumours were imaged the same way after the clearing process; however, the imaging points differed according to each protocol.

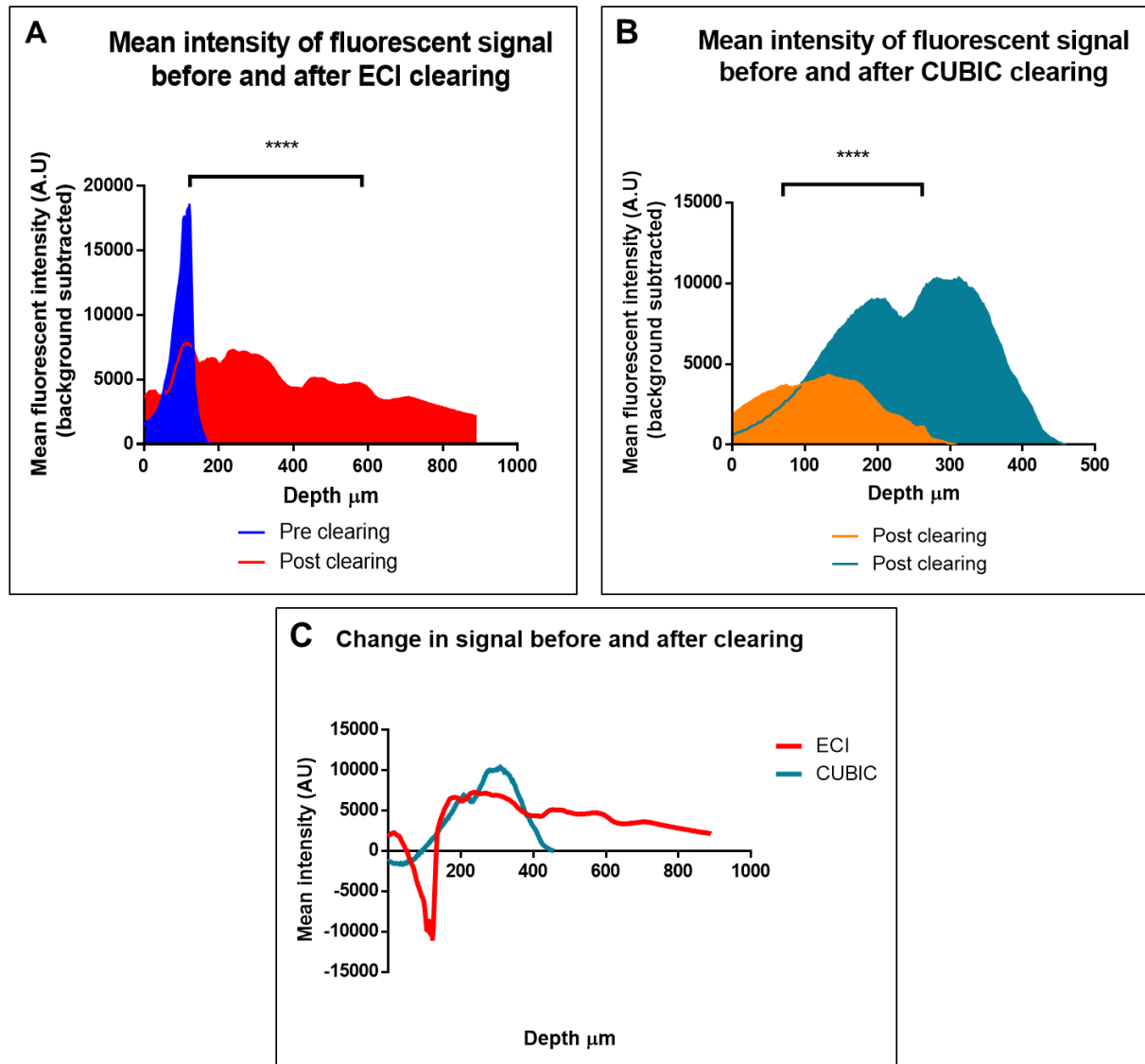
The depth penetration was calculated as the mean fluorescent intensity minus the background signal within each frame. The background signal was calculated as the lowest mean intensity frame from each z stack – this was a frame with no apparent GFP signal. The process was repeated for all z stacks. The average signal intensity (minus background) was plotted against depth (µm).

The graph for ECI clearing conditions (**Figure 5.8**) showed a high fluorescent mean intensity (17000 A.U. at 100 μm depth) before clearing. This signal rapidly decreased, with little signal detected over 200 μm depth. After clearing, the high-intensity peak was no longer seen, although there was a low-level signal up to 900 μm . It is important to note that the clearing efforts with ECI were highly variable; in some tumours, there was an increase in depth penetration and signal intensity, as shown in **Figure 5.8**. However, in other samples, there was no change in depth penetration but an increase in the GFP signal. This signal was not from the neuroblastoma GFP labelled cells but the chick tissue. ECI, therefore, increased the autofluorescence of the surrounding tissue. Despite subtracting the background signal in the data shown in **Figure 5.8**, it was not possible to accurately isolate only the neuroblastoma signal. The signal after 800 μm was not recorded as the microscope had reached the maximum imaging depth.

The graph for CUBIC CANCER cleared samples (**Figure 5.9**) shows that before clearing, the average fluorescent intensity signal was at a maximum of 4000 A.U. and reached a maximum depth of 300 μm . In contrast, after clearing, the maximum signal was 10000 A.U. with a maximum depth of 450 μm . Therefore, there was a doubling in signal strength and a 1.5-fold increase in depth. It is also worth noting that although there was a signal detected at over 400 μm before clearing, the image quality was poor.

When comparing the two clearing methods on the same graph (**Figure 5.9c**), CUBIC increased the depth and signal intensity; however, the ECI caused a reduction in the GFP signal with far less depth penetration overall. Images of tumours undergoing CUBIC clearing demonstrated a deeper light penetration and a higher signal than uncleared tumours. Images of ECI-cleared tumours may also display signals at greater depths, but this signal's overall intensity was weaker and may be derived from autofluorescence. In contrast, CUBIC Cancer achieved greater depth penetration, preserved endogenous GFP signal and had a minimal auto-fluorescence effect on the samples compared to ECI clearing.

Figure 5.9 Comparing the mean intensity of fluorescent signal over depth in samples before and after clearing

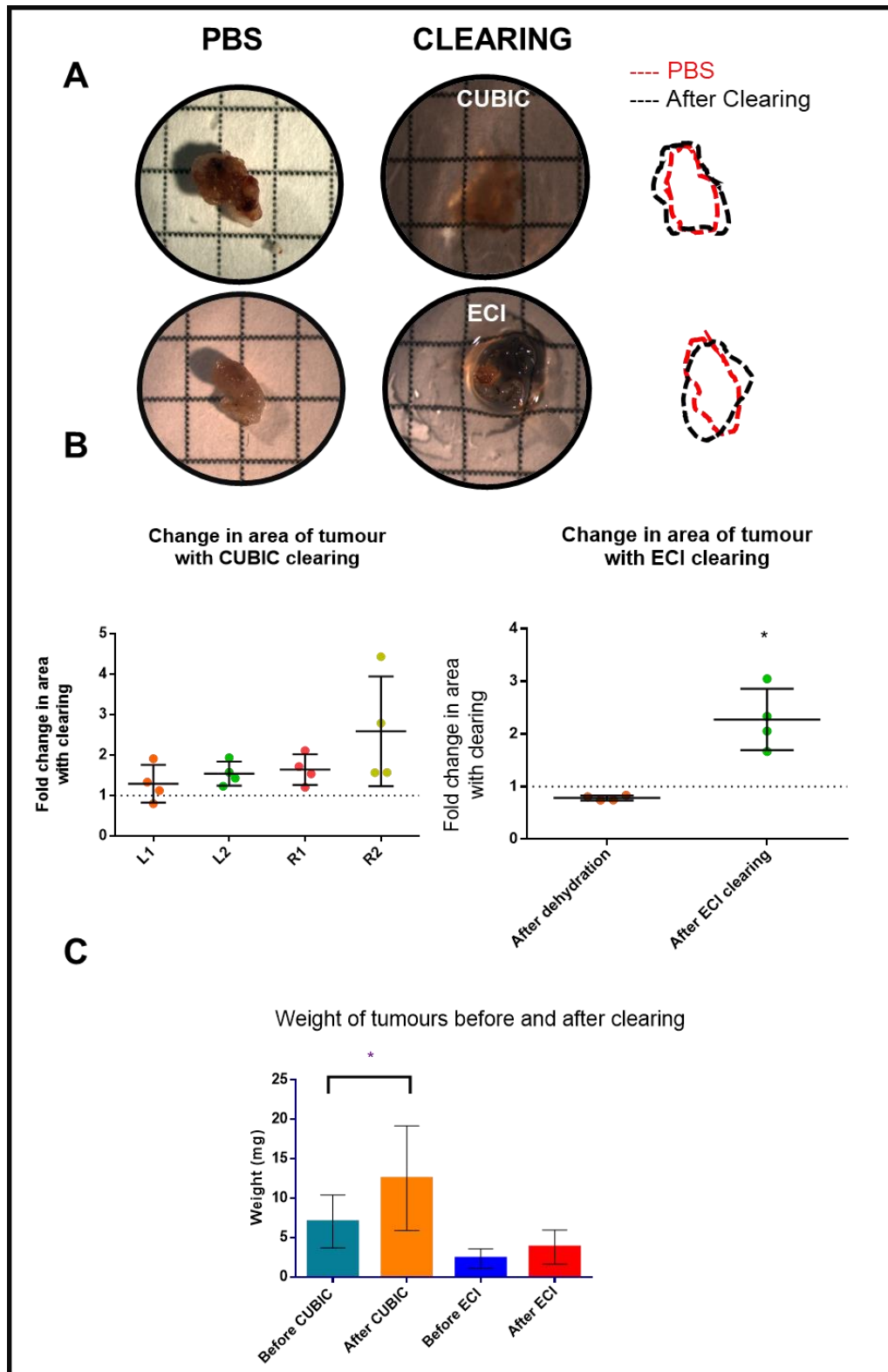


A) ECI clearing and B) CUBIC clearing. C) Comparing the change in mean fluorescent signal intensity over depth between ECI and CUBIC cleared samples after clearing. All values are means ($n = 4$); statistical significance in B ($****P < 0.0001$) was assessed by an unpaired two tailed t test.

5.3.5 Evaluating the distorting effect of clearing protocols on tumour samples

The macroscopic changes not only improve light penetration but can also impact the samples' weight and size. Indeed, clearing methods can cause samples to swell excessively or shrink, thereby distorting the microscopic architecture for analysis. We, therefore, decided to assess sample distortion. The sample linear expansion or shrinkage measurements were based on the brightfield images. The tumour was outlined to measure the area using FIJI software's polygon selections function. The pixel area change quantified the size change value (**Figure 5.10**).

Figure 5.10 Assessing gross change in area and weight of tumours after clearing. A) Example of tumour measurements before and after the clearing steps



A) Brightfield images of tumour samples before and after CUBIC and ECI clearing protocols. Dotted line diagrams demonstrate linear size change. B) Quantification of the tumour size changes upon clearing. Tumours were photographed as shown in A) and the area was calculated between each step, using IMAGEJ. The sample's overall area was calculated as the average area of 3 images taken in different positions. The fold change for each sample and mean \pm SD is shown. Two tailed paired t-test was used to test for statistical difference between each step. Statistical significance was assessed using paired t test ($P < 0.05$). There was no change in the CUBIC group. There was a statistically significant change between pre ECI and after ECI area ($p = 0.01$) C) Absolute weights of the samples before and after clearing. Values are means ($n = 4$) \pm SD. Statistical significance was assessed using paired t test (* $P < 0.05$). There was a statistically significant change in the weight of CUBIC tumours after clearing ($p = 0.04$) but no change in ECI tumours.*

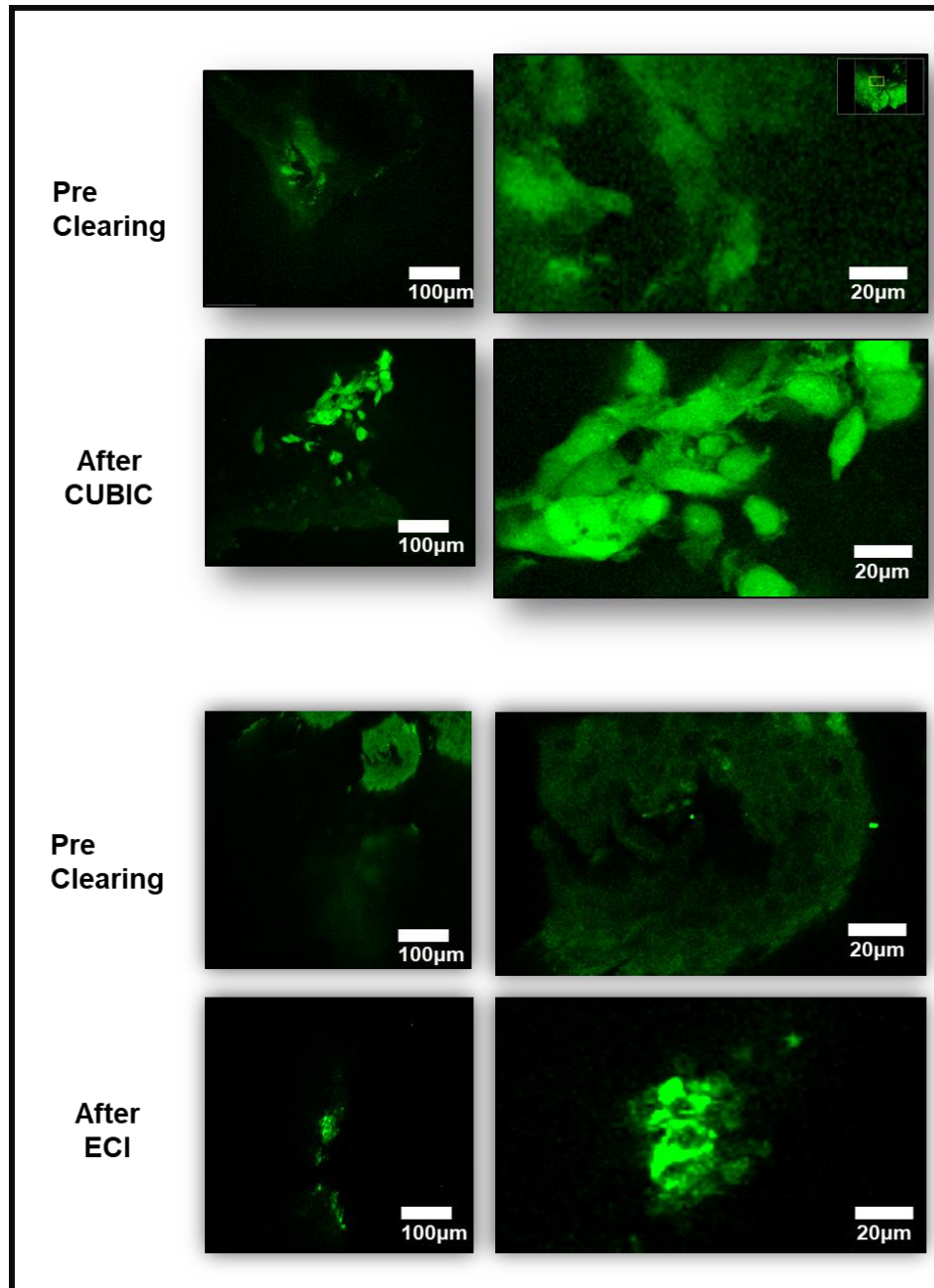
As shown in **Figure 5.10** there are changes to the tumour sample's overall size and weight upon clearing. For the CUBIC-cleared samples, we observed a significant 44% increase in the samples' weight ($p = 0.043$). This was accompanied by a size increase, albeit non-significant ($p = 0.06$). In contrast, upon ECI clearing, we observed a 36% increase in sample weight, which was not statistically significant ($p = 0.063$), and associated with an overall increased size ($p = 0.014$). It should be noted that the dehydration steps caused an initial sample shrinkage.

The average weight in the CUBIC clearing tumours was higher than in the ECI group. The absolute change is shown in **Figure 5.10 C**. A change in the weight of the sample without a change in the area is more likely to represent the storage liquid in which they are immersed. CUBIC cancer R2 storage liquid is a dense and viscous liquid, and when weighing the samples after immersion, it is likely to contribute to the weight observed.

5.3.6 Evaluation of microscopic appearance of cells with tumour sample after clearing

Investigating the relationship between tissue weight and area change with distortion to the cell morphology is necessary. The tumours were therefore imaged before and after clearing. (**Figure 5.11**). We confirmed that the cellular architecture was preserved with CUBIC despite the tumour's overall change in area and weight. However, this was not the case for ECI clearing, where there was little clear cellular structure visible afterwards.

Figure 5.11 Preservation of cellular morphology upon clearing.



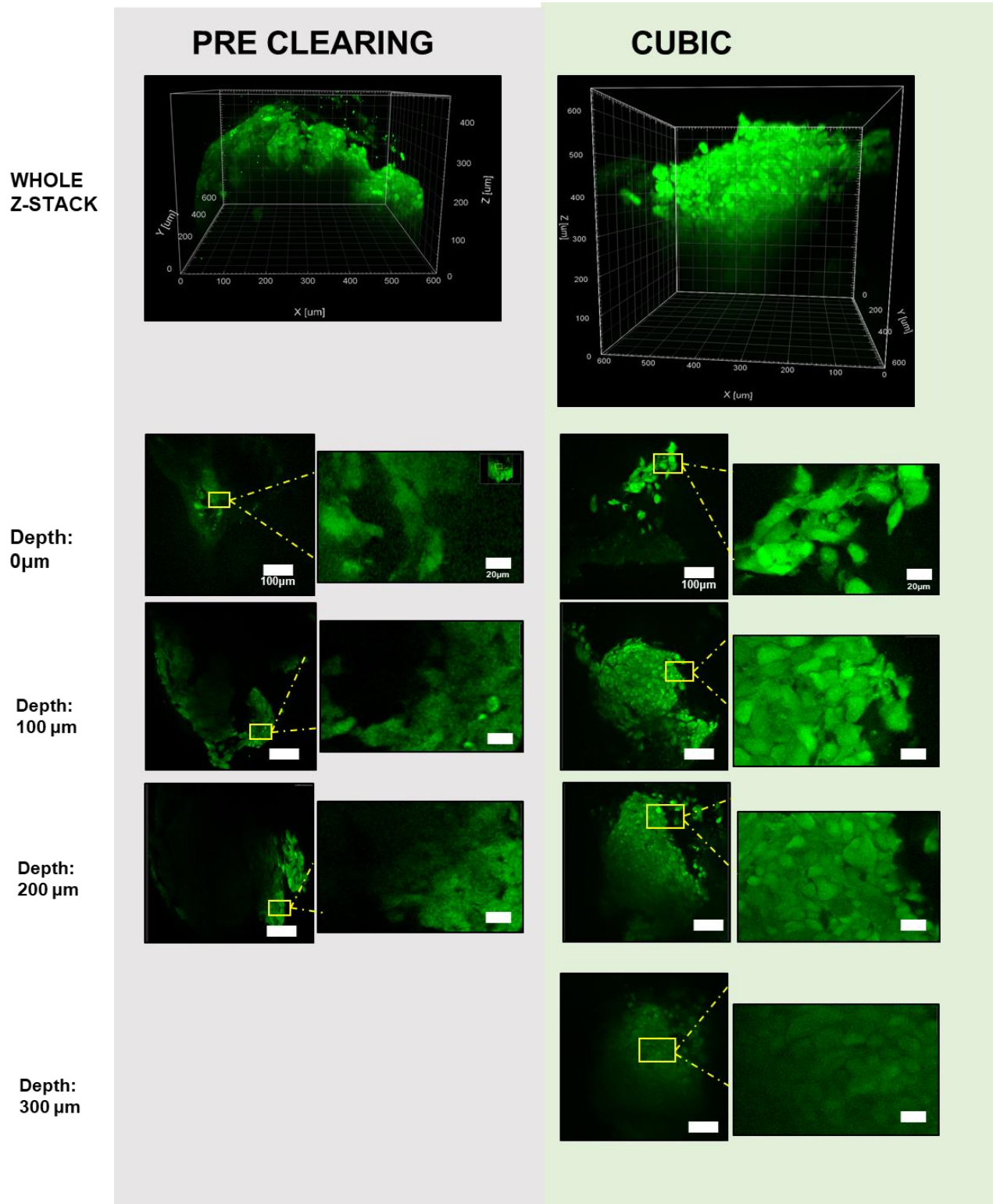
Images of GFP labelled neuroblastoma cells before and after clearing. The images were obtained with a spinning disk Dragonfly microscope (Andor), by scanning all samples under the same imaging settings and also displayed with the same settings. Pre-cleared samples were fixed in 4% PFA and imaged in PBS. Cleared samples were imaged in their respective refractive index matching solutions. Images taken at 10x and 20x times magnification. A) CUBIC treatment B) ECI treatment. Images of tumours were taken at depths of 50 µm before and after clearing.

5.3.7 Imaging depth: comparison between CUBIC and ECI cleared tumour samples

Clearing whole tumour samples aim to improve the laser depth penetration and allow 'deep tissue' images to be taken. A direct comparison of the depth penetration between samples before and after clearing was assessed. Also, the level of noise within the image was assessed. Laser intensity, display parameters and imaging settings were kept constant between pre-cleared (in PBS) and cleared samples (**Figure 5.11a** and **Figure 5.11b**). There was an increase in the depth of the z stack between the pre-cleared and the cleared samples for both clearing protocols. We observed a measurable GFP signal at 300 μm depth in CUBIC-cleared tissues compared to only 200 μm before clearing. However, there is a lower signal-to-noise ratio in the images taken at higher z positions (deeper within the tissue).

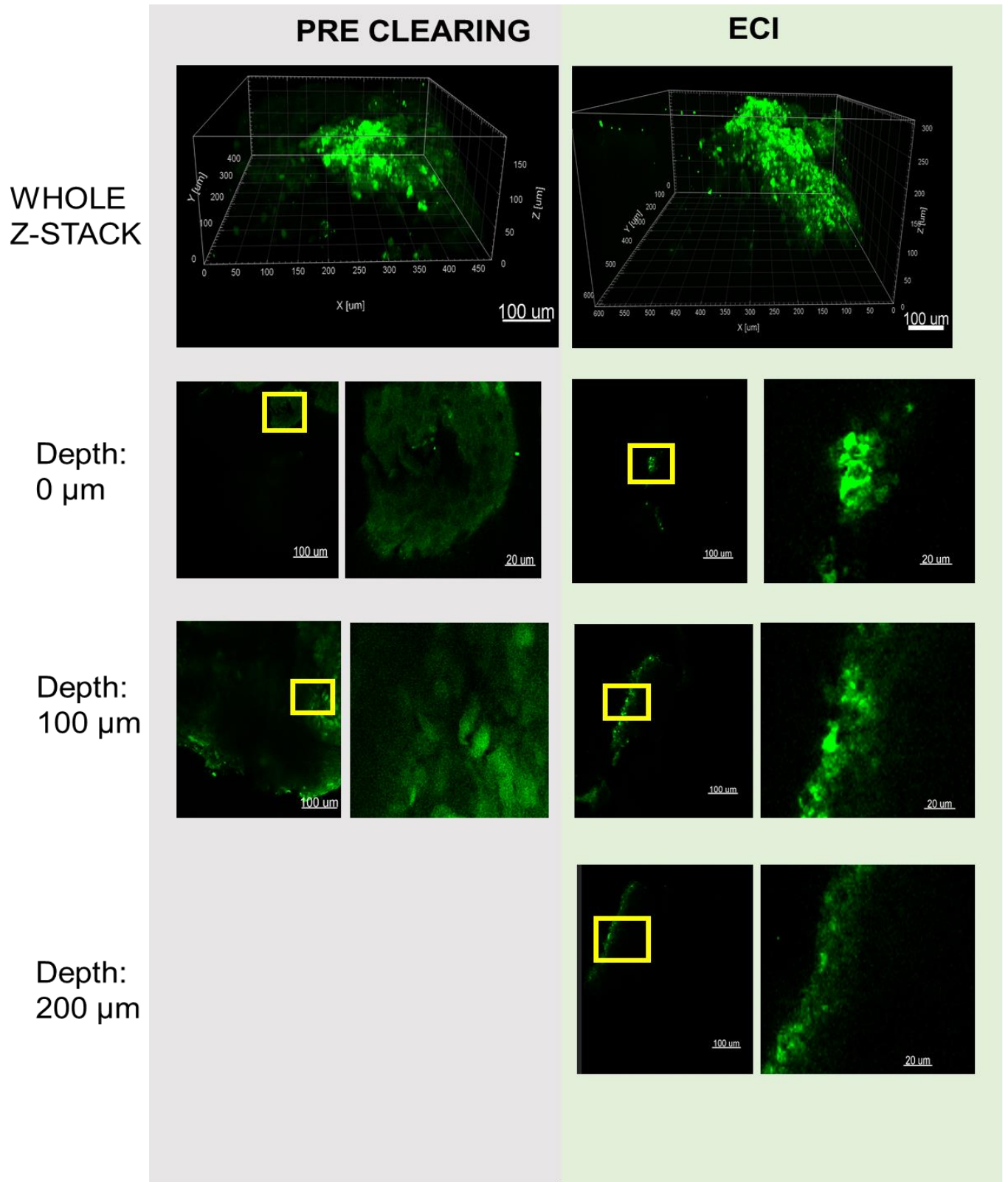
In contrast, the images taken of the ECI-cleared samples did not show any clear cell structure. The signal appears predominantly autofluorescence from the 'chick' tissue rather than the GFP-labelled cells. This implies that the signal detected was due to increased autofluorescence instead of the improved visibility of the fluorescently labelled cells of interest.

Figure 5.12 Imaging at depth before and after CUBIC clearing.



Three-dimensional reconstruction of GFP labelled neuroblastoma tumours before (imaged in PBS) and after (CUBIC – imaged in RIMS) clearing. Selected single images at the depth of 0 μm , 100 μm , 200 μm and 300 μm before and after clearing are shown. Images were taken with a Dragonfly spinning disk microscope at 10x (whole z-stack) and 20x magnification. The yellow boxes depict region of interest to assess single cell resolution at depth. All imaging parameters were kept constant between the before and after image acquisitions. Depths of greater than 300 μm were achieved after clearing some samples, however for ease of comparison with ECI, up to 300 μm is shown.

Figure 5.13 Imaging at depth before and after ECI clearing



Three-dimensional reconstruction of GFP labelled neuroblastoma tumours before imaged in PBS) and after (imaged in ECI solution) clearing. Selected single images at the depth of 0 μ m, 100 μ m, 200 μ m before and after clearing are shown. Images were taken with a spinning disk Dragonfly microscope at 10x (whole z-stack) and 20x magnification. The yellow boxes depict region of interest to assess single cell resolution at depth. All imaging parameters were kept constant between the before and after image acquisitions. With this sample there was no signal before clearing beyond 200 μ m depth, therefore no image is shown. The signal displayed at 200 μ m after clearing was detectable, yet largely nonspecific. Unlike upon CUBIC clearing, no signal could be detected at 300 μ m after clearing.

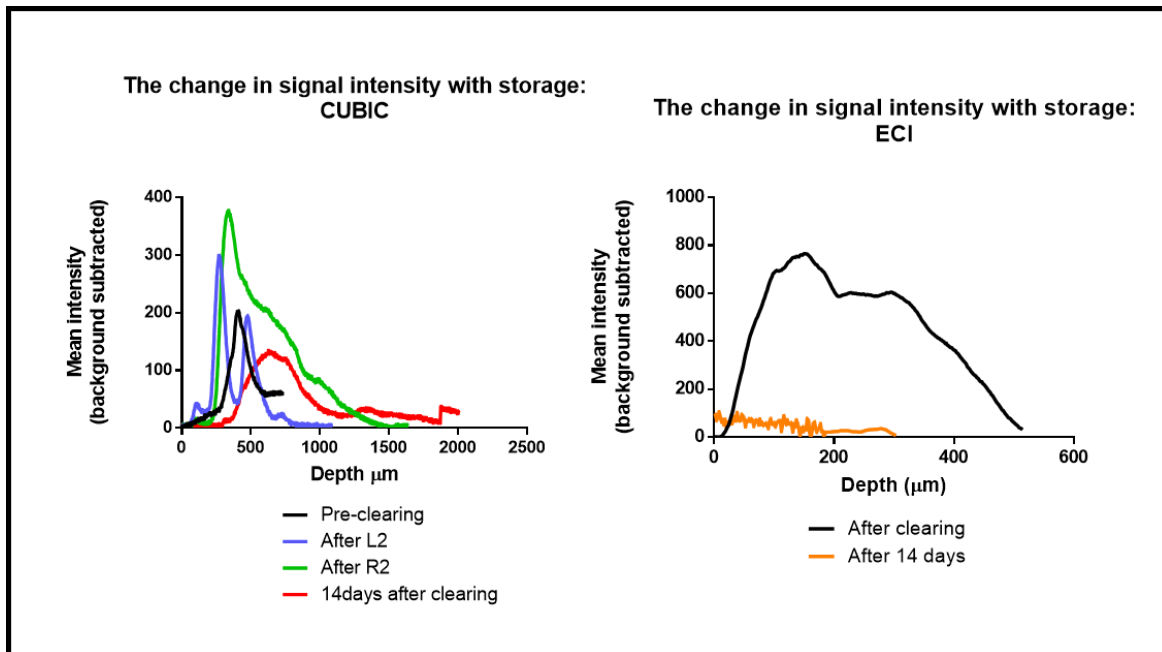
Occasionally tumour tissue may not be processed and imaged on the same day as it is harvested. A method that allows tissue storage and imaging acquisition at the desired time would be ideal.

5.3.8 Evaluating the change in sample fluorescence after storage in clearing solutions.

The effect of long-term storage of the samples in the clearing solutions was investigated. Once cleared, the samples were imaged on the same day. They were then stored for two weeks within the recommended clearing solutions for storage – R2 for CUBIC Cancer and ECI solution for ECI and imaged to assess signal strength and sample integrity. The mean signal intensity with the subtracted background is described and shown in **Figure 5.12**

As shown in **Figure 5.14**, The CUBIC samples displayed an increase in depth of imaging and intensity of GFP signal after L2 immersion, even more so after the R2 clearing step. After 14 days, the peak signal was reduced from 400 to 150 A.U. Although detecting a signal at depth was still possible, it was not specific and likely autofluorescence. The peak signal intensity also appeared deeper in the tissue after 14 days of storage. This change in intensity signature may be caused by imaging the tumour in a different orientation. The intensity at this depth and peak intensity was markedly reduced. After storing in ECI for 14 days, stored tumours had a homogenous low-intensity signal, but the signal signature was different to the one obtained immediately after the clearing protocol. Therefore, we concluded that ECI was incompatible with the long-term storage of neuroblastoma tumours for imaging and that immediate imaging was preferable even with the CUBIC protocol.

Figure 5.14 Comparison of fluorescence preservation during long-term storage of tumours.



Fluorescence-level quantification in tumours during long-term storage after 1 day and 14 days of clearing (CUBIC and ECI protocols). Samples were imaged before and after each clearing step, and then again after 14 day, using Andor Dragonfly SPIM microscope. CUBIC samples were stored in R2 solution at room temperature, protected from ambient light. ECI samples were stored in similar conditions in ECI solution. Z stack images were taken for each tumour at 2µm intervals at every stage using the same imaging parameters. The images were analysed using FIJI imaging software. The background signal was subtracted and the mean intensity was plotted against depth. All values are shown as the mean. (n=3 samples for CUBIC and n=2 samples for ECI).

In conclusion, ECI and CUBIC clearing macroscopically achieved good optical clarity (**Figure 5.4**). Both protocols were straightforward and relatively quick – making them more applicable to high throughput screening protocols. However, the CUBIC clearing could preserve GFP fluorescence at depth, which was not the case with ECI and sample storage was also better than with ECI. Of the two methods, CUBIC produced the most reliable results and better images at a cellular level, with all tumour sizes and was therefore used in further experiments.

5.3.9 Optimising advanced imaging for 3D samples

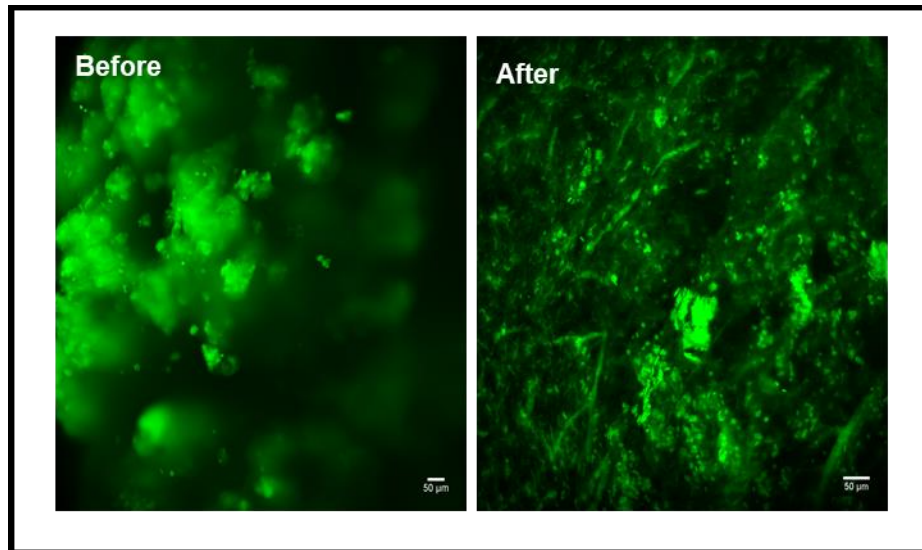
5.3.9.1 Outline of wholemount microscopy and the challenges

The next step was to optimise the image acquisition protocol for cleared samples. Numerous imaging and analysis modalities can be used to image large complex samples such as tumours. These include multiphoton, spinning disk and light-sheet microscopy. Each system has its merits and limitations, with differences in the working distance of objectives, imaging speed, user-friendliness, and compatibility with cleared samples to be considered. I have tested the three modalities available in the Centre for Cell Imaging at the University of Liverpool. The facility had no optimised workflows or protocols for clearing or imaging wholemount tissue when undertaking this work. Of the microscopes available, the most suitable for 'deep 'imaging' was a Zeiss Lightsheet Z1, a Zeiss lsm880 equipped with a two-photon laser, and an Andor Dragonfly spinning disk. Each modality was assessed for its suitability in imaging-cleared neuroblastoma tumours. Untreated SK-N-BE(2)C-GFP and SK-N-AS-GFP tumours were dissected from chick embryos and fixed in PFA as standard protocol. As sample preparation for the Lightsheet and lsm880 multiphoton microscopes required the samples to be set in agarose, the same sample could not be imaged across all systems. Samples of similar sizes and cell types were paired to reduce bias.

5.3.9.1.1 Lightsheet microscope

Lightsheet fluorescence microscopy (LSFM) is a powerful technology with the unique ability to image biological systems in three dimensions with sub-cellular resolution. Several protocols have been described for clearing opaque tissues using aqueous or organic solutions. We investigated CUBIC protocols in preliminary experiments.

Figure 5.15 Imaging whole mount tissues with light sheet microscope.



Maximum intensity projection of sample tissue before and after clearing with the ZEISS Z1 light sheet microscope is shown. Images taken with 5x objective.

Lightsheet microscopy uses a narrow plane of light travelling through the sample perpendicular to the objective. This single plane of illumination reduces interference from out-of-focus light. As the sample is suspended in 2% agarose, images can be taken from all angles and reconstitution into a 3D image is possible, displaying the whole tumour environment. However, the limiting factors were twofold:

1) The tumour sample was too large for the capillaries used to house the sample during imaging. Tumour samples were cut down further to allow them to be imaged. Given that this work aims to acquire images of whole tumours and capture and quantify the heterogeneity across the sample, further dissection of the samples was not ideal. The Z1 light-sheet microscope is built to image samples around 200-300µm in thickness, other systems compatible with imaging larger samples exist but were not available in Liverpool.

2) A new refractive index and light scattering are introduced when suspending the sample in agarose. This limitation is valid for all cleared samples with all imaging systems. Despite homogenising the refractive index within a sample, the light path must travel through the air, glass coverslips, and water/immersion media before reaching the camera. Water and agarose used in

light-sheet sample holders have a refractive index of 1.3. However, samples cleared using CUBIC Cancer have a refractive index between 1.4 – and 1.6. This mismatch will lead to the refraction of the light path and reduce the quality of the image. This may impede the ability to acquire images with single-cell resolution in whole tissue imaging.

Lightsheet microscopy is fast and uses low laser power, meaning it is gentle on the sample and minimises photobleaching. However, the predominant issue was reduced resolution at greater depths. The signal-to-noise ratio was reduced to around 400 μm in the cleared sample, and the single-cell resolution was lost. We concluded that the available lightsheet microscope was not optimal for the single-cell resolution imaging required.

5.3.9.1.2 LSM 880 Multiphoton

The LSM 880MP is a confocal microscope equipped with a two-photon laser. In conventional confocal microscopy, a single photon at a set wavelength excites a fluorophore to create an emission of light, whereas, in multiphoton microscopy, two or three photons of a higher wavelength are used for sample excitation. The fluorophore excitation from the photons must occur almost simultaneously. This further focuses the energy, and the emitted light is detected from a single focal point, reducing background noise. The longer wavelength allows for lower energy and deeper penetration, creating less tissue damage. We hypothesised that this improved depth penetration might obviate some of the issues faced with the light sheet.

The LSM880MP available in the CCI is an upright microscope, with both objectives and the camera sitting above the sample on the stage. Cleared samples should, ideally, be imaged within their refractive index matching solution, in this case, CUBIC-R2. However, even in aqueous-based clearing solutions such as CUBIC Cancer, there may be damage to the dipping objective, in this case, the 20x and 40x immersion objectives. Therefore, samples were mounted using 1% agarose and covered in distilled water for the 20x water immersion objective. The refractive indices introduced by imaging a sample in water and agarose must again be considered. Imaging chambers that allow samples to be submerged within the refractive index matching solution (RIMS) (CUBIC R2 solution) are commercially available. The chamber will often consist of a well upon which a coverslip can be placed. A similar imaging dish was designed and fabricated, and imaging benefits within RIMS versus agarose mounting were assessed. (**Figure 5.16**)

Figure 5.16 Differences in image quality when using an imaging well compared to embedding in agarose.

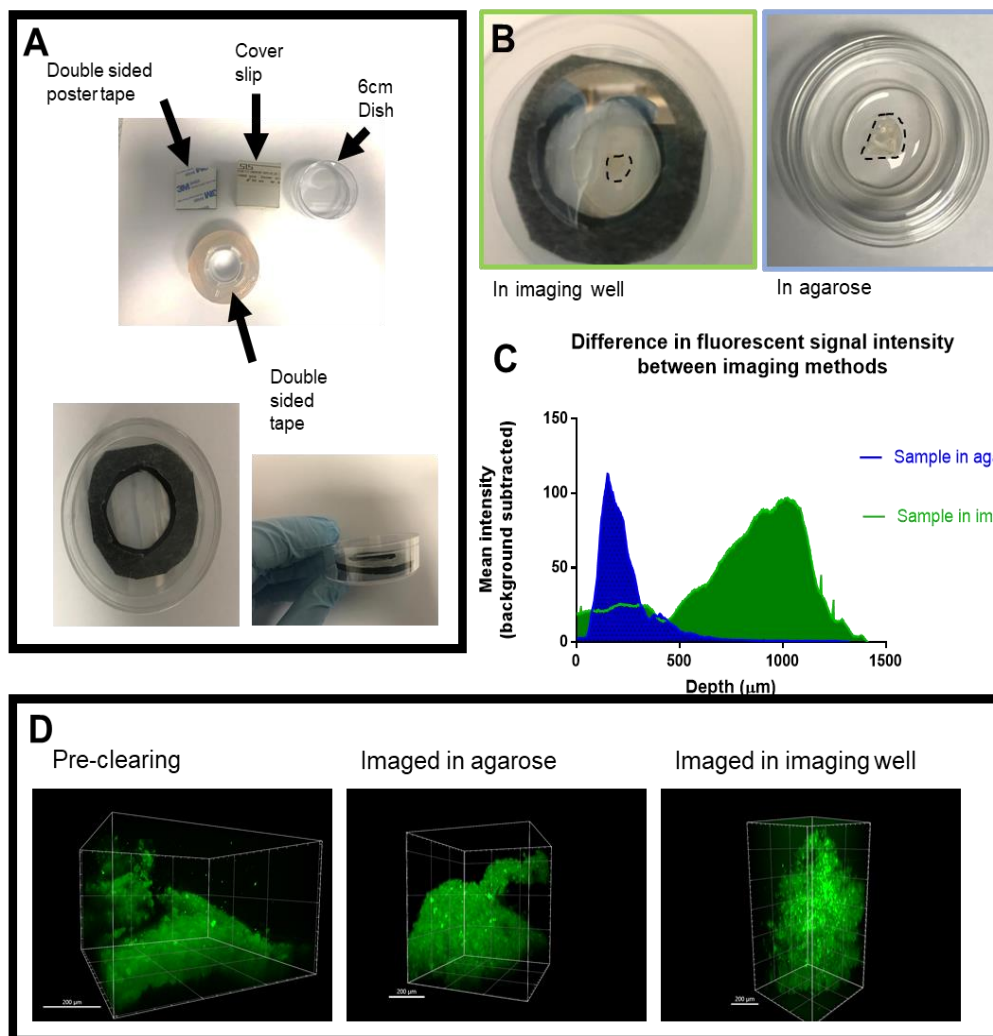


Image A shows the construction of the imaging chamber. A small circle was cut in the centre of the double-sided poster tape, and this was fixed onto the bottom of a 6cm glass bottom imaging dish. Thick double-sided tape was used to provide a water tight seal. The imaging well was filled with CUBIC R2 solution and the sample was placed inside. A cover slip was placed on top for imaging. B) Samples in imaging well and embedding in agarose for imaging. C) The mean intensity of the signal from tumour imaged in agarose and imaging well is shown. Calculating the differences between the fluorescent intensities at depth between imaging in the chamber vs. imaging in agarose demonstrates greater depth and high intensity of signal. The agarose sample shows an initial higher intensity peak, followed by a rapid tailing off of signal. The sample in the imaging well has a steady rise of intensity to the peak intensity at 1000 μm depth. The samples are at approximately the same distance from the objective. The bottom row of images demonstrates z stack reconstructions of maximum intensity projections of all three set ups: before clearing, after clearing in the agarose and after clearing in the home-made imaging well. This again shows that the home-made imaging well allows for a greater imaging depth within the sample. Images were acquired with the same imaging parameters using the 20x dipping objective.

The 20x objective is a dipping objective, and as **Figure 5.16** shows, there was a benefit to imaging within the RIMS. The signal-to-noise ratio was reduced, and a greater depth penetration was obtained.

Depth penetration was excellent using multiphoton microscopy going up to 1000 μ m in some cleared tumour samples compared to a maximum of 200 μ m in non-cleared samples (**Figure 5.13**). Imaging a 1000 μ m thick sample in a single position with a 2 μ m section per plane took approximately 40 minutes. This time varied depending on the number of channels and the pixel resolution. Higher pixel resolutions or multiple positions increased imaging times by 1 hour, damaging the sample.

5.3.9.2 Working distance and magnification.

However, the practicalities of imaging whole mount tumours may be limited in these systems, even with imaging wells or chambers. The objectives of a microscope may be defined by its magnification, numerical aperture, and working distance.

The working distance is from the objective's front lens element to the sample's closest surface when the sample is in focus. In general, as the magnification of an objective increases, so the working distance reduces. For 2D slides, where imaging at depth is not a priority, objectives with short working distances and higher numerical aperture provide a high resolution. However, in a thick sample of 1mm, an objective with a working distance of 0.1mm limits the depth that can be imaged. An objective with a long working distance but high magnification is therefore desired but was not available.

Immersion objectives, such as the 20x objective of the 880MP, operate with a liquid medium of set refractive index between the lens and the coverslip. Although CUBIC R would have been the optimum immersion medium, distilled water was used in these experiments to protect the lens. In this way, immersion lenses are also more restricted in the working distance lengths as there must be a layer of immersion liquid between the lens and the coverslip to function correctly. If an objective has too long a working distance, this layer produces a poor-quality image.

The spinning disk Dragonfly is an inverted microscope, so the objectives stand below the sample. The 20x objective is still an immersion objective in the Dragonfly, but as the objective comes from under the imaging dish, the sample can remain in the refractive index matching solution throughout the experiment.

The Dragonfly spinning disc microscope became available in the CCI after imaging protocols for 880MP were developed. Experiments were performed to compare whether the Dragonfly may be better at imaging 3D samples and avoid some of the limitations of the 880MP.

5.3.10 Comparing the Dragonfly and 880MP imaging systems.

Two imaging setups were used for imaging cleared neuroblastoma tissue: the Zeiss LSM 880 upright confocal laser-scanning microscope and the Dragonfly Andor high-speed/sensitivity spinning disk confocal imaging. The Zeiss LSM 880 was equipped with a 20x/1.0 water immersion objective, and the Dragonfly with a 10x/0.45 water immersion objective and a 20x/0.95 oil immersion objective.

The microscopes were compared on the following three aspects:

1. The system's ability to image at high resolution at depth
2. The ease of use of the tiling functions. Tiling functions allow multiple images in the same z plane to be stitched together, providing a high-resolution widefield view image.
3. The acquisition time and dataset size for 3D images

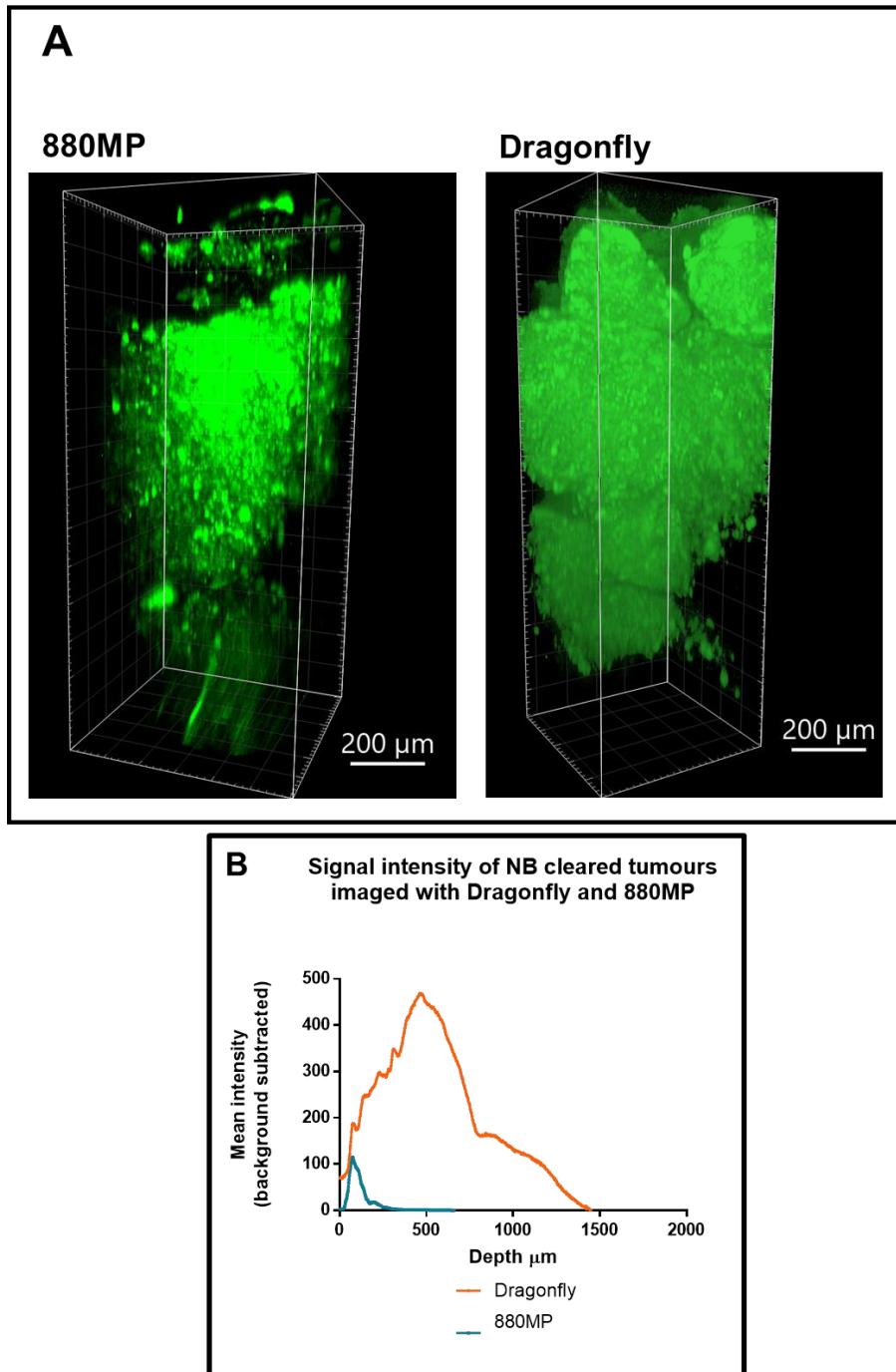
5.3.10.1 Imaging at high resolution at depth

CUBIC-cleared samples were set up on the 880MP in the imaging chamber, as described in **Figure 5.16**. Images were taken in the z plane at 2 μ m intervals. The depth obtained by each system is shown in **Figure 5.17**. Both microscopes could image the tumour up to depths >1000 μ m. When imaging deep into the stack using the lsm880MP, there was a point where no new images could be acquired at depth (**Figure 5.17**). This is because the working distance of the objective prevented deeper imaging as the objective had come into contact with the coverslip. What was shown was a 'blur' like the appearance of the signal where the same plane was imaged repeatedly but interpreted by the imaging programme as progressive planes.

The difference in signal intensity at depth was calculated (**Figure 5.17**). Each plane's mean intensity (after background subtraction) was plotted within the z-stack image. The signal from the lsm880MP was visibly lower when examining the images and plotting against depth. In contrast, the Dragonfly could image at depth with high signal detection. The original formats of the images were different – lsm880MP utilises its own Zeiss Zen software, and images were in CZI format. The Dragonfly saved images in '.IMS' format, which was directly compatible with the Imaris analysis software. In converting .CZI files to .IMS for display and analysis purposes, the data was

altered. Although the images looked similar, we could not quantify them to compare the two systems.

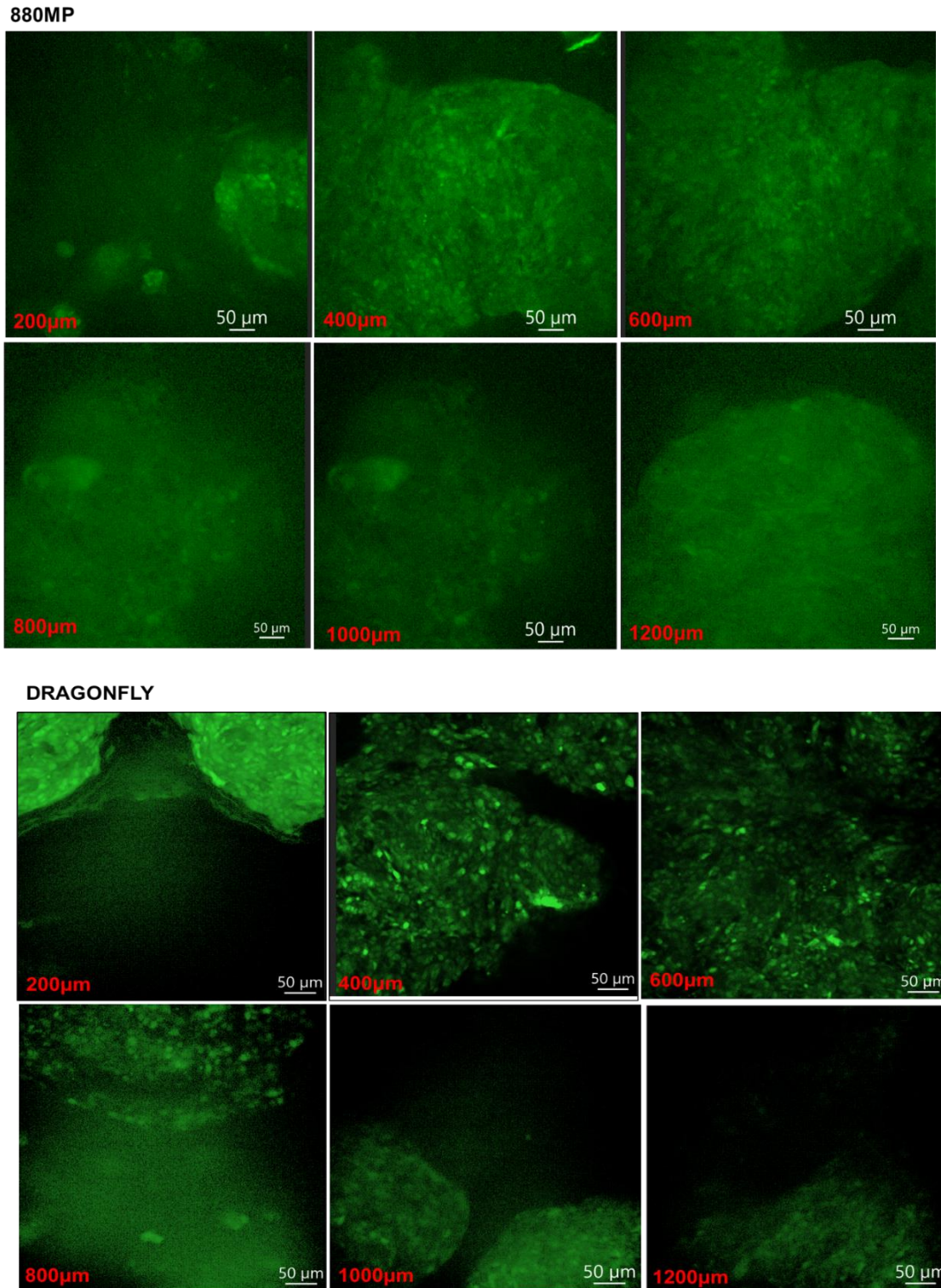
Figure 5.17 Comparing Dragonfly and 880MP microscopes.



Fluorescent neuroblastoma tumours were imaged using Dragonfly and Ism880MP microscopes. For the Dragonfly inverted microscope samples were imaged in a glass bottom imaging dish whilst suspended in the RIMS (R2 for CUBIC). 10x water immersion and 20x oil immersion objectives were used. For the 880 MP images, tumours were fixed within the imaging chamber as in Figure 5.17. 25x immersion objective was used. Where possible all imaging properties were kept the same. The laser powers function differently between the two microscopes and so this is an uncontrollable variable. A) Z stack images were taken from the first visible green signal through to the end. Each stack was 2µm below the previous b) Average signal intensity of neuroblastoma cleared tumours imaged with Dragonfly and Ism880MP the signal from the Dragonfly tumours (n=3) showed a peak fluorescent intensity signal of over 400 au. and a depth of 1600 µm. The depth of the Ism880MP was on average 1000-1300 µm, however it is likely that there was a change in the signal value with the post processing.

Images were taken at similar depths with both microscope systems from 'tops of the tumour'/first detectable signal. **(Figure 5.18)** The imaging depths were similar; however, there was an increased background signal in the Ism880MP images at depth.

Figure 5.18 Comparing Dragonfly and 880MP image quality at depth.



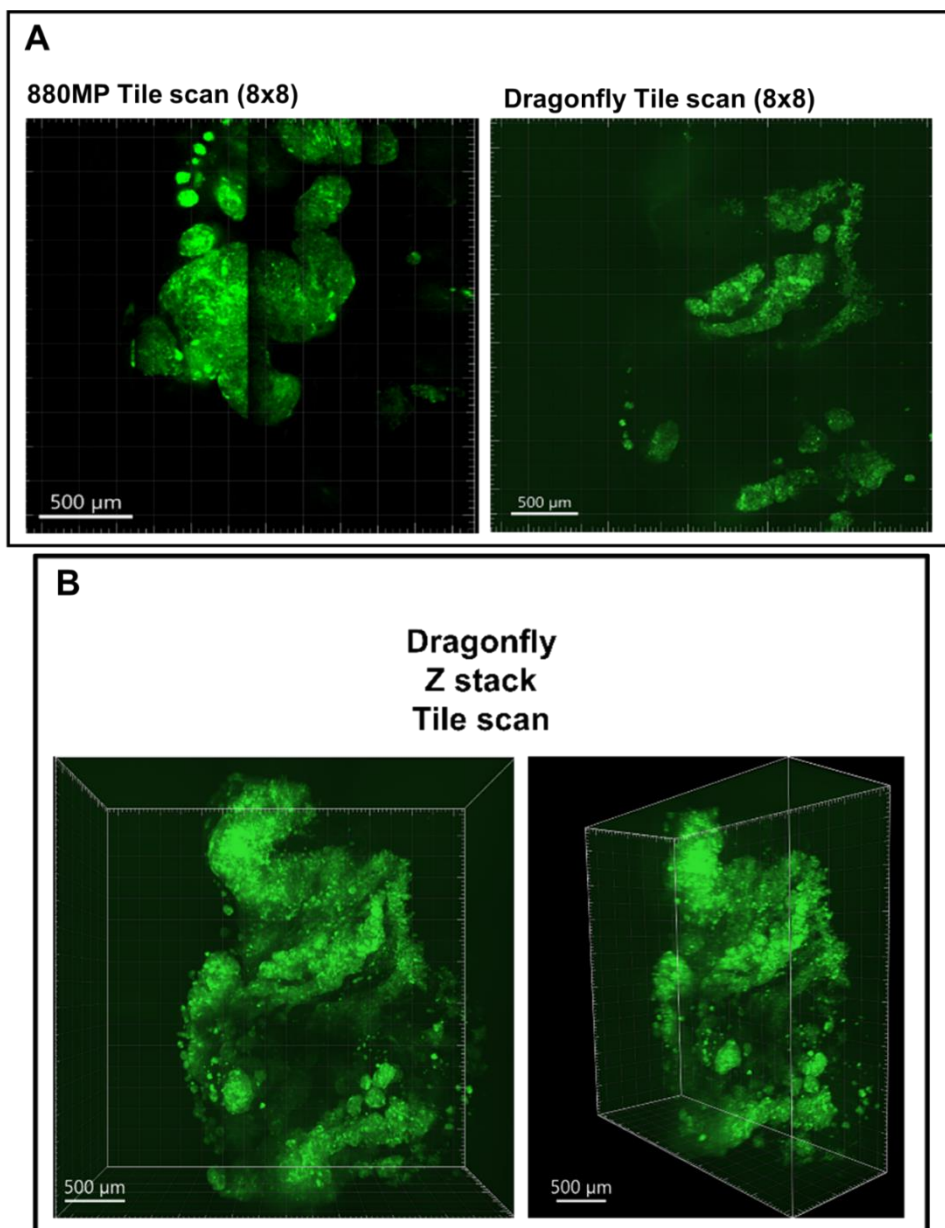
Panels show Dragonfly and 880MP imaged neuroblastoma tumours at different depths. Images were taken in an imaging chamber with the sample kept in CUBIC solution on both microscopes. Dragonfly was mounted with a 20x air objective (N.A. 0.95), and the Ism880MP with a 20x water immersion objective (N.A. 1.0). Imaging was started from the first detectable GFP signal (z=0). Z plane images were taken at 2µm intervals thereafter. Depths are indicated in red on the images. Both microscopes were able to image up to 1200µm depth. The images from the Dragonfly showed a better resolution of single cells at depth compared to the Ism880MP. In Ism880MP images at depths >800µm there was a reduced signal to noise making it difficult to differentiate individual cells.

5.3.10.2 Assessing the tiling functions on Dragonfly and Ism880MP microscopes.

An advantage of examining manually sectioned samples, such as paraffin slides, is gaining a wide field of view to assess areas of interest. 3D samples require more sophisticated imaging systems than those used routinely in histology. An objective's working distance and resolution often govern the breadth and granularity of detail within an image. In short, the high-resolution images obtained in these systems often come at a price: limited field of view. Tiled acquisitions require an image stitching step to align and fuse adjacent stacks to reconstruct the full image. This is a complex operation; good image positioning and blending are crucial to ensure a seamless 3D image without stripes/squaring, or duplication effects.

Multiple high-resolution images – or tiles – are taken over the sample within this process. These can then be "'stitched' together in post-processing to produce the whole sample in high resolution. The advantage of this system over traditional paraffin or cryostat slides is that once the widefield, high-resolution image is obtained, it can be stored and used repeatedly for analysis. The utility of this tiling in large, 3D, immunolabelled samples was assessed. The process was optimised on Ism880MP and Dragonfly microscopes. Tiled scans of 8x8 grids were obtained. This was initially done in a single optical plane and using z-stacks. Imaging multiple tiles in multiple plans were limited by time and damaging the sample through overexposure – this had to be abandoned with the Ism880MP as the acquisition times were too long, and the samples began to drift as the immersion fluid evaporated. However, we successfully acquired an 8x8 tiled tumour scan with the Dragonfly microscope in all three planes (**Figure 5.19**).

Figure 5.19 Tile scan functions for Ism880MP and Dragonfly microscopes.



Tumours were imaged in CUBIC solution in both systems. Tile scans were set to 8x8 scan, with a 10% overlap to reduce visible squaring. A) Tile scans with the Ism880MP and Dragonfly microscopes. Both microscopes performed stitching functions through the manufacturer software (ZEN and Dragonfly processing). B) Due to the long acquisition times it was not possible to obtain a tile and z stack image with the Ism880MP. However, with the Dragonfly we were able to successfully acquire a z stack tiles scan, showing a whole tumour in 3D.

5.3.10.3 Acquisition times and size of datasets

The Dragonfly is undoubtedly faster and more adept at deep 3D imaging when examining the overall comparison between the two microscopes. However, file sizes were large, with over 1GB for a tiled, z-stack scan. (Table 5.1).

Table 5.1 Comparison of acquisition times and dataset sizes for single images, single point z stacks, tiled image and tiled z stack images.

Microscope	Image type							
	Single high resolution image (1024x1024 pixels)		Tile-scan image (8x8 tiles overall)		Z stack image – single xy position		Z stack and tile scan image	
	Image size (Kb)	Acquisition time (mins)	Image size (Kb)	Acquisition time (mins)	Image size (Kb)	Acquisition time (mins)	Image size (Kb)	Acquisition time (mins)
880MP	34899	2	32895	18	1200561	40	n/a	n/a
Dragonfly	2336	15 seconds	14292	4	834436	10	4089913	28

The Ism880MP, in our experience, was better suited to single imaging points within the tumour at high resolution. However, the long acquisition times precluded deep imaging of very large structures.

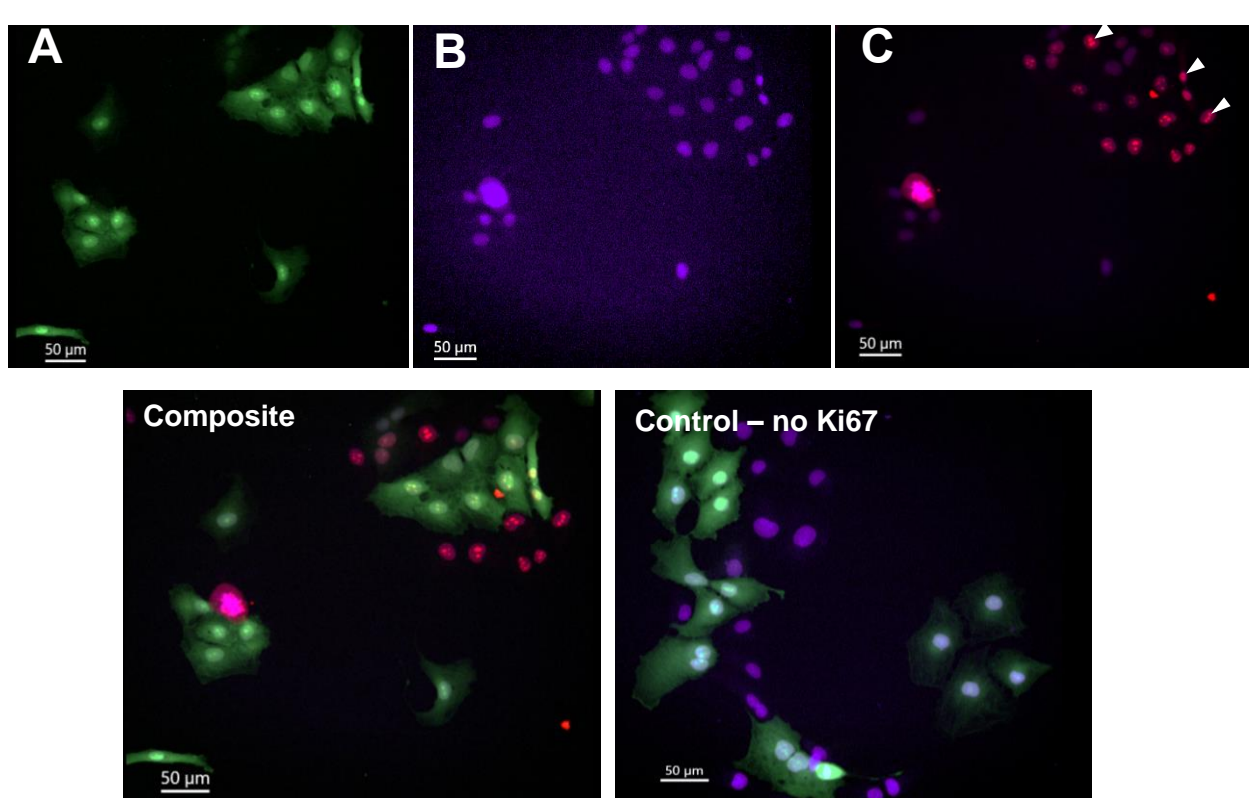
5.3.11 Optimising immunostaining in wholemount tumours.

Having shown that whole neuroblastoma tumours can be imaged without sectioning, the next aim was to optimise immunofluorescent antibody labelling of proteins of interest within the tumours. We selected several commonly used markers in histopathological analysis of tumour tissues and assessed whether labelling three-dimensional structures with immunofluorescent antibodies was possible.

5.3.11.1 Optimising immunostaining using Ki67 proliferation marker.

Ki67 is a commonly performed histological assay to assess proliferation. It can be used as an indicator of drug efficacy as an anti-proliferative agent within treated samples. Immunofluorescence analysis of thick samples required optimising incubation times and antibody concentrations. The first experiment was conducted on fixed cultured cells to check the antibody quality on neuroblastoma cells. (Figure 5.20)

Figure 5.20 *Ki67 antibody testing on fixed SK-N-AS cells.*



Cells were cultured on glass coverslip and fixed with 4% PFA, Cells were labelled with Ki67 (dilution 1 / 250) and Alexa 594 secondary antibody (dilution 1 / 500) and, Hoechst (1 / 1000). Images were taken using 20x objective on Dragonfly SPIM microscope. Images shown are A) GFP labelled neuroblastoma cells B) Hoechst C) Ki67. (Bottom row) D) Composite image and E) Control with no primary Ki67 antibody. It was noted that some neuroblastoma cells appeared to be labelled without displaying GFP fluorescence.

After assessing that Ki67 staining was positive in neuroblastoma cells and that there was no non-specific binding of the secondary Alexa 594, tumour sections were stained. It was also noted that some cells were positive for nuclear stain but had no green fluorescent signal, although transduced cells were initially FACS sorted. Tumour sections were tested with a series of primary and secondary antibody concentrations. Also, the incubation times were optimised, with different temperatures (room temperature vs 4°C) and incubation methods (static vs rocking). In addition, buffer solutions for antibody and blocking solutions were also optimised (with or without permeabilising Triton X100). All of these variables were examined in cleared and uncleared samples. Tumours were then imaged with the Dragonfly spinning disc confocal microscope using

the same acquisition parameters. Some exhibited minimal signal, whereas others had large amounts of non-specific signal.

Table 5.2 The optimisation steps for cleared tumour sections.

Stage	Method used	Reagents and Equipment	Non-specific signal	Result	Outcome
Antigen retrieval	No additional step	N/A	+	Tissue intact, but non-specific signal remains	Used
	Heat-induced epitope retrieval	Sodium Citrate Buffer (10mM Sodium Citrate, 0.05% Tween 20, pH 6.0) in a vegetable steamer	++	The tissue appears distorted and high levels of non-specific signal	Not used
Blocking and permeabilisation	BSA and Triton X100 – 5 hours at RT	5% BSA in DPBS and Triton x100 0.2%	+	The non-specific signal is seen. Low Ki67-specific signal	Increase incubation time
	BSA and Triton X100 – overnight at RT	5% BSA and Triton x100 0.2%	+ but increased Ki67 signal also	Better Ki67 specific signal, although non-specific signal remains	Used
	BSA and no Triton – overnight hours at RT	5% BSA	Reduced signal	No Ki67-specific signal	Triton needed for permeabilisation
Antibody labelling	Rabbit anti Ki67 1 hour Goat anti-rabbit Alexa 594 1 hour Room temperature Rotational agitation	Primary: 1:100 in blocking buffer Secondary: 1:500 in blocking buffer	+++	Sandwiching of the signal at the outside of the sample	Lower antibody concentration, longer incubation time in a cold environment
	Rabbit anti Ki67 4 hours Goat anti-rabbit Alexa 594 4 hours 4°C Rotational agitation	Primary: 1:100 in blocking buffer Secondary: 1:500 in blocking buffer	++	Reduced sandwiching but still high signal at the edges of the sample	Lower antibody concentration and increased incubation time
	Rabbit anti Ki67 8 hours Goat anti-rabbit Alexa 594 8 hours 4°C Rotational agitation	Primary: 1:200 in blocking buffer Secondary: 1:500 in blocking buffer	+	Better penetration was seen within the sample. Still, some sandwiching seen	Increase primary incubation times but reduce secondary incubation time
	Rabbit anti Ki67 12 hours	Primary: 1:200 in blocking buffer	+	Best penetration is seen within the	Used in protocol

	Goat anti-rabbit Alexa 594 2 hours 4°C Rotational agitation	Secondary: 1:500 in blocking buffer		sample. Still non-specific signal	
Treating for background signal	Hydrogen Peroxide is used to remove possible endogenous peroxidases.	0.3% hydrogen peroxide in methanol for 60 minutes at room temperature with agitation	+	Slightly improved background signal	Unclear of the interaction with clearing substances. This method was not used as the improvement in the background signal was minimal.

*Blocking Buffer: 5% Bovine Serum Albumin in DPBS; 0.1% Triton X-100; and 0.4% Tween 20.
RT – room temperature*

The optimal conditions for **tumour sections** from the previous optimisation steps are as follows:

- 5-hour blocking in 5% BSA solution
- Overnight permeabilisation in 5% BSA and 0.2% Triton X100
- Primary antibody concentration of 1/200 in blocking buffer
- Secondary antibody concentration of 1/500 in blocking buffer
- Primary antibody incubation at 4°C on a rocker for 12 hours
- Secondary antibody incubation at 4°C on a rocker for 2 hours

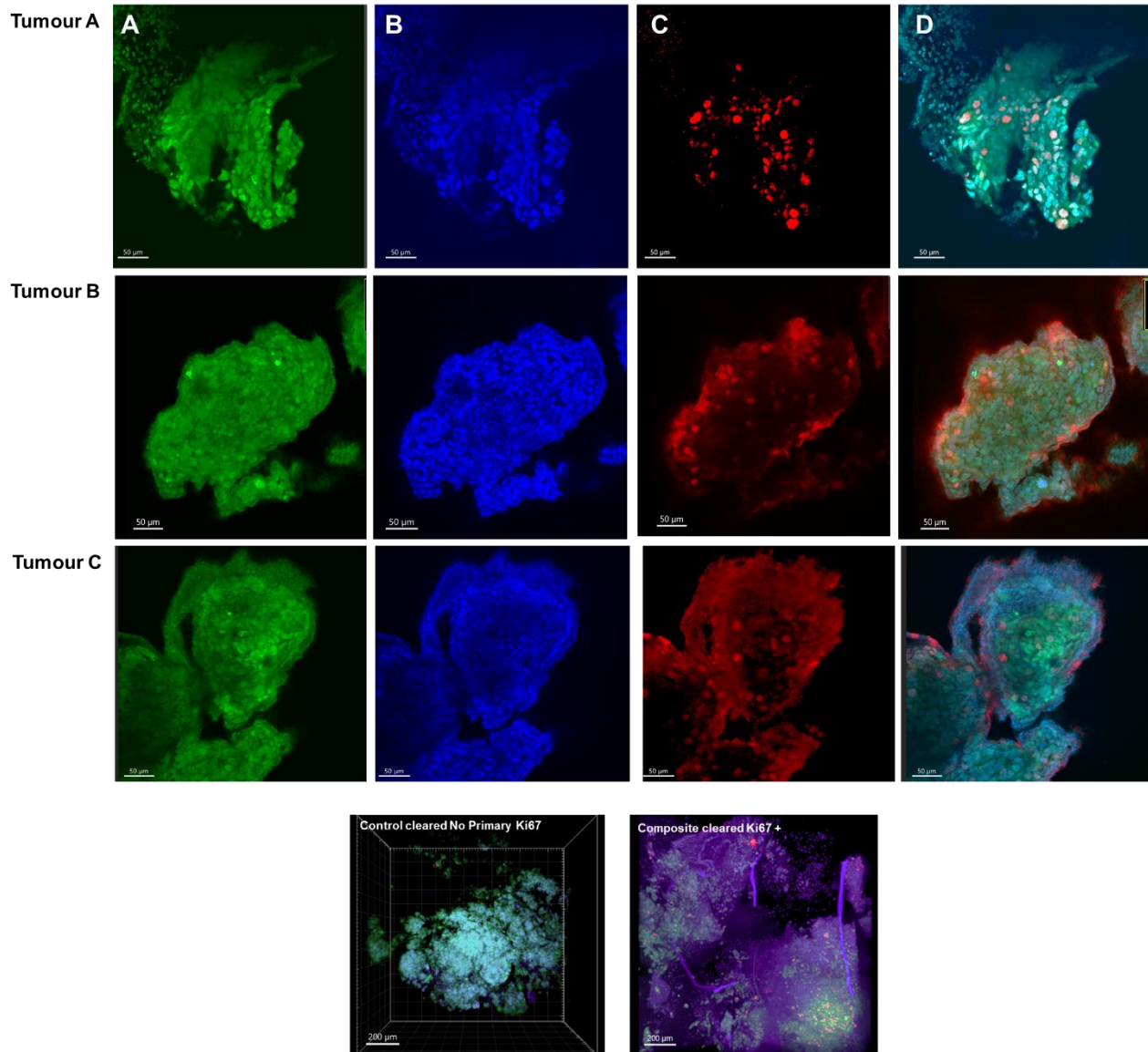
The incubation times were extended, but the antibody concentrations were kept the same for **whole tumours** to ensure thorough antibody penetration into the tissue:

- Primary antibody incubation at 4°C on a rocker 3 days
- Secondary antibody incubation at 4°C on a rocker for 2 days

Previous literature on whole-mount samples has indicated a total time of 1 week for staining similar-sized samples.

Kubota et al. recommended performing the first steps of clearing, staining, and refractory matching. (Shimpei I Kubota *et al.*, 2017) Following this, all cleared and labelled samples underwent L1/L2 clearing steps, followed by blocking, permeabilisation and primary/secondary antibody labelling, followed by CUBIC R1/R2 solution immersion. Cleared samples without antibody labelling were imaged using the same laser lines to ensure that the clearing process did not influence the antibody labelling or introduce autofluorescence. (**Figure 5.21**)

Figure 5.21 Tumour sections labelled with GFP, Hoechst and KI67.

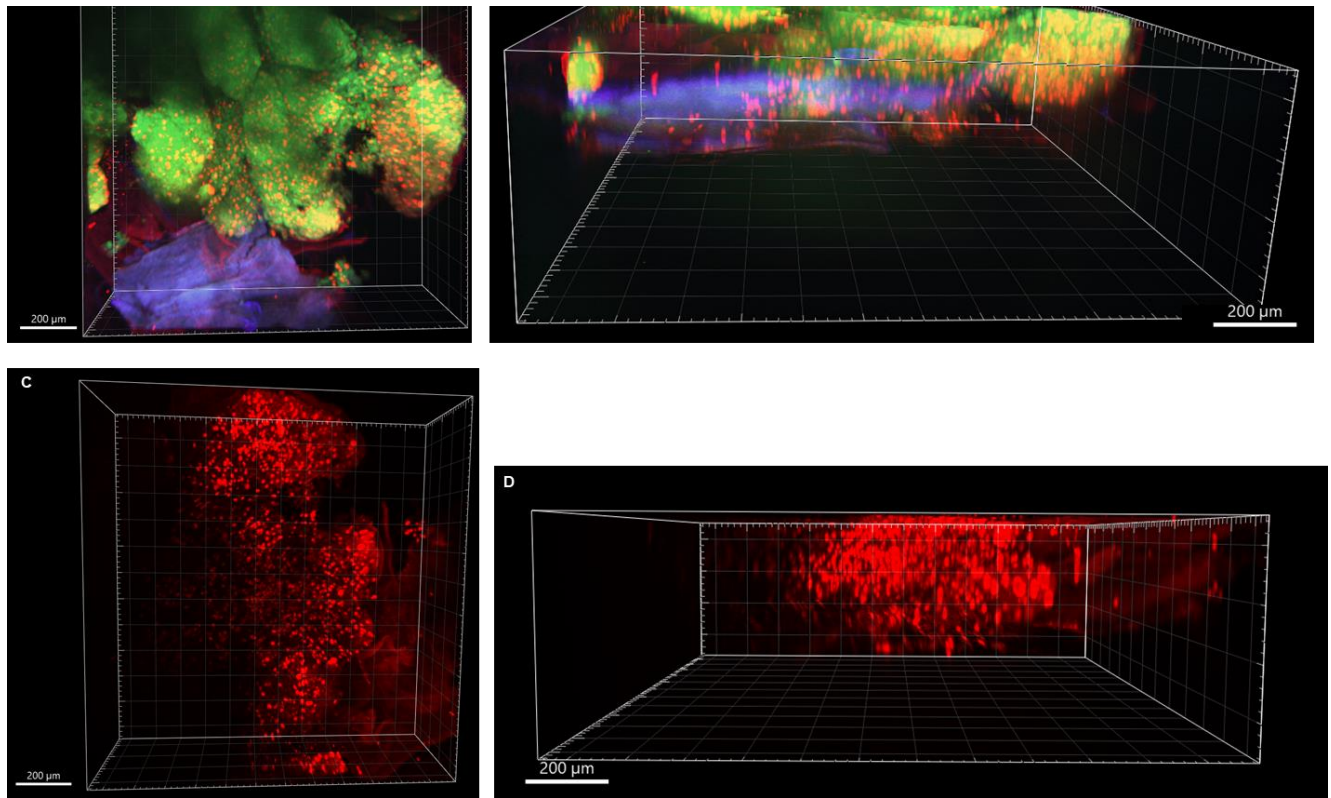


The top 3 rows show sections from three different tumours which were cleared and labelled with the final optimised protocol as outlined in the Materials and Methods. Channels shown are A) GFP B) Hoechst C) Ki67/Alexa 594 D) Composite. Images were acquired using the Andor dragonfly microscope with 10x air objective. The bottom row shows a whole tumour after clearing alone compared to after clearing and staining. The imaging parameters were the same for all images. No 'false' red auto-fluorescent signal was introduced by the chemicals used for clearing.

Following validation in tumour sections, wholemount tumour tissue was imaged in the same way. The incubation times were increased, but the concentrations and incubation conditions were kept the same. For whole tumours, the protocol as outlined in Materials and Methods was as follows:

Tumours were immersed in solution L1 for 1 hour and solution L2 for 1 hour under constant agitation to remove lipids. Tumours were then washed in 5% (w/v) BSA and immersed in blocking buffer overnight at room temperature. Primary antibody diluted 1:200/5% BSA was added for four days at 4°C under constant agitation. After primary incubation, tumours were washed in 5% BSA 3x 1 hour washes before secondary Alexa Fluor antibody diluted 1:500/5% BSA for three days at 4°C under constant agitation. Tumours were washed in 5% BSA 3x 1 hour before nuclear stain (Hoechst 1:500/PBS) for 2 hours. R1 solution was added for 5 hours and R2 solution for 5 hours. Tumours were stored in R2 in a dark drawer at room temperature. Based on previous experiments, tumours were imaged as soon after clearing as possible. **(Figure 5.22)**

Figure 5.22 Cleared and immunolabelled neuroblastoma tumour.

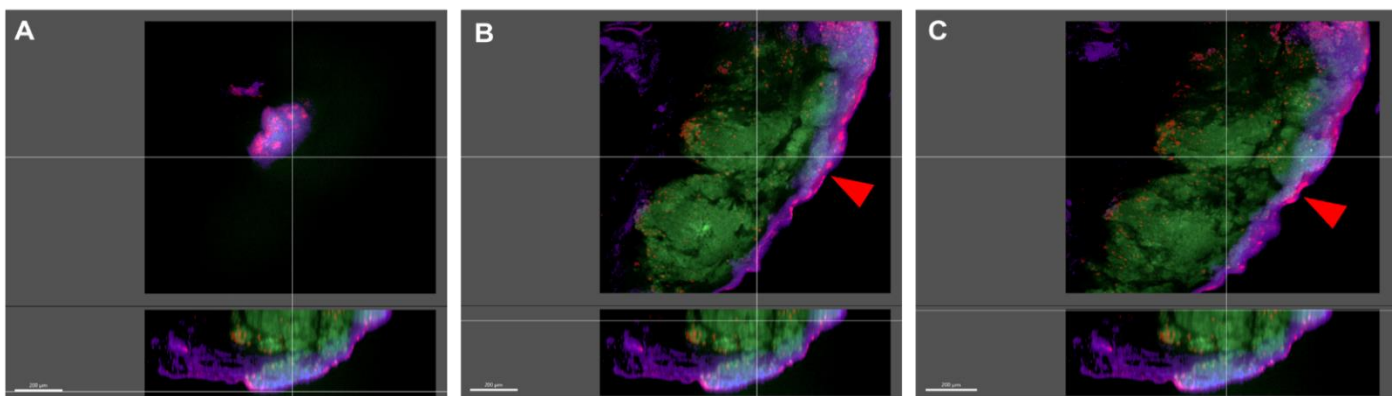


A, B: composite image of all three channels: Green – labelled neuroblastoma cells, Blue – Hoechst nuclear stain, (chick and human) and Red – Ki67 positive nuclei). C, D: Ki67/red channel only. There is a uniform staining of Ki67 positive nuclei across the surface of the tumour (XY view). D. Z view of the stack showing antibody penetration through the tumour. All images are maximum intensity projection. All images were taken on an Andor Dragonfly microscope with a 20x objective and the tiling function.

There was good antibody penetration throughout the sample, with the fluorescent signal detected in all z-stacks. However, in some samples 'sandwiching' was noted. Sandwiching occurs when the antibody does not adequately penetrate the sample and leads to a high-intensity signal, mainly at the edges of the sample. To avoid sandwiching, samples were incubated for longer at 4°C – the colder temperature limiting the movement of the molecules and promoting deeper penetration. However, despite these measures, sandwiching continued to be a problem in some samples. **(Figure 5.23)**

This signal distribution may have been because of the underlying architecture of the sample itself and potentially the tumour cells being more densely populated or more proliferative at its boundaries.

Figure 5.23 *Cross sectional images of tumour to demonstrate sandwiching of antibody.*



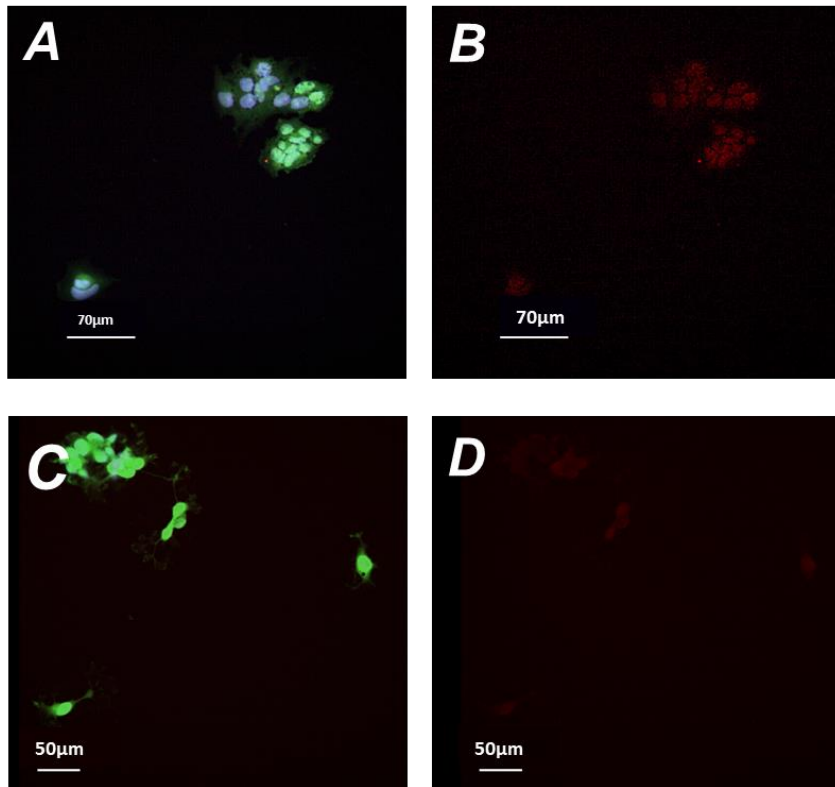
Tumour sample was harvested and fixed as previously described. The tumour underwent clearing – antibody labelling – clearing as described above. Images were taken using Andor Dragonfly microscope with 20x water immersion objective. Images shown are A) Top B) Middle and C) bottom of the tumour. The red arrows highlight where there is an accumulation of antibody and fluorescent signal at the edges of the sample.

5.3.12 Detecting apoptosis in neuroblastoma tumours using a cleaved caspase-8 antibody.

Alongside the optimisation of Ki67 as a proliferation marker, the characterisation of cells undergoing apoptosis was also attempted.

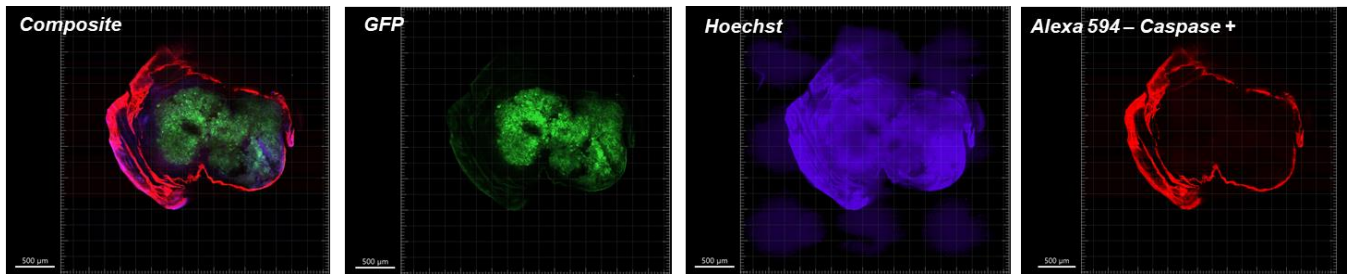
Caspase 8 is an integral protein in death receptor-associated apoptosis. In this experiment, the anti-cleaved caspase 8 antibody was incubated with neuroblastoma cells and tissue sections to assess the level of basal apoptosis. In the initial pilot and optimisation experiments, we observed minimal positive staining. We treated the cells with staurosporine, a broad kinase inhibitor well-known to induce apoptosis to optimise antibody dilutions in conditions with a high percentage of apoptotic cells. Despite increasing the concentration to 1 in 50 for the primary antibody, the signal detected remained very weak at the detection limit. (**Figure 5.24**) The same was observed in tissue sections, with non-specific staining surrounding chick tissue. (**Figure 5.25**)

Figure 5.24 Cleaved caspase-8 staining on neuroblastoma cells.



Cells were grown in imaging dishes for 12 hours. They were washed and fixed in PFA, and labelled as per the Immunocytochemistry protocol outlined in Materials and Methods. As a positive control apoptosis inducer 200nM staurosporine was added. A) A composite image of cells with Staurosporine only, with no antibody staining B) anti-cleaved caspase-8 staining (Red channel) in staurosporine treated cells showing no specific staining. C) A composite image of cells treated with staurosporine and labelled with anti-cleaved caspase-8 antibody. D) anti-cleaved caspase-8 staining (Red channel) in non- treated cells, showing no unspecific staining

Figure 5.25 Cleaved caspase-8 staining on neuroblastoma sections.



Tumour sections were fixed and labelled as previously described. Anti-cleaved caspase-8 antibody (1:50) and secondary anti-rabbit-Alexa 594 (1:250) was used. Images were taken using 10x magnification and tiling function on the Andor Dragonfly microscope.

Figure 5.25 demonstrates the non-specific signal detected in the red channel. There is minimal signal within the tumour, indicating that the antibody did not bind to these cells. A high signal is detected from the surrounding chick tissue, likely non-specific

Due to the lack of clear specific staining with this antibody and time constraints, we did not further use cleaved caspase staining for neuroblastoma whole tumours.

5.3.13 Image quantification.

Quantitatively analysing data obtained from cleared immunolabelled tissue is a complex undertaking. For cleared 3D samples to be comparable to immunohistochemistry, one must be able to extract critical data on cell morphology, the presence of proteins of interest and proximity to blood vessels from the images. The image analysis method used will vary depending on the data required.

5.3.13.1 Nuclear segmentation

Features of the cell that may be obvious to the human eye can be hard to delineate into quantitative algorithms for a computer to replicate. Computational algorithms such as standard edge detection can detect the lateral boundary of cells in low density. However, in high-density samples, such as tumour tissue, it becomes increasingly difficult to discriminate cells, and the most commonly encountered problem is identifying single objects when they are overlapping. Nuclear segmentation analysis identifies nuclei within cells, and by thresholding the known size of the cell, one can attempt to characterise each cell from the fluorescent signal around it. Different

morphological approaches have been developed to segment nuclei in 3D images collected from biological tissues such as mouse pancreatic islets and tumour spheroids. (Mathew *et al.*, 2015; Tran Thi Nhu *et al.*, 2017)

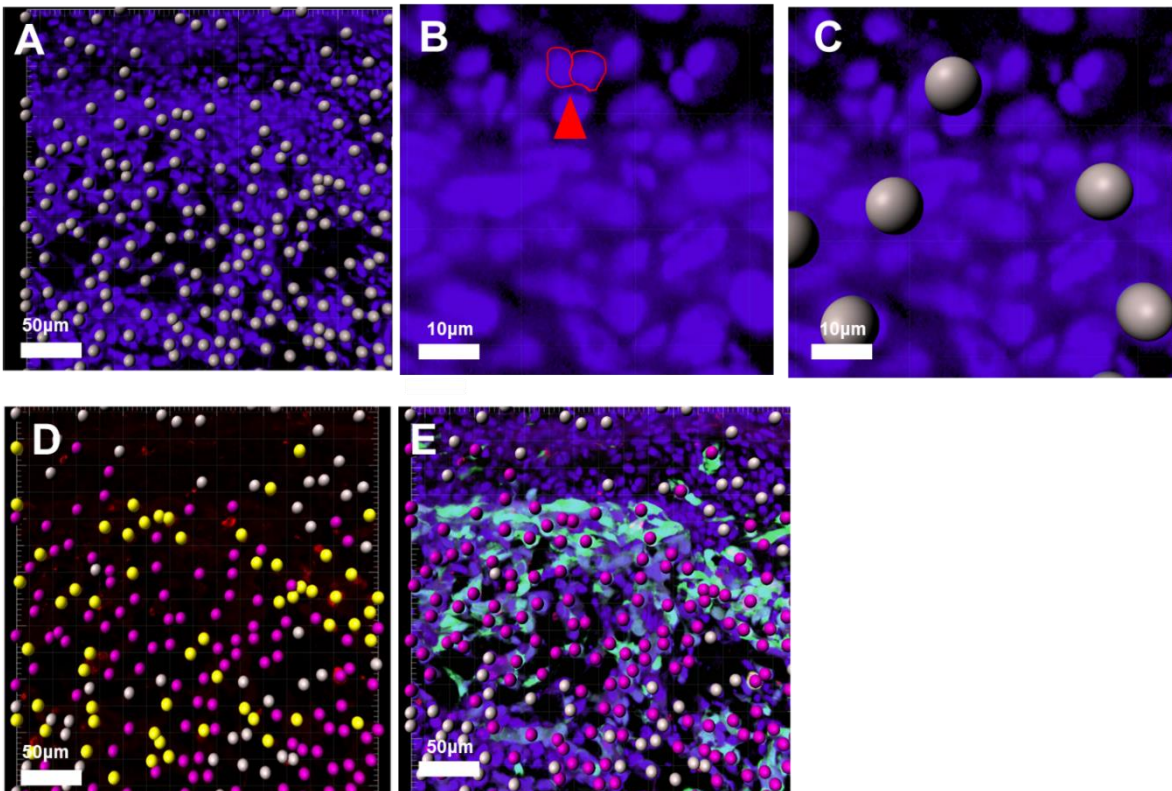
Immunohistochemistry analysis is often done by characterising morphology or counting the presence of positively stained cells. With Ki67, which labels the nuclei of actively proliferating cells, this is done through cell count. This is explained in chapter 3. Manual counting or machine counting is employed for frozen and paraffin embedding samples. Here programmed counting was attempted in two ways.

Firstly, using the Imaris spot function. The Imaris spot function allows spots of set threshold intensity or diameter to be detected and counted. This is a simple function if there are clear nuclear stains for the program to detect. In this dataset, both chick and human cell nuclei stained positive for Hoechst. As a result, the cells had to be categorised further into that above 8µm and those below. This value was determined by measuring several known human nuclei and calculating the average. As shown here, most of the human nuclei were detected correctly. However, in some circumstances, chick cells close together are also detected incorrectly as a human nucleus. Although it is possible to edit the selections manually, for high throughput screening, this is not desirable.

Figure 5.26 shows how the positive nuclei can be counted. Additional filters can be added, so only those with an average intensity in the red channel above a threshold amount are counted – positive KI67 cells. The workflow figure shows how to segment and count positive green cells if 100% of neuroblastoma cells showed a green signal. However, as seen in the previous immunocytochemistry, some neuroblastoma cells do not exhibit strong green fluorescence, so numbers of 'green' positive cells could not be used in the analysis.

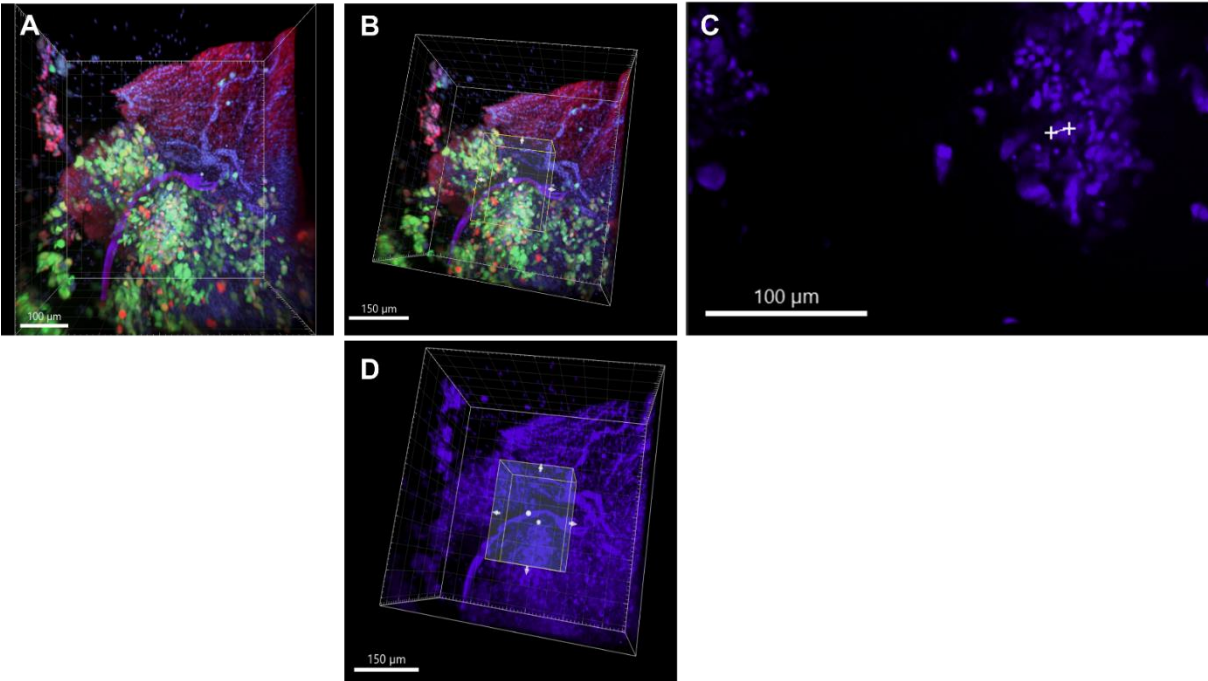
The next challenge was to extrapolate this into a 3D image. The z-stack for tumours can be up to 700µm, and I have previously shown that the Ki67 signal can be detected at depth. The same workflow was applied to the 3D tumour images, firstly by analysing a preset small area and then extrapolating to the whole image. (**Figure 5.27**)

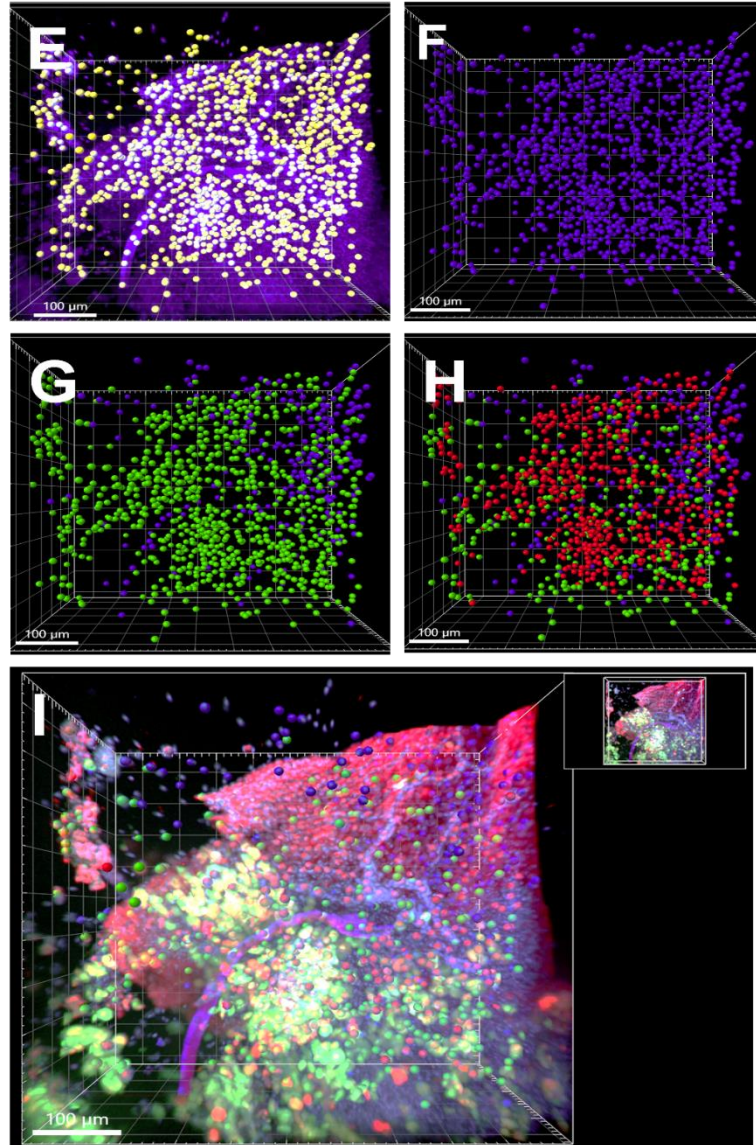
Figure 5.26 Using Imaris Spot function to segment nuclei.



Images are from whole GFP labelled neuroblastoma tumour, cleared and immune-stained with Ki67/Alexa 594 and labelled with Hoechst. Imaris spot detection algorithm was firstly applied to the Hoechst channel images. As Hoechst is a nuclear stain which labels both chick and human tissue the cells were then sorted by size. A) Those over $8\mu\text{m}$ were classified as human and counted, and those less than $8\mu\text{m}$ were considered to be chick. B+C) However spots close together or overlapping may give false positives as shown by red arrow and outline. Two chick nuclei are overlapping but give an overall impression of being $>8\mu\text{m}$ and so have been counted as positive by the program. D) The areas of red intensity are then segmented and areas where red and blue colocalise are shown in yellow. E) The overall images with the spots isolated. Counts can be performed to show the total number of 'blue', 'red' and 'red and blue' spots. .

Figure 5.27 Nuclear segmentation of 3D images using Imaris workflow.





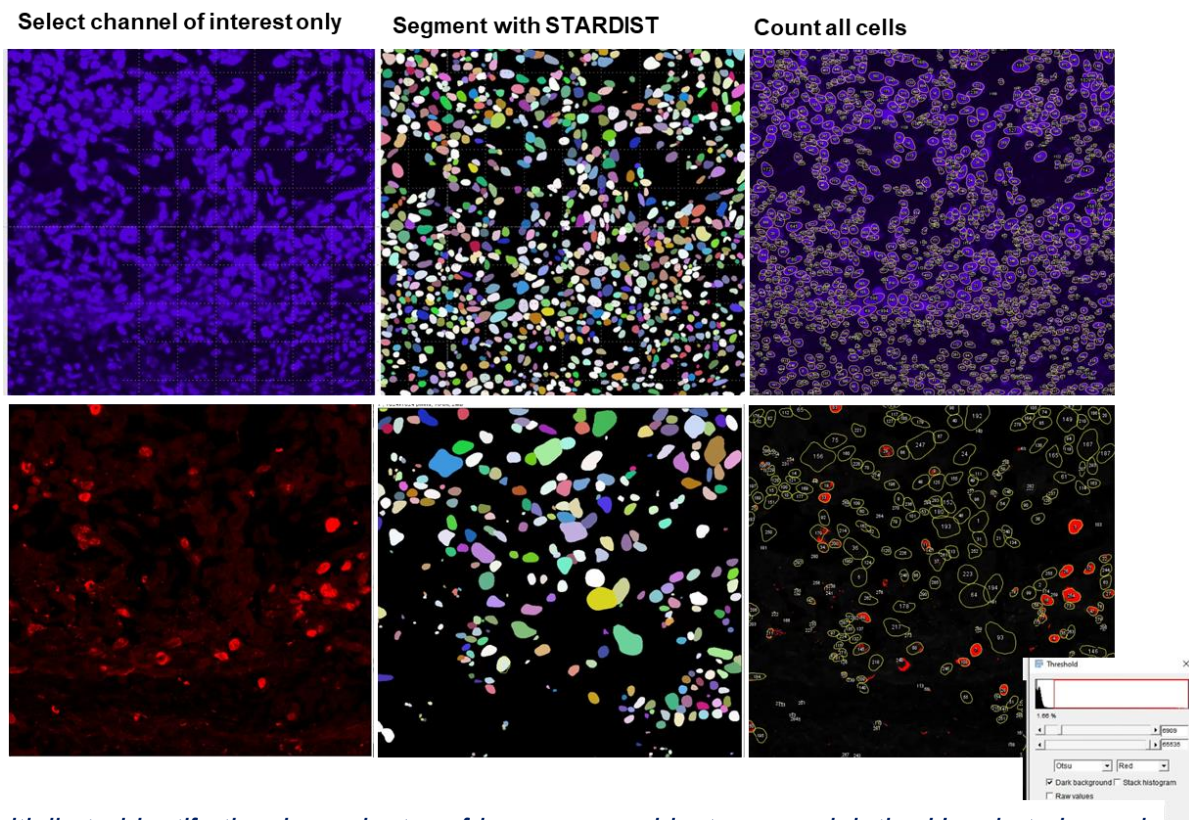
A) Original image B) Preset area selection: a preset area is selected to perform the preliminary segmentation C) Setting threshold by nuclear size - the thresholds for intensity and nuclear size are set within this set area. D) This is then extrapolated to the whole images E&F) Segmenting all spots $>8\mu\text{m}$ in blue channel. All the positive human nuclei are shown as blue spots G) Segmenting all spots 'green' + ' $>8\mu\text{m}$ in blue channel' – all neuroblastoma cells are shown green spots H) Segmenting all spots 'green' + ' $>8\mu\text{m}$ in blue channel' + 'colocalised with red'. All cells positive for green, blue and red signal are shown. I) Analysis is extended to the whole 3D image.

Here quality assurance became an issue. Whereas with 2D images, it was possible to scrutinise the automatic selection of nuclei, with the 3D images, the program does not allow this same function. Reviewing each z-plane to check the correct identification of nuclei is also highly inefficient. Also, a maximum intensity projection was used for analysis; the signal from deeper within the tissue is undoubtedly lower than at the surface. As a result, expanding the threshold to detect this signal leads to a greater level of noise being included in the analysis from the surface.

In comparing the two sample types, the first group being sectioned and stained and the second imaged as a whole; there was a discrepancy in positive Ki67 counts. Both tumour groups were from the same untreated cell type. The sectioned samples had a 30% positive Ki67 cell count (n=5 tumours with three sections from each tumour, taken near the top, middle, and bottom of each sample.) The wholemount tumour group had a 50% Ki67 cell count (n=4 tumours). This difference could reflect the signal loss through cryofixation of the frozen, sectioned samples. It could also incorporate the additional noise and non-specific signal from the higher signal intensity of the whole mount sample. By comparison, the sections analysed in chapter 3 using immunohistochemistry had, on average, 80% positive Ki67 cells in the control group. The antibody labelling for the immunofluorescence methods is not as representative as the paraffin-embedded sample labelling.

The second method of nuclear segmentation using Image J with the STARDIST plugin was also explored for completion. StarDIST is a deep learning nuclear detection typically trained on annotated training data. (StarDIST – QuPath: <https://qupath.readthedocs.io/en/stable/docs/advanced/stardist.html>. Accessed 18-04-2022) STARDIST assumes that the nuclear polygon for segmentation is a star complex – a shape where the boundary can be reached from the centre without crossing any other boundary. It uses this algorithm to 1) predict the probability of each polygon being a nucleus by calculating the distance from the centre of each object to its nearest boundary and 2) use the probability calculated to identify those with high probability and suppress those which are low probability. The advantage of doing this in a sample with 'crowded' nuclei is that whereby other segmentation might remove polygons with high overlap that is unlikely to be a nucleus, STARDIST recognises them as likely to be a nucleus and does not discount them. (Figure 5.28)

Figure 5.28 Workflow for nuclear segmentation in 2D images using STARDIST.



Initially to identify the denominator of human neuroblastoma nuclei, the Hoechst channel is selected and segmented. All cells are identified but those with a size below the set threshold were removed as likely chick cells. The process was repeated using Ki67 red channel images only. The difference between the two outputs gives the percentages of positive Ki67 cells.

When comparing the cell counts from 2D images using STARDIST and IMARIS software, they were 33% and 24%, respectively. STARDIST can be trained for the analysis of 3D images. However, this was not done due to the large number of samples needed for accurate training and available time.

|

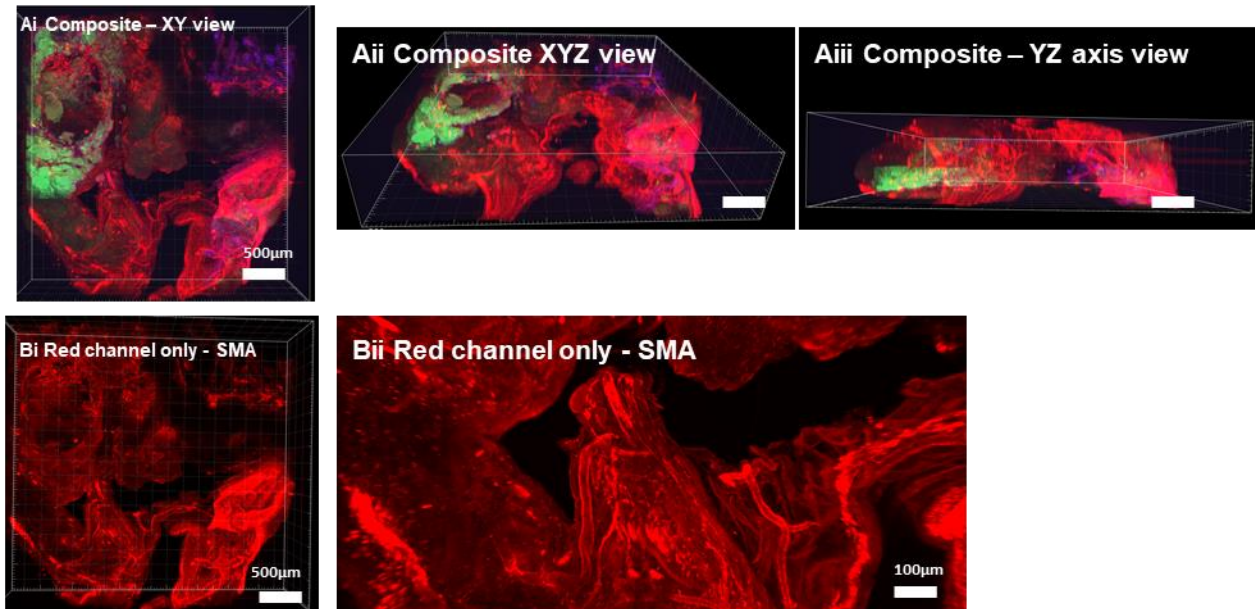
have shown that it is possible to clear, label and quantitatively image tumour samples. The greatest limitation is the significant amount of background signal. Although attempts were made to reduce it, it was present in all samples. This introduced a false positive rate when counting red

fluorescence. In addition, the number of positive Ki67 cells from the cleared 3D images was lower than the histopathology samples previously analysed, likely due to antibody penetrance into the sample. Further optimisation is needed to troubleshoot these issues. However, as a work in principle, I have shown it to be possible.

5.3.13.2 Tissue clearing and imaging methods for vessel analysis.

Another critical characteristic of tumour survival and growth is neo-angiogenesis. Labelling and quantifying blood vessels *in vivo* may be done through perfusion using lectin (specific carbohydrate-binding protein), fluorescent dyes such as long-chain carbocyanine dyes (DiI, DiO, DiD) and finally, immunohistochemistry using markers for endothelial cells such as CD31 (Cavallero *et al.*, 2015) or SMA (Sharma, Chang and Red-Horse, 2017) In this work, we chose to examine the feasibility of smooth muscle actin staining for characterising the density of the blood vessel network within the tumour tissue. Smooth muscle α -actin is also the first known marker of differentiated SMCs upregulated during vasculogenesis. (Owens and Irwin, 2012) Samples were cleared and stained using the previous workflow. As previously discussed, perfusion of an eluting agent, such as PFA, can clear the vessels' blood and provide views of the vasculature. Cleared and labelled samples showed immunolabelling of the blood vessels and staining of the surrounding chick tissue. The antibody is also sensitive to chick tissue. The chorioallantoic membrane upon which the tumours are grown originates from chick mesoderm and, as such, is a rich network of vasculature and connective tissue. This may explain the highly organised structures in the smooth muscle actin staining. (Figure 5.29)

Figure 5.29 Smooth muscle actin immunolabelling of cleared whole neuroblastoma tumours.



Tumours were cleared using CUBIC protocol. SMA antibody (1:200) /anti-rabbit-Alexa 594 (1:500) were used to identify vasculature. Images were taken on the Andor Dragonfly microscope, 10x times magnification and tiling function was used to provide an overview. Composite and red channel only images are shown. Vessels are clearly seen within the Chick CAM, but there is also significant non-specific signal from the surrounding membrane tissue.

Developing an analysis workflow to quantify vasculature density in these images was done with the help of Dr Marie Held, image analyst in the CCI. (**Figure 5.30**)

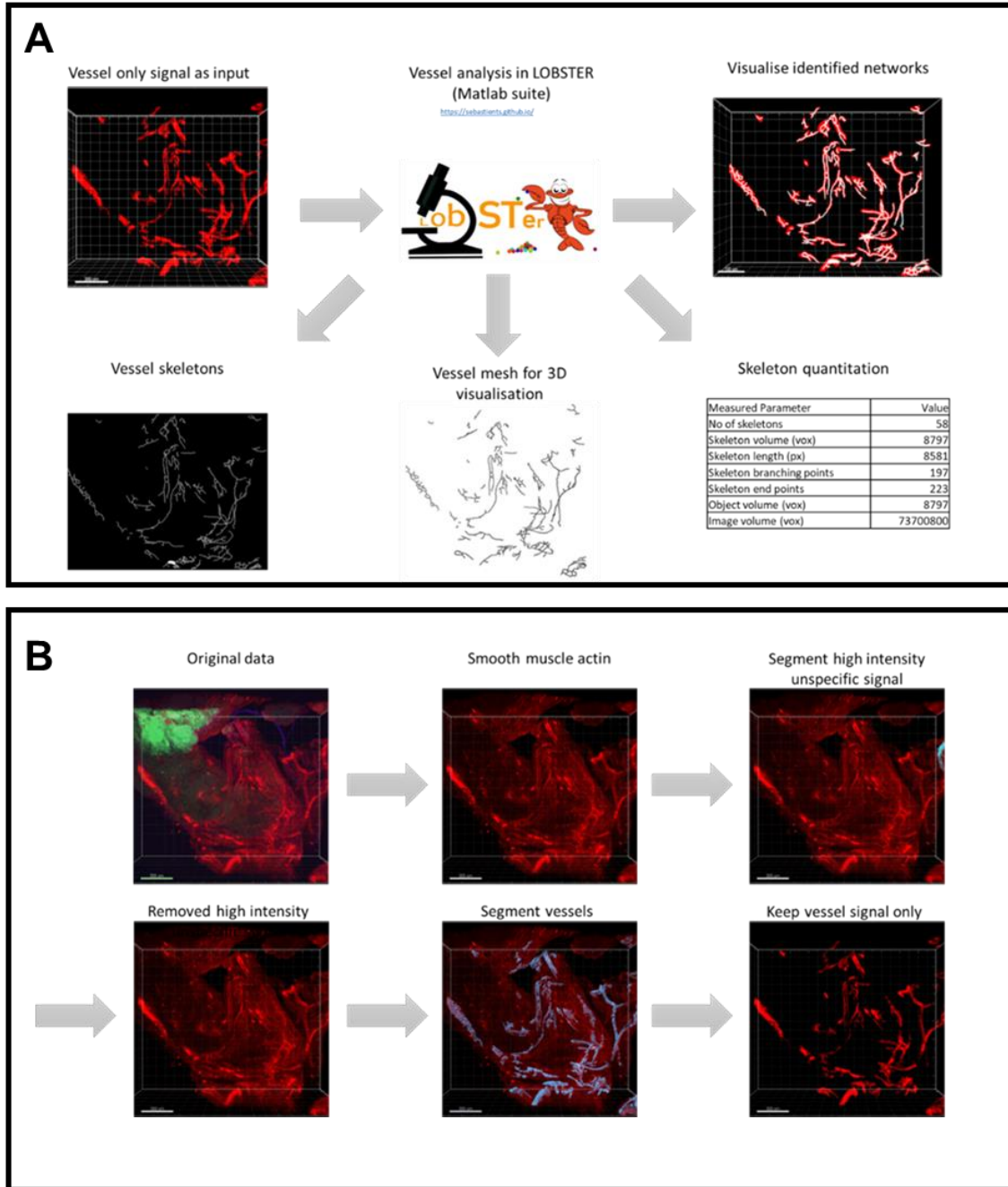
The programme used was LOBSTER. LOBSTER stands for Little OBjects Segmentation & Tracking EnviRonment and is an image analysis environment to identify, track, and model biological objects from large multi-dimensional microscopy images. LOBSTER requires Matlab and the Image processing Statistics & Machine learning toolboxes. The source code was downloaded from the *Github repository*). One possible output measurement for blood vessel analysis and quantification is the organisation and density of the vasculature network. Here, vessel segment length and vascular branching were assessed by skeletonising the binary image. This allowed the algorithm to tag all pixels in a skeleton image, count all its branches, and

measure their average and maximum length. (**Figure 5.30**) Skeletonisation is a process of computing single voxel thick lines through the centre of vessel boundaries. The surrounding signal is then systemically removed through thresholding until all that remains is the one voxel-thick structure delineating blood vessels. Images obtained through the clearing and labelling protocol shown in **Figure 5.29** were not optimal for this process. Although some tumour images could be segmented and analysed, they were inconsistent. One of the main issues was the high signal level from surrounding tissues. Perfusion of the vasculature alongside more specific vasculature labelling protocols should be used to reduce the background signal. The chick embryo involves accessing the blood vessels with fine glass needles and instilling the agent by gently blowing through the apparatus. The rate of chick death through this method is high, which may not be a problem if this is performed at the end of the incubation period. It is also a technically demanding method requiring specialist equipment to perform.

Khoradmehr et al. imaged the brain vasculature in a mouse model using FACT clearing methods, immunolabelling with CD31 and analysis with the Imaris filament algorithm. (Khoradmehr *et al.*, 2019) Similarly, Kostrikov et al. have recently published work in glioblastoma mouse models, using dextran perfusion to identify the vasculature. (Kostrikov *et al.*, 2021) However, as seen before, the sample will dictate the success of any given imaging technique. The ordered vasculature within the brain is different from the haphazard tumour vasculature. The tumours from the chick embryo also have their dense vasculature and the vasculature of the CAM within the sample.

There were multiple areas for errors to occur in our analysis. If the initial image has a strong signal outside the desired vascular tree, it can be difficult to distinguish this signal from the blood vessel. In addition, it is impossible to accurately threshold all vasculature when vasculature displays a haphazard arrangement and multiple small branches, which was the case in our images. Manually-guided approaches allow for comprehensively and accurately correcting skeletons but are labour-intensive. We, therefore, could not use this approach to assess the drug effects on the tumour vasculature and angiogenesis. One alternative possibility to assess drug distribution in the circulation was to use fluorescent retinoids, which I have briefly explored

Figure 5.30 Workflow for vessel segmentation in 3D rendered images.



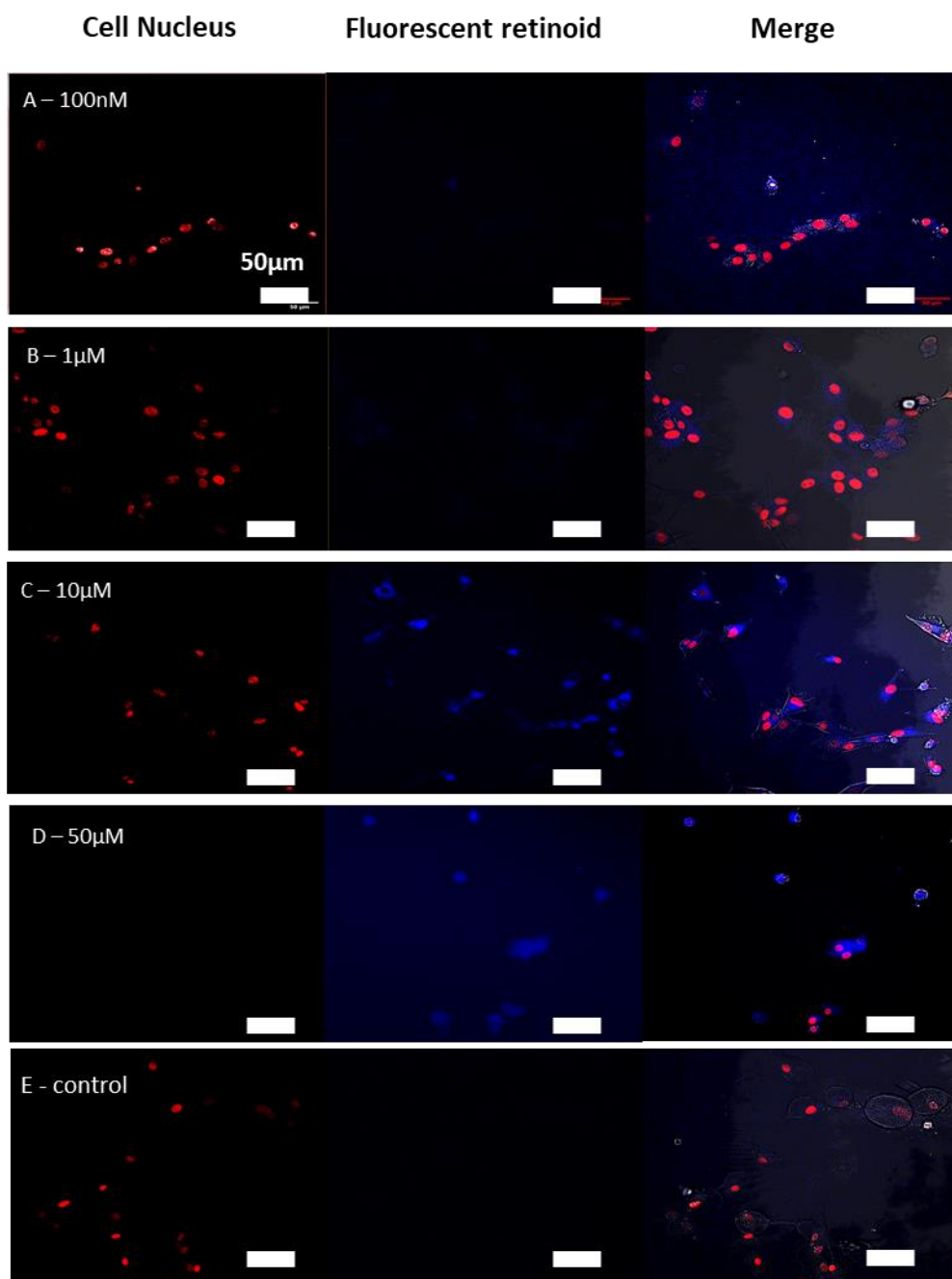
A) Lobster is able to segment and count vessel length and branches on processed images. Pre-processing was necessary to optimise the image segmentation for use in LOBSTER. B) Vessels should be the only structures present in the images presented to the LOBSTER vessel analysis. High intensity unspecific signal from unspecific staining and/or autofluorescence was removed using an image processing software - Imaris was used here. The vessels were segmented using the surface generation tool in Imaris. The signal outside of the segmented surfaces was deleted via masking and setting the pixels outside the masked area to 0. Workflow designed and taken with permission from Dr Marie Held, CCI University of Liverpool.

5.3.14 Evaluating the utility of fluorescent retinoids for vasculature labelling and tracking drug delivery

For the chick embryo to be effective as a preclinical drug testing model, drugs must be successfully delivered to tumour cells. For example, if all drugs injected simply aggregated in the liver and did not reach the desired tumour, the drug effect could not be adequately assessed. In clinical practice, retinoic acid is a differentiating agent in relapsing neuroblastoma. DC271 is a retinoic acid analogue that can be used to localise retinoic acid within cells (Chisholm *et al.*, 2019). The fluorescent retinoid can be imaged using UV-A (340-380nm) or violet excitation (405nm). In collaboration with David Chisholm's group at the University of Durham, I have chosen to assess the utility of this compound in the chick embryo model. (Tomlinson *et al.*, 2018; Chisholm *et al.*, 2019). The aim was to assess whether this compound can be used to track drug delivery in the chick embryo and if it can be used as a fluorescent label of the chick circulation.

The assessment of fluorescent retinoids was initially carried out in cell culture before progressing into living chick embryos.

Figure 5.31 Increasing cell concentration of DC271, to establish detection threshold.



Histone H2B-RFP expressing HeLa cells were used for this experiment as the nucleus expresses a red signal. These cells were treated with increasing concentrations of DC271 for 1h before imaging. The compound was dissolved in DMSO and the control was treated with the equivalent concentration of DMSO. Images taken using Zeiss LSM 780 confocal microscope with 40x magnification

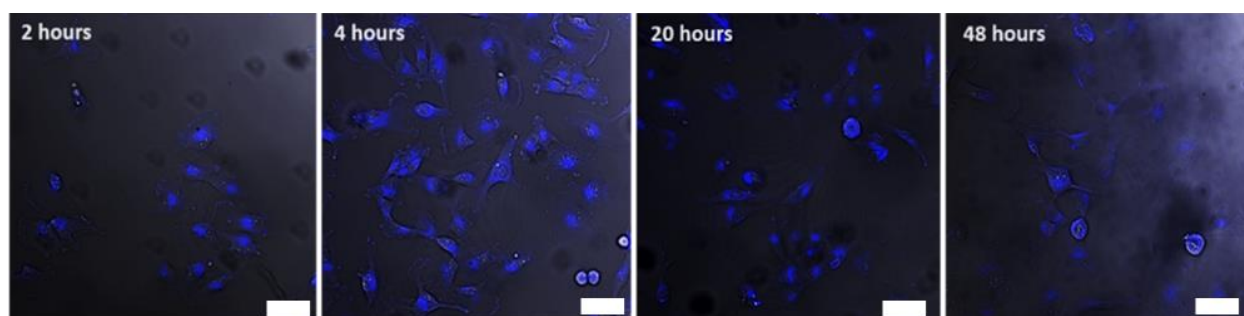
5.3.14.1 A low concentration of fluorescent retinoid can be detected in cell culture

Firstly the concentration needed to visualise the retinoid within the cell culture was assessed. Nuclear labelled Hela cells were used to assess the uptake. The DMSO-treated control showed no endogenous autofluorescence with the imaging parameters used. Increased cell death in control and 50 μ M DC271 groups indicated DMSO-related toxicity. The fluorescence at 100nM was hardly visible. A concentration between 1 μ M and 10 μ M was detectable and non-toxic and was therefore optimal.

5.3.14.2 Fluorescent retinoids can still be detected after incubation for 48 hours

As *in vivo* experiments often take several days, not hours, the fluorescence intensity over time was examined using serial imaging of treated cells over two days. These experiments were also performed in SK-N-BE(2)C neuroblastoma cells to assess compatibility. There was no appreciable deterioration of the fluorescent intensity over time using DC271.

Figure 5.32 *The intensity of DC271 fluorescence retained by cells over time.*

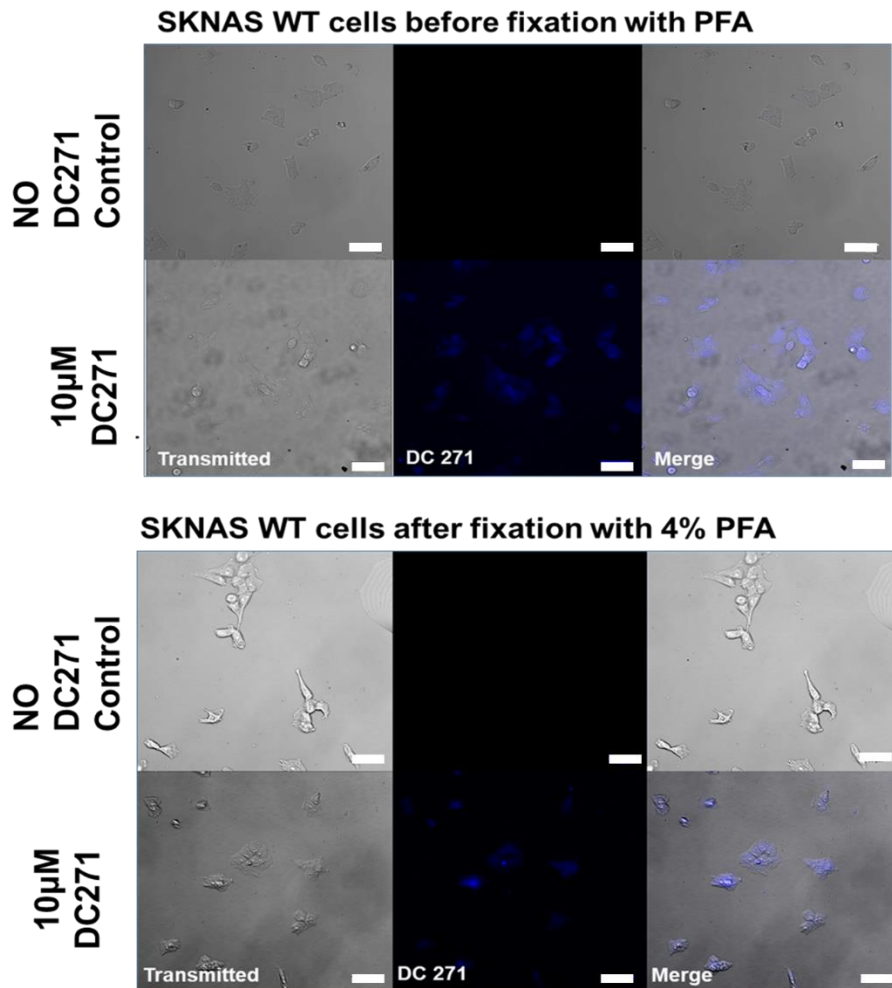


Cells were treated with 10 μ M of DC271 continuously and were imaged at 2, 4, 20 and 48 hours. There was still a detectable signal using the same imaging parameters after 48 hours of incubation. Images taken using Zeiss LSM 780 confocal microscope with 40x magnification. Scale bars represent 50 μ m

5.3.14.3 There is no change in fluorescence after the fixation of cells with paraformaldehyde.

Tumours are often fixed in paraformaldehyde after dissection. This fixation process is known to amplify autofluorescence and quench fluorophores. Therefore, the detection of fluorescent retinoids before and after PFA fixation was examined. There was no evidence of increased autofluorescence or diminished DC271 fluorescence after treatment with PFA.

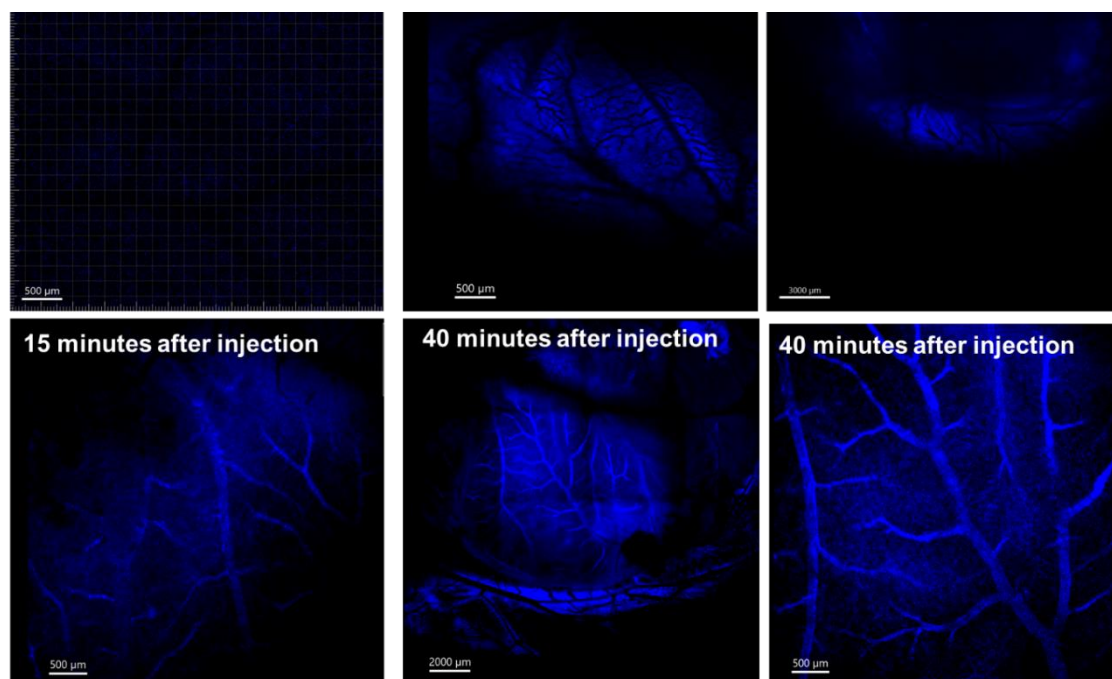
Figure 5.33 The fluorescence intensity of DC271 before and after fixation with PFA.



Cells were treated with 10 µM of DC271 for 4 hours. Fluorescence intensity was checked prior to 4% PFA fixation and imaged again. Control cultures were used to assess any increase in endogenous auto-fluorescence secondary to fixation. Images taken using Zeiss LSM 780 confocal microscope with 40x magnification. Scale bars represent 50 µm

Finally, the compatibility of the compound with injection into the chick embryo was assessed. Chick embryos were incubated until embryonic day 14. On day 14, the chicks were placed into the incubation chamber of the lsm880MP microscope. The incubation chamber was temperature-controlled, and humidity was optimised using a water bath within the chamber. 10µM of compound DC271 was injected into the chorioallantoic membrane. Images were then taken at serial time points to assess circulation through the vasculature. This experiment was also attempted ex-ovo with the chicks cultured in sterilised weighing boats. This advantage would have been a larger field of view over the embryo and CAM. However, the survival of chicks in this culturing method was very poor, and they did not tolerate rehousing into the microscope, so this protocol was abandoned. Reassuringly after 40 minutes, most embryos were still alive – and so the compound itself was not immediately lethal on injection.

Figure 5.34 *The distribution of DC271 through the chick embryo vasculature upon injection.*



In control chicks, in which no compound was injected there was no detectable signal at 405 nm range. After injection into the yolk sac of DC271, there was an immediate distribution within the yolk sac itself, with the vasculature appearing black on the background of blue signal. Over time the compounds were absorbed into the vasculature and by 40 minutes there was a clear signal in the vascular network. This further evidence that injections within the yolk sac reach adequately the chick circulation. Images were taken using EC-plan Neofluar objective (magnification 10x, NA 0.3) in a temperature and humidity controlled imaging chamber.

The continuation of this work would have been to assess the circulation of the compound into a tumour grown on the CAM. However, due to time constraints, this was not achievable.

5.4 Discussion

5.4.1 Choosing the most appropriate clearing method

Innovations in tissue clearing and microscopy methods have permitted the application of fluorescent imaging in understanding biology. Whole organ and even whole organism clearing methods have become more efficacious and refined in the last decade. The imaging techniques and analysis software that complements these have also been developed. This unprecedented access to intact tissues on a cellular and subcellular resolution has primarily been used to analyse neuronal structures and vessel analysis. (Shearer *et al.*, 2016) Although initially developed for imaging neuronal tissue, the techniques are now transferrable to interrogating tumour tissue and the surrounding extracellular matrix. (Susaki *et al.*, 2015) The ability to resolve complex 3D structures on a molecular and cellular level has opened the door for drug efficacy studies and the characterisation of mechanisms that preferentially drive tumour progression. For example, Kubota discusses the utility of single-cell resolution in identifying metastasis in whole animals (Shimpei I. Kubota *et al.*, 2017b). They could track single cells as they metastasised in the whole mouse by injecting fluorescently labelled tumour cells. This enabled the characterisation of metastasis and the assessment of new drugs.

This work aimed to, at least in part, assess the utility of the 3D whole tumour imaging approach to assess neuroblastoma tumour growth in the chick embryo model. We compared two tissue clearing protocols for their performance in terms of optical transparency, structural preservation and preservation of the fluorescent label of the neuroblastoma cells. This is the first study to combine neuroblastoma tumours and clearing protocols and tumours grown in the CAM clearing. This chapter is, therefore, about technology development and optimisation.

A concern around many clearing techniques is the observed change in sample size and possible change in cellular structure. (Becker *et al.*, 2012b)(Hama *et al.*, 2011). Here we observed with CUBIC clearing some sample expansion and increased sample weight. However, we did not see any morphological changes at a higher magnification than a non-cleared sample. However, the clear depiction of morphology for uncleared samples is complex by the nature of the sample's opacity, so a direct comparison to the cleared sample is difficult. Although the microscopic appearance of the cells appears similar in the CUBIC group, the actual integrity of the tumour after clearing content cannot be assessed through microscopy alone. Protein quantification

assays, such as Bradford assays, were not performed here for a few reasons: As each tumour is very different in size and structure, the number needed to provide an accurate control and treatment group is high. Secondly, the chemicals used in the clearing solutions interact with the assay and would not yield accurate results. The ECI group was different, with hardly any defined cellular structures observable. The changes observed in the CUBIC group are minimal and predictable, and as long as any control groups are cleared before analysis, this linear expansion can be considered. We concluded that the CUBIC clearing protocol is better than ECI for clearing neuroblastoma tissues.

The challenge of clearing tumours compared to brains is not insignificant to overcome. The heterogeneous nature of the tissue, from its size and cell type to the density and microarchitecture, all present hurdles to clearing and imaging. Haemoglobin is one of the primary molecules responsible for light absorption in tissues. The red blood cells carrying the haemoglobin can be removed with the perfusion of a buffer or fixative agent. (Susaki *et al.*, 2014b). This ensures that the vasculature is clear and aids in the clearing and post-clearing analysis of blood vessels. In the chick embryo model, any manipulation of the chick involves removal from the incubation chamber and exposure to cold surroundings. Cannulation of vessels is best performed on embryonic day 11. At this stage, the vessels are easy to visualise and manipulate without being too large, causing a haemorrhage and premature termination of the embryo when perfused.

Throughout our time course studies, embryos were euthanised, and tumours harvested at embryonic day 14, so PFA perfusion would terminate the experiment before this stage. Where perfusion is impossible, treatment with hydrogen peroxide or amino alcohol to remove the heme has been described. (Tainaka *et al.*, 2014). However, hydrogen peroxide decolours the haemoglobin, affects the GFP signal, and damages the overall tissues. (Alnuami *et al.*, 2008) As such, the samples from the CAM still have circulating blood cells, which will impact the optical clarity.

5.4.2 Challenges of immunolabelling in the 3D sample

Immunolabeling thick samples present a myriad of troubleshooting. Low antibody penetration hinders the high throughput large-scale imaging of thicker sample tissue. The large molecular weight of antibodies can limit their penetration and significantly increase the time taken for immunolabelling. Again, tumour tissue's haphazard and fibrous organisation only worsens the issue. We optimised antibody concentrations and tried longer incubation times to overcome these problems. However, the antibody penetration in many samples was non-uniform, and the

quantification data derived was poorly reliable. The phenomenon of 'sandwiching', whereby the antibody binds primarily at the edges of the sample, was often seen. Steps to avoid this have been described in the literature, using single-domain antibodies or nucleic acid aptamers which are a fraction of the size of standard antibodies and can better access epitopes deep in a sample in a shorter time. (Holliger and Hudson, 2005) (Bunka and Stockley, 2006) Additionally, direct fluorophore conjugation to these probes reduces signal amplification and the need for two antibody incubation steps. However, these antibodies are not readily available or compatible with all tissue types. Wang et al. showed that reduced formaldehyde concentrations within the hydrogen embedding PACT PARS clearing module reduced the crosslinking within the gel and permitted greater antibody penetration. (Wang, Khoradmehr and Tamadon, 2019) This method also allowed for the preservation of tissue architecture but was only shown on thick brain sections, not whole organs. Nevertheless, monoclonal antibodies are large molecules (150 kDa), which is why there is poor tissue penetration. Methods have been developed to use antibodies' unique affinity and specificity whilst troubleshooting pharmacokinetic issues. Antibody fragments such as Fab, single chain Fv (scFv), or variants like mini bodies have been engineered to create *in vivo* imaging agents. (Holliger and Hudson, 2005; Olafsen and Wu, 2010; Kaur *et al.*, 2012)

Nanobodies are antigen-binding fragments derived from camelid heavy chain-only antibodies, which fold and function without light chains. Typically, nanobodies have a molecular weight of ~12–16 kDa and are considered the smallest immunoglobulin-derived antigen-binding fragments, so nanobodies can penetrate tissues more efficiently and bind to antigens more effectively than antibodies and their smaller derivatives. (Harmand *et al.*, 2021) Protocols are also using nanobodies for whole organism labelling. Cai et al. introduced the vDISCO protocol, a pressure-driven nanobody-based whole-body immunolabelling technique which can enhance the fluorescent protein signal. (Cai *et al.*, 2019b). A disadvantage of nanobodies is that their relatively small size leads to rapid elimination from the circulation by renal clearance, and concentrations of the imaging agent in the kidneys may make imaging experiments in surrounding tissues difficult because of the high background signal and lead to renal toxicity. (Movahedi *et al.*, 2012). Also, nanobodies preferentially bind to discontinuous conformational epitopes and therefore do not always bind correctly to denatured proteins. (Allegra *et al.*, 2018) Many current nanobodies are designed for *in vivo* use, not fixed samples. Also, only limited nanobodies are currently commercially available. Non-antibody-based labelling methods have also been explored. In many

mouse models, compounds such as injectable lectin or dextran act as vascular markers. (Sarkar and Schmued, 2012).

5.4.3 Selecting the most suitable imaging tool and parameters

Several optical sectioning methods for volumetric imaging are now available with cleared tissue. These include confocal – including spinning disc, 2-photon and lightsheet microscopy. They each have their merits and drawbacks, as previously described. We explored the possibility of lightsheet microscopy and confocal and two-photon microscopy for this work. Lightsheet microscopy has been well described for its use with optically cleared samples. The system yields fast image acquisition with low laser power to preserve the sample. However, the broad field of view afforded by the low numerical aperture has come at the cost of spatial resolution – usually axial - in most systems. (Weber and Huisken, 2011). Models projecting thin light sheets (<5 μm), such as Objective-Coupled Planar Illumination Microscopy (Holekamp, Turaga and Holy, 2008) and Lattice Lightsheet (Chen et al., 2014), provide the best axial resolution but can only image samples a few hundreds of micrometres thick. Lightsheet systems with a thicker lightsheet (up to 40 μm) utilise lower NA objectives to gain a greater area and deeper imaging. In many cases, these are best for cleared thick tissue samples, where imaging the overall architecture but not a high sub-cellular resolution is desired. (Dodt et al., 2007; Verveer et al., 2007; Susaki et al., 2014; Tomer et al., 2014) The dual-plane illumination lightsheet microscope used in this work takes steps towards increasing sample depth penetration whilst preserving the resolution. The dual-plane illumination uses a pair of opposed illumination objectives for illumination. If perfectly aligned, the dual illumination of the sample using thin light sheets can allow for high-resolution extensive specimen imaging. (Weber and Huisken, 2011) Other new lightsheet models have, however, achieving high resolution on a subcellular level and have been used to map cell atlases of whole human embryos (Belle et al., 2017)

The main drawback of the Z1 lightsheet microscope used is the restricted size of the sample holder. Although mounting samples up to 4.5mm in a 1 ml syringe has since been described, this method was not widely used during experimentation. In addition, immersion lenses are fixed within the specimen chamber and cannot be moved to accommodate larger specimen sizes. The importance of imaging with the appropriate refractive index-matching medium is well documented, yet the clearing chemicals used here could damage the lenses and, therefore, not be used. New light sheets are now explicitly engineered for large cleared soft tissue samples. The 'Cleared

Tissue Lightsheet' from 3i boasts a chamber size of over 1cm and high numerical aperture objectives with long working distances of up to 114mm. This adaptation in microscope development is promising for future large cleared samples imaging. (*Cleared Tissue LightSheet - 3i*, no date)

Confocal microscopy uses a spatial pinhole to exclude out-of-focus light and generates in-focus high-resolution contrast fluorescence images. The disadvantage is the slow image acquisition. Also, the higher numerical aperture objectives required for high resolution have narrow free working distances and consequently reduced imaging depths. The two microscopes used here – the Zeiss lsm 880 multiphoton and the Andor Dragonfly spinning disc confocal, address different drawbacks of a conventional confocal. The spinning disc microscope uses hundreds of pinholes arranged in spirals on an opaque disc. The pinholes scan the sample and build an image as the disc rotates at high speed. The result is high-speed image acquisition with reduced photobleaching of the sample. (Oreopoulos, Berman and Browne, 2014) The acquisition speed and resolution achieved for the images obtained with the Dragonfly microscope were a great advantage with a sufficient resolution. However, spinning disc microscopy has disadvantages, impacting thick sample imaging. Unlike a single pinhole system where all out-of-focus light is blocked, the light scattered in areas adjacent to the focal plane can still reach the detector through adjacent pinholes. This pinhole cross-talk may explain an increased background signal in some samples. (Shimozawa *et al.*, 2013)

The lsm 880 MP system is a multiphoton imaging module. One of the main drawbacks is the working distance of the objectives. Although long working distance (>5 mm) and high NA (>0.9) objectives are now available from most manufacturers, they are still not installed on every microscope as routine. Also, some background noise is still detected at depth with multiphoton imaging, despite light scattering being reduced by clearing. (Richardson and Lichtman, 2015). Unlike the Dragonfly, laser scanning microscopes are time-consuming, and therefore multiphoton imaging of cleared tissue is only practical for high-resolution imaging of small regions or stable samples which are not easily damaged.

5.4.4 Handling large data sets

Acquiring high-volume, high-resolution data is only advantageous if it can be handled, analysed and quantified. (Tian, Yang and Li, 2021) These data pose a unique challenge in data storage,

retrieval and interpretation. Gigabytes or, in some cases, terabytes of images are produced with 3D imaging; therefore, dedicated workstations and analysis expertise are required. Commercial and open-source software modules are available. Fiji/ ImageJ is an example of an open-source tool engineered for image analysis. Commercial software includes Imaris, Vision4D, and Image-Pro plus. However, we noticed that samples were different in the case of tumour clearing. The challenges of such a heterogeneous sample group cannot be addressed by one single algorithm alone. Here I tested two different methods for identifying and counting positively labelled cells. We observed a discrepancy in the number of cells counted from the images and with the immunohistochemistry control. The issue of deep antibody penetration should be solved to obtain better-quality images for analysis. However, even in the thin tissue sections, where antibody accessibility should be more uniform, there was a background signal, and additionally, cell clumping made the individual counts difficult. A computational framework targeting the complexities of each sample type would have to be designed. Machine learning-driven segmentation tools were initially developed to analyse 2D immunofluorescence images, but now many are being adapted for 3D data. Machine and deep learning technologies can segment and recognise regions in z-stack images and can be used to analyse complex 3D data. (Todorov *et al.*, 2020). This is done through inputting many prototype images to ‘teach’ the programme how to identify correct parameters and manually correct any errors. DeepMACT (deep learning-enabled metastasis analysis in cleared tissue) is an example of deep learning, quantifying metastases in whole mice, exceeding human accuracy and dramatically reducing processing time. (Pan *et al.*, 2019). Investing time and effort in developing these methods can ultimately improve the speed and accuracy of 3D tumour sample analysis for integration into clinical applications in the future. (Kingston *et al.*, 2019b)

5.4.5 Tracking cells and compounds *in vivo*

In vivo tracking using fluorescent markers could provide valuable information about tumour angiogenesis and drug delivery in cancer models. However, it is a challenging field, mainly performed in live models, complicated by limited light penetration and variations in fluorescent probes and labelling brightness. New near-infra-red fluorescence emitting proteins such as Neptune is efficient at overcoming some of these hurdles, as in this range of the spectrum, light scattering and autofluorescence are less of a problem *in vivo*. (Lin *et al.*, 2009)(Zipfel *et al.*, 2003). Using fluorescent retinoids here, we clearly showed the circulation of the compound into the

vasculature. Further time course imaging would involve optimising the ex-ovo culture in chick embryos.

Early embryo imaging is limiting as the tissue is often fragile and difficult to manipulate. For our work later, stage embryo imaging is performed. However, at this point, the embryos often move. There are cardiac vibrations and drift of the embryo due to dehydration in the heated chamber. (McKinney and Kulesa, 2021) Work done in our group by Herrmann et al. previous involved imaging chicks ex ovo at embryonic day 10 for up to 30 hours. This work would have aimed to track cell invasion within the ex-ovo model with more time. (A Herrmann *et al.*, 2015)

5.4.6 Conclusion

The advantages of whole tissue clearing for visualising large areas of tumour tissue in 3D are considerable. These experiments have shown that we can image fluorescent proteins at improved depths and resolution than uncleared tissues. On commencing this work, very little was published about whole tumour imaging. The field has grown exponentially during this project, and many of the drawbacks and troubles encountered here are being addressed. New objectives with high NA and longer working distances are more readily available. Open source algorithms for large data set analysis have been published. Troubleshooting antibody penetration issues has produced conjugated antibodies in a broader range of species and tissues. The investment of time and resources in this field indicates its potential. Furthermore, we believe that optimisation of these protocols alongside improved imaging methods and image analysis algorithms will significantly enhance our understanding of the structural organisation, development and spread of neuroblastoma.

Chapter 6 : General Discussion

6.1 The overall aims of the thesis

The PhD project presented in this thesis examined the potential of the chick embryo as a preclinical *in vivo* model of metastatic advanced staged neuroblastoma. The chick embryo is a versatile, cheap, and widely available model and refining its use in neuroblastoma could be advantageous in better comprehending tumour growth and drug screening. We combined this original *in vivo* model with advanced light microscopy imaging to assess tumour growth and alteration of the tumour microenvironment. Indeed, three-dimensional imaging represents a new frontier in understanding tumour biology and drug efficacy. Imaging tumours in 3D offers a more physiological representation of their large-scale spatial organisation and cellular characteristics by providing quantifiable measurements of the effect of novel therapeutics on cellular features and the extracellular environment. We will discuss the choice of the chick embryo model for neuroblastoma studies, the choice of drugs to be assessed in this model and the usefulness and limitation of three-dimensional imaging and image quantification in cancer research.

6.1.1 Chick Embryo model

The chick embryo model has been widely described in the scientific literature for its use in studying embryological development, angiogenesis, and tumour biology. Previous work in Liverpool has developed its use for neuroblastoma research. (Carter *et al.*, 2012; Mather, 2014; A. Herrmann *et al.*, 2015; Herrmann *et al.*, 2018; Swadi, Pizer, *et al.*, 2018; Swadi *et al.*, 2019) The chick embryo was originally described to study melanoma. (Busch, Krochmann and Drews, 2013) Melanoma cells were injected into the developing chick embryo to recreate the embryonic neural crest cues necessary for melanoma metastasis. The origins of neuroblastoma as an embryological neural crest tumour inspired the use of the chick embryo model to study NB. The model then evolved from direct injection of cells (Carter *et al.*, 2012) to establishing neuroblastoma tumour development on the CAM (A. Herrmann *et al.*, 2015) to testing therapeutic intervention against neuroblastoma. (Mather, 2014; Swadi *et al.*, 2019)

Here, we further refined the time for the implantation and introduction of drugs. We also assessed the use of chick weight and survival as a potential proxy of drug toxicity. We employed the experimental model's in-ovo shell window technique described by Ribatti *et al.* (Ribatti *et al.*, 1996). This well-recognised method allows the CAM to be visualised and manipulated throughout

embryonic development. Ex ovo techniques have also been described where the chick is grown in a sterile container or cling film hammock. (Lokman *et al.*, 2012) Ribatti has reviewed both methods and found that the advantages of in-ovo experimentation include a high survival rate, a reflection of physiological conditions and the ability to reach hatching, and a straightforward methodology. In contrast, the advantages of ex ovo include a larger CAM area available for testing, direct visualisation of the entire structure, and evaluation of several samples in a single embryo. (Ribatti, 2008) In our experience, ex ovo culture significantly compromises the survival of the chicks, which limited its use for our experiments.

Patient-derived xenografts (PDX) are an increasingly valuable tool in oncology, providing biologically faithful models of different cancer types and potential methods to develop precision patient-specific therapies. PDX models are thus instrumental in assessing therapies for cancers driven by rare populations of highly aggressive cells or those with a high variance in molecular alterations between patients, such as neuroblastoma. (Dong *et al.*, 2010; Sapro *et al.*, 2013) Chick embryo PDX models have been developed with successful engraftment of several tumour subtypes being described. Importantly the PDX tumours resemble the original patient tumour and demonstrate micrometastasis into the chick mesenchyme. (DeBord *et al.*, 2018) With limited success, we attempted engraftment of patient-derived neuroblastoma tissue into the chick embryo. We found infection of the egg to be a significant issue when tumours were engrafted directly onto the CAM. In addition, these experiments were performed ad hoc as limited number of neuroblastoma resections are done by a single centre, and samples available for experimental work were often insufficient or damaged from the resection. However, this methodology does hold promise and deserves further exploration.

Some reports propose chick embryonic day nine as the ideal time for tumour cell implantation and the best time to harvest is seven days after incubation. (Sys *et al.*, 2013) Our experimentation timeframe ended on day 14 to comply with Home Office regulations. We, therefore, xenograft the cells on CAM at embryonic day 7 (E7) as this is the soonest time when the CAM is sufficiently developed to take the graft. Neuroblastoma cells have successfully implanted when pipetted onto the CAM. (Carter *et al.*, 2012) The cell lines chosen in previous works have demonstrated a reliable xenografting success rate.

SK-N-AS and SK-N-BE(2)C cells demonstrate two distinct tumour genotypes: MYC-N amplified and 11q deletions. Both cell lines can invade the epithelial layer of the CAM and form tumours

beneath the surface. In our experimentation, we noted similar rates of tumour formation, but previous experiments have shown that SK-N-AS implantation has higher rates of xenograft success. Overall, our xenografting rates were 75% in both cell lines. The tumour cells need to secrete active matrix metalloproteinases to invade successfully (Bjørnland *et al.*, 2001). I have seen that a critical concentration of MMPs secreted by many cells is needed to invade successfully, and this is best facilitated by a dense pellet of viable cells on a small surface of the CAM. In non-successful grafts, cells were seen with fluorescent microscopy dried in a layer on the CAM surface rather than beneath it, and tumours did not form in the model. This may be because the pellet was too dilute, causing the cells to spread across a large surface area. Another explanation is that the eggshell window did not provide a sufficient moisture seal, and the cells died before they could invade. Other methods of xenografting, such as collagen implants (Deryugina and Quigley, 2008), plastic rings (Balke *et al.*, 2010), and matrigel grafts (Klingenberg *et al.*, 2014), have been used by others. The method of xenografting cells should be tailored to the outcome measured: the advantage of sponge or matrigel grafts is that they are technically simple and suited for the study of angiogenesis within the model. However, the foreign material can cause unwanted non-specific granulation formation and inflammatory reactions.

It should also be considered that different cells will have different invasive capabilities, so implantation should be optimised for other cancer cell types. Numerous mouse and human, and even feline cell lines have been successfully xenografted into the chick embryo model, including breast carcinoma (Pinto *et al.*, 2020), melanoma (Kalirai *et al.*, 2015), cervical carcinoma (Paul *et al.*, 2014) and fibrosarcoma. (Zabielska-Koczywas *et al.*, 2017) The method of cell inoculation and preparation varies depending on the aim of the study and the cell line. We established tumour growth four days after implantation when examined with a fluorescent microscope. With this model, we can readily visualise and confirm xenograft success rate, unlike in murine models where tumours must be palpable or the animals sedated for advanced imaging. (Young *et al.*, 2009; Puaux *et al.*, 2011) We introduced the chemotherapy compounds into the embryos through injection into the allantois. Topical applications on the CAM and intravenous injection have also been described. (Vargas *et al.*, 2007a) Injections into the allantois are technically more straightforward than intravenous injections. Drug distribution from the allantoic injection can spread throughout the chick and cross the blood-brain barrier. (Zosen *et al.*, 2021) Although we did not examine the pharmacokinetics of drugs tested in the embryo due to time constraints in this work, other studies have done so. Several approaches have been described, including blood

sampling and drug plasma level measurement using high-performance liquid chromatography (HPLC). (Vargas *et al.*, 2007a) The biodistribution of the drug can also be measured by HPLC quantification of drug concentration in various organs. (Büchle *et al.*, 2005; Fotinos *et al.*, 2006). Fluorescent drugs can be used to measure drug penetration and distribution. This is something we started to explore within this work. The next step would be to analyse the extent of fluorescence inside and outside the blood vessels using fluorescent microscopy to quantify the distribution better. (Vargas *et al.*, 2007b)

Our measurement of the drug's pharmacodynamics was by measuring egg weight over the experiments and the overall survival of the embryo. Alternative methods are also available: Jarrosson *et al.* used different parameters, including embryo survival, morphological checkpoints, and global growth, to assess the effects of chemotherapies in their chick model. (Jarrosson *et al.*, 2021) This ability to measure pharmacokinetics and pharmacodynamics presents another advantage in using the chick embryo as a drug screening tool. Private research labs, such as INOVOTION, also offer the embryo as a "cutting-edge" technology that allows accelerated drug discovery at lower costs. The cancers listed on their website (www.inovotion.com) currently do not include neuroblastoma.

Using the chick embryo model to study neuroblastoma development and possible therapies is gaining momentum. In 2009 Volland *et al.* showed that when NB cells are transfected with glycoprotein stanniocalcin-2, the tumours formed are not solid but more cyst-like. They postulated that as stanniocalcin-2 increased the proliferation of tumour cells *in vitro* and the invasive potential *in vivo*, this protein may be used as a surrogate marker for metastatic neuroblastoma. (Volland *et al.*, 2009) Michaelis *et al.* showed that cell lines known to be chemo-resistant produced a strong angiogenic response in the embryo compared to the chemo-sensitive lines. This may indicate that a method of drug resistance is through increased angiogenic signalling – and potentially, a mode of treatment for these tumours is targeting these pathways directly. (Michaelis *et al.*, 2009) Ribatti, who has written extensively on the benefits of the chick embryo model, used the model to study the chick's response to neuroblastoma xenografting. He concluded that the neuroblastoma cells on the CAM demonstrated high expression of human VEGF-A and HIF2 α and that the tumours faithfully reproduced the human characteristics seen in clinical practice. (Ribatti and Tamma, 2019) More recently, Ben Amar *et al.* have used the chick embryo model to understand neuroblastoma's pathogenesis further. Utilising the embryonic environment, they examined the

signalling involved in the neural crest migration, which may predispose to neuroblastoma transformation, tumour formation and metastasis. (Ben Amar *et al.*, 2022)

We completed the experiments by day 14, as by this stage, we can treat the chick embryos with two separate drug doses, and tumours have enough time to become established. In addition, experimentation on chick embryos younger than EDD-14 does not require approval from an animal ethics committee.

6.1.1.1 Limitations of the CAM model

As with any experimental model, the chick embryo has pros and cons. Working with the model for several years has given us an appreciation of the limitations and, in some cases, led to developing troubleshooting ideas. As with any xenograft model, the implantation of human cells into the chick may cause local reactions within the chick and the cells, which are not fully understood. In the CAM assay, a non-specific inflammatory reaction is more prevalent in embryos after E15, as this is when the immune system starts to fully mature. However, a non-specific inflammatory response is much less likely when the test material is grafted as soon as the CAM begins to develop and while the embryo's immune system is still relatively undeveloped – which is what I have done in these experiments. (Leene, Duyzings and van Steeg, 1973). Although the immunocompromised nature of the embryo makes it ideal as a xenograft model, it cannot fully recapitulate the human body's response to invading cancer. Many new cancer therapies are immune mediating, and the lack of a functioning immune system in the chick embryo model prevents its use for testing these compounds. The embryonic nature of the model lends itself to the study of development and angiogenesis. However, in testing drug therapies, the rapidly changing nature of the model may lead to unpredictable changes in the metabolism and distribution of drugs. (Tay, Heng and Chan, 2011) The model is susceptible to environmental changes, such as oxygen tension, pH, osmolarity and humidity, and can be particularly susceptible to bacterial and fungal infections. (Ribatti, 2014a) This can make the model challenging, especially in facilities where the incubators are shared amongst many users. The frequent access to the incubators can influence the ambient temperature for all the eggs, and on occasion, significant losses of embryos have occurred. Another drawback is the low number of reagents compatible with avian species, including antibodies, cytokines, and primers which work in the chick.

Until recently, a significant setback of the model was the inability to generate genetically modified chicken lines. However, significant advances in molecular genetics have led to the generation of transgenic chickens. The development of transgenic technologies such as lentiviral and transposon vectors for transgene addition and the *in vitro* culture and genomic engineering of chicken primordial germ cells has provided opportunities for targeted, defined modifications of the chicken genome. One example is the development of the Chameleon cytbow chicken, which will allow single-cell fate mapping throughout the embryo. (Davey *et al.*, 2018) Another cited limitation of the CAM assay model is that, due to the short time frame of the assay, micro-metastasis – visible colonies in distant sites – cannot form. This limits the ability to assess any cell line's metastatic potential fully.

However, I have not found this to be the case. Dissection of the whole chick embryo demonstrated fluorescently labelled colonies of neuroblastoma cells within the chick feathers and intestine. Petruzelli *et al.* were the first to demonstrate the micro-metastasis with squamous cell carcinoma xenografts in the chick, and many more have followed suit. (Petruzelli *et al.*, 1993; Koop *et al.*, 1996; Al-Mehdi *et al.*, 2000) However, it is unlikely all cell lines follow this trend, and in our experiments, only cells cultured in hypoxia before implantation were seen to metastasise.

Another limitation of the model we could not avoid is the short timeframe for the experiments. Due to Home Office legislation, the experiments are terminated by E14, which only allows a maximum of 6 days of drug treatment. It is, therefore, difficult to assess drug resistance or accurately assess toxicity over a long period. (Taizi *et al.*, 2006b) However, licenses to extend the experiments to hatching can be sought.

6.1.2 CDK inhibitors in neuroblastoma

CDK4/6 inhibitors were the first of their group to be approved by the FDA for clinical treatment. These inhibitors' specificity and low toxicity have made them an attractive avenue for cancer therapy. The three CDK4/6 inhibitors currently approved are Palbociclib, Ribociclib and Abemaciclib. All three are currently approved for first-line HR+ve advanced breast cancer treatment. Their use has significantly reduced resistance to mono-endocrine therapy to extend survival in HR+/HER2- breast cancer patients. Off-target effects of CDK4/6 inhibitors also include enhancing cytostasis and modulating tumour immune responses. (Klein *et al.*, 2018) This has been exploited in combination therapy protocols. Such as with hormone receptor antagonist letrozole for breast cancer therapy. Palbociclib combined with letrozole showed significantly

longer progression-free survival than letrozole monotherapy, although the rates of myelotoxic effects were higher with the combination therapy. (Finn *et al.*, 2016) Array-based data have shown that cyclin D1 is far higher in neuroblastoma than in other malignancies. This, alongside the increased expression of CDK4 and CDK6, has led to the exploration of CDK inhibitors as potential therapies for neuroblastoma. In our work, we examined the efficacy of Palbociclib, a selective CDK4/6 inhibitor that suppresses the cyclin D1-pRB pathway. We found a different result between the two cell lines, with the MYC-N amplified line being more sensitive to CDK4/5 inhibition than the SK-N-AS. This may be explained by the higher levels of RB phosphorylation seen in MYCN amplified cell lines compared to non-amplified cell lines. (Whittaker *et al.*, 2017) In addition, the inhibition of cyclin D surprisingly has a different impact on different neuroblastoma cell lines. (Rihani *et al.*, 2015) This implies that in MYC-N non-amplified cells, there may be an independent pathway or alternative signalling to promote cell cycle progression in the absence of cyclin D. In testing the drug in the chick embryo model, we did note that Palbociclib treated systems had the lowest rate of tumour formation and the smallest tumours. In addition, histology showed that the rate of actively proliferating cells, as measured by Ki67 positive cells, was also the lowest compared to control and other drugs. (Chapter 3: **Figure 3.9**).

Other CDK inhibitors are also being evaluated in neuroblastoma. AT7519 is a potent pan-CDK inhibitor that acts on CDK1, 2, 4, 6 and 9. Preclinical trials have shown that AT7519 can induce apoptosis in various neuroblastoma cell lines. (Dolman *et al.*, 2015) Fadraciclib, a clinical inhibitor of CDK9 and CDK2, in combination with temozolomide, has demonstrated long-term suppression of MYC-N amplified neuroblastoma. Neuroblastoma has a complex genetic profile that can include *MYCN* amplification, somatic activating mutations in the *ALK* oncogene, *TERT* rearrangements, or *ATRX* mutations, and relapsed neuroblastomas are frequently associated with RAS/mitogen-activated protein kinase (MAPK) pathway mutations which could all influence CDK4/6 inhibitor sensitivity. With such a heterogeneous disease, combination therapy of CDK4/6 inhibitors is being extensively explored in research with varying levels of success. Wood *et al.* showed that combining CDK4/6 inhibitor, Ribociclib, and ALK inhibitor, Ceritinib resulted in synergistic effects on cell cycle arrest, growth inhibition and caspase-independent cell death. In neuroblastoma xenografts possessing ALK-F1245C and ALK-F1174L de novo resistance mutations, the combination therapy overcame Ceritinib resistance and resulted in complete regression. (Wood *et al.*, 2017) Combination therapy of Ribociclib and Binimetinib, a MEK1/2 inhibitor, was tested in patients with relapsed high-risk neuroblastoma.

MYC-N amplified tumours were often sensitive to CDK4/6 inhibition but resistant to MEK1/2 inhibition. The inverse is seen in tumours with increased MAPK signalling. Hart et al. showed that through administration of the combination therapy, there was a synergistic inhibition of cellular growth in all cell lines and tumour growth inhibition in multiple murine xenograft models. (Hart *et al.*, 2017) CDK4/6 inhibitors combined with immunotherapy have been studied with promising results in patients with breast cancer. PD-1 inhibition with humanised antibody pembrolizumab has been proposed in paediatric solid tumours. There is also growing evidence for high PD-L1 expression associated with poor prognosis in paediatric neuroblastoma. A phase I/II clinical trial (NCT02304458) is currently in progress, where PD-1 inhibitor nivolumab is used in 10 neuroblastoma patients, with results due in October 2022. (Wagner and Adams, 2017)

In vitro, CDK1 inhibition was more efficacious against MYC-N non-amplified cells than in the amplified line. Schwermer et al. postulated that the p53 status of the cell might determine the sensitivity to RO3306 CDK1 inhibitor. (Schwermer *et al.*, 2015) SK-N-AS cells have aberrantly expressed p53, which may explain the cell's susceptibility to CDK1 inhibition (Nakamura *et al.*, 2007). However, *in vivo* testing showed that the chick embryos could not tolerate CDK1 inhibition. There are currently no CDK1-specific inhibitors in use in clinical practice. Pan/Multi-CDK inhibitors, such as dinaciclib, have been tested with promising efficacy and good tolerability in phase II clinical trials for myeloma and phase III clinical trials for chronic lymphocytic leukaemia. (Ghia *et al.*, 2017) (Kumar *et al.*, 2015) The difference in toxicity may be explained by the different specificity to CDK1 and potentially an incomplete inhibition. The dinaciclib inhibition of CDK2 and CDK9 has reduced neuroblastoma formation in GEMM models. (Chen *et al.*, 2016) The complete inhibition of CDK1 does not seem compatible with organism survival. The potential of CDK1-inhibitors in combination with other targeted and ionising radiation therapy has been explored. CDK1 inhibition can sensitise tumour cells to radiation. (Prevo *et al.*, 2018). This may be due to the role of CDK1 in DNA damage repair. (Neganova *et al.*, 2014). The double-pronged approach of inducing DNA damage through targeted radiation and inhibiting DNA damage repair through CDK1 inhibition could potentially increase cancer cell death. However, targeted delivery systems need to be developed, as the tolerance of CDK1 systemically is poor.

I have not fully elucidated the pharmacokinetics of Palbociclib and RO-3306 in chick embryos. With more time, we would have conducted immunohistochemistry on kidneys and livers from treated chicks to assess the drug's hepato-and renal toxicity.

6.1.3 Hypoxia, HIF-2 α inhibition and neuroblastoma

Previous work from the group has shown phenotypical differences in normoxia and hypoxic precultured tumours. Preconditioning neuroblastoma cell lines with either 1% O₂ promotes metastasis of cells into the embryo, whereas cells grown in 21% O₂ have never been seen to metastasise. (A Herrmann *et al.*, 2015) Here I have confirmed that the preconditioning of neuroblastoma cells increases the likelihood of tumour metastasis (Chapter 4: **Figure 4.12**). Additionally, SK-N-AS cells preconditioned in hypoxia are more likely to form multiple tumours on the CAM than the MYCN amplified counterparts. Hypoxia also triggered drug response: Hypoxia-induced a greater resistance to the CDK4/6 inhibitor in both cell lines, more markedly so in SK-N-BE(2)C (**Chapter 3: Error! Reference source not found., Error! Reference source not found., Error! Reference source not found.**). Hypoxia is known to reduce cell metabolic activity, which reduces drug uptake through the surface. (Donovan *et al.*, 2010). Alternatively, hypoxia-induced cell proliferation may also lead to increased cell numbers, and an increased drug concentration would be needed to achieve the same effect. Additionally, microarray analyses has demonstrated that hypoxia induced the expression of genes encoding metallothioneins, MT2A and MT1H proteins may induce drug resistance. (Comerford *et al.*, 2002; Jögi *et al.*, 2004)

MYC signalling also plays a pivotal role in regulating cancer cell metabolism and vasculogenesis. (Dang, 2012) In hypoxia, MYC activity is inhibited by HIF-1 α as an adaptive response to promote cell survival under low oxygen conditions. In contrast, HIF-2 α has been shown to promote MYC activity. HIF-2 α deletion in murine models showed a reduced MYC target transcriptome. (Hoefflin *et al.*, 2020). Additionally, HIF-2 α promotes MYC activity by stabilising the MYC/MAX complex. (Zhang *et al.*, 2007; Xue *et al.*, 2015). Fascinatingly, HIF-2 α -induced stabilisation of MYC/MAX heterodimer is much stronger than HIF-1 α -induced degradation of MYC in cancer cells, leading to MYC activation under hypoxia. (Xue *et al.*, 2015). HIF inhibition is, therefore, an attractive anticancer target. However, the complexity of the HIF pathway, the multiple downstream targets, and their interactions have made this a challenging venture. Several direct and indirect HIF targets are currently being evaluated in phase I/II trials.

In particular, HIF-2 α has recently emerged as a promising target in clear cell renal cancer. Several HIF-2 α -specific antagonists have been discovered that disrupt the HIF-2 α dimerisation and show promising effects from preclinical to clinical trials. PT2385 inhibits HIF-2 α -driven gene expression

in clear cell renal cancers. (Wallace *et al.*, 2016b) Moreover, phase II clinical trials for PT2385 are ongoing in ccRCC (NCT03108066) and recurrent glioblastoma (NCT03216499).

From this work, the HIF2 inhibitor PT2385 showed a minimal effect *in vitro* in the cell cycle assays and downstream gene expression analysis. This is reflected by work from other groups; shRNA- or siRNA-mediated HIF2 α knockdown does not affect cell proliferation *in vitro*, and PT2385 did not affect the renal cell population *in vitro*. (Wallace *et al.*, 2016b). Overall the effects of HIF2 α on neuroblastoma *in vivo* were inconclusive. The drug's lack of efficacy in neuroblastoma may be accurate, but it must also be considered that there are compensatory mechanisms between HIF1 and HIF2. Although HIF2 may be abrogated, the HIF1 pathway may continue to drive the expression of these essential hypoxia genes. The use of HIF-2 α antagonists in combination protocols is best described in clear cell renal cell carcinoma (ccRCC). Immunotherapy agents, such as PD-L1 inhibitor, and PT2385, are being evaluated for their combined efficacy in specifically inducing PD-L1 expression against ccRCC. (Ruf, Moch and Schraml, 2016) Previously discussed is the synthetic lethality between HIF2 and CDK4/6. When Palbociclib was combined with the HIF-2 α inhibitor PT2399, data showed that the regimen synergistically suppresses VHL -/- cell growth in ccRCC cell lines. Moreover, the use of palbociclib suppressed orthotopic xenograft growth alone and in combination with PT2399. (Nicholson *et al.*, 2019) However, some pVHL-defective cell lines have shown resistance to the compound. This indicates that the sensitivity to HIF-2 α inhibition is not ubiquitous but varies depending on the cell type's dependence on HIF-2 α . In ccRCC, cells with high levels of HIF-2 α demonstrate the most sensitivity to its inhibition, whereas those with p53 mutations are resistant. Further research into predictive biomarkers predisposing to HIF-2 α inhibition sensitivity is needed to harness the full potential of these inhibitors. (Cho *et al.*, 2016)

6.1.4 Developing advanced microscopy for cancer research

Three-dimensional microscopy is an exciting advancement in cancer research, as it holds the promise to resemble and recapitulate the *in vivo* tumour microenvironment more faithfully than its conventional 2D counterpart. I have demonstrated the potential of clearing and imaging tumour tissues and highlighted some challenges. The field is fast-paced, and since this research began, several advances have been made. When developing such a protocol, one needs to consider imaging with adequate resolution, contrast (signal-to-background ratio), speed of imaging, ease

of use, and cost. In addition to image acquisition, there must be attention to data storage and the availability of open-source tools for data processing, visualisation and analysis.

The main challenges were adequate antibody staining and the penetration of available epitopes within the sample. Epitope detection can be improved by modifying the fixation, permeabilisation and dehydration steps. Paraformaldehyde fixative, which was used in these experiments, is commonly used and is known to preserve proteins and reduce the autofluorescence of tissues. Zwitterionic agents, which have a high critical micelle concentration, have been used to improve the penetration of labelling proteins into particularly dense samples such as tumours. (Zhao *et al.*, 2020; Messal *et al.*, 2021) Hydrophilic agents, such as the urea-based CUBIC system, are preferred to preserve endogenous labelling. However, newer organic solvent systems can preserve the endogenous signal – such as polyethylene glycol (PEG) based PEGASOS (PEG-associated solvent system). (Jing *et al.*, 2018). Although I have focussed mainly on antibody labelling, new techniques have emerged. Combining protein labelling with RNA in situ hybridisation techniques has been shown in cancer tissues. (Tanaka *et al.*, 2017) Novel methods are being trialled to detect smaller and more sparse molecules such as specific proteins, nucleic acids, and metabolites: Expansion microscopy uses a polymer gel that isometrically increases size to enable imaging of smaller structures. Click chemistry describes the covalent bonding of a biomolecule to the desired substrate to improve detection. (Sun *et al.*, 2020)

Understanding the intra-tumour and inter-tumour environment is vital for developing predictive molecular biomarkers for cancer staging and therapy. Identifying biomarkers through 2D paraffin sections is susceptible to sampling bias, impacting the reliability of the analysis. Three-dimensional imaging can allow complete sample imaging and produce a more robust and quantitative analysis of biomarkers' presence and location within tissue – especially in tumours with high heterogeneity, such as neuroblastoma. 3D histopathology is a method of whole slide imaging, where glass-mounted H&E stained slices are scanned and reconstructed into a 3D image for analysis. (Williams *et al.*, 2018) Several reasons have limited the clinical application of this method: firstly, the artefacts and errors introduced through mechanical sectioning and slicing are still an issue here; secondly, the scanning time for a slide is up to 10 minutes – taking nearly 24 hours per batch – with large file sizes. The method is also irreversible as the sample is no longer available for further staining. (Scott Campbell *et al.*, 2012) Dodt devised a workflow to optically clear and image resected tumours, followed by rehydration and standard immunohistochemistry protocols. They found a high correlation between the corresponding

structures present in H&E and IHC staining and cleared 3D tumour images. (Sabdyusheva Litschauer *et al.*, 2020)

This validation method is perhaps the next stage in this work to confirm that the 3D images and analysis of neuroblastoma tumours are faithful to the standard immunohistochemistry analysis. Currently, the time taken for sample preparation, imaging and analysis in three-dimensional protocols precludes its use in the clinical setting. Automated analysis is also critical for its application in the clinical setting. The sophisticated imaging hardware and image analysis software are also not commercially available. However, if these protocols are well established in research, private companies offering rapid diagnostic services to the health care sector are bound to develop.

6.2 Future Considerations

I have demonstrated in this work the potential of CDK inhibitors in MYC-N amplified neuroblastoma, the utility of the chick embryo and the considerable potential of three-dimensional imaging in cancer research. However, several unanswered questions remain around the role of hypoxia in neuroblastoma and how best to utilise the embryo to study metastasis. Hypoxia plays a role in the initiation and progression of neuroblastoma, but our understanding of the molecular mechanisms and pathways is still lacking. There is still confusion about the role of hypoxia in cell differentiation, with HIF2 overexpression being associated with both a poor and a good outcome in published research. The role of hypoxia on cell survival, and the impact of other genetic mutations, such as MYC-N amplification, on these pathways, is also unknown. Despite our attempts to quantify the hypoxia-related genes in the two cell lines and the expression changes with HIF-2 α inhibition, no clear pattern was seen. The inherent oxygen gradient within a tumour, alongside the well-documented heterogeneity of neuroblastoma, explains the inconclusive data. A robust analysis using extensive population data to observe trends in hypoxia signalling is potentially more helpful in predicting the role of hypoxia in different genotypes. Cangelosi *et al.* analysed the gene expression profile of nearly 2000 untreated primary neuroblastoma tumours and identified a seven-gene hypoxia biomarker with a reliable prognostic value. (Cangelosi *et al.*, 2020)

HIF inhibition through compound PT2385 was incomplete. HIF dependant genes continued to be expressed in treatment groups, indicating alternative signalling pathways or ineffective therapy. There are mechanisms of resistance to the drug which remain poorly understood; the role of

biomarkers such as p53 have been implicated in this. (Persson *et al.*, 2020b) Therefore, the future use of this compound in human cancers will require further investigation. Clinical trials using HIF inhibitors against clear cell renal cancers and glioblastoma are still ongoing, and although initially tolerated well by the patient groups, their clinical impact on disease remains to be seen.

I have shown the chick embryo CAM model to be a robust model for evaluating both the xenografting of cell lines and for evaluating drug therapies cost-efficiently. A significant advantage of the chick embryo is the breadth of knowledge accumulated about the development of the chick. Future research must build on this knowledge and utilise new resources such as *in ovo* imaging and genetic modification. The chick genome was sequenced in 2004, enabling genetic analysis and genome comparisons to humans. The genome publication enables the application of transgenic techniques within the model, such as *in ovo* electroporation and retrovirus-mediated protein expansion. (Funahashi *et al.*, 1999; Nakamura and Funahashi, 2013) Electroporation techniques to facilitate gain and loss of gene function experiments can allow a greater understanding of the early gene signalling influencing neuroblastoma growth. Genetic manipulation techniques such as CRISPR are not yet widely used in chick embryos; however, there is a strong interest in using these strategies in the model. (Gandhi *et al.*, 2017) (Ishii and Mikawa, 2005)

We envisage that future research will use this solid platform to combine existing techniques and molecular and genetic manipulation methods to understand better cancers' genetic expression, cell fate, and tissue differentiation. (Ohta *et al.*, 2003) The chick embryo should be developed further as a screening tool to identify subtype-specific targets for further preclinical validation in the mouse models. The success of xenografting in the model also opens the possibility of using patient-derived xenografts to grow and analyse individual tumour biology. This could provide a real-time platform for predicting the effectiveness of drugs and guide the administration of personalised cancer therapy. In conjunction with 3D microscopy, PDX tumours from the embryo can be characterised further to identify biomarkers. The chick embryo certainly has the potential to bridge the gap between *in vitro* and GEMM models to investigate complex biological systems.

6.3 Conclusions

Neuroblastoma development and metastasis is a multistep process, with changes at the molecular, cellular and tissue levels affecting upstream and downstream signalling. Investigating

these pathways through *in vitro* culture, 3D cell culture models, and complex *in vivo* models is ongoing. Each modality has its advantages. The chick embryo model provides a 3D representative model for tumour growth and metastasis, but it still has shortcomings, including a lack of an immune system to characterise the immunomodulation and a short time window for experimentation. One significant advantage of this model is the opportunity to address the principles of the 3Rs by reducing and replacing murine model use. I have shown that yolk sac injection provides a simple and effective way to deliver compounds in this model. In testing CDK4/6 inhibition, we showed an arrest in the cell cycle *in vitro* and, most importantly, a smaller tumour size with a lower number of actively proliferating cells *in vivo*. We hope that using this model as a drug screening tool can accelerate drug discovery for this rare disease and reduce the attrition rate in the therapy development pipeline. In addition, I have developed a system where the human xenografted tumour can be grown, harvested and imaged in 3D. We hope this might serve as a blueprint for the future incorporation of patient-derived cells into this platform, analyse the efficacy of drugs *in ovo* and provide a personalised point of care system through single-cell resolution microscopy.

References

- Agani, F. and Jiang, B.-H. (2013) 'Oxygen-independent regulation of HIF-1: novel involvement of PI3K/AKT/mTOR pathway in cancer', *Current cancer drug targets*. *Curr Cancer Drug Targets*, 13(3), pp. 245–251. doi: 10.2174/1568009611313030003.
- Al-Mehdi, A. B. *et al.* (2000) 'Intravascular origin of metastasis from the proliferation of endothelium-attached tumor cells: a new model for metastasis', *Nature medicine*. *Nat Med*, 6(1), pp. 100–102. doi: 10.1038/71429.
- Al-Mutawa, Y. (2017) 'The Effects of Hypoxic Preconditioning on the Oxygenation and Metabolic Profile of Neuroblastoma-Yousef Al-Mutawa The Effects of Hypoxic Preconditioning on the Oxygenation and Metabolic Profile of Neuroblastoma The Effects of Hypoxic Preconditioning on th', (November), pp. 1–67. Available at: https://livrepository.liverpool.ac.uk/3022489/1/200723591_Nov2017.pdf.
- Al-Mutawa, Y. K. *et al.* (2018) 'Effects of hypoxic preconditioning on neuroblastoma tumour oxygenation and metabolic signature in a chick embryo model', *Bioscience reports*. *Biosci Rep*, 38(4). doi: 10.1042/BSR20180185.
- Allegra, A. *et al.* (2018) 'Nanobodies and Cancer: Current Status and New Perspectives', <https://doi.org/10.1080/07357907.2018.1458858>. Taylor & Francis, 36(4), pp. 221–237. doi: 10.1080/07357907.2018.1458858.
- Allsopp, R. C. *et al.* (1995) 'Telomere Shortening Is Associated with Cell Division in Vitro and in Vivo', *Experimental Cell Research*. Academic Press, 220(1), pp. 194–200. doi: 10.1006/EXCR.1995.1306.
- Alnuami, A. A. *et al.* (2008) 'Oxyradical-induced GFP damage and loss of fluorescence', *International journal of biological macromolecules*. *Int J Biol Macromol*, 43(2), pp. 182–186. doi: 10.1016/J.IJBIOMAC.2008.05.002.
- Althoff, K. *et al.* (2015) 'A Cre-conditional MYCN-driven neuroblastoma mouse model as an improved tool for preclinical studies', *Oncogene*. *Oncogene*, 34(26), pp. 3357–3368. doi: 10.1038/ONC.2014.269.
- Althoff, Kristina *et al.* (2015) 'miR-542-3p exerts tumor suppressive functions in neuroblastoma by downregulating Survivin', *International journal of cancer*. *Int J Cancer*, 136(6), pp. 1308–1320. doi: 10.1002/IJC.29091.
- Althoff, K. and Schramm, A. (2017) 'MYCN-mediated murine cancer models', *Aging (Albany NY)*. Impact Journals, LLC, 9(4), p. 1084. doi: 10.18632/AGING.101222.
- Ben Amar, D. *et al.* (2022) 'Environmental cues from neural crest derivatives act as metastatic triggers in an embryonic neuroblastoma model', *Nature Communications 2022 13:1*. Nature Publishing Group, 13(1), pp. 1–18. doi: 10.1038/s41467-022-30237-3.
- Ambros, I. M. *et al.* (2014) 'Ultra-high density SNP array in neuroblastoma molecular diagnostics', *Front. Oncol.* Frontiers Research Foundation, 4, p. 202. doi: 10.3389/fonc.2014.00202.
- Ambros, P. F. *et al.* (2009) 'International consensus for neuroblastoma molecular diagnostics: report from the International Neuroblastoma Risk Group (INRG) Biology Committee', *Br. J.*

Cancer, 100(9), pp. 1471–1482. doi: 10.1038/sj.bjc.6605014.

Anders, L. *et al.* (2011) 'A Systematic Screen for CDK4/6 Substrates Links FOXM1 Phosphorylation to Senescence Suppression in Cancer Cells', *Cancer Cell*. doi: 10.1016/j.ccr.2011.10.001.

Applebaum, M. A. *et al.* (2016) 'Integrative genomics reveals hypoxia inducible genes that are associated with a poor prognosis in neuroblastoma patients', *Oncotarget*. Impact Journals LLC, 7(47), pp. 76816–76826. doi: 10.18632/ONCOTARGET.12713.

Armstrong, P. B., Quigley, J. P. and Sidebottom, E. (1982) 'Transepithelial Invasion and Intramesenchymal Infiltration of the Chick Embryo Chorioallantois by Tumor Cell Lines¹', *CANCER RESEARCH*, 42, pp. 1826–1837. Available at: <http://aacrjournals.org/cancerres/article-pdf/42/5/1826/2413127/cr0420051826.pdf> (Accessed: 17 May 2022).

Arora, S. *et al.* (2021) 'FDA Approval Summary: Olaparib Monotherapy or in Combination with Bevacizumab for the Maintenance Treatment of Patients with Advanced Ovarian Cancer', *The oncologist*. *Oncologist*, 26(1), pp. e164–e172. doi: 10.1002/ONCO.13551.

Asghar, W. *et al.* (2015) 'Engineering cancer microenvironments for in vitro 3-D tumor models', *Materials today (Kidlington, England)*. *Mater Today (Kidlington)*, 18(10), pp. 539–553. doi: 10.1016/J.MATTOD.2015.05.002.

Bäckman, U., Svensson, Å. and Christofferson, R. (2002) 'Importance of vascular endothelial growth factor A in the progression of experimental neuroblastoma', *Angiogenesis*. doi: 10.1023/A:1024564817563.

Baek, J. H. *et al.* (2000) 'Hypoxia-induced VEGF enhances tumor survivability via suppression of serum deprivation-induced apoptosis', *Oncogene*. doi: 10.1038/sj.onc.1203814.

Bagatell, R. *et al.* (2009) 'Significance of MYCN amplification in international neuroblastoma staging system stage 1 and 2 neuroblastoma: a report from the International Neuroblastoma Risk Group database.', *Journal of clinical oncology : official journal of the American Society of Clinical Oncology*. *American Society of Clinical Oncology*, 27(3), pp. 365–70. doi: 10.1200/JCO.2008.17.9184.

Bagnall, J. *et al.* (2014) 'Tight control of hypoxia-inducible factor- α transient dynamics is essential for cell survival in hypoxia', *Journal of Biological Chemistry*. Elsevier, 289(9), pp. 5549–5564. doi: 10.1074/JBC.M113.500405/ATTACHMENT/BAF162FE-E238-4049-BFE2-9304965CDDAD/MMC1.ZIP.

Balke, M. *et al.* (2010) 'Morphologic characterization of osteosarcoma growth on the chick chorioallantoic membrane', *BMC Research Notes*. BioMed Central, 3(1), pp. 1–8. doi: 10.1186/1756-0500-3-58/FIGURES/3.

Barnes, E. N. *et al.* (1981) 'The fine structure of continuous human neuroblastoma lines SK-N-SH, SK-N-BE(2), and SK-N-MC', *In Vitro*. Springer-Verlag, 17(7), pp. 619–631. doi: 10.1007/BF02618461.

Barone, G. *et al.* (2014) 'MDM2-p53 interaction in paediatric solid tumours: preclinical rationale, biomarkers and resistance', *Curr Drug Targets*, 15, pp. 114–123.

Barriga, E. H. *et al.* (2013) 'The hypoxia factor Hif-1 α controls neural crest chemotaxis and epithelial to mesenchymal transition', *Journal of Cell Biology*, 201(5), pp. 759–776. doi:

10.1083/jcb.201212100.

Bayer, C. and Vaupel, P. (2012) 'Acute versus chronic hypoxia in tumors: Controversial data concerning time frames and biological consequences', *Strahlentherapie und Onkologie : Organ der Deutschen Röntgengesellschaft ... [et al]*. *Strahlenther Onkol*, 188(7), pp. 616–627. doi: 10.1007/S00066-012-0085-4.

Becker, K. *et al.* (2012a) 'Chemical clearing and dehydration of GFP expressing mouse brains', *PLoS one*. *PLoS One*, 7(3). doi: 10.1371/JOURNAL.PONE.0033916.

Becker, K. *et al.* (2012b) 'Chemical Clearing and Dehydration of GFP Expressing Mouse Brains', *PLOS ONE*. *Public Library of Science*, 7(3), p. e33916. doi: 10.1371/JOURNAL.PONE.0033916.

Belenguer, P. *et al.* (1990) 'Mitosis-specific phosphorylation of nucleolin by p34cdc2 protein kinase', *Molecular and cellular biology*. *Mol Cell Biol*, 10(7), pp. 3607–3618. doi: 10.1128/MCB.10.7.3607-3618.1990.

Belle, M. *et al.* (2017) 'Tridimensional Visualization and Analysis of Early Human Development', *Cell*. *Cell Press*, 169(1), pp. 161-173.e12. doi: 10.1016/J.CELL.2017.03.008/ATTACHMENT/05299646-F843-4DD0-83D0-59E06CD0247D/MMC8.MP4.

Beltinger, C. and Debatin, K. M. (2001) 'Murine models for experimental therapy of pediatric solid tumors with poor prognosis', *International journal of cancer*. *Int J Cancer*, 92(3), pp. 313–318. doi: 10.1002/IJC.1210.

Berthold, F. *et al.* (2017) 'Incidence, Survival, and Treatment of Localized and Metastatic Neuroblastoma in Germany 1979-2015', *Paediatric drugs*. *Paediatr Drugs*, 19(6), pp. 577–593. doi: 10.1007/S40272-017-0251-3.

Berthold, F. and Simon, T. (2005) 'Clinical Presentation', in *Neuroblastoma, Clinical Presentation*. Springer, pp. 63–85.

Besançon, O. G. *et al.* (2012) 'Synergistic interaction between cisplatin and gemcitabine in neuroblastoma cell lines and multicellular tumor spheroids', *Cancer letters*. *Cancer Lett*, 319(1), pp. 23–30. doi: 10.1016/J.CANLET.2011.12.016.

Bian, X. *et al.* (2002) 'Constitutively active NFkappa B is required for the survival of S-type neuroblastoma', *The Journal of biological chemistry*. *J Biol Chem*, 277(44), pp. 42144–42150. doi: 10.1074/JBC.M203891200.

Bishop, T. *et al.* (2008) 'Abnormal sympathoadrenal development and systemic hypotension in PHD3^{-/-} mice', *Molecular and cellular biology*. *Mol Cell Biol*, 28(10), pp. 3386–3400. doi: 10.1128/MCB.02041-07.

Bjørnland, K. *et al.* (2001) 'Expression of matrix metalloproteinases and the metastasis-associated gene S100A4 in human neuroblastoma and primitive neuroectodermal tumor cells', *Journal of pediatric surgery*. *J Pediatr Surg*, 36(7), pp. 1040–1044. doi: 10.1053/JPSU.2001.24735.

Bluhm, E. *et al.* (2008) 'Prenatal and perinatal risk factors for neuroblastoma', *International journal of cancer*. *Int J Cancer*, 123(12), pp. 2885–2890. doi: 10.1002/IJC.23847.

Bourdeaut, F. *et al.* (2009) 'VIP hypersecretion as primary or secondary syndrome in

- neuroblastoma: A retrospective study by the Société Française des Cancers de l'Enfant (SFCE).', *Pediatric blood & cancer*, 52(5), pp. 585–90. doi: 10.1002/pbc.21912.
- Braekeveldt, N. *et al.* (2015) 'Neuroblastoma patient-derived orthotopic xenografts retain metastatic patterns and geno- and phenotypes of patient tumours', *International journal of cancer*. *Int J Cancer*, 136(5), pp. E252–E261. doi: 10.1002/IJC.29217.
- Bresler, S. C. *et al.* (2014) 'ALK mutations confer differential oncogenic activation and sensitivity to ALK inhibition therapy in neuroblastoma', *Cancer cell*. *Cancer Cell*, 26(5), pp. 682–694. doi: 10.1016/J.CCELL.2014.09.019.
- Brodeur, G. M. *et al.* (1988) 'International criteria for diagnosis, staging, and response to treatment in patients with neuroblastoma', *Journal of clinical oncology: official journal of the American Society of Clinical Oncology*. *J Clin Oncol*, 6(12), pp. 1874–1881. doi: 10.1200/JCO.1988.6.12.1874.
- Brodeur, G. M. (2003) 'Neuroblastoma: biological insights into a clinical enigma.', *Nature reviews. Cancer*, 3(3), pp. 203–16. doi: 10.1038/nrc1014.
- Brodeur, G. M. *et al.* (2009) 'Trk receptor expression and inhibition in neuroblastomas', *Clinical Cancer Research*, 15(10), pp. 3244–3250. doi: 10.1158/1078-0432.CCR-08-1815.
- Brodeur, G. M. and Bagatell, R. (2014) 'Mechanisms of neuroblastoma regression', *Nat. Rev. Clin. Oncol.* Nature Publishing Group, 11(12), pp. 704–713. doi: 10.1038/nrclinonc.2014.168.
- Brown, A. S. *et al.* (2010) 'Histologic Changes Associated With False-Negative Sentinel Lymph Nodes After Preoperative Chemotherapy in Patients With Confirmed Lymph Node-Positive Breast Cancer Before Treatment', *Cancer*. NIH Public Access, 116(12), p. 2878. doi: 10.1002/CNCR.25066.
- Bruick, R. K. (2000) 'Expression of the gene encoding the proapoptotic Nip3 protein is induced by hypoxia', *Proceedings of the National Academy of Sciences of the United States of America*. doi: 10.1073/pnas.97.16.9082.
- Bruick, R. K. and McKnight, S. L. (2001) 'A conserved family of prolyl-4-hydroxylases that modify HIF', *Science (New York, N.Y.)*. *Science*, 294(5545), pp. 1337–1340. doi: 10.1126/SCIENCE.1066373.
- Brunklaus, A. *et al.* (2012) 'Investigating neuroblastoma in childhood opsoclonus-myoclonus syndrome', *Archives of Disease in Childhood*, 97(5), pp. 461–463. doi: 10.1136/adc.2010.204792.
- Büchele, B. *et al.* (2005) 'High-performance liquid chromatographic determination of acetyl-11-keto-alpha-boswellic acid, a novel pentacyclic triterpenoid, in plasma using a fluorinated stationary phase and photodiode array detection: application in pharmacokinetic studies', *Journal of chromatography. B, Analytical technologies in the biomedical and life sciences*. *J Chromatogr B Analyt Technol Biomed Life Sci*, 829(1–2), pp. 144–148. doi: 10.1016/J.JCHROMB.2005.09.043.
- Bunka, D. H. J. and Stockley, P. G. (2006) 'Aptamers come of age - at last', *Nature reviews. Microbiology*. *Nat Rev Microbiol*, 4(8), pp. 588–596. doi: 10.1038/NRMICRO1458.
- Busch, C., Krochmann, J. and Drews, U. (2013) 'The Chick Embryo as an Experimental System for Melanoma Cell Invasion', *PLoS ONE*. *PLOS*, 8(1). doi: 10.1371/JOURNAL.PONE.0053970.

- Byrne, F. L. *et al.* (2014) 'RNAi-mediated stathmin suppression reduces lung metastasis in an orthotopic neuroblastoma mouse model', *Oncogene*, 33(7), pp. 882–890. doi: 10.1038/ONC.2013.11.
- Cai, R. *et al.* (2019a) 'Panoptic imaging of transparent mice reveals whole-body neuronal projections and skull-meninges connections', *Nat. Neurosci.* Nature Publishing Group, 22(2), pp. 317–327. doi: 10.1038/s41593-018-0301-3.
- Cai, R. *et al.* (2019b) 'Panoptic imaging of transparent mice reveals whole-body neuronal projections and skull-meninges connections', *Nature neuroscience*. Nat Neurosci, 22(2), pp. 317–327. doi: 10.1038/S41593-018-0301-3.
- Cangelosi, D. *et al.* (2020) 'Hypoxia predicts poor prognosis in neuroblastoma patients and associates with biological mechanisms involved in telomerase activation and tumor microenvironment reprogramming', *Cancers*, 12(9), pp. 1–45. doi: 10.3390/cancers12092343.
- Cantilena, S. *et al.* (2011) 'Frizzled receptor 6 marks rare, highly tumorigenic stem-like cells in mouse and human neuroblastomas', *Oncotarget*. Oncotarget, 2(12), pp. 976–983. doi: 10.18632/ONCOTARGET.410.
- Carcagno, A. L. *et al.* (2011) 'E2F1-Mediated Upregulation of p19INK4d Determines Its Periodic Expression during Cell Cycle and Regulates Cellular Proliferation', *PLOS ONE*. Public Library of Science, 6(7), p. e21938. doi: 10.1371/JOURNAL.PONE.0021938.
- Carén, H. *et al.* (2010) 'High-risk neuroblastoma tumors with 11q-deletion display a poor prognostic, chromosome instability phenotype with later onset.', *Proceedings of the National Academy of Sciences of the United States of America*, 107(9), pp. 4323–8. doi: 10.1073/pnas.0910684107.
- Carmeliet, P. and Jain, R. K. (2011) 'Principles and mechanisms of vessel normalization for cancer and other angiogenic diseases', *Nature Reviews Drug Discovery* 2011 10:6. Nature Publishing Group, 10(6), pp. 417–427. doi: 10.1038/nrd3455.
- Carpenter, E. L. and Mossé, Y. P. (2012) 'Targeting ALK in neuroblastoma--preclinical and clinical advancements', *Nature reviews. Clinical oncology*. Nat Rev Clin Oncol, 9(7), pp. 391–399. doi: 10.1038/NRCLINONC.2012.72.
- Carter, R. *et al.* (2012) 'Exploitation of chick embryo environments to reprogram MYCN-amplified neuroblastoma cells to a benign phenotype, lacking detectable MYCN expression', *Oncogenesis*. Nature Publishing Group, 1(8), pp. e24-11. doi: 10.1038/oncsis.2012.24.
- Casey, M. J. and Stewart, R. A. (2018) 'Zebrafish as a model to study neuroblastoma development', *Cell and Tissue Research*. Springer Verlag, 372(2), pp. 223–232. doi: 10.1007/s00441-017-2702-0.
- Castel, V., Segura, V. and Berlanga, P. (2013) 'Emerging drugs for neuroblastoma', *Expert opinion on emerging drugs*. Expert Opin Emerg Drugs, 18(2), pp. 155–171. doi: 10.1517/14728214.2013.796927.
- Cavallero, S. *et al.* (2015) 'CXCL12 signaling is essential for maturation of the ventricular coronary endothelial plexus and establishment of functional coronary circulation', *Developmental cell*. NIH Public Access, 33(4), p. 469. doi: 10.1016/J.DEVCEL.2015.03.018.
- Cerami, E. *et al.* (2012) 'The cBio cancer genomics portal: an open platform for exploring multidimensional cancer genomics data', *Cancer discovery*. Cancer Discov, 2(5), pp. 401–404.

doi: 10.1158/2159-8290.CD-12-0095.

Chen, C. C. *et al.* (2017a) 'Hypoxia and hyperoxia differentially control proliferation of rat neural crest stem cells via distinct regulatory pathways of the HIF1 α -CXCR4 and TP53-TPM1 proteins', *Developmental Dynamics*. John Wiley and Sons Inc., 246(3), pp. 162–185. doi: 10.1002/DVDY.24481.

Chen, C. C. *et al.* (2017b) 'Hypoxia and hyperoxia differentially control proliferation of rat neural crest stem cells via distinct regulatory pathways of the HIF1 α -CXCR4 and TP53-TPM1 proteins', *Developmental Dynamics*. doi: 10.1002/dvdy.24481.

Chen, E. X. *et al.* (2014) 'A Phase I study of cyclin-dependent kinase inhibitor, AT7519, in patients with advanced cancer: NCIC Clinical Trials Group IND 177', *British journal of cancer. Br J Cancer*, 111(12), pp. 2262–2267. doi: 10.1038/BJC.2014.565.

Chen, Q. *et al.* (2019) 'Cancer Immunotherapies and Humanized Mouse Drug Testing Platforms', *Translational Oncology*. Neoplasia Press, 12(7), p. 987. doi: 10.1016/J.TRANON.2019.04.020.

Chen, Y. *et al.* (2008) 'Oncogenic mutations of ALK kinase in neuroblastoma', *Nature*. Nature, 455(7215), pp. 971–974. doi: 10.1038/NATURE07399.

Chen, Y. L. *et al.* (2013) 'The E2F transcription factor 1 transactivates stathmin 1 in hepatocellular carcinoma', *Annals of surgical oncology*. Ann Surg Oncol, 20(12), pp. 4041–4054. doi: 10.1245/S10434-012-2519-8.

Chen, Y. and Stallings, R. L. (2007) 'Differential patterns of microRNA expression in neuroblastoma are correlated with prognosis, differentiation, and apoptosis', *Cancer research. Cancer Res*, 67(3), pp. 976–983. doi: 10.1158/0008-5472.CAN-06-3667.

Chen, Y., Tsai, Y.-H. and Tseng, S.-H. (2013) 'Inhibition of cyclin-dependent kinase 1-induced cell death in neuroblastoma cells through the microRNA-34a-MYCN-survivin pathway', *Surgery*. Mosby, 153(1), pp. 4–16. doi: 10.1016/J.SURG.2012.03.030.

Chen, Y., Tsai, Y. H. and Tseng, S. H. (2013) 'Inhibition of cyclin-dependent kinase 1-induced cell death in neuroblastoma cells through the microRNA-34a-MYCN-survivin pathway', *Surgery (United States)*. doi: 10.1016/j.surg.2012.03.030.

Chen, Z. *et al.* (2016) 'Multiple CDK inhibitor dinaciclib suppresses neuroblastoma growth via inhibiting CDK2 and CDK9 activity', *Scientific Reports*. Nature Publishing Group, 6(June), pp. 1–12. doi: 10.1038/srep29090.

Chesler, L. *et al.* (2007) 'Malignant progression and blockade of angiogenesis in a murine transgenic model of neuroblastoma', *Cancer Research*, 67(19), pp. 9435–9442. doi: 10.1158/0008-5472.CAN-07-1316.

Chesler, L. and Weiss, W. A. (2011) 'Genetically engineered murine models – Contribution to our understanding of the genetics, molecular pathology and therapeutic targeting of neuroblastoma', *Seminars in cancer biology*. NIH Public Access, 21(4), p. 245. doi: 10.1016/J.SEMCANCER.2011.09.011.

Cheung, N.-K. V and Dyer, M. A. (2013) 'Neuroblastoma: developmental biology, cancer genomics and immunotherapy.', *Nature reviews. Cancer*. NIH Public Access, 13(6), pp. 397–411. doi: 10.1038/nrc3526.

- Chisholm, D. R. *et al.* (2019) 'Fluorescent Retinoic Acid Analogues as Probes for Biochemical and Intracellular Characterization of Retinoid Signaling Pathways', *ACS Chemical Biology*, 14(3), pp. 369–377. doi: 10.1021/acscchembio.8b00916.
- Cho, H. *et al.* (2016) 'On-target efficacy of a HIF-2 α antagonist in preclinical kidney cancer models', *Nature*. *Nature*, 539(7627), pp. 107–111. doi: 10.1038/NATURE19795.
- Chu, P. Y. *et al.* (2022) 'Applications of the Chick Chorioallantoic Membrane as an Alternative Model for Cancer Studies', *Cells Tissues Organs*. Karger Publishers, 211(2), pp. 222–237. doi: 10.1159/000513039.
- Chung, K. *et al.* (2013a) 'Structural and molecular interrogation of intact biological systems', *Nature*, 497(7449), pp. 332–337. doi: 10.1038/NATURE12107.
- Chung, K. *et al.* (2013b) 'Structural and molecular interrogation of intact biological systems', *Nature*, 497(7449), pp. 332–337. doi: 10.1038/nature12107.
- Cimmino, F. *et al.* (2015) 'Inhibition of hypoxia inducible factors combined with all-trans retinoic acid treatment enhances glial transdifferentiation of neuroblastoma cells', *Scientific Reports* 2015 5:1. Nature Publishing Group, 5(1), pp. 1–15. doi: 10.1038/srep11158.
- Cimmino, F. *et al.* (2016) 'Proteomic Alterations in Response to Hypoxia Inducible Factor 2 α in Normoxic Neuroblastoma Cells', *Journal of Proteome Research*. American Chemical Society, 15(10), pp. 3643–3655. doi: 10.1021/ACS.JPROTEOME.6B00457.
- Cimpean, A. M., Ribatti, D. and Raica, M. (2008) 'The chick embryo chorioallantoic membrane as a model to study tumor metastasis', *Angiogenesis* 2008 11:4. Springer, 11(4), pp. 311–319. doi: 10.1007/S10456-008-9117-1.
- Cleared Tissue LightSheet - 3i* (no date). Available at: <https://www.intelligent-imaging.com/ctls> (Accessed: 2 June 2022).
- Clinicaltrials.gov (no date) *National Library of Medicine. Iobenguane I-131 or Crizotinib and Standard Therapy in Treating Younger Patients with Newly-Diagnosed High-Risk Neuroblastoma or Ganglioneuroblastoma. Identifier: NCT03126916.*
- Cohn, S. L. *et al.* (2009a) 'The International Neuroblastoma Risk Group (INRG) classification system: an INRG Task Force report', *J. Clin. Oncol.*, 27(2), pp. 289–297. doi: 10.1200/jco.2008.16.6785.
- Cohn, S. L. *et al.* (2009b) 'The International Neuroblastoma Risk Group (INRG) classification system: An INRG task force report', *Journal of Clinical Oncology*, 27(2), pp. 289–297. doi: 10.1200/JCO.2008.16.6785.
- Cohn, S. L. *et al.* (2009c) 'The International Neuroblastoma Risk Group (INRG) Classification System: An INRG Task Force Report', *Journal of Clinical Oncology*. American Society of Clinical Oncology, 27(2), p. 289. doi: 10.1200/JCO.2008.16.6785.
- Cole, K. A. *et al.* (2011) 'RNAi screen of the protein kinome identifies checkpoint kinase 1 (CHK1) as a therapeutic target in neuroblastoma', *Proceedings of the National Academy of Sciences of the United States of America*. doi: 10.1073/pnas.1012351108.
- Comerford, K. M. *et al.* (2002) 'Hypoxia-inducible Factor-1-dependent Regulation of the Multidrug Resistance (MDR1) Gene 1', *CANCER RESEARCH*, 62, pp. 3387–3394.

- Conlon, G. A. and Murray, G. I. (2019) 'Recent advances in understanding the roles of matrix metalloproteinases in tumour invasion and metastasis', *Journal of Pathology*, 247(5), pp. 629–640. doi: 10.1002/path.5225.
- Corallo, D. *et al.* (2016) 'The zebrafish as a model for studying neuroblastoma', *Cancer cell international*. *Cancer Cell Int*, 16(1). doi: 10.1186/S12935-016-0360-Z.
- Costantini, I. *et al.* (2015) 'A versatile clearing agent for multi-modal brain imaging', *Scientific Reports*. Nature Publishing Group, 5. doi: 10.1038/srep09808.
- Courtney, K. D. *et al.* (2020) 'HIF-2 complex dissociation, target inhibition, and acquired resistance with PT2385, a first-in-class HIF-2 inhibitor, in patients with clear cell renal cell carcinoma', *Clinical Cancer Research*. doi: 10.1158/1078-0432.CCR-19-1459.
- Covello, K. L. *et al.* (2006) 'HIF-2 α regulates Oct-4: Effects of hypoxia on stem cell function, embryonic development, and tumor growth', *Genes and Development*, 20(5), pp. 557–570. doi: 10.1101/GAD.1399906.
- Dajee, M. *et al.* (2003) 'NF- κ B blockade and oncogenic Ras trigger invasive human epidermal neoplasia', *Nature*. doi: 10.1038/nature01283.
- Daly, L. A. *et al.* (2021) 'Oxygen-dependent changes in binding partners and post-translational modifications regulate the abundance and activity of HIF-1 α /2 α ', *Science Signaling*. American Association for the Advancement of Science, 14(692). doi: 10.1126/SCISIGNAL.ABF6685/SUPPL_FILE/SCISIGNAL.ABF6685_TABLES_S1_TO_S9.ZIP.
- Dang, C. V. (2012) 'MYC on the path to cancer', *Cell*. Elsevier Inc., 149(1), pp. 22–35. doi: 10.1016/j.cell.2012.03.003.
- Daniels, J. L. *et al.* (2002) 'Breast-feeding and neuroblastoma, USA and Canada', *Cancer Causes & Control* 2002 13:5. Springer, 13(5), pp. 401–405. doi: 10.1023/A:1015746701922.
- Das, B. *et al.* (2005) 'A hypoxia-driven vascular endothelial growth factor/Flt1 autocrine loop interacts with hypoxia-inducible factor-1 α through mitogen-activated protein kinase/extracellular signal-regulated kinase 1/2 pathway in neuroblastoma', *Cancer Research*. doi: 10.1158/0008-5472.CAN-04-4575.
- Davey, M. G. *et al.* (2018) 'Illuminating the chicken model through genetic modification', *International Journal of Developmental Biology*. UPV/EHU Press, 62(1-2-3), pp. 257–264. doi: 10.1387/IJDB.170323MM.
- DeBord, L. C. *et al.* (2018) 'The chick chorioallantoic membrane (CAM) as a versatile patient-derived xenograft (PDX) platform for precision medicine and preclinical research', *American Journal of Cancer Research*. e-Century Publishing Corporation, 8(8), p. 1642. Available at: /pmc/articles/PMC6129484/ (Accessed: 17 May 2022).
- DeMichele, A. *et al.* (2013) 'A phase II trial of an oral CDK 4/6 inhibitor, PD0332991, in advanced breast cancer.', *Journal of Clinical Oncology*. American Society of Clinical Oncology (ASCO), 31(15_suppl), pp. 519–519. doi: 10.1200/JCO.2013.31.15_SUPPL.519.
- Derose, Y. S. *et al.* (2011) 'Tumor grafts derived from women with breast cancer authentically reflect tumor pathology, growth, metastasis and disease outcomes', *Nature medicine*. NIH Public Access, 17(11), p. 1514. doi: 10.1038/NM.2454.
- Deryugina, E. I. and Quigley, J. P. (2008) 'Chick embryo chorioallantoic membrane model

systems to study and visualize human tumor cell metastasis', *Histochemistry and Cell Biology*, 130(6), pp. 1119–1130. doi: 10.1007/s00418-008-0536-2.

Dewitt, J. *et al.* (2014) 'Constitutively active TrkB confers an aggressive transformed phenotype to a neural crest-derived cell line', *Oncogene*. *Oncogene*, 33(8), pp. 977–985. doi: 10.1038/ONC.2013.39.

Dickson, M. A. *et al.* (2013) 'Phase II trial of the CDK4 inhibitor PD0332991 in patients with advanced CDK4-amplified well-differentiated or dedifferentiated liposarcoma', *Journal of clinical oncology: official journal of the American Society of Clinical Oncology*. *J Clin Oncol*, 31(16), pp. 2024–2028. doi: 10.1200/JCO.2012.46.5476.

Dickson, M. A. *et al.* (2016) 'Progression-Free Survival Among Patients With Well-Differentiated or Dedifferentiated Liposarcoma Treated With CDK4 Inhibitor Palbociclib: A Phase 2 Clinical Trial', *JAMA oncology*. *JAMA Oncol*, 2(7), pp. 937–940. doi: 10.1001/JAMAONCOL.2016.0264.

Dotd, H. U. *et al.* (2007a) 'Ultramicroscopy: three-dimensional visualization of neuronal networks in the whole mouse brain', *Nature methods*. *Nat Methods*, 4(4), pp. 331–336. doi: 10.1038/NMETH1036.

Dotd, H. U. *et al.* (2007b) 'Ultramicroscopy: three-dimensional visualization of neuronal networks in the whole mouse brain', *Nat. Methods*, 4(4), pp. 331–336. doi: 10.1038/nmeth1036.

Dotd, H. U. *et al.* (2007c) 'Ultramicroscopy: Three-dimensional visualization of neuronal networks in the whole mouse brain', *Nature Methods*, 4(4), pp. 331–336. doi: 10.1038/nmeth1036.

Dolman, M. E. M. *et al.* (2015) 'Cyclin-Dependent Kinase Inhibitor AT7519 as a Potential Drug for MYCN-Dependent Neuroblastoma.', *Clinical Cancer Research: an Official Journal of the American Association for Cancer Research*. American Association for Cancer Research Inc., 21(22), pp. 5100–5109. doi: 10.1158/1078-0432.CCR-15-0313.

Dong, X. *et al.* (2010) 'Patient-derived first generation xenografts of non-small cell lung cancers: promising tools for predicting drug responses for personalized chemotherapy.', *Clinical Cancer Research: an Official Journal of the American Association for Cancer Research*, 16(5), pp. 1442–1451. doi: 10.1158/1078-0432.CCR-09-2878.

Donovan, L. *et al.* (2010) 'Hypoxia - Implications for pharmaceutical developments', *Sleep and Breathing*, 14(4), pp. 291–298. doi: 10.1007/s11325-010-0368-x.

Downes, N. L. *et al.* (2018) 'Differential but Complementary HIF1 α and HIF2 α Transcriptional Regulation', *Molecular Therapy*, 26(7), pp. 1735–1745. doi: 10.1016/j.ymthe.2018.05.004.

DuBois, S. G. *et al.* (1999) 'Metastatic sites in stage IV and IVS neuroblastoma correlate with age, tumor biology, and survival', *Journal of Pediatric Hematology/Oncology*, 21(3), pp. 181–189. doi: 10.1097/00043426-199905000-00005.

DuBois, S. G. *et al.* (2012) 'Evaluation of norepinephrine transporter expression and metaiodobenzylguanidine avidity in neuroblastoma: a report from the Children's Oncology Group', *Int. J. Mol. Imaging*. Hindawi Limited, 2012, p. 250834. doi: 10.1155/2012/250834.

Dunn, A. K. *et al.* (2013) 'Low-cost laser speckle contrast imaging of blood flow using a webcam', *Biomedical Optics Express*, Vol. 4, Issue 10, pp. 2269–2283. Optica Publishing Group, 4(10), pp. 2269–2283. doi: 10.1364/BOE.4.002269.

Durupt, F. *et al.* (2012) 'The chicken chorioallantoic membrane tumor assay as model for qualitative testing of oncolytic adenoviruses', *Cancer Gene Therapy*, 19(1), pp. 58–68. doi: 10.1038/CGT.2011.68.

Eleveld, T. F. *et al.* (2015) 'Relapsed neuroblastomas show frequent RAS-MAPK pathway mutations', *Nat Genet*, 47, pp. 864–871.

Eltzschig, H. K. and Carmeliet, P. (2011) 'Hypoxia and Inflammation', *The New England journal of medicine*. NIH Public Access, 364(7), p. 656. doi: 10.1056/NEJMRA0910283.

Erttmann, R. *et al.* (1998) '10 years' neuroblastoma screening in Europe: preliminary results of a clinical and biological review from the study group for evaluation of neuroblastoma screening in Europe (SENSE)', *European Journal of Cancer*. Pergamon, 34(9), pp. 1391–1397. doi: 10.1016/S0959-8049(98)00135-X.

Ertürk, A. *et al.* (2011) 'Three-dimensional imaging of the unsectioned adult spinal cord to assess axon regeneration and glial responses after injury', *Nature medicine*. Nat Med, 18(1), pp. 166–171. doi: 10.1038/NM.2600.

Ertürk, A. *et al.* (2012) 'Three-dimensional imaging of solvent-cleared organs using 3DISCO', *Nature Protocols*, 7(11), pp. 1983–1995. doi: 10.1038/nprot.2012.119.

Fathollahipour, S., Patil, P. S. and Leipzig, N. D. (2018) 'Oxygen Regulation in Development: Lessons from Embryogenesis towards Tissue Engineering', *Cells, tissues, organs*. NIH Public Access, 205(5–6), p. 350. doi: 10.1159/000493162.

FDA Approves Drug to Reduce Bone Marrow Suppression Caused by Chemotherapy (no date) *FDA Approves Drug to Reduce Bone Marrow Suppression Caused by Chemotherapy | FDA*. Available at: <https://www.fda.gov/news-events/press-announcements/fda-approves-drug-reduce-bone-marrow-suppression-caused-chemotherapy> (Accessed: 17 July 2022).

Federico, S. M. *et al.* (2017) 'A Pilot Trial of Humanized Anti-GD2 Monoclonal Antibody (hu14.18K322A) with Chemotherapy and Natural Killer Cells in Children with Recurrent/Refractory Neuroblastoma', *Clinical cancer research : an official journal of the American Association for Cancer Research*. Clin Cancer Res, 23(21), pp. 6441–6449. doi: 10.1158/1078-0432.CCR-17-0379.

Ferlay, J. *et al.* (2021) 'Cancer statistics for the year 2020: An overview', *International journal of cancer*. Int J Cancer, 149(4), pp. 778–789. doi: 10.1002/IJC.33588.

Finn, R. S. *et al.* (2009) 'PD 0332991, a selective cyclin D kinase 4/6 inhibitor, preferentially inhibits proliferation of luminal estrogen receptor-positive human breast cancer cell lines in vitro', *Breast cancer research : BCR*. Breast Cancer Res, 11(5). doi: 10.1186/BCR2419.

Finn, R. S. *et al.* (2016) 'Palbociclib and Letrozole in Advanced Breast Cancer', *New England Journal of Medicine*. New England Journal of Medicine (NEJM/MMS), 375(20), pp. 1925–1936. doi: 10.1056/NEJMORA1607303/SUPPL_FILE/NEJMORA1607303_DISCLOSURES.PDF.

Flemington, E. K., Speck, S. H. and Kaelin, W. G. (1993) 'E2F-1-mediated transactivation is inhibited by complex formation with the retinoblastoma susceptibility gene product', *Proceedings of the National Academy of Sciences of the United States of America*. Proc Natl Acad Sci U S A, 90(15), pp. 6914–6918. doi: 10.1073/PNAS.90.15.6914.

Fotinos, N. *et al.* (2006) '5-Aminolevulinic acid derivatives in photomedicine: Characteristics, application and perspectives', *Photochemistry and photobiology*. Photochem Photobiol, 82(4), p.

994. doi: 10.1562/2006-02-03-IR-794.

Frangioni, J. V. (2008) 'New technologies for human cancer imaging', *Journal of Clinical Oncology*. doi: 10.1200/JCO.2007.14.3065.

Franscini, L. C. *et al.* (2015) 'Pediatric reference intervals for plasma free and total metanephrines established with a parametric approach: relevance to the diagnosis of neuroblastoma', *Pediatr. Blood Cancer*. John Wiley and Sons Inc, 62(4), pp. 587–593. doi: 10.1002/pbc.25385.

French, A. E. *et al.* (2003) 'Folic acid food fortification is associated with a decline in neuroblastoma', *Clinical pharmacology and therapeutics*. Clin Pharmacol Ther, 74(3), pp. 288–294. doi: 10.1016/S0009-9236(03)00200-5.

Funahashi, J. *et al.* (1999) 'Role of Pax-5 in the regulation of a mid-hindbrain organizer's activity', *Development, growth & differentiation*. Dev Growth Differ, 41(1), pp. 59–72. doi: 10.1046/J.1440-169X.1999.00401.X.

Furlan, A. *et al.* (2017) 'Multipotent peripheral glial cells generate neuroendocrine cells of the adrenal medulla', *Science*. American Association for the Advancement of Science, 357(6346). doi: 10.1126/SCIENCE.AAL3753.

Gandhi, S. *et al.* (2017) 'Optimization of CRISPR/Cas9 genome editing for loss-of-function in the early chick embryo', *Developmental Biology*. Academic Press, 432(1), pp. 86–97. doi: 10.1016/J.YDBIO.2017.08.036.

Gardner, V., Madu, C. O. and Lu, Y. (2017) 'Anti-VEGF Therapy in Cancer: A Double-Edged Sword', *Physiologic and Pathologic Angiogenesis - Signaling Mechanisms and Targeted Therapy*. IntechOpen. doi: 10.5772/66763.

Garofalo, S. *et al.* (2015) 'Enriched environment reduces glioma growth through immune and non-immune mechanisms in mice', *Nat. Commun*. Nature Publishing Group, 6. doi: 10.1038/ncomms7623.

Gaustad, J. V. *et al.* (2012) 'Sunitinib treatment does not improve blood supply but induces hypoxia in human melanoma xenografts', *BMC Cancer*, 12. doi: 10.1186/1471-2407-12-388/FIGURES/1.

Georger, B. *et al.* (2017) 'A Phase I Study of the CDK4/6 Inhibitor Ribociclib (LEE011) in Pediatric Patients with Malignant Rhabdoid Tumors, Neuroblastoma, and Other Solid Tumors', *Clinical cancer research : an official journal of the American Association for Cancer Research*. Clin Cancer Res, 23(10), pp. 2433–2441. doi: 10.1158/1078-0432.CCR-16-2898.

Gherardi, S. *et al.* (2013) 'MYCN-mediated transcriptional repression in neuroblastoma: The other side of the coin', *Frontiers in Oncology*. Frontiers, 3 MAR, p. 42. doi: 10.3389/FONC.2013.00042/BIBTEX.

Ghia, P. *et al.* (2017) 'Efficacy and safety of dinaciclib vs ofatumumab in patients with relapsed/refractory chronic lymphocytic leukemia', *Blood*. American Society of Hematology, 129(13), pp. 1876–1878. doi: 10.1182/blood-2016-10-748210.

Goda, N. *et al.* (2003) 'Hypoxia-Inducible Factor 1 α Is Essential for Cell Cycle Arrest during Hypoxia', *Molecular and Cellular Biology*. doi: 10.1128/mcb.23.1.359-369.2003.

Goel, S. *et al.* (2018) 'CDK4/6 Inhibition in Cancer: Beyond Cell Cycle Arrest', *Trends in Cell*

Biology, 28(11), pp. 911–925. doi: 10.1016/j.tcb.2018.07.002.

Goetz, M. P. *et al.* (2017) 'MONARCH 3: Abemaciclib as initial therapy for advanced breast cancer', *Journal of Clinical Oncology*. American Society of Clinical Oncology, 35(32), pp. 3638–3646. doi: 10.1200/JCO.2017.75.6155.

Goga, A. *et al.* (2007) 'Inhibition of CDK1 as a potential therapy for tumors over-expressing MYC', *Nature Medicine*, 13(7), pp. 820–827. doi: 10.1038/nm1606.

Gogolin, S. *et al.* (2013) 'CDK4 inhibition restores G1-S arrest in MYCN-amplified neuroblastoma cells in the context of doxorubicin-induced DNA damage', *Cell Cycle*, 12(7), pp. 1091–1104. doi: 10.4161/cc.24091.

Golias, C. H., Charalabopoulos, A. and Charalabopoulos, K. (2004) 'Cell proliferation and cell cycle control: A mini review', *International Journal of Clinical Practice*. doi: 10.1111/j.1742-1241.2004.00284.x.

Gordan, J. D. *et al.* (2007a) 'HIF-2 α promotes hypoxic cell proliferation by enhancing c-Myc transcriptional activity', *Cancer cell*. Howard Hughes Medical Institute, 11(4), p. 335. doi: 10.1016/J.CCR.2007.02.006.

Gordan, J. D. *et al.* (2007b) 'HIF-2 α Promotes Hypoxic Cell Proliferation by Enhancing c-Myc Transcriptional Activity', *Cancer Cell*. doi: 10.1016/j.ccr.2007.02.006.

Graeber, T. G. *et al.* (1996) 'Hypoxia-mediated selection of cells with diminished apoptotic potential in solid tumours', *Nature*, 379(6560), pp. 88–91. doi: 10.1038/379088A0.

Gronau, S. *et al.* (2006) 'An autologous system for culturing head and neck squamous cell carcinomas for the assessment of cellular therapies on the chorioallantois membrane', *European Archives of Oto-Rhino-Laryngology*, 263(4), pp. 308–312. doi: 10.1007/S00405-005-1008-0.

Guan, J. *et al.* (2016) 'The ALK inhibitor PF-06463922 is effective as a single agent in neuroblastoma driven by expression of ALK and MYCN', *Disease models & mechanisms*. Dis Model Mech, 9(9), pp. 941–952. doi: 10.1242/DMM.024448.

Hahne, M. *et al.* (2018) 'Unraveling the role of hypoxia-inducible factor (HIF)-1 α and HIF-2 α in the adaption process of human microvascular endothelial cells (HMEC-1) to hypoxia: Redundant HIF-dependent regulation of macrophage migration inhibitory factor', *Microvascular research*. Microvasc Res, 116, pp. 34–44. doi: 10.1016/J.MVR.2017.09.004.

Hama, H. *et al.* (2011) 'Scale: a chemical approach for fluorescence imaging and reconstruction of transparent mouse brain.', *Nature neuroscience*, 14(11), pp. 1481–8. doi: 10.1038/nn.2928.

Hamburger, V. and Hamilton, H. L. (1951) 'A series of normal stages in the development of the chick embryo', *Journal of Morphology*, 88(1), pp. 49–92. doi: 10.1002/jmor.1050880104.

Hanahan, D. (2022) 'Hallmarks of Cancer: New Dimensions', *Cancer Discovery*. American Association for Cancer Research, 12(1), pp. 31–46. doi: 10.1158/2159-8290.CD-21-1059.

Hanahan, D. and Weinberg, R. A. (2000) 'The hallmarks of cancer', *Cell*, 100(1), pp. 57–70. doi: 10.1016/S0092-8674(00)81683-9.

Hanahan, D. and Weinberg, R. A. (2011a) 'Hallmarks of cancer: The next generation', *Cell*,

144(5), pp. 646–674. doi: 10.1016/J.CELL.2011.02.013.

Hanahan, D. and Weinberg, R. A. (2011b) 'Hallmarks of cancer: The next generation', *Cell*. doi: 10.1016/j.cell.2011.02.013.

Hardy, P. C. and Nesbit, M. E. (1972) 'Familial neuroblastoma: Report of a kindred with a high incidence of infantile tumors', *The Journal of Pediatrics*. Mosby, 80(1), pp. 74–77. doi: 10.1016/S0022-3476(72)80456-6.

Harmand, T. J. *et al.* (2021) 'Nanobodies as in vivo , non-invasive, imaging agents', *RSC Chemical Biology*. Royal Society of Chemistry, 2(3), pp. 685–701. doi: 10.1039/D1CB00023C.

Hart, L. S. *et al.* (2017) 'Preclinical Therapeutic Synergy of MEK1/2 and CDK4/6 Inhibition in Neuroblastoma', *Clinical cancer research : an official journal of the American Association for Cancer Research*. Clin Cancer Res, 23(7), pp. 1785–1796. doi: 10.1158/1078-0432.CCR-16-1131.

Hatipoglu, O. F. *et al.* (2009) 'ADAMTS1 is a unique hypoxic early response gene expressed by endothelial cells', *Journal of Biological Chemistry*, 284(24), pp. 16325–16333. doi: 10.1074/jbc.M109.001313.

Helmchen, F. and Denk, W. (2005) 'Deep tissue two-photon microscopy', *Nature Methods*, 2(12), pp. 932–940. doi: 10.1038/NMETH818.

Hendrix, M. J. C. *et al.* (2007) 'Reprogramming metastatic tumour cells with embryonic microenvironments', *Nature Reviews Cancer*, 7(4), pp. 246–255. doi: 10.1038/NRC2108.

Henriksson, M. and Lüscher, B. (1996) 'Proteins of the Myc Network: Essential Regulators of Cell Growth and Differentiation', *Advances in Cancer Research*. Academic Press, 68, pp. 109–182. doi: 10.1016/S0065-230X(08)60353-X.

Henssen, A. *et al.* (2016) 'Targeting MYCN-Driven Transcription By BET-Bromodomain Inhibition', *Clinical cancer research : an official journal of the American Association for Cancer Research*. Clin Cancer Res, 22(10), pp. 2470–2781. doi: 10.1158/1078-0432.CCR-15-1449.

Her, Z. P. *et al.* (2021) 'Zebrafish Model of Neuroblastoma Metastasis', *Journal of visualized experiments : JoVE*. NIH Public Access, 2021(169). doi: 10.3791/62416.

Herbert, S. P. *et al.* (2009) 'Arterial-venous segregation by selective cell sprouting: an alternative mode of blood vessel formation', *Science*, 326(5950), pp. 294–298. doi: 10.1126/science.1178577.

Herder, M. (2017) 'What Is the Purpose of the Orphan Drug Act?', *PLOS Medicine*. Public Library of Science, 14(1), p. e1002191. doi: 10.1371/JOURNAL.PMED.1002191.

Hero, B. *et al.* (2008) 'Localized infant neuroblastomas often show spontaneous regression: Results of the prospective trials NB95-S and NB97', *Journal of Clinical Oncology*, 26(9), pp. 1504–1510. doi: 10.1200/JCO.2007.12.3349.

Herrmann, A *et al.* (2015) 'Cellular memory of hypoxia elicits neuroblastoma metastasis and enables invasion by non-aggressive neighbouring cells.', *Oncogenesis*, 4(2), p. e138. doi: 10.1038/oncsis.2014.52.

Herrmann, A. *et al.* (2015) 'Cellular memory of hypoxia elicits neuroblastoma metastasis and enables invasion by non-aggressive neighbouring cells', *Oncogenesis*. Nature Publishing

Group, 4(2). doi: 10.1038/ONCSIS.2014.52.

Herrmann, A. *et al.* (2018) 'Magnetic Resonance Imaging for Characterization of a Chick Embryo Model of Cancer Cell Metastases', *Molecular Imaging*. SAGE Publications Inc., 17. doi: 10.1177/1536012118809585.

Herrmann, A., Moss, D. and Sée, V. (2016) 'The chorioallantoic membrane of the chick embryo to assess tumor formation and metastasis', in *Methods in Molecular Biology*. doi: 10.1007/978-1-4939-3999-2_9.

Hillman, E. M. C. *et al.* (2019) 'Light-Sheet Microscopy in Neuroscience', *Annual Review of Neuroscience*. Annual Reviews Inc., 42, pp. 295–313. doi: 10.1146/ANNUREV-NEURO-070918-050357.

Hiroshi, T. and Masaji, M. (1977) 'Oxygen analyses of chicken embryo blood', *Respiration Physiology*. Elsevier, 31(2), pp. 203–215. doi: 10.1016/0034-5687(77)90103-7.

Hoebeeck, J. *et al.* (2006) 'The von Hippel-Lindau tumor suppressor gene expression level has prognostic value in neuroblastoma', *International Journal of Cancer*. doi: 10.1002/ijc.21888.

Hoefflin, R. *et al.* (2020) 'HIF-1 α and HIF-2 α differently regulate tumour development and inflammation of clear cell renal cell carcinoma in mice', *Nature Communications* 2020 11:1. Nature Publishing Group, 11(1), pp. 1–21. doi: 10.1038/s41467-020-17873-3.

Holekamp, T. F., Turaga, D. and Holy, T. E. (2008) 'Fast three-dimensional fluorescence imaging of activity in neural populations by objective-coupled planar illumination microscopy', *Neuron*. Neuron, 57(5), pp. 661–672. doi: 10.1016/J.NEURON.2008.01.011.

Holliger, P. and Hudson, P. J. (2005) 'Engineered antibody fragments and the rise of single domains', *Nature Biotechnology* 2005 23:9. Nature Publishing Group, 23(9), pp. 1126–1136. doi: 10.1038/nbt1142.

Holmes, K. *et al.* (2020) 'Influence of Surgical Excision on the Survival of Patients With Stage 4 High-Risk Neuroblastoma: A Report From the HR-NBL1/SIOPEN Study', *Journal of clinical oncology : official journal of the American Society of Clinical Oncology*. J Clin Oncol, 38(25), pp. 2902–2915. doi: 10.1200/JCO.19.03117.

Holmquist-Mengelbier, L. *et al.* (2006) 'Recruitment of HIF-1 α and HIF-2 α to common target genes is differentially regulated in neuroblastoma: HIF-2 α promotes an aggressive phenotype', *Cancer Cell*, 10(5), pp. 413–423. doi: 10.1016/j.ccr.2006.08.026.

Hong, M. *et al.* (2020) 'RNA sequencing: new technologies and applications in cancer research', *Journal of Hematology & Oncology* 2020 13:1. BioMed Central, 13(1), pp. 1–16. doi: 10.1186/S13045-020-01005-X.

Hortobagyi, G. N. *et al.* (2016) 'Ribociclib as First-Line Therapy for HR-Positive, Advanced Breast Cancer', *The New England journal of medicine*. N Engl J Med, 375(18), pp. 1738–1748. doi: 10.1056/NEJMOA1609709.

Huang, M. and Weiss, William A (2013) 'Neuroblastoma and MYCN.', *Cold Spring Harbor perspectives in medicine*, 3(10), p. a014415. doi: 10.1101/cshperspect.a014415.

Huang, M. and Weiss, William A. (2013) 'Neuroblastoma and MYCN', *Cold Spring Harbor perspectives in medicine*. Cold Spring Harb Perspect Med, 3(10). doi: 10.1101/CSHPERSPECT.A014415.

- Huang, W. T. *et al.* (2017) 'Effect of miR-146a-5p on tumor growth in NSCLC using chick chorioallantoic membrane assay and bioinformatics investigation', *Molecular Medicine Reports*. Spandidos Publications, 16(6), pp. 8781–8792. doi: 10.3892/MMR.2017.7713.
- Hubbi, M. E. and Semenza, G. L. (2015) 'Regulation of cell proliferation by hypoxia-inducible factors', *American Journal of Physiology - Cell Physiology*. doi: 10.1152/ajpcell.00279.2015.
- Hurwitz, H. *et al.* (2004) 'Bevacizumab plus Irinotecan, Fluorouracil, and Leucovorin for Metastatic Colorectal Cancer', <https://doi.org/10.1056/NEJMoa032691>. Massachusetts Medical Society, 350(23), pp. 2335–2342. doi: 10.1056/NEJMoa032691.
- Ilardi, G. *et al.* (2014) 'Histopathological Determinants of Tumor Resistance: A Special Look to the Immunohistochemical Expression of Carbonic Anhydrase IX in Human Cancers', *Current Medicinal Chemistry*. doi: 10.2174/09298673113209990227.
- Irwin, M. S. *et al.* (2021) 'Revised Neuroblastoma Risk Classification System: A Report From the Children's Oncology Group', *Journal of clinical oncology: official journal of the American Society of Clinical Oncology*. *J Clin Oncol*, 39(29), pp. 3229–3241. doi: 10.1200/JCO.21.00278.
- Ishii, Y. and Mikawa, T. (2005) 'Somatic transgenesis in the avian model system', *Birth Defects Research Part C: Embryo Today: Reviews*. John Wiley & Sons, Ltd, 75(1), pp. 19–27. doi: 10.1002/BDRC.20033.
- Iyer, R. *et al.* (2015) 'Nanoparticle delivery of an SN38 conjugate is more effective than irinotecan in a mouse model of neuroblastoma', *Cancer letters*. *Cancer Lett*, 360(2), pp. 205–212. doi: 10.1016/J.CANLET.2015.02.011.
- J. Yuan, L. N. S. R. P. M. G. (2000) 'Diminished DNA repair and elevated mutagenesis in mammalian cells exposed to hypoxia and low pH', *Cancer Research*, 60, pp. 4372–4376.
- J Ribelles, A. *et al.* (2019) 'Clinical Features of Neuroblastoma With 11q Deletion: An Increase in Relapse Probabilities In Localized And 4S Stages', *Scientific Reports*, 9(1), pp. 1–9. doi: 10.1038/s41598-019-50327-5.
- Jarrosso, L. *et al.* (2021) 'An avian embryo patient-derived xenograft model for preclinical studies of human breast cancers', *iScience*. Elsevier, 24(12), p. 103423. doi: 10.1016/J.ISCI.2021.103423.
- Jing, D. *et al.* (2018) 'Tissue clearing of both hard and soft tissue organs with the PEGASOS method', *Cell Research 2018 28:8*. Nature Publishing Group, 28(8), pp. 803–818. doi: 10.1038/s41422-018-0049-z.
- Jögi, A. *et al.* (2002) 'Hypoxia alters gene expression in human neuroblastoma cells toward an immature and neural crest-like phenotype', *Proceedings of the National Academy of Sciences of the United States of America*, 99(10), pp. 7021–7026. doi: 10.1073/PNAS.102660199.
- Jögi, A. *et al.* (2004) 'Human neuroblastoma cells exposed to hypoxia: Induction of genes associated with growth, survival, and aggressive behavior', *Experimental Cell Research*. Academic Press Inc., 295(2), pp. 469–487. doi: 10.1016/J.YEXCR.2004.01.013.
- Johnsen, J. I., Dyberg, C. and Wickström, M. (2019a) 'Neuroblastoma—A neural crest derived embryonal malignancy', *Frontiers in Molecular Neuroscience*, 12(January), pp. 1–11. doi: 10.3389/fnmol.2019.00009.
- Johnsen, J. I., Dyberg, C. and Wickström, M. (2019b) 'Neuroblastoma—A neural crest derived

embryonal malignancy', *Frontiers in Molecular Neuroscience*. Frontiers Media S.A., 12, p. 9. doi: 10.3389/FNMOL.2019.00009/BIBTEX.

Jonkman, J. *et al.* (2020) 'Tutorial: guidance for quantitative confocal microscopy', *Nature Protocols* 2020 15:5. Nature Publishing Group, 15(5), pp. 1585–1611. doi: 10.1038/s41596-020-0313-9.

Jonkman, J. and Brown, C. M. (2015) 'Any way you slice it — a comparison of confocal microscopy techniques', *J. Biomol. Tech.* Association of Biomolecular Resource Facilities, 26(2), pp. 54–65. doi: 10.7171/jbt.15-2602-003.

Kain, K. H. *et al.* (2014) 'The chick embryo as an expanding experimental model for cancer and cardiovascular research', *Developmental dynamics: an official publication of the American Association of Anatomists*. Dev Dyn, 243(2), pp. 216–228. doi: 10.1002/DVDY.24093.

Kalirai, H. *et al.* (2015) 'Use of the Chick Embryo Model in Uveal Melanoma', *Ocular Oncology and Pathology*, 1(3), pp. 133–140. doi: 10.1159/000370151.

Kamihara, J. *et al.* (2017) 'Socioeconomic status and global variations in the incidence of neuroblastoma: call for support of population-based cancer registries in low-middle-income countries', *Pediatric blood & cancer*. Pediatr Blood Cancer, 64(2), pp. 321–323. doi: 10.1002/PBC.26244.

Kamijo, T. and Nakagawara, A. (2012) 'Molecular and genetic bases of neuroblastoma', *International Journal of Clinical Oncology* 2012 17:3. Springer, 17(3), pp. 190–195. doi: 10.1007/S10147-012-0415-7.

Kang, J. *et al.* (2008) 'N-myc is a novel regulator of PI3K-mediated VEGF expression in neuroblastoma.', *Oncogene*, 27(28), pp. 3999–4007. doi: 10.1038/onc.2008.15.

Kang, J. *et al.* (2014) 'Targeting cyclin-dependent kinase 1 (CDK1) but not CDK4/6 or CDK2 is selectively lethal to MYC-dependent human breast cancer cells', *BMC Cancer*. doi: 10.1186/1471-2407-14-32.

Karnofsky, D. A., Ridgeway, L. P. and Patterson, P. A. (1952) 'Tumor transplantation to the chick embryo.', *Annals of the New York Academy of Sciences*, 55(2), pp. 313–329. doi: 10.1111/J.1749-6632.1952.TB26547.X.

Kato, J. *et al.* (1993a) 'Direct binding of cyclin D to the retinoblastoma gene product (pRb) and pRb phosphorylation by the cyclin D-dependent kinase CDK4', *Genes & development*. Genes Dev, 7(3), pp. 331–342. doi: 10.1101/GAD.7.3.331.

Kato, J. *et al.* (1993b) 'Direct binding of cyclin D to the retinoblastoma gene product (pRb) and pRb phosphorylation by the cyclin D-dependent kinase CDK4', *Genes and Development*. doi: 10.1101/gad.7.3.331.

Katt, M. E. *et al.* (2016) 'In vitro tumor models: Advantages, disadvantages, variables, and selecting the right platform', *Frontiers in Bioengineering and Biotechnology*. Frontiers Media S.A., 4(FEB), p. 12. doi: 10.3389/FBIOE.2016.00012/BIBTEX.

Kaur, S. *et al.* (2012) 'Recent trends in antibody-based oncologic imaging', *Cancer Letters*. Elsevier, 315(2), pp. 97–111. doi: 10.1016/J.CANLET.2011.10.017.

Keith, B., Johnson, R. S. and Simon, M. C. (2011) 'HIF1 α and HIF2 α : sibling rivalry in hypoxic tumour growth and progression', *Nature reviews. Cancer*. Nat Rev Cancer, 12(1), pp. 9–22. doi:

10.1038/NRC3183.

Keller, P. J. and Dodt, H. U. (2012) 'Light sheet microscopy of living or cleared specimens', *Current Opinion in Neurobiology*, 22(1), pp. 138–143. doi: 10.1016/j.conb.2011.08.003.

Khong, T. Y. and Malcomson, R. D. G. (2015) *Keeling's fetal and neonatal pathology, Keeling's Fetal and Neonatal Pathology*. Springer International Publishing. doi: 10.1007/978-3-319-19207-9.

Khoradmehr, A. *et al.* (2019) 'A Simple Technique for Three-Dimensional Imaging and Segmentation of Brain Vasculature Using Fast Free-of-Acrylamide Clearing Tissue in Murine', *Cell journal. Cell J*, 21(1), pp. 49–56. doi: 10.22074/CELLJ.2019.5684.

Kim, S. Y., Chung, K. and Deisseroth, K. (2013) 'Light microscopy mapping of connections in the intact brain', *Trends in cognitive sciences. Trends Cogn Sci*, 17(12), pp. 596–599. doi: 10.1016/J.TICS.2013.10.005.

King, C. R. and Long, J. P. (2000) 'Prostate Biopsy Grading Errors: A Sampling Problem?', *Int. J. Cancer (Radiat. Oncol. Invest.)*, 90, pp. 326–330. doi: 10.1002/1097-0215.

Kingston, B. R. *et al.* (2019a) 'Assessing micrometastases as a target for nanoparticles using 3D microscopy and machine learning', *Proceedings of the National Academy of Sciences of the United States of America*. National Academy of Sciences, 116(30), pp. 14937–14946. doi: 10.1073/PNAS.1907646116.

Kingston, B. R. *et al.* (2019b) 'Assessing micrometastases as a target for nanoparticles using 3D microscopy and machine learning', *Proceedings of the National Academy of Sciences of the United States of America*. National Academy of Sciences, 116(30), pp. 14937–14946. doi: 10.1073/PNAS.1907646116/SUPPL_FILE/PNAS.1907646116.SM05.MOV.

Kleihues, P. (Paul), Cavenee, W. K. (Webster K. . and International Agency for Research on Cancer. (2000) *Pathology and genetics of tumours of the nervous system*. IARC Press. Available at: <http://publications.iarc.fr/Book-And-Report-Series/Who-Iarc-Classification-Of-Tumours/Pathology-And-Genetics-Of-Tumours-Of-The-Nervous-System-2000> (Accessed: 4 November 2018).

Klein, M. E. *et al.* (2018) 'CDK4/6 Inhibitors: The Mechanism of Action May Not Be as Simple as Once Thought', *Cancer cell. Cancer Cell*, 34(1), pp. 9–20. doi: 10.1016/J.CCELL.2018.03.023.

Klingberg, A. *et al.* (2017) 'Fully automated evaluation of total glomerular number and capillary tuft size in nephritic kidneys using lightsheet microscopy', *Journal of the American Society of Nephrology*. doi: 10.1681/ASN.2016020232.

Klingenberg, M. *et al.* (2014) 'The chick chorioallantoic membrane as an in vivo xenograft model for Burkitt lymphoma', *BMC Cancer. BioMed Central Ltd.*, 14(1), pp. 1–12. doi: 10.1186/1471-2407-14-339/TABLES/2.

Knoepfler, P. S., Cheng, P. F. and Eisenman, R. N. (2002) 'N-myc is essential during neurogenesis for the rapid expansion of progenitor cell populations and the inhibition of neuronal differentiation.', *Genes & development. Cold Spring Harbor Laboratory Press*, 16(20), pp. 2699–712. doi: 10.1101/gad.1021202.

Koop, S. *et al.* (1996) 'Independence of metastatic ability and extravasation: metastatic ras-transformed and control fibroblasts extravasate equally well', *Proceedings of the National Academy of Sciences of the United States of America. Proc Natl Acad Sci U S A*, 93(20), pp.

11080–11084. doi: 10.1073/PNAS.93.20.11080.

Koppen, A. *et al.* (2007) 'Dickkopf-1 is down-regulated by MYCN and inhibits neuroblastoma cell proliferation', *Cancer letters*. *Cancer Lett*, 256(2), pp. 218–228. doi: 10.1016/J.CANLET.2007.06.011.

Kostrikov, S. *et al.* (2021) 'Optical tissue clearing and machine learning can precisely characterize extravasation and blood vessel architecture in brain tumors', *Communications Biology* 2021 4:1. Nature Publishing Group, 4(1), pp. 1–16. doi: 10.1038/s42003-021-02275-y.

Kraal, K. C. J. M. *et al.* (2015) 'Upfront treatment of high-risk neuroblastoma with a combination of 131I-MIBG and Topotecan', *Pediatric Blood and Cancer*. John Wiley and Sons Inc., 62(11), pp. 1886–1891. doi: 10.1002/PBC.25580.

Kreeger, P. K. and Lauffenburger, D. A. (2010) 'Cancer systems biology: a network modeling perspective', *Carcinogenesis*. *Carcinogenesis*, 31(1), pp. 2–8. doi: 10.1093/CARCIN/BGP261.

Krtolica, A., Krucher, N. A. and Ludlow, J. W. (1998) 'Hypoxia-induced pRB hypophosphorylation results from downregulation of CDK and upregulation of PP1 activities', *Oncogene*. *Oncogene*, 17(18), pp. 2295–2304. doi: 10.1038/SJ.ONC.1202159.

Kryh, H. *et al.* (2011) 'Comprehensive SNP array study of frequently used neuroblastoma cell lines; copy neutral loss of heterozygosity is common in the cell lines but uncommon in primary tumors', *BMC Genomics*. BioMed Central, 12(1), pp. 1–11. doi: 10.1186/1471-2164-12-443/FIGURES/4.

Kubota, Shimpei I *et al.* (2017) 'Whole-Body Profiling of Cancer Metastasis with Single-Cell Resolution.', *Cell reports*, 20(1), pp. 236–250. doi: 10.1016/j.celrep.2017.06.010.

Kubota, Shimpei I. *et al.* (2017a) 'Whole-Body Profiling of Cancer Metastasis with Single-Cell Resolution', *Cell Reports*. Elsevier Company., 20(1), pp. 236–250. doi: 10.1016/j.celrep.2017.06.010.

Kubota, Shimpei I. *et al.* (2017b) 'Whole-Body Profiling of Cancer Metastasis with Single-Cell Resolution', *Cell Reports*. Elsevier B.V., 20(1), pp. 236–250. doi: 10.1016/J.CELREP.2017.06.010.

Kue, C. S. *et al.* (2014) 'Chick embryo chorioallantoic membrane (CAM): An alternative predictive model in acute toxicological studies for anti-cancer drugs', *Experimental Animals*, 64(2), pp. 129–138. doi: 10.1538/expanim.14-0059.

Kuhlicke, J. *et al.* (2007) 'Hypoxia Inducible Factor (HIF)-1 Coordinates Induction of Toll-Like Receptors TLR2 and TLR6 during Hypoxia', *PLOS ONE*. Public Library of Science, 2(12), p. e1364. doi: 10.1371/JOURNAL.PONE.0001364.

Kulesa, P. M. *et al.* (2006) 'Reprogramming metastatic melanoma cells to assume a neural crest cell-like phenotype in an embryonic microenvironment', *Proceedings of the National Academy of Sciences of the United States of America*, 103(10), pp. 3752–3757. doi: 10.1073/PNAS.0506977103.

Kumar, S. *et al.* (2018) 'Hypoxia-Targeting Drug Evofosfamide (TH-302) Enhances Sunitinib Activity in Neuroblastoma Xenograft Models', *Translational Oncology*. Elsevier, 11(4), pp. 911–919. doi: 10.1016/J.TRANON.2018.05.004.

Kumar, S. K. *et al.* (2015) 'Dinaciclib, a novel CDK inhibitor, demonstrates encouraging single-

agent activity in patients with relapsed multiple myeloma', *Blood*. *Blood*, 125(3), pp. 443–448. doi: 10.1182/BLOOD-2014-05-573741.

Kurihara, S. *et al.* (2014) 'Clinical features of ATRX or DAXX mutated neuroblastoma', *Journal of pediatric surgery*. *J Pediatr Surg*, 49(12), pp. 1835–1838. doi: 10.1016/J.JPESURG.2014.09.029.

Kuriyama, S. and Mayor, R. (2008) 'Molecular analysis of neural crest migration', *Philosophical Transactions of the Royal Society B: Biological Sciences*. Royal Society, 363(1495), pp. 1349–1362. doi: 10.1098/RSTB.2007.2252.

Kushner, B. H. *et al.* (1996) 'Survival from locally invasive or widespread neuroblastoma without cytotoxic therapy', *Journal of Clinical Oncology*. American Society of Clinical Oncology, 14(2), pp. 373–381. doi: 10.1200/JCO.1996.14.2.373.

Ladenstein, R. *et al.* (2017) 'Busulfan and melphalan versus carboplatin, etoposide, and melphalan as high-dose chemotherapy for high-risk neuroblastoma (HR-NBL1/SIOPEN): an international, randomised, multi-arm, open-label, phase 3 trial', *The Lancet. Oncology*. *Lancet Oncol*, 18(4), pp. 500–514. doi: 10.1016/S1470-2045(17)30070-0.

Lagerweij, T. *et al.* (2017) 'Optical clearing and fluorescence deep-tissue imaging for 3D quantitative analysis of the brain tumor microenvironment', *Angiogenesis*, 20(4), pp. 533–546. doi: 10.1007/s10456-017-9565-6.

Lando, D. *et al.* (2002) 'FIH-1 is an asparaginyl hydroxylase enzyme that regulates the transcriptional activity of hypoxia-inducible factor', *Genes and Development*, 16(12), pp. 1466–1471. doi: 10.1101/GAD.991402.

Laoukili, J. *et al.* (2008) 'Activation of FoxM1 during G2 requires cyclin A/Cdk-dependent relief of autorepression by the FoxM1 N-terminal domain', *Molecular and cellular biology*. *Mol Cell Biol*, 28(9), pp. 3076–3087. doi: 10.1128/MCB.01710-07.

Lee, D. W. and Ho, G. F. (2020) 'Palbociclib in the treatment of recurrent ovarian cancer', *Gynecologic Oncology Reports*. Elsevier, 34. doi: 10.1016/J.GORE.2020.100626.

Lee, J. *et al.* (2012) 'BAY 11-7082 is a broad-spectrum inhibitor with anti-inflammatory activity against multiple targets', *Mediators of Inflammation*. doi: 10.1155/2012/416036.

Lee, J. W. *et al.* (2019) 'Hypoxia signaling in human diseases and therapeutic targets', *Experimental & Molecular Medicine 2019 51:6*. Nature Publishing Group, 51(6), pp. 1–13. doi: 10.1038/s12276-019-0235-1.

Leene, W., Duyzings, M. J. M. and van Steeg, C. (1973) 'Lymphoid stem cell identification in the developing thymus and bursa of Fabricius of the chick', *Zeitschrift fur Zellforschung und mikroskopische Anatomie (Vienna, Austria : 1948)*. *Z Zellforsch Mikrosk Anat*, 136(4), pp. 521–533. doi: 10.1007/BF00307368.

Lenz, G. and Staudt, L. M. (2010) 'Aggressive Lymphomas', *New England Journal of Medicine*. doi: 10.1056/nejmra0807082.

Leong, H. S., Chambers, A. F. and Lewis, J. D. (2012) 'Assessing cancer cell migration and metastatic growth in vivo in the chick embryo using fluorescence intravital imaging', *Methods in Molecular Biology*, 872, pp. 1–14. doi: 10.1007/978-1-61779-797-2_1.

Li, G. *et al.* (2013) 'Interleukin-17A promotes rheumatoid arthritis synoviocytes migration and

- invasion under hypoxia by increasing MMP2 and MMP9 expression through NF- κ B/HIF-1 α pathway', *Molecular Immunology*. doi: 10.1016/j.molimm.2012.08.018.
- Li, Huanhuan *et al.* (2019) 'Therapeutic targeting of circ-CUX1/EWSR1/MAZ axis inhibits glycolysis and neuroblastoma progression', *EMBO molecular medicine*. EMBO Mol Med, 11(12). doi: 10.15252/EMMM.201910835.
- Li, S. *et al.* (2021) 'Zebrafish as a neuroblastoma model: Progress made, promise for the future', *Cells*. MDPI, 10(3), pp. 1–18. doi: 10.3390/cells10030580.
- Li, Y. *et al.* (2020) 'Molecular Crosstalk Between MYC and HIF in Cancer', *Frontiers in Cell and Developmental Biology*, 8(November), pp. 1–11. doi: 10.3389/fcell.2020.590576.
- Lim, S. and Kaldis, P. (2013) 'Cdks, cyclins and CKIs: roles beyond cell cycle regulation', *Development (Cambridge, England)*. Development, 140(15), pp. 3079–3093. doi: 10.1242/DEV.091744.
- Van Limpt, V. *et al.* (2004) 'The Phox2B homeobox gene is mutated in sporadic neuroblastomas', *Oncogene*. Oncogene, 23(57), pp. 9280–9288. doi: 10.1038/SJ.ONC.1208157.
- Lin, M. Z. *et al.* (2009) 'Autofluorescent proteins with excitation in the optical window for intravital imaging in mammals', *Chemistry & biology*. Chem Biol, 16(11), pp. 1169–1179. doi: 10.1016/J.CHEMBIOL.2009.10.009.
- Lokman, N. A. *et al.* (2012) 'Chick chorioallantoic membrane (CAM) assay as an in vivo model to study the effect of newly identified molecules on ovarian cancer invasion and metastasis', *International journal of molecular sciences*. Int J Mol Sci, 13(8), pp. 9959–9970. doi: 10.3390/IJMS13089959.
- London, W. B. *et al.* (2005) 'Evidence for an age cutoff greater than 365 days for neuroblastoma risk group stratification in the Children's Oncology Group', *J. Clin. Oncol.*, 23(27), pp. 6459–6465. doi: 10.1200/jco.2005.05.571.
- Lonergan, G. J. *et al.* (2002) 'Neuroblastoma, ganglioneuroblastoma, and ganglioneuroma: radiologic-pathologic correlation', *Radiographics : a review publication of the Radiological Society of North America, Inc.* Radiographics, 22(4), pp. 911–934. doi: 10.1148/RADIOGRAPHICS.22.4.G02JL15911.
- Longo, L. *et al.* (2008) 'PHOX2A and PHOX2B genes are highly co-expressed in human neuroblastoma', *International journal of oncology*. Int J Oncol, 33(5), pp. 985–991. doi: 10.3892/ijo_00000086.
- Louis, C. U. and Shohet, J. M. (2015) 'Neuroblastoma: molecular pathogenesis and therapy.', *Annual review of medicine*, 66(1), pp. 49–63. doi: 10.1146/annurev-med-011514-023121.
- Marais, A. *et al.* (2010) 'Cell cycle-dependent regulation of the forkhead transcription factor FOXK2 by CDK-cyclin complexes', *The Journal of biological chemistry*. J Biol Chem, 285(46), pp. 35728–35739. doi: 10.1074/JBC.M110.154005.
- Maris, J. M. *et al.* (2007) 'Neuroblastoma.', *Lancet (London, England)*, 369(9579), pp. 2106–20. doi: 10.1016/S0140-6736(07)60983-0.
- Masselink, W. *et al.* (2019) 'Broad applicability of a streamlined ethyl cinnamate-based clearing procedure', *Development (Cambridge)*. doi: 10.1242/dev.166884.

- Mather, G. B. (2014) 'The Chick Embryo; A new drug delivery model for neuroblastoma'.
- Mathew, B. *et al.* (2015) 'Robust and automated three-dimensional segmentation of densely packed cell nuclei in different biological specimens with Lines-of-Sight decomposition', *BMC Bioinformatics*. BioMed Central Ltd., 16(1), pp. 1–14. doi: 10.1186/S12859-015-0617-X/FIGURES/9.
- Matthay, K. K. *et al.* (1999) 'Treatment of high-risk neuroblastoma with intensive chemotherapy, radiotherapy, autologous bone marrow transplantation, and 13-cis-retinoic acid. Children's Cancer Group', *The New England journal of medicine*. N Engl J Med, 341(16), pp. 1165–1173. doi: 10.1056/NEJM199910143411601.
- Matthay, K. K. *et al.* (2016) 'Neuroblastoma', *Nature Reviews Disease Primers 2016 2:1*. Nature Publishing Group, 2(1), pp. 1–21. doi: 10.1038/nrdp.2016.78.
- Mattick, J. S. and Makunin, I. V. (2006) 'Non-coding RNA', *Human Molecular Genetics*. Oxford Academic, 15(suppl_1), pp. R17–R29. doi: 10.1093/HMG/DDL046.
- Maxwell, P. H. *et al.* (1999) 'The tumour suppressor protein VHL targets hypoxia-inducible factors for oxygen-dependent proteolysis', *Nature*. Nature, 399(6733), pp. 271–275. doi: 10.1038/20459.
- Mayo, M. W. and Baldwin, A. S. (2000) 'The transcription factor NF- κ B: Control of oncogenesis and cancer therapy resistance', *Biochimica et Biophysica Acta - Reviews on Cancer*. doi: 10.1016/S0304-419X(00)00002-0.
- McGregor, L. M. *et al.* (2005) 'The impact of early resection of primary neuroblastoma on the survival of children older than 1 year of age with stage 4 disease: the St. Jude Children's Research Hospital Experience', *Cancer*. Cancer, 104(12), pp. 2837–2846. doi: 10.1002/CNCR.21566.
- McKinney, M. C. and Kulesa, P. M. (2021) 'Live Imaging of the Neural Crest Cell Epithelial-to-Mesenchymal Transition in the Chick Embryo', *Methods in Molecular Biology*. Humana, New York, NY, 2179, pp. 107–114. doi: 10.1007/978-1-0716-0779-4_10.
- Messal, H. A. *et al.* (2019) 'Tissue curvature and apicobasal mechanical tension imbalance instruct cancer morphogenesis', *Nature*. Nature Publishing Group, 566(7742), pp. 126–130. doi: 10.1038/s41586-019-0891-2.
- Messal, H. A. *et al.* (2021) 'Antigen retrieval and clearing for whole-organ immunofluorescence by FLASH', *Nature protocols*. Nat Protoc, 16(1), pp. 239–262. doi: 10.1038/S41596-020-00414-Z.
- Mestdagh, P. *et al.* (2010) 'An integrative genomics screen uncovers ncRNA T-UCR functions in neuroblastoma tumours', *Oncogene*. Oncogene, 29(24), pp. 3583–3592. doi: 10.1038/ONC.2010.106.
- Meyerson, M., Gabriel, S. and Getz, G. (2010) 'Advances in understanding cancer genomes through second-generation sequencing', *Nature reviews. Genetics*. Nat Rev Genet, 11(10), pp. 685–696. doi: 10.1038/NRG2841.
- Meyerson, M. and Harlow, E. D. (1994) 'Identification of G1 kinase activity for cdk6, a novel cyclin D partner.', *Molecular and Cellular Biology*. American Society for Microbiology (ASM), 14(3), p. 2077. doi: 10.1128/MCB.14.3.2077.

- Michaelis, M. *et al.* (2009) 'Chemoresistance acquisition induces a global shift of expression of angiogenesis-associated genes and increased pro-angiogenic activity in neuroblastoma cells', *Molecular Cancer*. BioMed Central, 8, p. 80. doi: 10.1186/1476-4598-8-80.
- Miettinen, M., Lindenmayer, A. E. and Chaubal, A. (1994) 'Endothelial cell markers CD31, CD34, and BNH9 antibody to H- and Y-antigens--evaluation of their specificity and sensitivity in the diagnosis of vascular tumors and comparison with von Willebrand factor.', *Modern pathology : an official journal of the United States and Canadian Academy of Pathology, Inc.*
- Mlakar, V. *et al.* (2017) '11q deletion in neuroblastoma: A review of biological and clinical implications', *Molecular Cancer*. Molecular Cancer, 16(1), pp. 1–12. doi: 10.1186/s12943-017-0686-8.
- Mole, D. R. *et al.* (2009) 'Genome-wide association of hypoxia-inducible factor (HIF)-1alpha and HIF-2alpha DNA binding with expression profiling of hypoxia-inducible transcripts', *The Journal of biological chemistry*. J Biol Chem, 284(25), pp. 16767–16775. doi: 10.1074/JBC.M901790200.
- Molenaar, J. J. *et al.* (2008) 'Cyclin D1 and CDK4 activity contribute to the undifferentiated phenotype in neuroblastoma', *Cancer Research*, 68(8), pp. 2599–2609. doi: 10.1158/0008-5472.CAN-07-5032.
- Molenaar, J. J., Koster, J., *et al.* (2012) 'Copy number defects of G1-Cell cycle genes in neuroblastoma are frequent and correlate with high expression of E2F target genes and a poor prognosis', *Genes Chromosomes and Cancer*. doi: 10.1002/gcc.20926.
- Molenaar, J. J., Domingo-Fernández, R., *et al.* (2012) 'LIN28B induces neuroblastoma and enhances MYCN levels via let-7 suppression', *Nat. Genet.*, 44(11), pp. 1199–1206. doi: 10.1038/ng.2436.
- Monclair, T. *et al.* (2009a) 'The International Neuroblastoma Risk Group (INRG) staging system: an INRG Task Force report', *J. Clin. Oncol.*, 27(2), pp. 298–303. doi: 10.1200/jco.2008.16.6876.
- Monclair, T. *et al.* (2009b) 'The International Neuroblastoma Risk Group (INRG) staging system: An INRG Task Force report', *Journal of Clinical Oncology*, 27(2), pp. 298–303. doi: 10.1200/JCO.2008.16.6876.
- Moreno, L. *et al.* (2017) 'Accelerating drug development for neuroblastoma - New Drug Development Strategy: an Innovative Therapies for Children with Cancer, European Network for Cancer Research in Children and Adolescents and International Society of Paediatric Oncology Europe Neuroblastoma project', *Expert Opinion on Drug Discovery*, 12(8), pp. 1–11. doi: 10.1080/17460441.2017.1340269.
- Mossé, Y. P. *et al.* (2008) 'Identification of ALK as a major familial neuroblastoma predisposition gene', *Nature*. Nature, 455(7215), pp. 930–935. doi: 10.1038/NATURE07261.
- Movahedi, K. *et al.* (2012) 'Nanobody-based targeting of the macrophage mannose receptor for effective in vivo imaging of tumor-associated macrophages', *Cancer Research*, 72(16), pp. 4165–4177. doi: 10.1158/0008-5472.CAN-11-2994.
- Moy, A. J. *et al.* (2015) 'Optical properties of mouse brain tissue after optical clearing with FocusClear™', *Journal of Biomedical Optics*. Society of Photo-Optical Instrumentation Engineers, 20(9), p. 095010. doi: 10.1117/1.JBO.20.9.095010.
- Mueller, S. and Matthay, K. K. (2009) 'Neuroblastoma: biology and staging.', *Current oncology*

reports, 11(6), pp. 431–8. Available at: <http://www.ncbi.nlm.nih.gov/pubmed/19840520> (Accessed: 4 November 2018).

Mullassery, D., Farrelly, P. and Losty, P. D. (2014) 'Does aggressive surgical resection improve survival in advanced stage 3 and 4 neuroblastoma? A systematic review and meta-analysis', *Pediatric hematology and oncology*. *Pediatr Hematol Oncol*, 31(8), pp. 703–716. doi: 10.3109/08880018.2014.947009.

Müller-Schulte, E., Kurlemann, G. and Harder, A. (2018) 'Tobacco, alcohol and illicit drugs during pregnancy and risk of neuroblastoma: systematic review', *Archives of disease in childhood. Fetal and neonatal edition*. *Arch Dis Child Fetal Neonatal Ed*, 103(5), pp. F467–F473. doi: 10.1136/ARCHDISCHILD-2017-313615.

Murphy, J. B. and Rous, P. (1912) 'THE BEHAVIOR OF CHICKEN SARCOMA IMPLANTED IN THE DEVELOPING EMBRYO', *Journal of Experimental Medicine*. The Rockefeller University Press, 15(2), pp. 119–132. doi: 10.1084/JEM.15.2.119.

Na, X. *et al.* (2003) 'Overproduction of vascular endothelial growth factor related to von Hippel-Lindau tumor suppressor gene mutations and hypoxia-inducible factor-1 α expression in renal cell carcinomas', *Journal of Urology*. Lippincott Williams and Wilkins, 170(2 I), pp. 588–592. doi: 10.1097/01.ju.0000074870.54671.98.

Nakamura, H. and Funahashi, J. (2013) 'Electroporation: past, present and future', *Development, growth & differentiation*. *Dev Growth Differ*, 55(1), pp. 15–19. doi: 10.1111/DGD.12012.

Nakamura, Y. *et al.* (2007) 'Functional characterization of a new p53 mutant generated by homozygous deletion in a neuroblastoma cell line', *Biochemical and Biophysical Research Communications*. doi: 10.1016/j.bbrc.2007.01.057.

Neganova, I. *et al.* (2014) 'CDK1 plays an important role in the maintenance of pluripotency and genomic stability in human pluripotent stem cells', *Cell Death & Disease* 2014 5:11. Nature Publishing Group, 5(11), pp. e1508–e1508. doi: 10.1038/cddis.2014.464.

Negróni, A. *et al.* (1991) 'Decrease of proliferation rate and induction of differentiation by a MYCN antisense DNA oligomer in a human neuroblastoma cell line.', *Cell growth & differentiation: the molecular biology journal of the American Association for Cancer Research*.

Nevins, J. R. (1992) 'E2F: a link between the Rb tumor suppressor protein and viral oncoproteins', *Science (New York, N. Y.)*. *Science*, 258(5081), pp. 424–429. doi: 10.1126/SCIENCE.1411535.

Nevins, J. R. (2001) 'The Rb/E2F pathway and cancer', *Human molecular genetics*. *Hum Mol Genet*, 10(7), pp. 699–703. doi: 10.1093/HMG/10.7.699.

Nguyen, R. *et al.* (2021) 'Next-generation humanized patient-derived xenograft mouse model for pre-clinical antibody studies in neuroblastoma', *Cancer immunology, immunotherapy: CII*. *Cancer Immunol Immunother*, 70(3), pp. 721–732. doi: 10.1007/S00262-020-02713-6.

Nicholson, H. E. *et al.* (2019) 'HIF-independent synthetic lethality between CDK4/6 inhibition and VHL loss across species', *Science Signaling*. doi: 10.1126/scisignal.aay0482.

Nie, L. *et al.* (2022) 'Overexpression of Stathmin 1 Predicts Poor Prognosis and Promotes Cancer Cell Proliferation and Migration in Ovarian Cancer', *Disease Markers*. Hindawi Limited, 2022. doi: 10.1155/2022/3554100.

- Nojima, S. *et al.* (2017) 'CUBIC pathology: Three-dimensional imaging for pathological diagnosis', *Scientific Reports*, 7(1), pp. 1–14. doi: 10.1038/s41598-017-09117-0.
- Noujaim, D. *et al.* (2002) 'N-Myc and Bcl-2 coexpression induces MMP-2 secretion and activation in human neuroblastoma cells', *Oncogene*, 21(29), pp. 4549–4557. doi: 10.1038/SJ.ONC.1205552.
- Nuchtern, J. G. *et al.* (2012) 'A prospective study of expectant observation as primary therapy for neuroblastoma in young infants: A children's oncology group study', *Annals of Surgery*, 256(4), pp. 573–580. doi: 10.1097/SLA.0B013E31826CBBBD.
- Ohta, S. *et al.* (2003) 'Microbubble-enhanced sonoporation: efficient gene transduction technique for chick embryos', *Genesis (New York, N.Y. : 2000)*. *Genesis*, 37(2), pp. 91–101. doi: 10.1002/GENE.10232.
- Olafsen, T. and Wu, A. M. (2010) 'Antibody Vectors for Imaging', *Seminars in Nuclear Medicine*, 40(3), pp. 167–181. doi: 10.1053/J.SEMNUCLMED.2009.12.005.
- Olshan, A. F. *et al.* (2002) 'Maternal vitamin use and reduced risk of neuroblastoma', *Epidemiology (Cambridge, Mass.)*. *Epidemiology*, 13(5), pp. 575–580. doi: 10.1097/00001648-200209000-00014.
- Oreopoulos, J., Berman, R. and Browne, M. (2014) 'Spinning-disk confocal microscopy: present technology and future trends', *Methods in cell biology*. *Methods Cell Biol*, 123, pp. 153–175. doi: 10.1016/B978-0-12-420138-5.00009-4.
- Ortmann, B., Druker, J. and Rocha, S. (2014) 'Cell cycle progression in response to oxygen levels', *Cellular and Molecular Life Sciences*, 71(18), pp. 3569–3582. doi: 10.1007/s00018-014-1645-9.
- Otto, T. *et al.* (2009) 'Stabilization of N-Myc is a critical function of Aurora A in human neuroblastoma', *Cancer cell*. *Cancer Cell*, 15(1), pp. 67–78. doi: 10.1016/J.CCR.2008.12.005.
- Owens, C. and Irwin, M. (2012) 'Neuroblastoma: The impact of biology and cooperation leading to personalized treatments', *Critical Reviews in Clinical Laboratory Sciences*, 49(3), pp. 85–115. doi: 10.3109/10408363.2012.683483.
- Ozer, E. *et al.* (2007) 'Association of MYCN amplification and 1p deletion in neuroblastomas with high tumor vascularity', *Applied immunohistochemistry & molecular morphology : AIMM*. *Appl Immunohistochem Mol Morphol*, 15(2), pp. 181–186. doi: 10.1097/01.PAI.0000210418.38246.58.
- P. Vaupel, A. M. M. H. (2004) 'Tumor hypoxia and malignant progression', *Methods in Enzymology*, 381, pp. 335–354.
- Pan, C. *et al.* (2019) 'Deep Learning Reveals Cancer Metastasis and Therapeutic Antibody Targeting in the Entire Body', *Cell*. *Cell*, 179(7), pp. 1661-1676.e19. doi: 10.1016/J.CELL.2019.11.013.
- Park, J. R. *et al.* (2019) 'Effect of tandem autologous stem cell transplant vs single transplant on event-free survival in patients with high-risk neuroblastoma: a randomized clinical trial', *J Am Med Assoc*, 322, pp. 746–755.
- Patterson, D. M. *et al.* (2011) 'Effect of MDM2 and vascular endothelial growth factor inhibition on tumor angiogenesis and metastasis in neuroblastoma', *Angiogenesis*. doi: 10.1007/s10456-

011-9210-8.

Paul, P. *et al.* (2014) 'Novel action modality of the diterpenoid anisomelic acid causes depletion of E6 and E7 viral oncoproteins in HPV-transformed cervical carcinoma cells', *Biochemical Pharmacology*. Elsevier, 89(2), pp. 171–184. doi: 10.1016/J.BCP.2014.02.011.

Perel, P. *et al.* (2007) 'Comparison of treatment effects between animal experiments and clinical trials: systematic review', *BMJ (Clinical research ed.)*. BMJ, 334(7586), pp. 197–200. doi: 10.1136/BMJ.39048.407928.BE.

Persson, C. U. *et al.* (2020a) 'ARNT-dependent HIF-2 transcriptional activity is not sufficient to regulate downstream target genes in neuroblastoma', *Experimental Cell Research*. doi: 10.1016/j.yexcr.2020.111845.

Persson, C. U. *et al.* (2020b) 'ARNT-dependent HIF-2 transcriptional activity is not sufficient to regulate downstream target genes in neuroblastoma', *Experimental Cell Research*, 388(2). doi: 10.1016/j.yexcr.2020.111845.

Peter, M. *et al.* (1990a) 'Identification of major nucleolar proteins as candidate mitotic substrates of cdc2 kinase', *Cell*. Cell, 60(5), pp. 791–801. doi: 10.1016/0092-8674(90)90093-T.

Peter, M. *et al.* (1990b) 'In vitro disassembly of the nuclear lamina and M phase-specific phosphorylation of lamins by cdc2 kinase', *Cell*. Cell, 61(4), pp. 591–602. doi: 10.1016/0092-8674(90)90471-P.

Petruzzelli, G. J. *et al.* (1993) 'Angiogenesis induced by head and neck squamous cell carcinoma xenografts in the chick embryo chorioallantoic membrane model', *Annals of Otology, Rhinology & Laryngology*, 102(3), pp. 215–221. doi: 10.1177/000348949310200309.

Peuchmaur, M. *et al.* (2003) 'Revision of the International Neuroblastoma Pathology Classification: Confirmation of Favorable and Unfavorable Prognostic Subsets in Ganglioneuroblastoma, Nodular', *Cancer*, 98(10), pp. 2274–2281. doi: 10.1002/CNCR.11773.

Peyressatre, M. *et al.* (2015) 'Targeting cyclin-dependent kinases in human cancers: From small molecules to peptide inhibitors', *Cancers*, 7(1), pp. 179–237. doi: 10.3390/cancers7010179.

Pietras, A. *et al.* (2008) 'High levels of HIF-2 α highlight an immature neural crest-like neuroblastoma cell cohort located in a perivascular niche', *Journal of Pathology*. John Wiley and Sons Ltd, 214(4), pp. 482–488. doi: 10.1002/PATH.2304.

Pietras, A. *et al.* (2009a) 'HIF-2 α maintains an undifferentiated state in neural crest-like human neuroblastoma tumor-initiating cells', *Proceedings of the National Academy of Sciences of the United States of America*, 106(39), pp. 16805–16810. doi: 10.1073/pnas.0904606106.

Pietras, A. *et al.* (2009b) 'HIF-2 α maintains an undifferentiated state in neural crest-like human neuroblastoma tumor-initiating cells', *Proceedings of the National Academy of Sciences of the United States of America*, 106(39), pp. 16805–16810. doi: 10.1073/PNAS.0904606106.

Pinto, M. T. *et al.* (2020) 'The Chick Chorioallantoic Membrane Model: A New In Vivo Tool to Evaluate Breast Cancer Stem Cell Activity', *International Journal of Molecular Sciences 2021, Vol. 22, Page 334*. Multidisciplinary Digital Publishing Institute, 22(1), p. 334. doi: 10.3390/IJMS22010334.

Ponder, K. G. *et al.* (2016) 'Dual inhibition of Mcl-1 by the combination of carfilzomib and TG02 in multiple myeloma'. doi: 10.1080/15384047.2016.1192086.

- Poomthavorn, P. *et al.* (2009) 'Activation of a prometastatic gene expression program in hypoxic neuroblastoma cells', *Endocrine-Related Cancer*. Society for Endocrinology, 16(3), pp. 991–1004. doi: 10.1677/ERC-08-0340.
- Power, R. M. and Huisken, J. (2017) 'A guide to light-sheet fluorescence microscopy for multiscale imaging', *Nat. Methods*. Nature Publishing Group, 14(4), pp. 360–373. doi: 10.1038/nmeth.4224.
- Prevo, R. *et al.* (2018) 'CDK1 inhibition sensitizes normal cells to DNA damage in a cell cycle dependent manner', *Cell cycle (Georgetown, Tex.)*. Cell Cycle, 17(12), pp. 1513–1523. doi: 10.1080/15384101.2018.1491236.
- Puax, A.-L. *et al.* (2011) 'A Comparison of Imaging Techniques to Monitor Tumor Growth and Cancer Progression in Living Animals', *International Journal of Molecular Imaging*. Hindawi Limited, 2011, pp. 1–12. doi: 10.1155/2011/321538.
- Pugh, T. J. *et al.* (2013) 'The genetic landscape of high-risk neuroblastoma', *Nature genetics*. Nat Genet, 45(3), pp. 279–284. doi: 10.1038/NG.2529.
- Qi, Y. *et al.* (2019) 'FDISCO: Advanced solvent-based clearing method for imaging whole organs', *Archivio di Studi Urbani e Regionali*, 48(122), pp. 1–14. doi: 10.1126/sciadv.aau8355.
- Qing, G. *et al.* (2010) 'Combinatorial regulation of neuroblastoma tumor progression by N-Myc and hypoxia inducible factor HIF-1 α ', *Cancer Research*, 70(24), pp. 10351–10361. doi: 10.1158/0008-5472.CAN-10-0740.
- Rader, J. *et al.* (2013) 'Dual CDK4/CDK6 inhibition induces cell-cycle arrest and senescence in neuroblastoma', *Clinical Cancer Research*. doi: 10.1158/1078-0432.CCR-13-1675.
- Raval, R. R. *et al.* (2005) 'Contrasting properties of hypoxia-inducible factor 1 (HIF-1) and HIF-2 in von Hippel-Lindau-associated renal cell carcinoma', *Molecular and cellular biology*. Mol Cell Biol, 25(13), pp. 5675–5686. doi: 10.1128/MCB.25.13.5675-5686.2005.
- Reiff, T. *et al.* (2010) 'Neuroblastoma Phox2b Variants Stimulate Proliferation and Dedifferentiation of Immature Sympathetic Neurons', *The Journal of Neuroscience*. Society for Neuroscience, 30(3), p. 905. doi: 10.1523/JNEUROSCI.5368-09.2010.
- Reiff, T. *et al.* (2011) 'Midkine and Alk signaling in sympathetic neuron proliferation and neuroblastoma predisposition', *Development*. The Company of Biologists, 138(21), pp. 4699–4708. doi: 10.1242/DEV.072157.
- Renier, N. *et al.* (2014) 'iDISCO: a simple, rapid method to immunolabel large tissue samples for volume imaging', *Cell*. Cell, 159(4), pp. 896–910. doi: 10.1016/J.CELL.2014.10.010.
- Ribatti, D. *et al.* (2002) 'In vivo angiogenic activity of neuroblastoma correlates with MYCN oncogene overexpression', *International Journal of Cancer*, 102(4), pp. 351–354. doi: 10.1002/ijc.10742.
- Ribatti, D. (2008) 'Chick embryo chorioallantoic membrane as a useful tool to study angiogenesis', *International review of cell and molecular biology*. Int Rev Cell Mol Biol, 270(C), pp. 181–224. doi: 10.1016/S1937-6448(08)01405-6.
- Ribatti, D. *et al.* (2010) 'Erythropoietin is involved in angiogenesis in human primary melanoma', *International Journal of Experimental Pathology*. Wiley-Blackwell, 91(6), p. 495. doi: 10.1111/J.1365-2613.2010.00731.X.

- Ribatti, D. (2013) 'Anti-angiogenesis in neuroblastoma', *Critical Reviews in Oncology/Hematology*. doi: 10.1016/j.critrevonc.2012.11.004.
- Ribatti, D. (2014a) 'The chick embryo chorioallantoic membrane as a model for tumor biology', *Experimental Cell Research*, 328(2), pp. 314–324. doi: 10.1016/j.yexcr.2014.06.010.
- Ribatti, D. (2014b) 'The chick embryo chorioallantoic membrane as a model for tumor biology', *Experimental Cell Research*. Academic Press Inc., 328(2), pp. 314–324. doi: 10.1016/J.YEXCR.2014.06.010.
- Ribatti, D. (2016) 'The chick embryo chorioallantoic membrane (CAM). A multifaceted experimental model', *Mechanisms of Development*. Elsevier Ltd, 141, pp. 70–77. doi: 10.1016/j.mod.2016.05.003.
- Ribatti, D. and Tamma, R. (2019) 'The chick embryo chorioallantoic membrane as an in vivo experimental model to study multiple myeloma', *Enzymes*. Academic Press, 46, pp. 23–35. doi: 10.1016/BS.ENZ.2019.08.006.
- Richards, R. *et al.* (2016) 'Cell cycle progression in glioblastoma cells is unaffected by pathophysiological levels of hypoxia', *PeerJ*. PeerJ, 4(3). doi: 10.7717/PEERJ.1755.
- Richardson, D. S. and Lichtman, J. W. (2015) 'Clarifying Tissue Clearing', *Cell*, 162(2), pp. 246–257. doi: 10.1016/j.cell.2015.06.067.
- Rihani, A. *et al.* (2015) 'Inhibition of CDK4/6 as a novel therapeutic option for neuroblastoma.', *Cancer cell international*, 15(1), p. 76. doi: 10.1186/s12935-015-0224-y.
- Rios, P. *et al.* (2019) 'Parental smoking, maternal alcohol consumption during pregnancy and the risk of neuroblastoma in children. A pooled analysis of the ESCALE and ESTELLE French studies', *International journal of cancer*. Int J Cancer, 145(11), pp. 2907–2916. doi: 10.1002/IJC.32161.
- Rius, J. *et al.* (2008) 'NF-kappaB links innate immunity to the hypoxic response through transcriptional regulation of HIF-1alpha', *Nature*. Nature, 453(7196), pp. 807–811. doi: 10.1038/NATURE06905.
- Rössler, J. *et al.* (2001a) 'Hypoxia promotes apoptosis of human neuroblastoma cell lines with enhanced N-myc expression', *Biochemical and Biophysical Research Communications*, 281(2), pp. 272–276. doi: 10.1006/bbrc.2001.4342.
- Rössler, J. *et al.* (2001b) 'Hypoxia promotes apoptosis of human neuroblastoma cell lines with enhanced N-myc expression', *Biochemical and Biophysical Research Communications*. doi: 10.1006/bbrc.2001.4342.
- Rovithi, M. *et al.* (2017) 'Development of bioluminescent chick chorioallantoic membrane (CAM) models for primary pancreatic cancer cells: A platform for drug testing', *Scientific Reports*. Nature Publishing Group, 7. doi: 10.1038/SREP44686.
- Royds, J. A. *et al.* (1998) 'Response of tumour cells to hypoxia: role of p53 and NFkB', *Molecular pathology: MP*. Mol Pathol, 51(2), pp. 55–61. doi: 10.1136/MP.51.2.55.
- Ruf, M., Moch, H. and Schraml, P. (2016) 'PD-L1 expression is regulated by hypoxia inducible factor in clear cell renal cell carcinoma', *International journal of cancer*. Int J Cancer, 139(2), pp. 396–403. doi: 10.1002/IJC.30077.

- Sabdyusheva Litschauer, I. *et al.* (2020) '3D histopathology of human tumours by fast clearing and ultramicroscopy', *Scientific Reports*. Nature Publishing Group UK, 10(1), pp. 1–16. doi: 10.1038/s41598-020-71737-w.
- Sadasivam, S., Duan, S. and DeCaprio, J. A. (2012) 'The MuvB complex sequentially recruits B-Myb and FoxM1 to promote mitotic gene expression', *Genes & development*. Genes Dev, 26(5), pp. 474–489. doi: 10.1101/GAD.181933.111.
- Sanmamed, M. F. *et al.* (2016) 'Defining the optimal murine models to investigate immune checkpoint blockers and their combination with other immunotherapies', *Annals of oncology : official journal of the European Society for Medical Oncology*. Ann Oncol, 27(7), pp. 1190–1198. doi: 10.1093/ANNONC/MDW041.
- Santamaría, D. *et al.* (2007) 'Cdk1 is sufficient to drive the mammalian cell cycle', *Nature*. doi: 10.1038/nature06046.
- Sapra, P. *et al.* (2013) 'Long-term tumor regression induced by an antibody-drug conjugate that targets 5T4, an oncofetal antigen expressed on tumor-initiating cells', *Molecular cancer therapeutics*. Mol Cancer Ther, 12(1), pp. 38–47. doi: 10.1158/1535-7163.MCT-12-0603.
- Sarkar, S. and Schmued, L. (2012) 'In vivo administration of fluorescent dextrans for the specific and sensitive localization of brain vascular pericytes and their characterization in normal and neurotoxin exposed brains', *Neurotoxicology*. Neurotoxicology, 33(3), pp. 436–443. doi: 10.1016/J.NEURO.2012.04.004.
- Sawada, T. *et al.* (2009) 'Mass Screening for Neuroblastoma in Japan', <http://dx.doi.org/10.3109/08880019109033437>. Taylor & Francis, 8(2), pp. 93–109. doi: 10.3109/08880019109033437.
- Saxena, K., Jolly, M. K. and Balamurugan, K. (2020) 'Hypoxia, partial EMT and collective migration: Emerging culprits in metastasis', *Translational Oncology*. doi: 10.1016/j.tranon.2020.100845.
- Scardigli, M. *et al.* (2021) 'Comparison of Different Tissue Clearing Methods for Three-Dimensional Reconstruction of Human Brain Cellular Anatomy Using Advanced Imaging Techniques', *Frontiers in Neuroanatomy*. Frontiers Media S.A., 15. doi: 10.3389/FNANA.2021.752234/FULL.
- Schettini, F. *et al.* (2018) 'CDK 4/6 inhibitors as single agent in advanced solid tumors', *Frontiers in Oncology*. Frontiers Media S.A., 8, p. 608. doi: 10.3389/FONC.2018.00608/BIBTEX.
- Schmittgen, T. D. and Livak, K. J. (2008) 'Analyzing real-time PCR data by the comparative CT method', *Nature Protocols* 2008 3:6. Nature Publishing Group, 3(6), pp. 1101–1108. doi: 10.1038/nprot.2008.73.
- Schneider, C. *et al.* (1999) 'Bone morphogenetic proteins are required in vivo for the generation of sympathetic neurons', *Neuron*. Neuron, 24(4), pp. 861–870. doi: 10.1016/S0896-6273(00)81033-8.
- Schnepp, R. W. *et al.* (2015) 'A LIN28B–RAN–AURKA signaling network promotes neuroblastoma tumorigenesis', *Cancer Cell*. Cell Press, 28(5), pp. 599–609. doi: 10.1016/j.ccell.2015.09.012.
- Schöning, J. P., Monteiro, M. and Gu, W. (2017) 'Drug resistance and cancer stem cells: the shared but distinct roles of hypoxia-inducible factors HIF1 α and HIF2 α ', *Clinical and*

experimental pharmacology & physiology. Clin Exp Pharmacol Physiol, 44(2), pp. 153–161. doi: 10.1111/1440-1681.12693.

Schulte, J. H. *et al.* (2013) 'MYCN and ALKF1174L are sufficient to drive neuroblastoma development from neural crest progenitor cells', *Oncogene*. Oncogene, 32(8), pp. 1059–1065. doi: 10.1038/ONC.2012.106.

Schweigerer, L. *et al.* (1990) 'Augmented MYCN Expression Advances the Malignant Phenotype of Human Neuroblastoma Cells: Evidence for Induction of Autocrine Growth Factor Activity', *Cancer Research*.

Schwermer, M. *et al.* (2015) 'Sensitivity to cdk1-inhibition is modulated by p53 status in preclinical models of embryonal tumors', *Oncotarget*, 6(17), pp. 15425–15435. doi: 10.18632/oncotarget.3908.

Scott Campbell, W. *et al.* (2012) 'Concordance between whole-slide imaging and light microscopy for routine surgical pathology', *Human pathology*. Hum Pathol, 43(10), pp. 1739–1744. doi: 10.1016/J.HUMPATH.2011.12.023.

Scully, D. *et al.* (2016) 'Hypoxia promotes production of neural crest cells in the embryonic head', *Development (Cambridge)*, 143(10), pp. 1742–1752. doi: 10.1242/dev.131912.

Seitz, G. *et al.* (2012) 'Animal models of extracranial pediatric solid tumors (Review)', *Oncology Letters*. Spandidos Publications, 4(5), pp. 859–864. doi: 10.3892/OL.2012.852/HTML.

Semenza, G. L. (2003) 'Targeting HIF-1 for cancer therapy', *Nature reviews. Cancer*. Nat Rev Cancer, 3(10), pp. 721–732. doi: 10.1038/NRC1187.

Semenza, G. L. (2013) 'HIF-1 mediates metabolic responses to intratumoral hypoxia and oncogenic mutations', *The Journal of clinical investigation*. J Clin Invest, 123(9), pp. 3664–3671. doi: 10.1172/JCI67230.

Semenza, G. L. and Wang, G. L. (1992) 'A nuclear factor induced by hypoxia via de novo protein synthesis binds to the human erythropoietin gene enhancer at a site required for transcriptional activation.', *Molecular and Cellular Biology*. American Society for Microbiology (ASM), 12(12), p. 5447. doi: 10.1128/MCB.12.12.5447.

Sharma, B., Chang, A. and Red-Horse, K. (2017) 'Coronary Artery Development: Progenitor Cells and Differentiation Pathways', *Annual review of physiology*. Annu Rev Physiol, 79, pp. 1–19. doi: 10.1146/ANNUREV-PHYSIOL-022516-033953.

Sharp, S. E. *et al.* (2009) '123I-MIBG scintigraphy and 18F-FDG PET in neuroblastoma', *J. Nucl. Med.*, 50(8), pp. 1237–1243. doi: 10.2967/jnumed.108.060467.

Shearer, T. *et al.* (2016) 'Three-dimensional visualisation of soft biological structures by X-ray computed micro-tomography', *Journal of Cell Science*, 129(13), pp. 2483–2492. doi: 10.1242/jcs.179077.

Sherr, C. J. and Roberts, J. M. (1999) 'CDK inhibitors: positive and negative regulators of G1-phase progression', *Genes & development*. Genes Dev, 13(12), pp. 1501–1512. doi: 10.1101/GAD.13.12.1501.

Shimada, H. *et al.* (1984) 'Histopathologic prognostic factors in neuroblastic tumors: definition of subtypes of ganglioneuroblastoma and an age-linked classification of neuroblastomas', *J. Natl Cancer Inst.*, 73(2), pp. 405–416. doi: 10.1093/jnci/73.2.405.

Shimozawa, T. *et al.* (2013) 'Improving spinning disk confocal microscopy by preventing pinhole cross-talk for intravital imaging', *Proceedings of the National Academy of Sciences of the United States of America*. Proc Natl Acad Sci U S A, 110(9), pp. 3399–3404. doi: 10.1073/PNAS.1216696110/-/DCSUPPLEMENTAL/SM06.MOV.

Shioda, T. *et al.* (1997) 'Early events of metastasis in the microcirculation involve changes in gene expression of cancer cells. Tracking mRNA levels of metastasizing cancer cells in the chick embryo chorioallantoic membrane.', *The American Journal of Pathology*. American Society for Investigative Pathology, 150(6), p. 2099. Available at: /pmc/articles/PMC1858325/?report=abstract (Accessed: 17 May 2022).

Simon, M. C. and Keith, B. (2008) 'The role of oxygen availability in embryonic development and stem cell function', *Nature reviews. Molecular cell biology*. Nat Rev Mol Cell Biol, 9(4), pp. 285–296. doi: 10.1038/NRM2354.

Simon, T. *et al.* (2013) 'Role of surgery in the treatment of patients with stage 4 neuroblastoma age 18 months or older at diagnosis', *Journal of clinical oncology : official journal of the American Society of Clinical Oncology*. J Clin Oncol, 31(6), pp. 752–758. doi: 10.1200/JCO.2012.45.9339.

Sjostrom, S. K. *et al.* (2005) 'The Cdk1 complex plays a prime role in regulating N-myc phosphorylation and turnover in neural precursors', *Developmental Cell*. doi: 10.1016/j.devcel.2005.07.014.

Slack, A. *et al.* (2005) 'The p53 regulatory gene MDM2 is a direct transcriptional target of MYCN in neuroblastoma', *Proceedings of the National Academy of Sciences of the United States of America*. National Academy of Sciences, 102(3), p. 731. doi: 10.1073/PNAS.0405495102.

Song, L. *et al.* (2007) 'Oncogene MYCN regulates localization of NKT cells to the site of disease in neuroblastoma', *The Journal of clinical investigation*. J Clin Invest, 117(9), pp. 2702–2712. doi: 10.1172/JCI30751.

Soni, S. and Padwad, Y. S. (2017) 'HIF-1 in cancer therapy: two decade long story of a transcription factor', *Acta oncologica (Stockholm, Sweden)*. Acta Oncol, 56(4), pp. 503–515. doi: 10.1080/0284186X.2017.1301680.

Spalteholz, W. (1914) *Über das Durchsichtigmachen von menschlichen und tierischen Präparaten und seine theoretischen Bedingungen, nebst Anhang: Über Knochenfärbung*. 2., erw. Aufl. Leipzig: S. Hirzel.

Speeckaert, R. *et al.* (2011) 'Immune reactions in benign and malignant melanocytic lesions: lessons for immunotherapy', *Pigment cell & melanoma research*. Pigment Cell Melanoma Res, 24(2), pp. 334–344. doi: 10.1111/J.1755-148X.2010.00799.X.

Von Stedingk, K., Gisselsson, D. and Bexell, D. (2019) 'Multidimensional intratumour heterogeneity in neuroblastoma', *Oncotarget*. doi: 10.18632/oncotarget.26524.

Stehelin, D. *et al.* (1976) 'DNA related to the transforming gene(s) of avian sarcoma viruses is present in normal avian DNA', *Nature* 1976 260:5547. Nature Publishing Group, 260(5547), pp. 170–173. doi: 10.1038/260170a0.

Steliarova-Foucher, E. *et al.* (2005) 'International Classification of Childhood Cancer, third edition', *Cancer*. Cancer, 103(7), pp. 1457–1467. doi: 10.1002/CNCR.20910.

Steliarova-Foucher, E. *et al.* (2017) 'International incidence of childhood cancer, 2001–10: a

population-based registry study', *The Lancet Oncology*. Lancet Publishing Group, 18(6), pp. 719–731. doi: 10.1016/S1470-2045(17)30186-9/ATTACHMENT/D5279E92-7174-4FDA-9099-C998E708047B/MMC1.PDF.

Stewart, E. *et al.* (2015) 'Development and characterization of a human orthotopic neuroblastoma xenograft', *Developmental biology*. Dev Biol, 407(2), pp. 344–355. doi: 10.1016/J.YDBIO.2015.02.002.

Stillier, C. (2007) *Childhood cancer in Britain : incidence, survival, mortality*. Oxford University Press.

Stock, K. *et al.* (2016) 'Capturing tumor complexity in vitro: Comparative analysis of 2D and 3D tumor models for drug discovery', *Scientific reports*. Sci Rep, 6. doi: 10.1038/SREP28951.

Stovroff, M., Dykes, F. and Teague, W. G. (1995) 'The complete spectrum of neurocristopathy in an infant with congenital hypoventilation, Hirschsprung's disease, and neuroblastoma', *Journal of pediatric surgery*. J Pediatr Surg, 30(8), pp. 1218–1221. doi: 10.1016/0022-3468(95)90027-6.

Strenger, V. *et al.* (2007) 'Diagnostic and prognostic impact of urinary catecholamines in neuroblastoma patients', *Pediatr. Blood Cancer*, 48(5), pp. 504–509. doi: 10.1002/pbc.20888.

Strese, S. *et al.* (2013) 'Effects of hypoxia on human cancer cell line chemosensitivity', *BMC Cancer*. doi: 10.1186/1471-2407-13-331.

Strother, D. R. *et al.* (2012) 'Outcome after surgery alone or with restricted use of chemotherapy for patients with low-risk neuroblastoma: results of Children's Oncology Group study P9641', *J. Clin. Oncol.*, 30(15), pp. 1842–1848. doi: 10.1200/jco.2011.37.9990.

Sugiura, Y. *et al.* (1998) 'Matrix metalloproteinases-2 and -9 are expressed in human neuroblastoma: Contribution of stromal cells to their production and correlation with metastasis', *Cancer Research*, 58(10), pp. 2209–2216.

Sun, D. *et al.* (2020) 'Click-ExM enables expansion microscopy for all biomolecules', *Nature Methods* 2020 18:1. Nature Publishing Group, 18(1), pp. 107–113. doi: 10.1038/s41592-020-01005-2.

Sung, P. J. *et al.* (2013) 'Identification and characterisation of STMN4 and ROBO2 gene involvement in neuroblastoma cell differentiation', *Cancer Letters*. Elsevier Ireland Ltd, 328(1), pp. 168–175. doi: 10.1016/j.canlet.2012.08.015.

Susaki, E. A. *et al.* (2014a) 'Whole-brain imaging with single-cell resolution using chemical cocktails and computational analysis', *Cell*. doi: 10.1016/j.cell.2014.03.042.

Susaki, E. A. *et al.* (2014b) 'Whole-brain imaging with single-cell resolution using chemical cocktails and computational analysis', *Cell*. Elsevier Inc., 157(3), pp. 726–739. doi: 10.1016/j.cell.2014.03.042.

Susaki, E. A. *et al.* (2015) 'Advanced CUBIC protocols for whole-brain and whole-body clearing and imaging.', *Nature protocols*, 10(11), pp. 1709–27. doi: 10.1038/nprot.2015.085.

Susaki, E. A. and Ueda, H. R. (2016) 'Whole-body and whole-organ clearing and imaging techniques with single-cell resolution: toward organism-level systems biology in mammals', *Cell Chem. Biol*. Elsevier Ltd, 23(1), pp. 137–157. doi: 10.1016/j.chembiol.2015.11.009.

- Swadi, R. (2018) 'Characterisation of Potential Therapeutic Molecules for Neuroblastoma Using Chick Chorioallantoic Membrane Xenograft Model', (July).
- Swadi, R., Pizer, B. L., *et al.* (2018) 'Optimising the chick chorioallantoic membrane xenograft model of neuroblastoma for drug delivery.', *BMC cancer*, 18(1), p. 28. doi: 10.1186/s12885-017-3978-x.
- Swadi, R., Mather, G., *et al.* (2018) 'Optimising the chick chorioallantoic membrane xenograft model of neuroblastoma for drug delivery', *BMC Cancer*. BioMed Central Ltd., 18(1). doi: 10.1186/s12885-017-3978-x.
- Swadi, R. R. *et al.* (2019) 'CDK inhibitors reduce cell proliferation and reverse hypoxia-induced metastasis of neuroblastoma tumours in a chick embryo model', *Scientific Reports* 2019 9:1. Nature Publishing Group, 9(1), pp. 1–15. doi: 10.1038/s41598-019-45571-8.
- Swann, J. B. and Smyth, M. J. (2007) 'Immune surveillance of tumors', *The Journal of clinical investigation*. J Clin Invest, 117(5), pp. 1137–1146. doi: 10.1172/JCI31405.
- Swarbrick, A. *et al.* (2010) 'miR-380-5p represses p53 to control cellular survival and is associated with poor outcome in MYCN-amplified neuroblastoma', *Nature medicine*. Nat Med, 16(10), pp. 1134–1140. doi: 10.1038/NM.2227.
- Sys, G. M. L. *et al.* (2013) 'The in ovo CAM-assay as a xenograft model for sarcoma', *Journal of visualized experiments : JoVE*. J Vis Exp, (77). doi: 10.3791/50522.
- T. Y. Reynolds, S. R. P. M. G. (1996) 'Genetic instability induced by the tumor microenvironment', *Cancer Research*, 56, pp. 5754–5757.
- Tafari, M. *et al.* (2013) 'Modulators of HIF1 α and NF κ B in Cancer Treatment: Is it a Rational Approach for Controlling Malignant Progression?', *Frontiers in Pharmacology*. Frontiers Media SA, 4. doi: 10.3389/FPHAR.2013.00013.
- Tainaka, K. *et al.* (2014) 'Whole-body imaging with single-cell resolution by tissue decolorization', *Cell*. Cell, 159(4), pp. 911–924. doi: 10.1016/J.CELL.2014.10.034.
- Taizi, M. *et al.* (2006a) 'A novel and rapid in vivo system for testing therapeutics on human leukemias', *Experimental Hematology*, 34(12), pp. 1698–1708. doi: 10.1016/J.EXPHEM.2006.07.005.
- Taizi, M. *et al.* (2006b) 'A novel and rapid in vivo system for testing therapeutics on human leukemias', *Experimental hematology*. Exp Hematol, 34(12), pp. 1698–1708. doi: 10.1016/J.EXPHEM.2006.07.005.
- Tanaka, N. *et al.* (2017) 'Whole-tissue biopsy phenotyping of three-dimensional tumours reveals patterns of cancer heterogeneity', *Nat. Biomed. Eng.* Nature Publishing Group, 1(10), pp. 796–806. doi: 10.1038/s41551-017-0139-0.
- Tanaka, N. and Fukuzawa, M. (2008) 'MYCN downregulates integrin α 1 to promote invasion of human neuroblastoma cells', *International Journal of Oncology*, 33(4), pp. 815–821. doi: 10.3892/IJO_00000069/DOWNLOAD.
- Taneyhill, L. A. (2008) 'To adhere or not to adhere: The role of Cadherins in neural crest development', *Cell Adhesion & Migration*. Taylor & Francis, 2(4), p. 223. doi: 10.4161/CAM.2.4.6835.

- Tang, D. G. and Honn, K. V. (1994) 'Adhesion molecules and tumor metastasis: An update', *Invasion and Metastasis*.
- Tannock, I. F. (1998) 'Conventional cancer therapy: promise broken or promise delayed?', *Lancet (London, England)*. *Lancet*, 351 Suppl 2(SUPPL.2). doi: 10.1016/S0140-6736(98)90327-0.
- Tay, S. L. M., Heng, P. W. S. and Chan, L. W. (2011) 'An investigation of the chick chorioallantoic membrane as an alternative model to various biological tissues for permeation studies', *The Journal of pharmacy and pharmacology*. *J Pharm Pharmacol*, 63(10), pp. 1283–1289. doi: 10.1111/J.2042-7158.2011.01338.X.
- Teicher, B. A. (1994) 'Hypoxia and drug resistance', *Cancer metastasis reviews*. *Cancer Metastasis Rev*, 13(2), pp. 139–168. doi: 10.1007/BF00689633.
- Teitz, T. *et al.* (2011) 'Preclinical Models for Neuroblastoma: Establishing a Baseline for Treatment', *PLOS ONE*. Public Library of Science, 6(4), p. e19133. doi: 10.1371/JOURNAL.PONE.0019133.
- Teitz, T. *et al.* (2013) 'Th-MYCN mice with caspase-8 deficiency develop advanced neuroblastoma with bone marrow metastasis', *Cancer Research*, 73(13), pp. 4086–4097. doi: 10.1158/0008-5472.CAN-12-2681.
- Theveneau, E. and Mayor, R. (2012) 'Neural crest delamination and migration: from epithelium-to-mesenchyme transition to collective cell migration', *Developmental biology*. *Dev Biol*, 366(1), pp. 34–54. doi: 10.1016/J.YDBIO.2011.12.041.
- Thiele, C. J. (1998) *Neuroblastoma Cell Lines*, In (Ed.) *Masters, J. Human Cell Culture*. Kluwer Academic Publishers. Available at: https://ccr.cancer.gov/sites/default/files/neuroblastoma_cell_lines_-_molecular_features.pdf (Accessed: 4 November 2018).
- Tian, T., Yang, Z. and Li, X. (2021) 'Tissue clearing technique: Recent progress and biomedical applications', *Journal of Anatomy*, 238(2), pp. 489–507. doi: 10.1111/joa.13309.
- Timmerman, R. (2003) 'Raccoon Eyes and Neuroblastoma', *New England Journal of Medicine*. *New England Journal of Medicine (NEJM/MMS)*, 349(4), p. e4. doi: 10.1056/ENEJMICM020675.
- Todorov, M. I. *et al.* (2020) 'Machine learning analysis of whole mouse brain vasculature', *Nature Methods* 2020 17:4. Nature Publishing Group, 17(4), pp. 442–449. doi: 10.1038/s41592-020-0792-1.
- Tolbert, V. P. *et al.* (2017) 'Genetic susceptibility to neuroblastoma', *Current opinion in genetics & development*. *Curr Opin Genet Dev*, 42, pp. 81–90. doi: 10.1016/J.GDE.2017.03.008.
- Tomer, R. *et al.* (2014) 'Advanced CLARITY for rapid and high-resolution imaging of intact tissues', *Nature Protocols*, 9(7), pp. 1682–1697. doi: 10.1038/nprot.2014.123.
- Tomlinson, C. W. E. *et al.* (2018) 'Novel Fluorescence Competition Assay for Retinoic Acid Binding Proteins', *ACS Medicinal Chemistry Letters*. American Chemical Society, 9(12), pp. 1297–1300. doi: 10.1021/ACSMEDCHEMLETT.8B00420.
- Tomlinson, I. P. M., Novelli, M. R. and Bodmer, W. F. (1996) 'The mutation rate and cancer', *Proceedings of the National Academy of Sciences of the United States of America*. National

- Academy of Sciences, 93(25), pp. 14800–14803. doi: 10.1073/PNAS.93.25.14800/ASSET/0C1D29BD-C1BC-45CE-9157-DA5464C7D954/ASSETS/GRAPHIC/PQ2462716003.JPEG.
- Tran Thi Nhu, H. *et al.* (2017) 'A novel toolbox to investigate tissue spatial organization applied to the study of the islets of Langerhans', *Scientific reports*. Sci Rep, 7. doi: 10.1038/SREP44261.
- Tsai, P. S. *et al.* (2009) 'Correlations of Neuronal and Microvascular Densities in Murine Cortex Revealed by Direct Counting and Colocalization of Nuclei and Vessels', *Journal of Neuroscience*. Society for Neuroscience, 29(46), pp. 14553–14570. doi: 10.1523/JNEUROSCI.3287-09.2009.
- Vargas, A. *et al.* (2007a) 'The chick embryo and its chorioallantoic membrane (CAM) for the in vivo evaluation of drug delivery systems', *Advanced Drug Delivery Reviews*, 59(11), pp. 1162–1176. doi: 10.1016/j.addr.2007.04.019.
- Vargas, A. *et al.* (2007b) 'The chick embryo and its chorioallantoic membrane (CAM) for the in vivo evaluation of drug delivery systems', *Advanced drug delivery reviews*. Adv Drug Deliv Rev, 59(11), pp. 1162–1176. doi: 10.1016/J.ADDR.2007.04.019.
- Vassal, G. *et al.* (2014) 'Challenges for children and adolescents with cancer in Europe: The SIOP-Europe agenda', *Pediatric Blood and Cancer*. John Wiley and Sons Inc., 61(9), pp. 1551–1557. doi: 10.1002/PBC.25044.
- Vaupel, P., Kallinowski, F. and Okunieff, P. (1990) 'Blood flow, oxygen consumption and tissue oxygenation of human tumors', *Advances in Experimental Medicine and Biology*, 277, pp. 895–905. doi: 10.1007/978-1-4684-8181-5_103.
- Vega, F. M. *et al.* (2020a) 'Hypoxia in the initiation and progression of neuroblastoma tumours', *International Journal of Molecular Sciences*, 21(1). doi: 10.3390/ijms21010039.
- Vega, F. M. *et al.* (2020b) 'Hypoxia in the initiation and progression of neuroblastoma tumours', *International Journal of Molecular Sciences*. doi: 10.3390/ijms21010039.
- Vermeulen, K., Van Bockstaele, D. R. and Berneman, Z. N. (2003) 'The cell cycle: a review of regulation, deregulation and therapeutic targets in cancer', *Cell Proliferation*. John Wiley & Sons, Ltd, 36(3), pp. 131–149. doi: 10.1046/J.1365-2184.2003.00266.X.
- Verveer, P. J. *et al.* (2007) 'High-resolution three-dimensional imaging of large specimens with light sheet-based microscopy', *Nature Methods*, 4(4), pp. 311–313. doi: 10.1038/nmeth1017.
- Victorelli, F. D. *et al.* (2020) 'Chick embryo chorioallantoic membrane as a suitable in vivo model to evaluate drug delivery systems for cancer treatment: A review', *European Journal of Pharmaceutics and Biopharmaceutics*, 153(June), pp. 273–284. doi: 10.1016/j.ejpb.2020.06.010.
- Vogelstein, B. *et al.* (2013) 'Cancer genome landscapes', *Science (New York, N.Y.)*. Science, 339(6127), pp. 1546–1558. doi: 10.1126/SCIENCE.1235122.
- Volland, S. *et al.* (2009) 'Stanniocalcin 2 promotes invasion and is associated with metastatic stages in neuroblastoma', *International Journal of Cancer*. John Wiley & Sons, Ltd, 125(9), pp. 2049–2057. doi: 10.1002/IJC.24564.
- Wagner, L. M. and Adams, V. R. (2017) 'Targeting the PD-1 pathway in pediatric solid tumors

and brain tumors', *OncoTargets and therapy*. Dove Press, 10, p. 2097. doi: 10.2147/OTT.S124008.

Wallace, E. M. *et al.* (2016a) 'A small-molecule antagonist of HIF2 α is efficacious in preclinical models of renal cell carcinoma', *Cancer Research*. doi: 10.1158/0008-5472.CAN-16-0473.

Wallace, E. M. *et al.* (2016b) 'A Small-Molecule Antagonist of HIF2 α Is Efficacious in Preclinical Models of Renal Cell Carcinoma', *Cancer research*. *Cancer Res*, 76(18), pp. 5491–5500. doi: 10.1158/0008-5472.CAN-16-0473.

Wang, H., Khoradmehr, A. and Tamadon, A. D. V. M. (2019) 'FACT or PACT: A Comparison between Free-Acrylamide and Acrylamide-Based Passive Sodium Dodecyl Sulfate Tissue Clearing for whole Tissue Imaging', *Cell journal*. *Cell J*, 21(2), pp. 103–114. doi: 10.22074/CELLJ.2019.5989.

Wang, S., Akhtar, J. and Wang, Z. (2015) 'Anti-STMN1 therapy improves sensitivity to antimicrotubule drugs in esophageal squamous cell carcinoma', *Tumour biology: the journal of the International Society for Oncodevelopmental Biology and Medicine*. *Tumour Biol*, 36(10), pp. 7797–7806. doi: 10.1007/S13277-015-3520-1.

Wang, Y. *et al.* (2016) 'High-yield synthesis of bioactive ethyl cinnamate by enzymatic esterification of cinnamic acid', *Food Chemistry*. doi: 10.1016/j.foodchem.2015.06.017.

Wang, Y. *et al.* (2017) 'Annexin A2 could enhance multidrug resistance by regulating NF- κ B signaling pathway in pediatric neuroblastoma', *Journal of Experimental and Clinical Cancer Research*. doi: 10.1186/s13046-017-0581-6.

Wang, Z. *et al.* (2011) 'FoxM1 in tumorigenicity of the neuroblastoma cells and renewal of the neural progenitors', *Cancer Research*. doi: 10.1158/0008-5472.CAN-10-4087.

Warfel, N. A. *et al.* (2013) 'CDK1 stabilizes HIF-1 α via direct phosphorylation of Ser668 to promote tumor growth', *Cell Cycle*, 12(23), pp. 3689–3701. doi: 10.4161/cc.26930.

Warnock, G. *et al.* (2013) 'In vivo PET/CT in a human glioblastoma chicken chorioallantoic membrane model: a new tool for oncology and radiotracer development', *Journal of nuclear medicine: official publication, Society of Nuclear Medicine*. *J Nucl Med*, 54(10), pp. 1782–1788. doi: 10.2967/JNUMED.112.117150.

Waterston, R. H. *et al.* (2002) 'Initial sequencing and comparative analysis of the mouse genome', *Nature* 2003 420:6915. Nature Publishing Group, 420(6915), pp. 520–562. doi: 10.1038/nature01262.

Weber, M. and Huisken, J. (2011) 'Light sheet microscopy for real-time developmental biology', *Current Opinion in Genetics & Development*. Elsevier Current Trends, 21(5), pp. 566–572. doi: 10.1016/J.GDE.2011.09.009.

Weiss, W. A. *et al.* (1997) 'Targeted expression of MYCN causes neuroblastoma in transgenic mice.', *The EMBO Journal*. European Molecular Biology Organization, 16(11), p. 2985. doi: 10.1093/EMBOJ/16.11.2985.

Westerlund, I. *et al.* (2017a) 'Combined epigenetic and differentiation-based treatment inhibits neuroblastoma tumor growth and links HIF2 α to tumor suppression', *Proceedings of the National Academy of Sciences of the United States of America*, 114(30), pp. E6137–E6146. doi: 10.1073/pnas.1700655114.

- Westerlund, I. *et al.* (2017b) 'Combined epigenetic and differentiation-based treatment inhibits neuroblastoma tumor growth and links HIF2 α to tumor suppression', *Proceedings of the National Academy of Sciences of the United States of America*. doi: 10.1073/pnas.1700655114.
- Westerlund, I., Shi, Y. and Holmberg, J. (2019) 'EPAS1/HIF2 α correlates with features of low-risk neuroblastoma and with adrenal chromaffin cell differentiation during sympathoadrenal development', *Biochemical and Biophysical Research Communications*. Elsevier B.V., 508(4), pp. 1233–1239. doi: 10.1016/J.BBRC.2018.12.076.
- Whittaker, S. R. *et al.* (2017) 'Inhibitors of cyclin-dependent kinases as cancer therapeutics', *Pharmacology and Therapeutics*. doi: 10.1016/j.pharmthera.2017.02.008.
- Wierstra, I. and Alves, J. (2006) 'Transcription factor FOXM1c is repressed by RB and activated by cyclin D1/Cdk4', in *Biological Chemistry*. doi: 10.1515/BC.2006.119.
- Williams, B. J. *et al.* (2018) 'Digital pathology for the primary diagnosis of breast histopathological specimens: an innovative validation and concordance study on digital pathology validation and training', *Histopathology*. John Wiley & Sons, Ltd, 72(4), pp. 662–671. doi: 10.1111/HIS.13403.
- Winkler, J. *et al.* (2020) 'Concepts of extracellular matrix remodelling in tumour progression and metastasis', *Nature Communications*. Springer US, 11(1), pp. 1–19. doi: 10.1038/s41467-020-18794-x.
- Wood, A. C. *et al.* (2017) 'Dual ALK and CDK4/6 Inhibition Demonstrates Synergy against Neuroblastoma', *Clinical cancer research : an official journal of the American Association for Cancer Research*. Clin Cancer Res, 23(11), pp. 2856–2868. doi: 10.1158/1078-0432.CCR-16-1114.
- Xue, G. *et al.* (2015) 'c-Myc-mediated repression of miR-15-16 in hypoxia is induced by increased HIF-2 α and promotes tumor angiogenesis and metastasis by upregulating FGF2', *Oncogene*. Oncogene, 34(11), pp. 1393–1406. doi: 10.1038/ONC.2014.82.
- Yalcin, H. C. *et al.* (2010) 'An ex-ovo Chicken Embryo Culture System Suitable for Imaging and Microsurgery Applications', *Journal of Visualized Experiments : JoVE*. MyJoVE Corporation, (44), p. 44. doi: 10.3791/2154.
- Yang, B. *et al.* (2014) 'Single-cell phenotyping within transparent intact tissue through whole-body clearing', *Cell*. Elsevier B.V., 158(4), pp. 945–958. doi: 10.1016/J.CELL.2014.07.017.
- Yanik, G. A. *et al.* (2013) 'Semiquantitative mIBG scoring as a prognostic indicator in patients with stage 4 neuroblastoma: a report from the Children's Oncology Group', *J. Nucl. Med.*, 54(4), pp. 541–548. doi: 10.2967/jnumed.112.112334.
- Yeung, P. *et al.* (2015) 'Microencapsulation of Neuroblastoma Cells and Mesenchymal Stromal Cells in Collagen Microspheres: A 3D Model for Cancer Cell Niche Study', *PLOS ONE*. Public Library of Science, 10(12), p. e0144139. doi: 10.1371/JOURNAL.PONE.0144139.
- Yin, C. P. *et al.* (2015) 'Upregulation of HIF-1 α protects neuroblastoma cells from hypoxia-induced apoptosis in a RhoA-dependent manner', *Molecular medicine reports*. Mol Med Rep, 12(5), pp. 7123–7131. doi: 10.3892/MMR.2015.4267.
- Yin, W. *et al.* (2013) 'The migration of neural progenitor cell mediated by SDF-1 is NF- κ B/HIF-1 α dependent upon hypoxia', *CNS Neuroscience and Therapeutics*. doi: 10.1111/cns.12049.

- Young, M. R. *et al.* (2009) 'Monitoring of Tumor Promotion and Progression in a Mouse Model of Inflammation-Induced Colon Cancer with Magnetic Resonance Colonography', *Neoplasia*. Elsevier, 11(3), pp. 237-IN1. doi: 10.1593/NEO.81326.
- Yu, A. L. *et al.* (2010) 'Anti-GD2 antibody with GM-CSF, interleukin-2, and isotretinoin for neuroblastoma.', *The New England journal of medicine*, 363(14), pp. 1324–34. doi: 10.1056/NEJMoa0911123.
- Yushchenko, D. A. and Schultz, C. (2013) 'Tissue clearing for optical anatomy', *Angewandte Chemie - International Edition*, 52(42), pp. 10949–10951. doi: 10.1002/ANIE.201306039.
- Zaatiti, H. *et al.* (2018a) 'Tumorigenic proteins upregulated in the MYCN-amplified IMR-32 human neuroblastoma cells promote proliferation and migration', *International Journal of Oncology*. Spandidos Publications, 52(3), pp. 787–803. doi: 10.3892/IJO.2018.4236.
- Zaatiti, H. *et al.* (2018b) 'Tumorigenic proteins upregulated in the MYCN-amplified IMR-32 human neuroblastoma cells promote proliferation and migration', *International Journal of Oncology*. doi: 10.3892/ijo.2018.4236.
- Zabielska-Koczywas, K. *et al.* (2017) '3D chick embryo chorioallantoic membrane model as an in vivo model to study morphological and histopathological features of feline fibrosarcomas', *BMC Veterinary Research*. BioMed Central, 13(1). doi: 10.1186/S12917-017-1114-4.
- Zamora, B. *et al.* (2019) 'Comparing access to orphan medicinal products in Europe', *Orphanet Journal of Rare Diseases*. BioMed Central Ltd., 14(1), pp. 1–12. doi: 10.1186/S13023-019-1078-5/FIGURES/2.
- Zhang, B. *et al.* (2014) 'Upregulation of HIF-1 α by hypoxia protect neuroblastoma cells from apoptosis by promoting survivin expression', *Asian Pacific Journal of Cancer Prevention*. doi: 10.7314/APJCP.2014.15.19.8251.
- Zhang, H. *et al.* (2007) 'HIF-1 inhibits mitochondrial biogenesis and cellular respiration in VHL-deficient renal cell carcinoma by repression of C-MYC activity', *Cancer cell*. Cancer Cell, 11(5), pp. 407–420. doi: 10.1016/J.CCR.2007.04.001.
- Zhang, H. *et al.* (2014) 'MicroRNA-145 inhibits the growth, invasion, metastasis and angiogenesis of neuroblastoma cells through targeting hypoxia-inducible factor 2 alpha', *Oncogene*. doi: 10.1038/onc.2012.574.
- Zhang, J. *et al.* (2015) 'Germline Mutations in Predisposition Genes in Pediatric Cancer', *The New England journal of medicine*. N Engl J Med, 373(24), pp. 2336–2346. doi: 10.1056/NEJMoa1508054.
- Zhang, L. *et al.* (2009) 'In vivo antitumor and antimetastatic activity of Sunitinib in preclinical Neuroblastoma mouse model', *Neoplasia*. doi: 10.1593/neo.09166.
- Zhao, J. *et al.* (2015) 'The emerging role of hypoxia-inducible factor-2 involved in chemo/radioresistance in solid tumors', *Cancer Treatment Reviews*. W.B. Saunders, 41(7), pp. 623–633. doi: 10.1016/J.CTRV.2015.05.004.
- Zhao, S. *et al.* (2020) 'Cellular and Molecular Probing of Intact Human Organs', *Cell*. Cell, 180(4), pp. 796-812.e19. doi: 10.1016/J.CELL.2020.01.030.
- Zhao, X. *et al.* (2018) 'Risk-Associated Long Noncoding RNA FOXD3-AS1 Inhibits Neuroblastoma Progression by Repressing PARP1-Mediated Activation of CTCF', *Molecular*

Therapy. American Society of Gene & Cell Therapy, 26(3), p. 755. doi: 10.1016/J.YMTHE.2017.12.017.

Zhi, Y., Duan, Y., Zhou, X., Yin, X., Guan, Ge, *et al.* (2014) 'NF- κ B signaling pathway confers neuroblastoma cells migration and invasion ability via the regulation of CXCR4.', *Medical science monitor : international medical journal of experimental and clinical research*. International Scientific Information, Inc., 20, pp. 2746–52. doi: 10.12659/MSM.892597.

Zhi, Y., Duan, Y., Zhou, X., Yin, X., Guan, G., *et al.* (2014) 'NF- κ B Signaling Pathway Confers Neuroblastoma Cells Migration and Invasion Ability via the Regulation of CXCR4', *Medical Science Monitor : International Medical Journal of Experimental and Clinical Research*. International Scientific Information, Inc., 20, p. 2746. doi: 10.12659/MSM.892597.

Zhu, S. *et al.* (2012) 'Activated ALK Collaborates with MYCN in Neuroblastoma Pathogenesis', *Cancer Cell*. Cell Press, 21(3), pp. 362–373. doi: 10.1016/J.CCR.2012.02.010.

Van Zijl, F., Krupitza, G. and Mikulits, W. (2011) 'Initial steps of metastasis: Cell invasion and endothelial transmigration', *Mutation Research*. Elsevier, 728(1–2), p. 23. doi: 10.1016/J.MRREV.2011.05.002.

Zipfel, W. R. *et al.* (2003) 'Live tissue intrinsic emission microscopy using multiphoton-excited native fluorescence and second harmonic generation', *Proceedings of the National Academy of Sciences of the United States of America*, 100(12), pp. 7075–7080. doi: 10.1073/PNAS.0832308100/ASSET/9C450999-19ED-4C88-A87E-79FE1190BC5E/ASSETS/GRAPHIC/PQ1232308004.JPEG.

Zosen, D. *et al.* (2021) 'Chicken embryo as animal model to study drug distribution to the developing brain', *Journal of Pharmacological and Toxicological Methods*. Elsevier, 112, p. 107105. doi: 10.1016/J.VASCN.2021.107105.